FROM PROCESSES TO PREDICTIONS IN HYDROLOGICAL MODELLING OF GLACIERIZED BASINS

A Thesis Submitted to the

College of Graduate and Postdoctoral Studies

In Partial Fulfillment of the Requirements

For the Degree of Doctor of Philosophy

In the Department of Geography and Planning

(Centre for Hydrology)

University of Saskatchewan

Saskatoon

By

Caroline Aubry-Wake

PERMISSION TO USE

In presenting this thesis in partial fulfillment of the requirements for a Postgraduate degree from the University of Saskatchewan, I agree that the Libraries of this University may make it freely available for inspection. I further agree that permission for copying of this thesis in any manner, in whole or in part, for scholarly purposes may be granted by the professor or professors who supervised my thesis work or, in their absence, by the Head of the Department or the Dean of the College in which my thesis work was done. It is understood that any copying or publication or use of this thesis or parts thereof for financial gain shall not be allowed without my written permission. It is also understood that due recognition shall be given to me and to the University of Saskatchewan in any scholarly use which may be made of any material in my thesis.

DISCLAIMER

Reference in this thesis to any specific commercial products, process, or service by trade name, trademark, manufacturer, or otherwise, does not constitute or imply its endorsement, recommendation, or favoring by the University of Saskatchewan. The views and opinions of the author expressed herein do not state or reflect those of the University of Saskatchewan and shall not be used for advertising or product endorsement purposes.

Requests for permission to copy or to make other use of materials in this thesis in whole or part should be addressed to:

Head of the Department of Geography and Planning
Kirk Hall Building, 117 Science Place
University of Saskatchewan
Saskatoon, Saskatchewan S7N 5C8 Canada

OR

Dean of the College of Graduate and Postdoctoral Studies
116 Thorvaldson Building, 110 Science Place
University of Saskatchewan
Saskatoon, Saskatchewan S7N 5C9 Canada

ABSTRACT

Glacierized mountain headwaters act as water towers, providing critical water resources to downstream environments when other sources are unavailable. These headwaters are currently witnessing a shift in their coupled hydrological and glaciological systems. This shift is reducing glacier volume, extent and elevation range, in addition to changing the snow dynamics across both glacierized and non-glacierized areas. These interconnected changes occur simultaneously, driven by complex physical feedbacks, and they impact streamflow generation processes.

To properly characterize this transition period and predict future hydrological behaviour in these glacierized basins, physically based glacio-hydrological models representing the full range of both glacier and basin hydrological processes are needed. However, obtaining the data to apply such modelling approaches is complicated by the scarce data availability in mountain regions. New approaches to collect the required data and parametrize these complex processes need to be developed in parallel with increased process representations in glacio-hydrological models.

This thesis aims to assess the impact of future climate and glacier change on glacierized basin hydrological processes and streamflow generation. Its specific objectives are to (1) develop and apply innovative approaches to characterize hydro-glaciological processes in glacierized basins, (2) diagnose hydrological and glaciological processes resulting in streamflow generation and variability and (3) assess the coupled impacts of climate and landscape change on the hydrological processes and streamflow generation in a glacierized basin. Field-based investigations of streamflow measurement uncertainty, sub-debris melt and surface energy balance were conducted and used to guide new and revised algorithms for the Cold Region Hydrological Modelling (CRHM) platform. Using CRHM with the newly added process representations for katabatic wind turbulent transfer, hourly energy balance and sub-debris melt, a physically based glacio-hydrological model was developed and tested in the Peyto Glacier Research Basin, a 53% glacierized headwater basin (as of 2013) located in the Canadian Rockies. This glacio-hydrological model was used to investigate the recent past and current (1990-2020) hydrology of the basin using *in-situ* weather observations. Over the 32 years, strong inter-annual variability in the meteorological forcings caused highly variable streamflow in this cold alpine basin. Snowmelt always provided the largest fraction of annual streamflow (44 to 89%), with lower snowmelt contributions occurring in high streamflow years. Ice melt provided between 10 to 45% of total streamflow, with a higher contribution associated with

high flow years. Both rainfall-runoff and firn melt contributed less than 13% of annual streamflow. Years with high streamflow were on average 1.43˚C warmer than low streamflow years, and high streamflow years had lower winter snow accumulation, earlier snowmelt and higher summer rain than years with low streamflow. The glacier hydrology of current (2000-2015) and future periods (2085-2100) was compared, using bias-corrected, dynamically downscaled, convection-permitting high-resolution atmospheric model outputs. The simulations show that the end-of-century increase in precipitation, mainly expressed as an increase in rainfall at the expense of snowfall, will nearly compensate for the decreased ice melt associated with almost complete deglaciation, resulting in a decrease of 7% in annual streamflow. However, the timing of streamflow will advance substantially, with the timing of peak flow shifting from July to June, and August streamflow dropping by 68%. To examine the sensitivity of future hydrology to possible future post-glacial landscapes, the end-of-century simulations were run under a range of boundary conditions and were most sensitive to initial ice volume and surface water storage. This research provides better modelling techniques to represent the complex systems of headwater glacierized basins, as well as robust estimates of future glacier contributions to streamflow in reference basins of the Canadian Rockies and should be useful for water availability studies and water management mitigation strategies.

ACKNOWLEDGEMENTS

I could not fit the names of everyone I am grateful for in the entire length of this Ph.D. thesis. The doctoral journey is remarkable, and it is only possible because of the support of countless individuals. But this thesis is already very long, so I will keep it short. First, thank you to my supervisor John Pomeroy for his guidance and support along this incredible scientific journey. His attention to detail, high scientific standards, and his care for precise wording was balanced by enough space and freedom to explore my ideas. Thank you to my committee members, for their helpful insights to improve this dissertation and the honest, but sometimes tough, questioning to get there.

Thank you to Joni Onclin and Phyllis Baynes for their invaluable travel and logistic support throughout my Ph.D. I could not navigate the paperwork and online systems without your help.

Thank you to my friends and colleagues at the Coldwater Laboratory and Centre for Hydrology for the good chats, scientific exchanges, and inspiration. Thank you to my co-authors for the multiple discussions, rounds of edits and comments to improve my science. And thank you to all my science friends dispersed across the world, with whom the few interactions on Zoom, via emails and at conferences are not enough. I look forward to more interactions and collaborations in the future!

Thank you to all the wonderful individuals with whom I interacted through the Canadian Young Hydrologic Society, Girls* on Ice Canada and Inspiring Girls* Expeditions. The opportunities to grow and develop new skills while being part of these wonderful and supportive communities made a huge difference in my Ph.D. journey.

Thank you to my adventure partners. Sharing a rope, a trail or an uptrack while sharing fun facts about the mountains allowed me to find a necessary balance with my science work.

And most of all, infinite thank you to my partner Tom and my family, who have been supportive, curious, and patient.

TABLE OF CONTENTS

LIST OF TABLES

LIST OF FIGURES

1. INTRODUCTION

1.1. Background and literature review

1.1.1. Motivation

Mountains are an important part of the Earth system as sources of water, energy, minerals, forests and agricultural products, as well as areas of recreation. They are seeing rapid changes, amplified by elevation-dependent air temperature warming (Pepin *et al.*, 2015). These rapid changes are threatening the snow and ice found in many mountain ranges and the downstream population relying on these water resources (Beniston, 2003; Barnett *et al.*, 2005). For example, in Western Canada, the glacierized Canadian Rockies form the headwaters of some of the largest rivers in the country, providing critical water resources across North America. In these headwater systems, glacier meltwater contributes up to 50% of the late summer flow, when water demand is at its highest (Naz *et al.*, 2014). Meanwhile, the number of people who depend on mountain water resources is expected to increase (Viviroli *et al.*, 2020).

Mountain climates are in a transition phase, moving towards a situation where permanent snow and ice volumes and cover will be strongly reduced (Huss *et al.*, 2017). In recent decades, alpine glacier loss has accelerated globally (Hugonnet *et al.*, 2021). Most mountain glaciers will lose up to one-third of their volume to achieve an equilibrium with the current climate (Mernild *et al.*, 2013), and in some low-latitude mountain ranges, glaciers have already disappeared (Rabatel *et al.*, 2013). Based on multiple studies, by the end of the 21st century, glacier loss is expected to reach 30% in Alaska, 50% in high-mountain Asia and 80% in the European Alps and low-latitude South American Andes compared with their 2010 volume (Huss *et al.*, 2017). Glaciers in the Canadian Rockies have already lost up to 15% of their area since 1985 (DeBeer and Sharp, 2007; Bolch *et al.*, 2010) and are projected to continue this decrease, with a predicted loss of 90% of the 2005 volume by 2100 (Clarke *et al.*, 2015).

As glaciers retreat, many human systems are impacted such as agriculture, hydropower, potable water, recreation, spirituality and demography (Carey *et al.*, 2017). In addition to threatening water resources by decreasing streamflow in summer, glacier retreat increases the risk of natural hazards in mountain communities, especially glacial lake outburst floods (Frey *et al.*, 2010). Glacier retreat is also impacting the biochemical processes of alpine lakes and streams (Milner *et al.*, 2017). As agents of erosions, glaciers deliver sediments and nutrients downstream (Hudson and Ferguson, 1999; Hood

et al., 2015; Milner *et al.*, 2017). They also help to maintain a unique thermal regime in glacier lakes and streams (Milner *et al.*, 2001; Lencioni *et al.*, 2015). Globally, mountain glaciers contribute to sea-level change, accounting for between one-third and one-half of global sea-level rise during the last decades, and contributing substantial uncertainty to this rise (Kaser *et al.*, 2006; Cogley, 2009; Gardner *et al.*, 2013; Hock *et al.*, 2019).

1.1.2. Mountains as water towers

Mountains are widely regarded as the "water towers" of the world, expressing the importance of mountains for providing fresh water for the adjacent areas downstream (Viviroli *et al.*, 2007; Immerzeel *et al.*, 2020). Compared to their downstream areas, mountains generate higher runoff from rain due to the orographic effects of precipitation. Due to their higher elevation and colder temperature, they seasonally store water as snow and ice and release it in warmer and drier seasons where other sources of water are limited. A key component of this buffering capacity is the presence of glaciers in the mountain system.

Glaciers significantly affect the hydrology of a basin at multiple scales, impacting both the quantity and timing of streamflow even with a small glacier area in the basin (Meier and Tangborn, 1961; Fountain and Tangborn, 1985; Hopkinson and Young, 1998; see Jansson *et al.*, 2003 for review). Glacier runoff contributions to streamflow can exceed 25% of monthly river runoff, even in basins where the glacierized area is less than 1% (Huss and Hock, 2018). On a daily timescale, streamflow in glacierized basins will have a pronounced melt-induced peak discharge. At the seasonal scale, glaciers act as reservoirs, accumulating precipitation in the winter and spring as snow, and slowly releasing water through the summer season. Glacier meltwater is typically not a large contributor to streamflow on an annual basis but can have significant importance on a seasonal basis. This is well illustrated in a study of glacier melt and wastage contribution to river discharge in the North and South Saskatchewan Rivers, originating in the Canadian Rockies, by Comeau *et al.* (2009). It is important to differentiate between glacier melt and wastage when considering the contribution of glacier snow and ice meltwater to downstream hydrology. Glacier wastage is defined as the volume of ice and firn melt exceeding the annual volume of snow accumulation on the glacier and causing an annual net loss of glacier volume, while the melt component is defined as the glacier melt volume that is equal to, or less than, the water equivalent volume of snow that accumulates into the glacier system in a hydrological year, as in Comeau *et al.*, (2009). Annually, the contribution of glacier wastage to streamflow is low; glacier wastage in the headwater of the North and South

Saskatchewan River, in the Canadian Rockies, provides under 3% of annual streamflow to the downstream cities of Calgary and Edmonton. Seasonally, glacier melt contribution to streamflow becomes more important, with the relative glacier melt contribution to streamflow depending on the glacierized area in the headwater basin. Glacier melt contribution to streamflow was greater than 60% for basins with greater than 10% glacierized areas but decreased to less than 16% for basins with 1% glacierized area (Comeau *et al.*, 2009). Glacier wastage also helps to buffer inter-annual streamflow variability, as glaciers accumulate snow and ice during wet, cool years, and release more water in dry, warm years (van Tiel *et al.*, 2021). However, this inter-annual buffer capacity is not constant; based on a study in the Canadian Rockies, Hopkinson and Young (1998) showed that glacier meltwater does not always augment streamflow during low-flow, "dry" years. This supports research showing that during cold years, glacier meltwater can be significantly reduced and induce "glacier melt drought" (Van Loon *et al.*, 2015; van Tiel *et al.*, 2020a). Both these results provide hints about the complex interactions between glacier melt, streamflow generation and seasonal meteorological conditions.

1.1.3. Beyond peak water

Mountain glaciers around the world are in a transition phase, losing mass quickly. They are expected to lose up to 90% of their ice volume by the end of the century (Huss *et al.*, 2017). The impact of glacier retreat on glacier runoff is commonly explained by the concept of peak water (Baraer *et al.*, 2012). As glaciers lose mass, their contribution to streamflow first increases, to a "peak water" level, after which glacier runoff steadily decreases as the glacier volume becomes too small to maintain a significant glacier contribution to streamflow. This "peak water" threshold value is an important signal to point out a regime shift and indicates the probable future behaviour of the glacier-fed stream (Jansson *et al.*, 2003; Moore *et al.*, 2009; Baraer *et al.*, 2012). In a global analysis of peak water timing, Huss and Hock (2018) found that this tipping point has already passed in approximately half of the world's glacierized macro-basins. This is also reflected in a review of glacierized basin streamflow trends across the globe by Casassa *et al*. (2009), which report varying streamflow trends for the last few decades. In Canada, a north-south trend is noticeable, with flows in the southern glacierized basin reported to be decreasing (Hopkinson and Young, 1998; Stahl and Moore, 2006), but increasing in the northwestern Canadian mountains (Déry *et al.*, 2009; Moore *et al.*, 2009). In Switzerland, summer streamflow trends in glacierized basins were linked to the extent of glacier cover; most basins with more than 10% glacier cover showed increasing summer streamflow, while basins with less than 10% glacier cover have exhibited negative trends (Birsan *et al.*, 2005), trends

that are also noticeable across the European Alps (Casassa *et al.*, 2009). For Central Asia mountain river basins, peak water has not yet been reached, as shown by increasing streamflow trends (Lutz *et al.*, 2014). However, these estimates are uncertain in this transitional climate and differ depending on measurement methods and timescale. For example, Baraer *et al.* (2012) found that peak water was already past in 7 out of 9 watersheds in the Cordillera Blanca (Peru), and peak water possibly reached as early as the 1960s, which contradicted previous findings by Pouyaud *et al*. (2005), who reported increasing trends and suggested peak water is not past yet for the same area. This conceptual understanding is seen in various glacierized headwater basins around the globe, but the timing, volume and amount of this change in streamflow are highly variable and are dependent upon local climate and basin characteristics (Bliss *et al.*, 2014; Huss and Hock, 2018).

The "peak water" signal can be difficult to detect, because of the simultaneous changes in precipitation amount, timing and phase happening in alpine basins and because of the wide range of alpine hydrological processes, including snow hydrology, that strongly influence streamflow from glacierized basins. Even though glaciers have a strong influence on streamflow generation in headwater glacierized basins, other hydrological processes are at play. Therefore, even a robust estimate of the change in glacier volume and meltwater generation due to a changing climate will not give a complete picture of changes. Specifically, other cold-region hydrological processes, such as snow accumulation and ablation, infiltration in seasonally frozen soils, groundwater storage and flow, potential permafrost, and changing land cover type as glaciers retreat, also have to be included in a hydrological assessment of glacierized headwater basin.

This peak water signal is also not easily detected when future changes in glacier-fed basins are analyzed. When predicting future streamflow trends associated with glacier retreat, results are highly variable, and highly depend on basin characteristics (Bliss *et al.*, 2014; Huss and Hock, 2018). Globally, glacier runoff (including snowmelt and precipitation on the glacier), is expected to increase in June, but to decrease in July and August (Huss, 2011; Huss and Hock, 2018). Both glacier melt and wastage are expected to have less importance to streamflow composition, with a shift towards snow and rain (Horton *et al.*, 2006; Jeelani *et al.*, 2012). These global results are supported by regional studies. Ragettli *et al.* (2016) projected rising flows with limited shifts in the seasonality for the Langtang basin in the Himalayas but found a reduced and shifted peak in streamflow for the Juncal basin in Chile. Flow in the High Asian mountain rivers is expected to increase in the future, due to increasing precipitation (Immerzeel *et al.*, 2013; Lutz *et al.*, 2014), but with intra-seasonal shift

caused by a decrease in summer flows and an increase in other season flows (Lutz *et al.*, 2016). In Oregon, U.S.A. Frans *et al.* (2016) found an opposite trend, with glacier runoff decreasing by 78% from current averages by 2100. In the Cordillera Blanca, Peru, Juen *et al.* (2007) found that the mean annual runoff barely changes, but seasonality intensifies, with increased runoff in wet seasons, and decreased runoff in dry seasons. Farinotti *et al*. (2012) found both trends for the period 1900-2100 for multiple glacierized basins in Switzerland, with increasing streamflow to peak water, followed by a decrease. Large uncertainties in these predictions are caused by the global climate models used, with varying results depending on the period considered or the GCM used (Duethmann *et al.*, 2016). For example, Lutz *et al.* (2016) pointed out the inability of current GCMs to represent the complex climate of High Mountain Asia and the propagation of uncertainty in future climates for future hydrology. Therefore, there is currently a need to expand upon the concept of peak water to include other processes that can obscure, and even mask, the glacier melt signal in glacierized basin hydrological response to climate change.

1.1.4. Alpine glacierized basin hydrological processes

Alpine glacierized basins are complex, with multiple hydrological processes interacting, enhancing, or compensating their effects on the streamflow. A brief overview of the processes acting in headwater-glacierized basins is described below and illustrated in Figure 1.1.

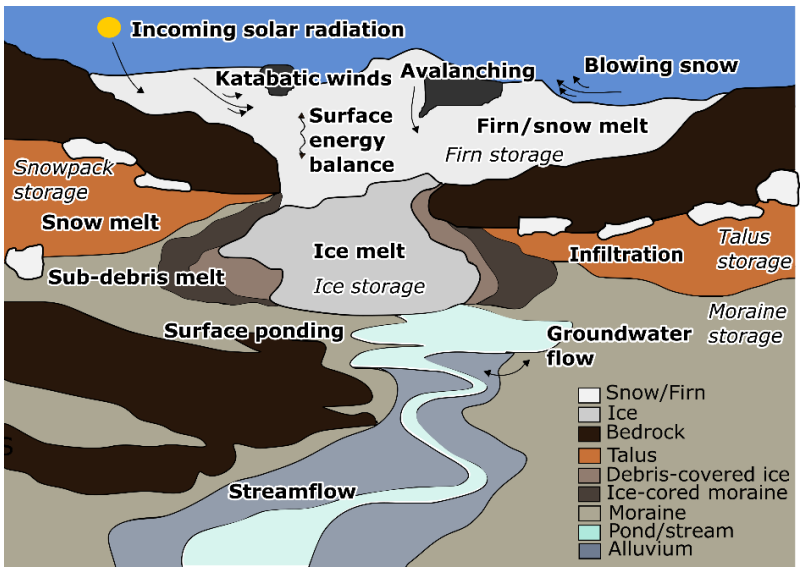

Figure 1.1. Conceptual illustration of the range of hydrological processes occurring in a glacierized alpine basin. Mass and energy fluxes are shown in bold and storages are in italic.

The mountain climate is driven by their steep and complex topography, which includes some of the sharpest gradients found in continental areas (Beniston, 2003). These steep elevation gradients drive changes in temperature and precipitation over short distances. Because temperature decreases with altitude by 5–10 ˚C km^{-1}, mountain environments have colder air temperatures. This allows precipitation and accumulation of snow, which over time, transforms into glacier ice by metamorphosis and compaction. Mountains also typically have higher precipitation than adjacent lowlands due to orographic precipitations, where moist air masses are forced upwards against the mountainside, causing condensation and precipitation (Roe, 2005). Due to the complexity of the topography, local effects can significantly alter the global and regional climate signal. For example, glacier winds, or katabatic winds, significantly alter the temperature gradient in glacierized mountain ranges (Ayala *et al.*, 2017) and the presence of the steep topography modifies wind speed and direction (Taylor and Lee, 1984; Musselman *et al.*, 2015). The complex topography also alters the energy reaching the surface. Varying slope and aspect, as well as shading from surrounding topography, results in a complex and variable radiation balance (Marsh *et al.*, 2012), and preferential energy available for melt for both snow and ice surfaces.

This complex topography also causes complex snow accumulation and redistribution patterns, resulting in a snow accumulation pattern that can depend as much on elevation and local topography

(DeBeer and Pomeroy, 2009). Preferential snowfall deposition of snow in sheltered areas, erosion and deposition of snow by the wind as well as sloughing and avalanching commonly occur in mountain environments with steep slopes, strong winds, and low vegetation cover. These snow redistribution processes cause variable snow cover at a spatial scale up to one kilometre (Kuhn, 2003; Clark *et al.*, 2011). Wind-driven snow redistribution, or blowing snow, via saltation and suspension, does not only result in a spatially variable snowpack but also leads to a net loss of the snowpack due to the sublimation of snow particles during transport (Pomeroy and Gray, 1990; Pomeroy and Male, 1992). MacDonald *et al*. (2010) found that blowing snow sublimation amounted to a net loss of 17-19% of cumulative snowfall near an alpine ridge environment in the Canadian Rockies. Snow avalanching and sloughing following gravity is essential to redistribute high-elevation snow accumulation to a lower area, where it is exposed to higher temperatures, and contributes to lower-elevation snow accumulation and meltwater production (Ragettli *et al.*, 2015; Shea *et al.*, 2015).

The melt of seasonal snow and glacier ice M is dictated by the energy available for melt Q_m (Eq. 1.1). The energy available for melt is calculated from the surface energy balance, the sum of the incoming and outgoing energy fluxes, with positive fluxes towards the surface layer (Eq. 1.2, Figure 1.2).

$$M = \frac{Q_m}{\rho_w L_f} \tag{1.1}$$

$$Q_m = SW_{net} + LW_{net} + Q_h + Q_e + Q_r + Q_g - \frac{dU}{dt} \tag{1.2}$$

Where ρ_w is the density of water (1000 kg m^{-3}) and L_f is the latent heat of fusion (334 J g^{-1}). SW_{net} is the net shortwave radiation, LW_{net} is the net longwave radiation, Q_h is the sensible heat flux and Q_e is the latent heat flux, Q_r is the energy from advection from precipitation, Q_G is the energy conducted into the ice or snow and dU/dt is the change in internal energy of the snow layer. For mid-latitude alpine glaciers, a common approach is to assume isothermal ice and neglect conduction into the ice layer. The sum of the fluxes results in the energy available for melt, Q_m (all in W m^{-2}).

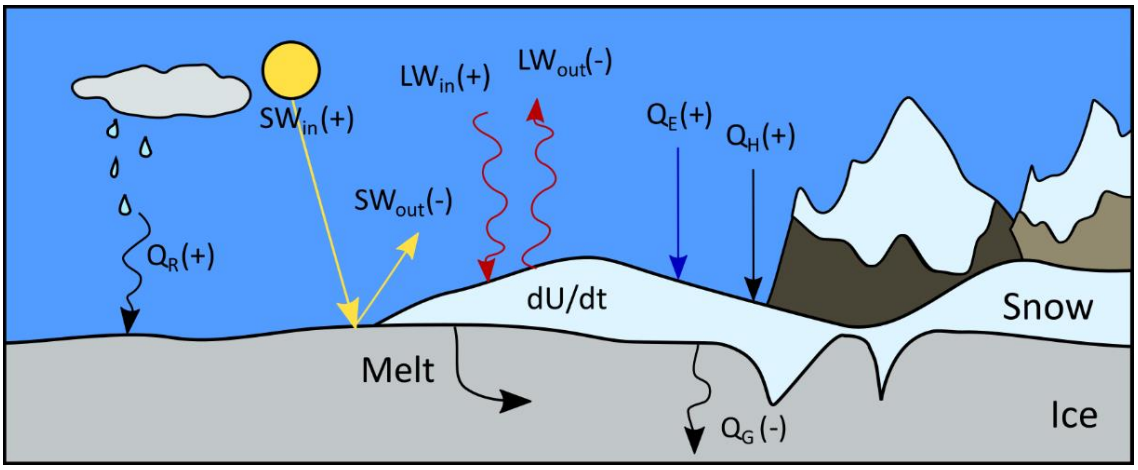

Figure 1.2. Energy fluxes of snow and/or ice surface layer with positive fluxes towards the surface, SW_{in} is the incoming shortwave radiation, SW_{out} is the reflected shortwave radiation, Q_r is the energy from precipitation, LW_{in} is the incoming longwave radiation, LW_{out} is the outgoing longwave radiation, Q_e is the latent heat flux, Q_h is the turbulent heat flux, Q_g is the conduction into the snow or ice flux, and dU/dt is the change in internal energy of the snow layer. All fluxes are in Wm^{-2}. When positive, the sum of the fluxes leads to melt. For the snow, the control volume is the entire snowpack due to the change in internal energy. For the ice, the control volume is just the surface.

As the surface temperature of the snowpack reaches the melting point, the meltwater percolates through the snowpack, forming flow fingers, and sometimes refreezing in the cold snowpack. As it refreezes, it releases latent heat, which warms the snowpack. Once the entire snowpack reaches the melting point, all snowmelt is then available for infiltration or runoff. The snowmelt can refreeze at the snow-ice interface, causing superimposed ice layers, a process that predominantly occurs on polar glaciers or at very high altitudes and is negligible for mid-latitude mountain ranges (Schneider and Jansson, 2004; Samimi and Marshall, 2017; Stigter *et al.*, 2021). When glacier ice is present below the snow, the disappearance of the snowpack results in surface glacier melt, which depends on the energy available for melt, mainly originating from incoming solar radiation and strongly depending on the surface albedo. The surface of the snowpack and glacier can also sublimate, reducing the energy available for melt. Snow surface sublimation has however been shown to be an important component of the snow budget in the high mountains such as the Himalayas (Mott *et al.*, 2018; Stigter *et al.*, 2018) but also for ice surface in tropical regions (Winkler *et al.*, 2009). Additional factors, such as the presence of debris cover or light-absorbing impurities on the ice surface, can significantly affect the surface energy and mass balance of the glacier and snow surface (Skiles *et al.*, 2018).

A key process of glaciers is their capacity to flow downhill, following two processes: deformation (creep) of the ice crystal within the glacier and movement at the bed surface by sliding or

deformation of subglacial sediments. Deformation of the ice crystals is due to gravity and the weight of the overbearing ice. The rate of internal deformation changes with glacier depth, with the highest rates of deformation near the base and valley walls. The fastest ice movement is observed near the surface, and the slowest is near the base and valley walls (Jiskoot, 2011). The driving stresses of glacier flow are functions of gravity and ice thickness, as well as the ability of ice to deform. Sliding can only happen in a temperate or polythermal ice regime, with water present at the glacier base. Temperate glaciers are common for mid-latitude and mountain glaciers. Ice melts under pressure, and therefore basal water can be found due to overbearing ice and bedrock roughness (Benn and Evans, 1998). Ice flow transfers mass from high altitude to lower altitude, partially replenishing glacier loss in ablation areas and slowing glacier retreat rates. At the same time, glaciers respond to changes in surface mass balance by retreating to higher elevations and colder air temperatures.

Once the snow has melted off the glacier surface, evaporation occurs from sediments and open water surfaces, as well as transpiration from vegetation. Evaporation occurs when enough energy is available to produce a phase change between liquid (or solid) and vapour, and the air above the surface is sufficiently dry, causing a gradient in water vapour pressure between the surface and the atmosphere. As there is only minimal vegetation (lichen, moss) in these headwater glacierized basins, there is very little transpiration. With glacier retreat and earlier snowmelt, open surface water is becoming more common in glacierized basins, increasing open water evaporative loss. Lakes often fill the depressions left behind by glacier retreat, and water from snowmelt infiltrates the proglacial field, changing the amount of evaporation happening in the basin (Shugar *et al.*, 2020).

Some of this meltwater, and direct rainfall, will infiltrate the ground to form sub-surface storage and runoff, and some might flow as surface runoff. The separation of these components between infiltration and surface runoff depends on the type of ground cover, with many factors such as its hydraulic conductivity, the presence of ice in pore space, the water storage capacity and the presence of preferential flow path. In these headwater glacierized basins, the non-glaciated area is composed of rock debris and exposed bedrock. The debris range from talus field located below cliffs, moraine sediments, and alluvium. Alluvium is found in the braided stream channel below the glacier and is typically composed of fine sediments to coarse rocks deposited by water movement. Infiltration into frozen soils is less studied, but the presence of ice in pore space limits the infiltration rate and can restrict infiltration. As meltwater infiltrates in frozen soil and refreezes, it releases latent heat, adding energy the frozen ground. Frozen soil can be classified into three categories (Granger

et al., 1984): unlimited, where considerable preferential path controls infiltration, limited, where infiltration depends on both snow water equivalent and water/ice content in the top soil layer, and restricted, where ice lenses near the surface prevent infiltration. In the coarse debris from the talus field, infiltration into frozen soils is likely to be unlimited due to the large spaces between the debris. In the moraine and alluvium debris, infiltration is likely to be limited or restricted due to the smaller sediment size. The infiltrated water contributes to the soil moisture reservoirs, from which interflow or percolation to the groundwater reservoirs occur. The combination of surface runoff, subsurface runoff, and groundwater discharge travels through the basin and makes its way to the stream network and the basin outlet.

1.1.5. Modelling glacierized basin hydrology

Glacio-hydrological models can be grouped into two broad categories based on their dominant focus: hydrology-based or glaciology-based models. van Tiel *et al.* (2020b), in a review of 145 glacio-hydrological modelling studies, show that the level of process representation in glacio-hydrological models is typically related to the focus of the study and the model legacy. Hydrology-based models often have detailed off-ice representations but minimal glacier representations and are typically applied to large basins with low glacier coverage. An example of such a model is found in Comeau *et al*. (2009), who use the hydrological model WATFLOOD (Kouwen, 1988), a semi-distributed model with a temperature-index melt algorithm for snow and ice melt, to study the South and North Saskatchewan River basins, extensive basins with low glacier coverage. Instead of including a glacier flow model, the model was run with different initial glacier cover representatives of different periods. A similar approach is to use a stand-alone glacier dynamics model to force the glacier extent in a hydrological model simulation, at specific intervals, typically decadal, such as in Jost *et al.* (2012). At the other end of the spectrum, complex cryosphere models, with a focus on snow and ice representation, can be developed to include off-glacier processes. These models with complex flow models often use temperature index models for glacier melt (Huss *et al.*, 2010; Immerzeel *et al.*, 2012; Clarke *et al.*, 2015), which are based on a calibrated factor relating surface melt and daily air temperature, are not reliable for use outside of their calibration condition, which is problematic for predictions. In addition, these models typically focus on glacier runoff and less on basin hydrology.

A third glacio-hydrological model type emerges from ongoing model development: a hybrid model with both hydrological and glaciological process representation at a similar level of complexity. For example, Naz *et al.* (2014) develop a fully-coupled glacio-hydrological model, combining the

distributed hydrology soil vegetation model, DHSVM (Wigmosta *et al.*, 1994) with the GDM ice dynamic model (Jarosch *et al.*, 2013). The DHSVM model is physically based and spatially distributed and includes snowmelt, evapotranspiration, and analytical representations for routing of surface and subsurface flow with a glacier surface energy balance and flow dynamics. Frans *et al*. (2016) further developed the model by including the ice dynamic scheme from Clarke *et al*. (2015) and debris-covered ice melt from Reid and Brock (2010). Similarly, The Cold Region Hydrological Modeling platform (CHRM) (Pomeroy *et al.*, 2007) can represent the physical processes driving glacier melt and other cold-region hydrological processes such as snow redistribution by wind and avalanching. CHRM is a flexible object-oriented, process-based modelling platform (Pomeroy *et al.*, 2007) and has been extensively used in mountains recently, with applications over different terrain and climate and at different spatial scales (DeBeer and Pomeroy, 2009; MacDonald *et al.*, 2010; Fang *et al.*, 2013). A glacier module has recently been developed to represent ice and firn melt using an energy-balance approach, sub-glacial runoff routing and ice flow using a 1D flowline methodology (Pradhananga and Pomeroy, 2022a). TOPKAPI-ETH is another example of a process-oriented glacio-hydrological model widely used in mountainous, high-altitude basins, but with simple basin hydrology representation and limited ice dynamics (Finger *et al.*, 2011; Ragettli *et al.*, 2013, 2015, 2016; Fatichi *et al.*, 2014). It operates at an hourly timescale, with grid-cell at high resolution (100m), but it uses an enhanced temperature-index melt model for snow and ice melt and includes routines for debris-covered ice, avalanching and topographic shading. Despite its high complexity for glacier melt modelling, it uses a relatively simple representation for non-glacierized areas, typically including only potential evapotranspiration and using linear soil water storage and recharge as calibration parameters (Immerzeel *et al.*, 2012).

However, despite these hybrid glacio-hydrological models being further developed to include the range of processes occurring in mountain basins, studies incorporating both the complex physically based glacier and hydrological components are still uncommon. As described above, the range and complexity of processes occurring in glacierized mountain basins are high. The knowledge of these processes is typically developed from detailed, field-based studies. Building upon these field-based studies, parametrization of varying complexity can then be developed. However, there is typically a disconnect between these complex process representations developed in data-rich environments and their inclusion in glacio-hydrological models. For various reasons, from lack of data, uncertainty linked to parametrization, or lack of computational power leads to the incorporation of lower complexity process representation than the state of knowledge of these processes. To showcase this

disconnect between mountain hydrology process understanding in process representation in glacio-hydrological models, five topics are further discussed. First, the different approaches used to obtain meteorological forcings for current and future simulations in mountain terrain, followed by four hydrological processes occurring in mountain basins: blowing snow redistribution, surface snow and ice melt, ice melt under debris, and groundwater flow and routing.

1.1.5.1. *Mountain meteorology*

As discussed in the previous sections, the complex topography of mountain landscapes causes a highly localized and variable meteorology. The high variability of precipitation and temperature lapse rate has been showcased in many studies (Rolland, 2003; Minder *et al.*, 2010; Petersen and Pellicciotti, 2011; Immerzeel *et al.*, 2014b; Shen *et al.*, 2016; Kattel and Yao, 2018), as well as the complex shading effect linked with topography (Marsh *et al.*, 2012; Olson and Rupper, 2019). This complexity is somewhat reflected in the large number of approaches used to extrapolate limited meteorological records to the rest of the basin in glacio-hydrological models (van Tiel *et al.*, 2020b). For periods or locations with no available observations or incomplete records, atmospheric models are used, such as reanalysis datasets (Dee *et al.*, 2011; Hersbach *et al.*, 2020), available at regional (30-50 km) scales. This regional scale flattens out the topography and therefore, is unable to reproduce the complex meteorological patterns occurring in mountain regions. A spatial and temporal downscaling must be performed to obtain data at a local or basin scale. Downscaling approaches are classified into two groups: dynamical downscaling and statistical downscaling, both with their advantages and disadvantages as reviewed by Fowler *et al.* (2007). Comparing downscaling approaches to assess the impacts on hydrological model performance has been an ongoing research topic over the last decades (Hay and Clark, 2003; Gutmann *et al.*, 2012; Li *et al.*, 2016; Mizukami *et al.*, 2016). Dynamical downscaling is associated with the use of numerical weather prediction models, which can resolve atmospheric processes using physically based equations at a high spatial and/or temporal resolution using lateral boundary conditions from larger-scale reanalysis products,. Dynamically downscaled products at a convection-permitting resolution, widely regarded as a 4x4 km grid, allows for a more realistic topography and permit convection and orographic precipitations (Prein *et al.*, 2013; Rasmussen *et al.*, 2014; Liu *et al.*, 2017). An example of this approach is the Weather and Forecasting (WRF) model (Skamarock *et al.*, 2008), which has been used to created improved atmospheric forcings at convection-permitting scales in Colorado (Rasmussen *et al.*, 2011, 2014), the Himalayas (Collier and Immerzeel, 2015; Potter *et al.*, 2018), the Cordillera Blanca (Fyffe

et al., 2021), and for interior North America (Liu *et al.*, 2017). However, dynamically downscaling at a convective-permitting resolution is computationally expensive, which limits the number, and lengths, of runs that can be done.

On the other hand, statistical downscaling establishes a long-term statistical relationship between the large-scale data and the locally observed weather, obtained from in-situ observation. This statistical downscaling can rely on weather generators, numerical tools often using stochastic-statistical approaches to derive synthetic time series of various meteorological variables based on historical observations (Papalexiou *et al*., 2011; Papalexiou, 2018). This approach has many advances in recent decades, and can be computationally efficient, but continues to face issues related to underlying data uncertainty, representation of extreme values and the interpretation of future scenarios (Beven, 2021).

To obtain meteorological forcings under future climates, similar downscaling procedures need to be applied to outputs from General Circulation Models (GCMs).. GCMs are gridded, numerical coupled models representing the various Earth systems including the atmosphere, oceans, land surface and sea-ice. These models are forced with greenhouse gas concentration scenarios, referred to as Representative Concentration Pathways (RCPs). Four RCPs exist (2.6, 4.5, 6 and 8.5), where the number indicates the increase in radiative forcing (W m^{-2}) by 2100 relative to pre-industrial values, and represent different trajectories for anthropogenic greenhouse gas emissions, energy use, population growth and land use (Collins *et al*. 2013).

Because of the high computational cost of processing GCMs, these products are only available at a coarser scale, which does not resolve sub-grid scale features such as topography, clouds and land use (Grotch and MacCracken, 1991). They also parameterize convection in their precipitation physics and so cannot represent extreme precipitation spatiotemporal dynamics and phase (snowfall or rainfall) accurately. The GCMs outputs have to be downscaled to be representative or regional to local weather patterns. At the regional scale, regional climate models (RCMs) can be used to dynamically downscale GCMs outputs to account for sub-grid forcing such as topography and enhance the simulation of atmospheric and climatic variables at a finer spatial scale. In the last 30 years, the horizontal grid at which RCMs have been applied has gradually decreased from the commonly-used 50 km to 12 km (Giorgi, 2019). RCMs can realistically simulate regional climates such as orographic precipitation (Frei *et al.*, 2003), extreme climate events (Fowler *et al.*, 2005; Frei *et al.*, 2006) and regional scale climate anomalies, such as El Nino (Leung *et al.*, 2003). With mounting

evidence indicating the importance of having convection-permitting scales (~4km horizontal scale) (Prein *et al.*, 2015), and increased computational powers, the scale between typically-applied RCMs simulation and weather-prediction models such as WRF is shrinking. This is showcased by recent, RCMs simulations conducted at a 3km scale in the greater Alps region (Ban *et al.*, 2021; Pichelli *et al.*, 2021). However, large and systematic bias can persist in RCMs, from an imperfect representation of physical processes, numerical approximations, and other assumptions. Convection-permitting RCMs simulations available over long periods are not a common feature in mountain regions.

A popular approach to generate inputs for hydrological models to analyze the impact of climate change on mountain hydrology is to statistically downscale GCMs outputs into a finer resolution following a "perturbation", or "delta-change" approach. Differences between the control and future GCM simulations are applied to baseline observations by adding or scaling a change factor (Farinotti *et al.*, 2012; Huss *et al.*, 2014; Lutz *et al.*, 2016; Khanal *et al.*, 2021). Built upon this approach is the pseudo-global warming (PGW) method, where a change factor derived from GCMs simulation is added to reanalysis data, and dynamically downscaled to convection-permitting scales in numerical weather predictions models such as WRF (Rasmussen *et al.*, 2011; Liu *et al.*, 2017; Fang and W. Pomeroy, 2020). Other statistical downscaling approaches include regression models, or as mentioned previously, weather generator models (Fowler *et al.*, 2007).

In a non-stationary climate, such as experienced in the high-altitude mountain environment, dynamical downscaling, based on physical equations, presents a large advantage over statistical downscaling. However, this dynamically downscaled approach is not widely used in glacio-hydrological modelling approaches, which often relies on statistically downscaled RCMs or GCMs at coarse resolutions. With increasing available computational power, common limitations of dynamically downscaled products, such as the lack of uncertainty assessment from multi-model ensemble simulations and their typical short duration, are beginning to be addressed, but more work is needed to comprehensively assess their performance for their use in glacio-hydrological simulations.

1.1.5.2. *Snow redistribution by wind and gravity*

It is now increasingly common to include snow sublimation in snow transport and snowpack models (Zwaaftink *et al.*, 2011; Vionnet *et al.*, 2014; Weber *et al.*, 2016; Marsh *et al.*, 2020a; Vionnet *et al.*, 2021) and in some process-based hydrological models (Pomeroy *et al.*, 2007; Rasouli *et al.*, 2014,

2015; Krogh *et al.*, 2017; Fang and Pomeroy, 2020; Marsh *et al.*, 2020b). However, these developments in snow sublimation and transport algorithms are not typically explicitly accounted for in many basin-scale hydrological models (e.g. Freudiger *et al.,* 2017). For example, Naz *et al*. (2014) designed a coupled glacier dynamic and distributed hydrological model for the Upper Bow Valley basin in the Canadian Rockies but did not mention process representation for snow transport. Similarly, Comeau *et al*. (2009) and Chernos *et al.* (2020) simulated the glacier contributions to streamflow in the North and South Saskatchewan Rivers, both basins containing cold, snow-dominated headwater areas, and do not mention blowing snow transport and sublimation in their modelling approach.

This disconnect between, and within, the snow hydrology community and the glacio-hydrological community likely stems from the related issues of data availability and model complexity. In addition, the varying snow redistribution representation in hydrological models likely results from the environment in which they were developed – a conceptual snow model able to mimic temperate snowmelt but lacking representation of snow physic will likely fail in cold regions, while they might perform reasonably in warmer regions. Most blowing snow transport and sublimation algorithms require a detailed representation of the wind flow over complex topography to compute the mass exchange between the snowpack and the atmosphere (Mott and Lehning, 2010; Vionnet *et al.*, 2014). For example, Musselman *et al.* (2015) showed that simulated snow sublimation calculated with the Prairie Blowing Snow Model (Pomeroy and Li, 2000) along an alpine ridge in the Canadian Rockies using wind fields from a computational fluid dynamics model outperformed an empirical parametrization of complex terrain wind flow. Vionnet *et al.* (2021) used pre-computed wind fields to perturb winds over large regions and showcased the importance of correcting wind speed and direction to account for the influence of topography and capture snow cover heterogeneity in mountain terrain. The level of complexity of these snow models, with associated data requirements and computational cost, is typically at odds with the goals of many conceptual glacio-hydrological modelling studies (Freudiger *et al.*, 2017). These glacio-hydrological models often applied in data-poor regions and using calibrated melt factors, can produce reasonable estimates of streamflow while ignoring snow redistribution processes, and therefore likely being right for the wrong reason and have weak predictive capabilities.

1.1.5.3. *Surface melt*

Considering that the main objective of most glacio-hydrological models is to assess snow and ice melt contribution to streamflow, the snow and ice melt representation can be considered the most important component of glacio-hydrological models.

Incoming shortwave radiation tends to dominate the energy budget and ablation patterns of glaciers. As mentioned above, the complex topography of mountain landscapes causes strong variation in the radiation budget and the radiation reaching the surface. Another strong control on the radiation budget is the surface albedo, which varies in space and time for both snow and ice. Including an explicit albedo parametrization allows the inclusion of changes in the surface albedo caused by ageing snow, dust deposition, or soot from forest fires (Skiles *et al.*, 2018). Longwave radiation is especially important under cloudy conditions, or when surrounded by steep mountain walls that reflect and emit longwave radiation (Sicart *et al.*, 2006). Net radiation, the main energy source to the glacier surface, can be reliably measured and spatially distributed using elevation models to replicate shading, slope, and aspect with reasonable accuracy (Munro, 2004).

The turbulent fluxes (sensible heat flux Q_h and water vapour associated with the latent heat flux Q_e) are more challenging to accurately measure. Eddy covariance (EC) systems provide the capacity to directly measure the flux in the field (Munro, 1989; Cullen *et al.*, 2007; Litt *et al.*, 2014; Fitzpatrick *et al.*, 2017; Radic *et al.*, 2017). These measurements are typically limited in time from a few days to a few weeks due to both the fragility and sensitivity of these instruments installed in harsh glacier conditions. The more common method to calculate turbulent fluxes in glaciology is to measure profiles of temperature, wind speed and humidity to apply the bulk method (Radic *et al.*, 2017). On a glacier, the surface temperature and humidity are well constrained during the melting season, and therefore, a bulk transfer approach requiring only one measurement height is commonly applied. However, the bulk transfer approach was developed for homogeneous, flat surfaces with steady-state conditions and fully developed boundary layers. It assumes a constant flux layer, stationarity and negligible advection, which are rarely attained on sloping glacier surfaces (Denby *et al.*, 2000). It does not account for katabatic winds, a common glacier feature during the melting season, caused by the cooling of the near-surface air layer by the colder glacier surface. These winds can be extensive, well developed and persistent in the Canadian Rockies (Conway *et al.*, 2021). This local cooling results in winds flowing down-glacier along the flow line and modifies the near-surface air temperature distribution (Ayala *et al.*, 2015), causing a near-surface wind maximum and reversing

surface temperature profiles. Parametrizations have been developed to include these glacier winds in the turbulent transfer calculation (Oerlemans and Grisogono, 2002a). A comparison between these different calculation methods finds that using a hybrid approach with a katabatic parametrization and bulk transfer approach yields the best result to simulate turbulent fluxes (Radic *et al.*, 2017).

Ice conduction, or subsurface flux, can be an important energy flux for the glacier surface energy balance but has often been neglected during the melt season and the assumption that surface temperature is at zero degrees is typically used (Hock, 2005). However, this is not the case at night or in conditions with strong radiative cooling, and leads to an overestimation of modelled melt, especially for snow-covered glaciers. Pellicciotti *et al.* (2009) found that estimating a surface temperature of zero degrees leads to a 10-13% overestimation of melt in the accumulation area, but less than 3% in the ablation area. The inclusion of a heat conduction flux is particularly important at the beginning and end of the melt season.

For snowpack, internal energy storage is an important component. A positive energy balance at the snowpack surface induces surface melt. The meltwater percolates through the snowpack in both matrix flow through the porous media and in flow fingers, preferential paths that accelerate water transport through the snowpack (Marsh and Woo, 1984; Leroux and Pomeroy, 2017; Leroux *et al.*, 2020). In deep, cold snowpack, water can refreeze, causing delayed flow rates and the formation of ice layers (e.g. DeBeer and Pomeroy, 2009), which is sometimes parametrized using a refreezing coefficient. Once the whole snowpack is saturated with liquid water and at 0˚C, all snowmelt is then available for infiltration or runoff. An important process for snowmelt is rain-on-snow events. When relatively warm rainfall occurs on a snowpack, melt rates increases. These increased melt rates are not only due to the advected energy from rain, but also from the latent and sensible heat from saturated atmospheric conditions, and air and dew point temperature above 0˚C (Pomeroy *et al.*, 2016). Several models have been developed to represent these snowmelt processes, from simple empirical functions to more complex physically based, multi-layered energy and mass-balance models (Gray and Landine, 1988; Marks *et al.*, 1998; Bartelt and Lehning, 2002).

However, even though there exists a rich body of literature on the measurement and calculation of the different components of the energy balance, most glacio-hydrological models do not include an energy-balance surface melt approach, and instead use a simplified empirical relationship between

positive air temperature and melt rate, called temperature-index or degree-day models (Hock, 2003):

$$M = DDF_{(snow,\ ice)} * (T-T_t) \quad (1.3)$$

Where M is the melt rate (mm/time step), DDF is the degree-day factor (mm $°C^{-1}$ time $step^{-1}$) that linearly relates temperature T to the melt rate and is typically differentiated for snow and ice. A melt rate is only calculated when T is above a threshold temperature (T_t). Temperature-index models rely on the assumption that temperature is the largest contributor to melt, and temperature and several components of the energy balance highly correlate (Hock, 2003). This simplified approach model type is widely used due to its lower data requirement. However, the main driver of surface melt for snow and ice is not temperature, but incoming shortwave radiation. Using air temperature as a driving input to simulate melt appears to work due to the correlation of cumulative melt and cumulative temperature index. This causes temperature-index models to perform adequately on a longer timescale, but not on a daily to sub-daily basis. Degree-day factors are derived to minimize discrepancies between observed historical and simulated results, their transferability in time and space is limited. This is especially problematic in the context of climate change, as the climate during which the melt factors were derived is different from the climate during which the factors are applied. For example, Huss *et al.* (2008) found that the degree-day factor of a temperature index melt model changed significantly over the 20th century. More evidence from energy-balance studies indicates that even on short time scales, degree-day factors vary widely (Carenzo *et al.*, 2009). To make temperature-index models more physically based, hybrid models have been developed (Cazorzi and Dalla Fontana, 1996; Daly *et al.*, 2000; Hock, 2005; Ragettli and Pellicciotti, 2012). These hybrid models, or enhanced temperature-index, allow for a spatial variation of the melt factors and often include a parametrization for incoming radiation to account for shading and slope. In these hybrid models, this amount of input data becomes close to a physically based model. Moreover, considering the existence of algorithms to estimate the radiation fluxes based on temperature, which have been tested and developed in different environments (Bristow and Campbell, 1984; Meza and Varas, 2000; Annandale *et al.*, 2002; Wu *et al.*, 2007; Bandyopadhyay *et al.*, 2008; Rahimikhoob, 2010; Samani *et al.*, 2011; Shook and Pomeroy, 2011), it is possible to estimate the input variables necessary to run a distributed energy balance model. For a more detailed review of snow and ice melt models, see Hock (2005).

1.1.5.4. *Ice melt under debris*

Debris-covered glaciers are prominent features of the world's glacierized mountain regions, with the presence of supraglacial debris modifying both the glacier ablation patterns and its response to climatic forcing (Scherler *et al.*, 2018; Herreid and Pellicciotti, 2020). Ice-cored moraines are another type of debris-covered ice, common in the Canadian Rockies and around the globe. Even though the formation of ice-cored moraines is still not well understood, it is known that they contribute to meltwater generation from glacierized basins. Hopkinson *et al.* (2010) found that on the Peyto glacier, runoff from the periglacial areas accounts for 8% of the water losses from basin storage. Ice-cored moraines are likely to play a larger role as glacier retreat leaves a larger ratio of buried ice in glacierized basins.

The effects of debris on glacier surface melt are well-understood: a thin layer of debris on the glacier surface (less than several centimetres) enhances melt, while a thick layer of debris insulates the underlying ice and reduces melt (Østrem, 1959; Nicholson and Benn, 2006). This understanding of the impacts of debris on glacier surface melt was first studied at the plot-scale on multiple glaciers (e.g. Østrem, 1959). Simulated melt under debris at the distributed scale first was applied using degree-day models (e.g. Mihalcea *et al.*, 2008a) or relied on measurements of surface temperature (e.g. Nakawo and Young, 1982; Nicholson and Benn, 2006). Energy balance based on resolving the conduction and conduction occurring within the debris layer, forced only by hourly meteorological observation, were then developed at the point scale (Reid and Brock, 2010), and then expanded to distributed glacier melt modelling (Fyffe *et al.*, 2014). In summary, there now exist many approaches of varying complexity, based on different input data availability, that can be used to simulate sub-debris glacier melt.

However, these modelling approaches are not commonly included in glacio-hydrological models. Moreover, these modelling approaches, as complex as they seem, omit different complexities of the debris-covered glacier system. First, these modelling approaches do not capture the high spatial variability in debris thickness, as they usually rely on point-based measurements or larger-scale values derived from satellite imagery. Even though the general pattern of debris thickness is known – debris thickness generally increases towards a glacier terminus (Anderson and Anderson, 2018), the debris exhibits a strong small-scale variability caused by a variety of factors (Nicholson *et al.*, 2018; Shah *et al.*, 2019). Local debris morphology is reshaped by melt channels or mass movement causing differential ablation and creating a hummocky terrain with uneven debris thickness. Ignoring

this small-scale variability and using a spatially averaged debris thickness can have a strong impact on the melt predicted by glacier models, underestimating the ablation rate by 11-30% (Nicholson *et al.*, 2018). Additionally, these debris-covered melt models do not include the processes linked to ice cliffs and supraglacial ponds (Steiner *et al.*, 2015; Miles *et al.*, 2016, 2018; Buri *et al.*, 2021; Sato *et al.*, 2021), which act as hotspots of ablation.

1.1.5.5. *Subsurface flow and storage*

Moraine sediments were thought to store very little glacier meltwater. However, recent studies in the Canadian Rockies (Mcclymont *et al.*, 2010; Langston *et al.*, 2011, 2013; Muir *et al.*, 2011; Hood and Hayashi, 2015; Hayashi, 2020), the Alps (Winkler *et al.*, 2016) and Peru (Baraer *et al.*, 2015; Gordon *et al.*, 2015; Somers *et al.*, 2016), amongst others, and as reviewed by Somers and McKenzie (2020), have shown that moraine, talus and alluvium are important storage and conduits of groundwater in high mountain environments. These geomorphological units contribute to basin streamflow through shallow, fractured bedrock aquifers, by holding water and slowly releasing it into the stream network. On a larger scale, bedrock aquifers contribute to mountain block recharge through large deep fault systems. This understanding challenges the assumption found in many mountain hydrological studies that all groundwater flow is returned to a river within the surface watershed, which neglects the possibility of "leaky basins", with groundwater export being a non-negligible component of the water budget. However, quantifying properties such as porosity, transmissivity and storage capacity of talus, moraines or rock glaciers is challenging. In the Canadian Rockies, Muir *et al.* (2011) characterized an alpine talus as an aquifer with storage limited to a week, but able to sustain a baseflow throughout the summer from meltwater supplied by late-season snowmelt. The few studies investigating groundwater levels in the proglacial field report a damped and lagged diurnal fluctuation following the daily glacier meltwater signal, associated with a slow decline in groundwater level throughout the summer season (Cooper *et al.*, 2011; Magnusson *et al.*, 2014). The time of lag increased with distance from the stream, but the amplitude variability highlighted the heterogeneous nature of the proglacial groundwater flow path. This supports the findings by Langston *et al.* (2011), who found that multiple flow paths had to be considered to represent the groundwater system in a glacier moraine system. However, due to the difficult fieldwork environment, monitoring of the hydrology of alpine basins is often focused on one aspect, more commonly the glacier mass balance or snow accumulation or melt (Hood and Hayashi, 2015). As the proglacial field area increases as glaciers retreat, it is possible that the storage in the proglacial

field somewhat buffers decrease in glacier runoff (Tague *et al.*, 2008; Tague and Grant, 2009; Somers *et al.*, 2018).

Only a few mountain groundwater studies explicitly consider interactions with glaciers (Saberi *et al.*, 2019; Somers *et al.*, 2019). In glacio-hydrological models, these off-glacier subsurface processes are often not described with the same focus as the cryospheric processes, as discussed in van Tiel *et al.*, (2020b). Subsurface processes (i.e., infiltration, percolation, soil moisture storage, interflow, and groundwater storage and runoff) are typically parametrized based on land use and land cover, with simplified representation for reservoir storage and outflow coefficient to determine the amount of water leaving these conceptual reservoirs.

1.2. Research Gap and Objectives

Glacierized basins are a complex system, with several hydrological processes on and off the glacier. As alpine glaciers retreat, land cover in the basin responds and evolves, and the relative importance of these different processes is affected. With changing temperature and precipitation, these processes can have contrasting and compensating behaviour, resulting in non-linear, non-stationary and non-uniform changes in the streamflow magnitude and timing. Some of these changes are already noticeable in mountain basins across the globe (Huss and Hock, 2018). These changes have consequences for downstream water resources, as mountain water reaches the population far away from the mountain and is used for agriculture, irrigation and drinking water.

To properly capture how the transition from glacier-dominated to potentially glacier-free will impact the hydrology of headwater basins and streamflow generation, models including the wide range of existing processes at a high complexity would be advantageous. However, most glacio-hydrological models do not include the whole range of processes operating in a headwater-glacierized basin. Glaciological-based models simplify or ignore non-glacierized processes, and hydrological-based models, on the other hand, often simplify glacier processes and often have limited representations of cold-region hydrology. Some hybrid models, including both on and off-ice processes, have been emerging in recent years, but they often rely on calibrated and conceptual approaches, which are not adequate to represent the quickly changing climate and landscape of mountain alpine basins.

For some key mountain processes, physically based approaches exist but are often not included in glacio-hydrological models. This is likely due to a lack of data to both develop, parametrize, and evaluate the processes occurring within remote alpine basins, but also to legacy approaches in model

development. For example, a temperature-index conceptual hydrological model requiring only temperature and precipitation as meteorological forcings is unlikely to include blowing snow transport requiring high-resolution wind speed due to model complexity mismatch. Therefore, to assess changes in the hydrological behaviour of glacierized headwater basin, there is a need for process-based, glacio-hydrological models flexible enough to include a wide range of mountain hydrological processes in combination with improvement and development of approaches to gather the needed data to include and evaluate these processes.

This study aims to explore the impact of future climate, glacier, and landscape change on glacierized basin hydrology and streamflow generation using a process-oriented glacio-hydrological model including the suite of processes occurring in mountain basins, with a focus on quantifying the on and off glacier processes, their changes, and the combined impact on streamflow generations. Three specific objectives are proposed to fulfil this research:

1.2.1. Objective 1: Develop and apply innovative approaches to characterize processes in glacierized basins

A key ongoing challenge in mountain hydrology is the lack of reliable observations to derive and parametrize hydrological processes. This prevents key hydrological processes from being included in glacio-hydrological models. This objective focuses on developing and applying novel approaches to measuring three essential processes: streamflow, debris thickness, and the glacier surface energy balance. Streamflow is a critical variable in hydrological modelling but obtaining accurate streamflow in a dynamic proglacial environment is challenging and fraught with uncertainty. To address this objective, an innovative automated salt dilution system has been deployed at the Peyto Glacier Research basin, and a robust assessment of both streamflow and its uncertainty is provided. Debris thickness is another key variable essential to simulate melt under debris cover, but difficult and time-consuming to obtain at the needed high spatial resolution. An innovative approach to estimate debris thickness using ground-based thermal infrared imagery is developed and applied, followed by a discussion of the varied factors that need to be considered to optimally use this approach. Turbulent transfer parametrization are tested for their influence on the surface energy balance under katabatic wind conditions, and finally, the influence of forest fire smoke and ashes on the glacier surface energy and mass balance is investigated. Forest fire activity has been increasing worldwide in recent years and is expected to continue in the future. Forest fires can modulate the energy balance by both modifying the atmospheric transmissivity through smoke and, ash, once

deposited on the surface, lowering the albedo. An approach to investigate and characterize these modifications to the surface energy balance, and their impact on surface melt, is developed and applied at the Athabasca glacier.

1.2.2. Objective 2: Diagnose hydrological and glaciological processes resulting in streamflow generation and variability

Glacierized alpine basins showcase a range of hydrological and glaciological processes. These processes are interconnected, occur simultaneously, and are driven by complex physical feedbacks. The use of models allows diagnostic analysis, to increase the understanding of the hydrological processes in the basin and the resulting streamflow. In this objective, the Cold Region Hydrological Modelling (CRHM) platform is used to design a glacio-hydrological model for the Peyto Glacier Research basin for the current condition and recent past. This CRHM glacio-hydrological model is used to diagnose and characterize the suite of mountain hydrology processes occurring in the basin, both on-ice and off-ice. The model is also used to investigate the hydrological behaviour of the Peyto basin, and how the varied processes relate to streamflow variability.

1.2.3. Objective 3: Assess the coupled impacts of climate and landscape change on the hydrological processes and streamflow generation in a glacierized basin

The combined climate and landscape change occurring in mountain basins worldwide are leading to a shift in their hydrological behaviour. To predict how these ongoing changes will continue to modify mountain streamflow and associated processes, a purpose-built glacio-hydrological model designed using the Cold Region Hydrological Modelling (CRHM) platform is coupled with high resolution, dynamically downscaled atmospheric forcings to assess future conditions in the Peyto Glacier Research Basin. To obtain a comprehensive assessment of future hydrological behaviour, simulations are performed with a perturbed climate, but also under varying landscape changes representing a range of glacier retreat and landscape evolution scenarios.

1.3. Organization of chapters

This thesis consists of an introduction, six chapters in the form of journal articles, and a concluding chapter. Chapter 1 introduces the study's background, objectives, and targeted literature review. Chapters 2 to 7 consist of six manuscripts designed for submission to peer-reviewed journals. Chapter 2 showcases the collection and processing of streamflow measurements with associated uncertainties at the Peyto Glacier Research Basin (Objective 1). Chapter 3 describes a novel

methodology to estimate debris thickness using ground-based infrared imagery (Objective 1). Chapter 4 describes the addition of turbulent transfer over glaciers to the modular Cold Regions Hydrological Modelling Platform. Chapter 5 presents an analysis of the compensating impacts of forest fire smoke on the surface energy balance and melt of the Athabasca glacier (Objective 1). Chapter 6 describes the development and application of a glacio-hydrological model within the CHRM platform to investigate the streamflow generating processes at the Peyto Glacier Research basin, and their relationship to streamflow variability (Objective 2). Chapter 7 uses the CRHM model designed in Chapter 6 and adapts it to predict end-of-century hydrological behaviour at the Peyto Glacier Research Basin, under a range of possible future climate and landscape scenarios. (Objective 3). Chapter 8 synthesizes the findings and the conclusions drawn from the last seven chapters.

2. SALT DILUTION STREAMFLOW MEASUREMENTS AND UNCERTAINTY IN A REMOTE DYNAMIC PROGLACIAL LANDSCAPE: A CASE STUDY AT PEYTO GLACIER RESEARCH BASIN

Paper manuscript status: Contents of this chapter have been submitted to the Canadian Water Resources Journal.

Author contribution: Caroline Aubry-Wake participated in fieldwork organization and data collection, compiled, organized and processed the field measurements and wrote the first draft of the manuscript. Gabe Sentlinger provided the automated salt dilution sensors and oversaw their installation. He also provided access to the software to process the salt dilution measurements and guidance on the processing of the salt dilution measurements. Eric Courtin, Robin Heavens and Greg Galloway conducted fieldwork. John Pomeroy initiated and funded the project, selected and installed the acoustic stream gauging site, provided critical feedback on installation and data processing and edited the manuscript.

Role in thesis: This chapter presents the data collection and processing of the salt dilution measurements into streamflow data for 2013-2020 in the Peyto Glacier Research Basin. The manuscript focuses on different sources of uncertainty associated with the usage of an automated salt-dilution system to develop a rating curve in this dynamic, proglacial landscape. Using the insights developed over the three years of salt dilution, the limitations, benefits, and improvements to using salt dilution in a proglacial landscape are discussed. This chapter contributes to fulfilling objective 1 of this thesis by providing an innovative way to quantify streamflow in glacierized basins. The streamflow time series developed in this chapter is used to evaluate the glacio-hydrological models in Chapters 6 and 7.

2.1. Abstract

Streamflow is a key variable in glacio-hydrological studies but obtaining reliable measurement in remote, dynamic, unstable and flashy proglacial streams is challenging. Salt dilution measurements are useful to quantify streamflow in environments where other techniques are not suitable, but still have considerable logistical challenges and uncertainty in proglacial landscapes. In the Peyto Glacier Research Basin, a small and heavily glacierized headwater basin in the Canadian Rockies, 105 measurements of streamflow were made over the 2017-2019 melt seasons using a combination of

automated and manual salt injections with water levels measured from a sonic range depth sensor. Measurement uncertainty averaged 12% of streamflow, ranging between 4 and 41%, with the largest source of uncertainty stemming from calculating the salt dilution breakthrough curve. Large errors were caused by incomplete mixing of the salt injection due to the problematic positioning of one of the two electric conductivity probes, and these measurements were discarded. The rating curve developed from the valid measurements, stable between the different years, was used to calculate streamflow for the 2013-2020 melt seasons. The Peyto streamflow was found to be highly variable, with peak flow varying from early July to early September, and a characteristic glacier melt diurnal signal occurring from mid-July to early September. Hourly peak streamflow varied between 5.7 and 10.1 m^3s^{-1}. This streamflow record will be highly useful to monitor the changes occurring in this quickly changing headwater system as well as evaluate the hydrological simulations used to diagnose past changes and predict future ones.

2.2. Introduction

Glacierized mountain headwaters are witnessing a range of changes affecting their hydrological behaviour, from warming temperature, shifting snow patterns and glacier retreat (Milner *et al.*, 2017). These changes have consequences for downstream environments, which rely on mountain water for hydropower, irrigation and drinking water. Streamflow is a key variable to monitor the ongoing changes in these headwaters, but it is also essential to evaluate hydrological models used to diagnose past hydrologic behaviour as well as predict future conditions (Frenierre *et al.*, 2013).

As the water level is easier to monitor continuously than streamflow, streamflow is usually calculated using a water level-discharge relationship (a rating curve). By obtaining simultaneous measurements of discharge and water level, a relationship between water level and streamflow can be developed and used to convert the continuous water level measurements into streamflow (Dingman, 1978). However, a range of factors complicates obtaining quality water level and streamflow measurements in proglacial settings (Nolin *et al.*, 2010; Frenierre *et al.*, 2013). For proglacial landscapes, the remote location of headwater glacierized environments makes it time-consuming to reach the measurement sites, limiting the number of visits one can do. The fast-flowing and cold proglacial stream can be dangerous to cross, limiting access to low and medium flow conditions. In addition to difficult access to the measurements site, the proglacial environment itself complicates measuring flow. From the glacier toe, the meltwater typically makes its way through a series of ponds, sand bars, loose moraine sediments and braided channels, and is only occasionally constrained by bedrock features. This

unstable and dynamic proglacial geomorphology limits the locations where monitoring instrumentation can be installed.

These difficulties linked to the proglacial landscape can limit the usefulness of traditional discharge measurement methodologies. For example, the most common method used to measure discharge, the velocity-area method via current metering or acoustic Doppler current profiling, is impractical in channels with complex geometries, such as steep mountain streams. It can also be unfeasible except during low flow conditions in glacial streams with a strong diurnal signal due to dangerously high flow velocities and turbulence. Remote mountain streams do not normally have bridges from which streamflow velocity measurements can be conducted safely, and at high flows can be too cold, fast and deep for hydrometric observers to stand in to take velocity measurements. Dilution methods with tracers such as salt or Rhodamine WT have gained interest in recent decades and are now commonly used to monitor steep, rough mountain streams (Moore, 2005). Tracer dye, such as Rhodamine WT, have been shown to have non-conservative behaviour linked to significant in-channel loss due to sorption onto suspended sediment and photolysis from sunlight, making it inappropriate for highly turbulent streams exposed to sunlight (Clow and Fleming, 2008; Runkel, 2015). Salt dilution addresses some of the concerns faced with proglacial landscapes, such as unstable and complex stream channel geometry and has a strong history of development in Canada for cold region streamflow estimation (Kite, 1989, 1993; Moore, 2005; Richardson *et al.*, 2017a). The development of automated salt dilution systems can now address the limited access issues faced by remote headwater basins. By installing a brine reservoir at the salt injection site, remotely triggered salt dilution measurements can be obtained, limiting the number of field visits.

A considerable amount of literature has been published to guide the streamflow measurements using salt dilution methods (e.g. Moore, 2005). However, most guidelines for salt dilution experiments were not developed or tested in a dynamic alluvium proglacial landscape or for the installation of an automated system, and the challenges associated with this landscape have not been thoroughly discussed. This paper aims to provide a comprehensive description of the installation and use of an automated salt dilution system to calculate streamflow in a dynamic proglacial environment and discuss the sources of uncertainty associated with the measurements. Additionally, key challenges and ways forward to obtain quality flow measurement in highly dynamic glacierized headwater basins are highlighted.

2.3. Field site and data

2.3.1. Peyto Glacier Research Basin

The Peyto Glacier Research Basin (Peyto basin) is a well-studied, heavily glacierized basin located on the eastern side of the Continental Divide in the Canadian Rockies, Alberta at latitude 51.67 N and longitude 116.55 W (Pradhananga *et al.*, 2021). The basin covers an area of 19.6 km^2 and ranges in elevation from 1907 to 3152 m. The Peyto glacier has been continuously losing mass and area since at least the 1920s (Tennant *et al.*, 2012) and now covers 50% of the basin area, shrinking to an area of 9.87 km^2 as of 2018. As of 2020, the Peyto glacier ends approximately 1.2 km from the basin outlet location. Glacier retreat is currently causing a proglacial lake to expand where the glacier toe used to be. The expanding proglacial lake drains through a series of bedrock notches. Below the bedrock notches, towards the outlet of the basin, the stream is flowing through glacio-fluvial sediments. The entire basin shows minimal vegetation, limited to the occasional alpine moss or shrub. The basin outlet is located just before the stream plunges in a steep bedrock canyon.

In summer, accessing the site requires a 5.6 km hike on steep moraine sediments with 650 m elevation gain, including a proglacial stream crossing. On average, the hike-in takes around 3 hours. Due to the stream crossing, field visits have to be timed to cross this stream at relatively low flows. The challenging nature of the access also limits field visits to experienced hikers. Helicopter access is possible but is limited due to park regulation and cost.

2.3.2. Field instrumentation

In 2013, an SR50 sonic height sensor was installed on a bedrock notch below the proglacial lake (51.68111 N, 116.54472 W, 2150 m; Figure 2.1. a-b). This provides a continuous 15-min water level for approximately mid-May to mid-October, as snow covers the channel for the rest of the year. On September 7, 2017, a pressure transducer was installed in a second bedrock notch located approximately 100m downstream from the height sensor. On May 14, 2018, an automated salt system was deployed at the Peyto outlet creek, with the injection site located next to the pressure transducers, and the conductivity sensors installed approximately 450 m downstream above a bedrock constriction forming a steep canyon (Figure 2.1 c-d). For the 2018 and 2019 summer, salt dilution measurements were performed using the automated salt dilution system. These were supplemented by manual salt dilution measurements, which started in September 2017. A time-lapse camera was installed at the location of the AutoSalt system, taking pictures every two hours

between 8:00 AM and 4:00 PM (Figure 2.1. e-g). Details of the salt dilution measurement systems are presented in section 2.4. and details regarding the instrumentations are found in table 2.1.

Figure 2.1. Peyto Glacier Outlet Creek area and instrumentation: (a) overview of the Peyto Glacier Research basin area, (b) SR50 sensor, (c) location of the AutoSalt system, (d) close-up view of the AutoSalt injection site and pressure transducer location and (e-f) time-lapse camera images showing early season conditions with snow blocking the channel, low flow conditions on September 6, 2018, at 4:00 PM and high flow condition on Aug. 2nd, 2018 at 4:00 PM. The time-lapse images show the mixing reach length.

Table 2.1. Summary of instrumentation and measurements at the Peyto Outlet Creek

Instrument	Measurements	Period
Campbell Scientific Sonic Ranger (SR50A)	Water level (m)	01-May-2013 to 17-Sep-2020
KPSI pressure transducer	Water level (m)	07-Sep-2017 to 30-Sep-2019
Peyto Moraine Barometric logger	Air pressure (hPa)	07-Sep-2017 to 30-Sep-2019
FT2 handheld Acoustic Doppler Velocimeter (ADV)	Discharge (m^3 s^{-1})	intermittent
Fathom scientific AutoSalt AQAc	Discharge by brine injection (m^3 s^{-1})	intermittent
Fathom Scientific QiQuac	Discharge by dry mass injection ($m^3 s^{-1}$)	intermittent
Time-lapse camera	Images of mixing reach	15-May-2018 to 25-Jun-2019

2.4. Method: Streamflow measurements using salt dilution

For a slug tracer dilution measurement, tracer material is injected into a stream and its concentration is monitored at a downstream location. For salt dilution, the temperature-corrected electrical conductivity is recorded until it returns to the pre-injection background level. It is then summed to calculate discharge Q:

$$Q = \frac{M}{CF_T * \Delta t \sum_{i=1}^{n} [EC_T(t) - EC_{BG}]} \quad (2.1)$$

Where Q is the discharge ($m^3 s^{-1}$), M is the mass of salt injected (kg), CF_T (mg cm μS^{-1} L^{-1}) is a calibration constant relating salt concentration to EC_T (μS cm^{-1}), EC_T and EC_{BG} are the measured temperature-corrected electrical conductivity and the background electrical conductivity (μS cm^{-1}) and Δt is the measurement time interval (s).

The calibration factor CF_T is obtained by creating a secondary solution with a known mass of salt mixed with stream water. The amount of water in the second solution is then incrementally increased, and the change in salt concentration and electrical conductivity is recorded. The slope of the relationship between electrical conductivity and salt mass concentration is used as the

calibration factor CF_T. The uncertainty associated with relating EC_T and salt mass is assessed following Richardson *et al.* (2017b). As suggested in Moore (2005), the tracer dosage was obtained by conducting trial injections with low salt mass and then increasing the mass as necessary.

Salt dilution measurements were conducted with two systems. The first system consisted of a manual dry mass injection, where the salt was injected as a brine of known mass of salt and arbitrary volume of water (Moore, 2004). The electrical conductivity probes were placed downstream in approximately the same location for each measurement. This system consisted of Quick Instream flow and Uncertainty Analysis Calculator (QiQuac) system from Fathom Scientific. Manual calibration was performed before each measurement following the procedure outlined in Richardson *et al.* (2017b).

An automated salt dilution system, the Aqac M5 by Fathom Scientific, was also deployed. The AutoSalt system consists of a control system, a 300-litre brine tank, two T-HRECS self-logging EC-T probes, and a proprietary salt injection system. This is combined with data from a pressure transducer installed in the creek. The AutoSalt system is programmed to release a specific amount of brine into the channel at a specific time, which can be triggered remotely by telemetry, or programmed to occur at specific intervals or within a given stage range. The brine is typically a well-mixed 20% NaCl mixture, and the salinity in the tank is monitored with a salinity probe during field visits. Manual calibration of the electrical conductivity probes is done at the initial installation. The AutoSalt system was drained, and the pressure transducer was removed from the stream over winter to prevent damage.

Considerations of mixing length and injection sites were based both on literature and local geomorphological features. A range of models have been proposed to determine mixing lengths based on hydraulic and geometric parameters of the stream, but a common recommendation is based on Day (1977), who suggested the mixing length should equal or exceed 25 wetted stream widths. Manual stream width measurements provided values ranging between 8 and 13m. This would result in a mixing reach of 200 to 325m. Based on the local geomorphology, the mixing length was set to 420m. This corresponds to the distance between two bedrock constrictions where the flow converges, providing appropriate injection and recording location. Between the injection site and the EC_T probes, the channel is braided with occasional pools.

The salt dilution measurements from both the manual and automated systems were post-processed in the Salt Portal provided by Fathom Scientific. Each salt dilution trace was manually inspected and calibrated to minimize calculation error.

2.5. Results

2.5.1. Water level correction

After an initial inspection of the water level measured by the KPSI pressure transducer for the 2019 summer, it appeared that the pressure transducer sensor shifted between 2018 and 2019, possibly when it was removed for data download. Additionally, the sensor was also moved after its initial installation in fall 2017, as it was not placed low enough to capture low flows. To ensure consistency between the years, a synthetic SR50 water level corrected to the 2018 KPSI water level was created using linear regression. This synthetic SR50 water level was used as a water level measurement for the 2017-2019 period. The synthetic SR50 provides high agreement with the KPSI measurements (Figure 2.2).

2.5.2. Salt dilution measurements

Over the 2017-2019 melt season, 29 manual salt dilution flow measurements were performed under varying conditions using the QiQuac sensors. This provided 54 individual salt traces as each measurement is recorded by two sensors. However, of these 54 individual measurements, only 12 were useable for evaluation. Multiple measurements were conducted in the early season when no corresponding water level was available due to snow and ice blocking the channel and had to be discarded. Other salt injections did not have enough salt injected to provide a clear breakthrough curve in the electrical conductivity data and had to be rejected. Over the 2018-2019 season, the AutoSalt pump activated 84 times. However, for a number of these events, the brine reservoir was empty and therefore, there was no resulting salt injection. There were also six manual salt injections recorded by the AutoSalt probes during field visits. In total, there are 105 streamflow measurements, 12 with the QiQuac and 93 with the AutoSalt system (Table 2.2).

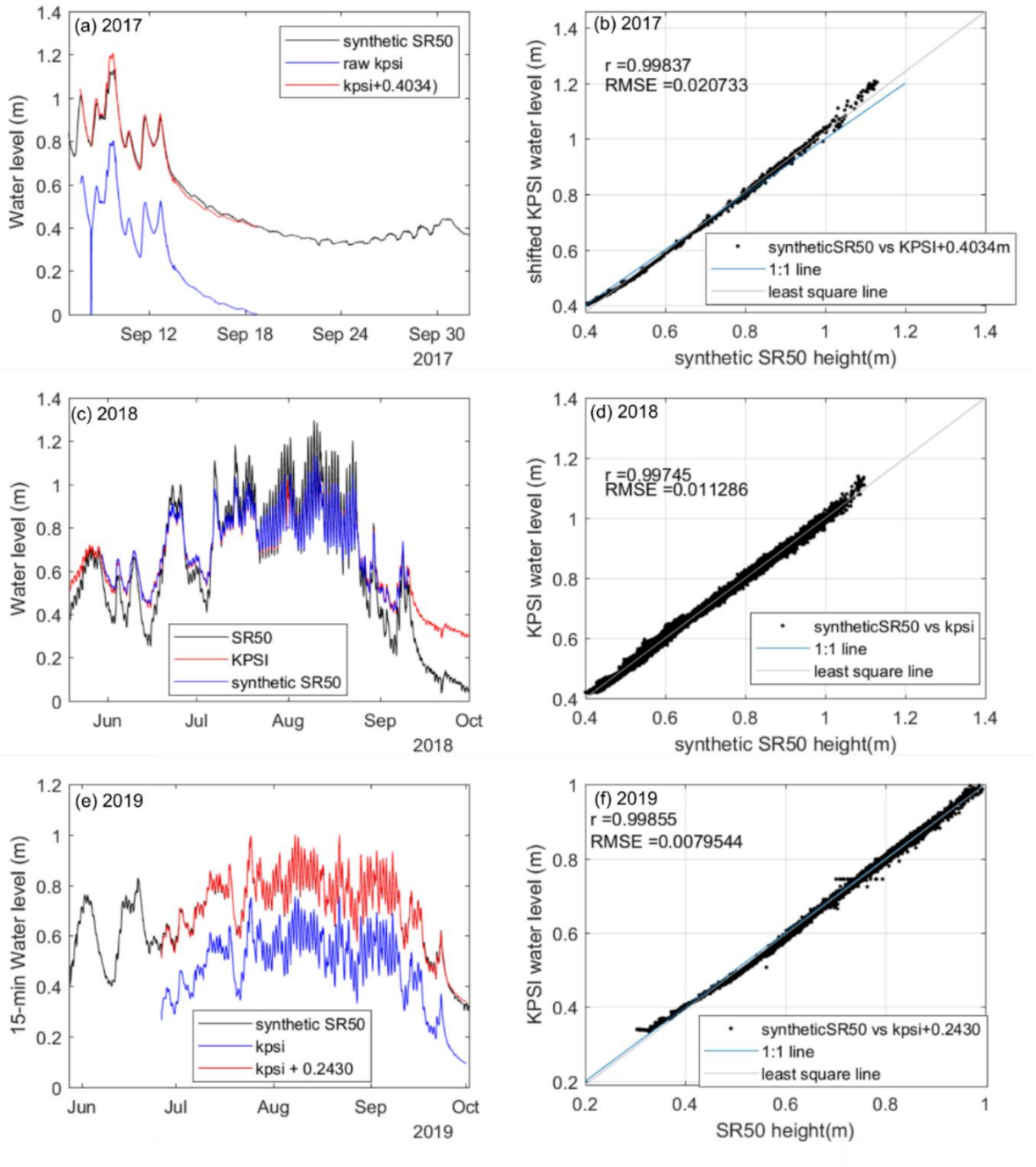

Figure 2.2. Synthetic SR50 (black), raw KPSI (blue) and corrected KPSI (red) for 2017, 2018 and 2019 data, with the corresponding scatterplot.

Table 2.2. Number of salt dilution events

		2017	2018	2019
QiQuac	CH0	2	2	1
	CH1	4	2	1
Autosalt	AT04	0	29	17
	AT07	0	28	19

2.5.3. Uncertainty in Salt dilution Streamflow measurements

2.5.3.1. *Quantifiable uncertainty*

For each streamflow measurement, uncertainty originated from three quantifiable sources: the calibration factor CF_T, the injected salt mass, and the salt dilution breakthrough curve (Table 2.3). Each uncertainty source is further discussed. Across the 105 measurements, the smallest and most consistent source of uncertainty came from the calibration factor CF_T. The calibration factor was defined as the average of 25 manual calibrations conducted at the site. The average CF_T value used for the AutoSalt measurement was 0.506 ± 0.01 mg cm μS^{-1} L^{-1}, with minimum and maximum values of 0.494 and 0.533 mg cm μS^{-1} L^{-1}.

The most variable source of uncertainty was the salt mass injection, linked with the alternative approach to measure salt injection by the AutoSalt system. For the six manual salt injections that were performed during field visits and recorded by the AutoSalt EC probes located downstream, the injected mass of brine volume was recorded in field notes. For the injection triggered by the AutoSalt system, the amount of salt required for each injection was calculated internally based on a provisional rating curve. The AutoSalt system read the water level, calculated the amount of salt needed to obtain a measurement at this water level, and then injected the required amount of brine. The number of injection pulses combined with a user setting of pulse-per-litre recorded the volume of brine injected in the stream. Unfortunately, in August 2018, the AutoSalt system stopped injecting the prescribed volume, likely due to some salt precipitant clogging the flow meter or air intrusion from the injection line. The issues with the brine injection volume resulted in a growing difference between the internally calculated salt injection and the actual volume change in the brine reservoir (Figure 2.3). This difference became highly noticeable in August 2019. Therefore, the amount of salt injected into the stream had to be calculated in a different way, with higher uncertainty. The change

in reservoir volume as recorded by the reservoir pressure transducer and corrected for the density of brine was used to obtain the accurate volume of brine injected into the stream. To assess the error in the salt mass injection, the absolute difference in salt mass calculated between the AutoSalt system method and the reservoir change method before the tank malfunctioned was calculated. This gave an absolute difference of 0.147 kg, which corresponds to an error between 1 and 22% of the calculated salt mass using the reservoir volume change approach. As the difference between the two measurement methods was not correlated to the mass of salt injected (the difference was not larger when a higher mass of salt is injected), the uncertainty value for the period before the pump malfunctioned was set to half the difference between the two-measurement method and for the period after the pump malfunctioned, the error was set to the average difference of 0.147 kg. These two uncertainty values were considerably higher than the difference between the two methods before the flow meter was faulty. In May 2018, the average absolute error between the two calculations method (flow method and volume change) was 5%, which corresponds to a standard error in the salt mass of 0.02 kg.

Even if the flow meter had not malfunctioned, there would still be an uncertainty associated with its use and the amount of salt injected. Based on manufacturer information, the calculated uncertainty on the flow meter is ± 5% and can be reduced to ± 3% when calibrated *in situ*, which was done at the Peyto site at the initial installation. Using a secondary method to measure the salt injection, therefore, did not create a new source of uncertainty, but identified an existing one. A third method, the pump time, was also tested to calculate the salt injection mass and compared well with the other two methods but showed a larger difference and therefore was not selected. For each of these methods, the mass of salt was obtained by multiplying the volume of saltwater by the salt concentration in the brine, which was measured using a refractometer during field visits and ranged between 18 and 20.4%.

These issues associated with the faulty flow meter were addressed in the updated AutoSalt design by having the flow meter constantly submerged. Additionally, continuous use of satellite telemetry, which was used in 2018 but not 2019, would have allowed the identification of the difference between the two methods remotely and a quick problem diagnosis the following field visit.

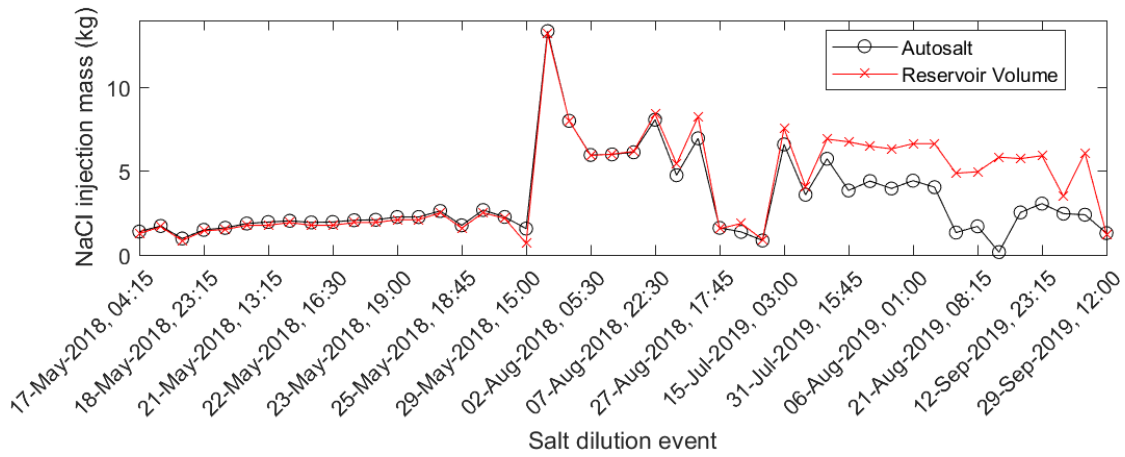

Figure 2.3. Injected salt mass calculated by the Autosalt system (black) and by the change in brine reservoir volume. The two measurements approach show very similar results until August 2018, when the difference starts to appear.

The total uncertainty is subdivided between the different components, and the statistics for the total measurement uncertainty and its different component was calculated (Table 2.3). The largest sources of uncertainty originated from the calculation of the salt dilution breakthrough curve (Table 2.3, Figure 2.4a). This source of uncertainty is linked with the background noise, as well as the strength of the salt breakthrough curve. In certain situations, the volume of salt injected into the stream was too low, which produced a weak electrical conductivity signal at the downstream probes and caused a large uncertainty. In other settings, a changing background electrical conductivity also increased the uncertainty.

Table 2.3. Sources of uncertainty for the 105 salt dilution streamflow and water level measurements.

	Salt dilution				Water level
	CFT	Salt Mass	Salt Breakthrough curve	Total	
Average (%)	1.5	3.3	7.6	12	1.3
Standard deviation (%)	<0.1	4.0	5.6	7.2	1.2
Minimum (%)	1.5	<0.1	2.1	4.1	<0.1
Maximum (%)	1.8	20	39	41	7.6

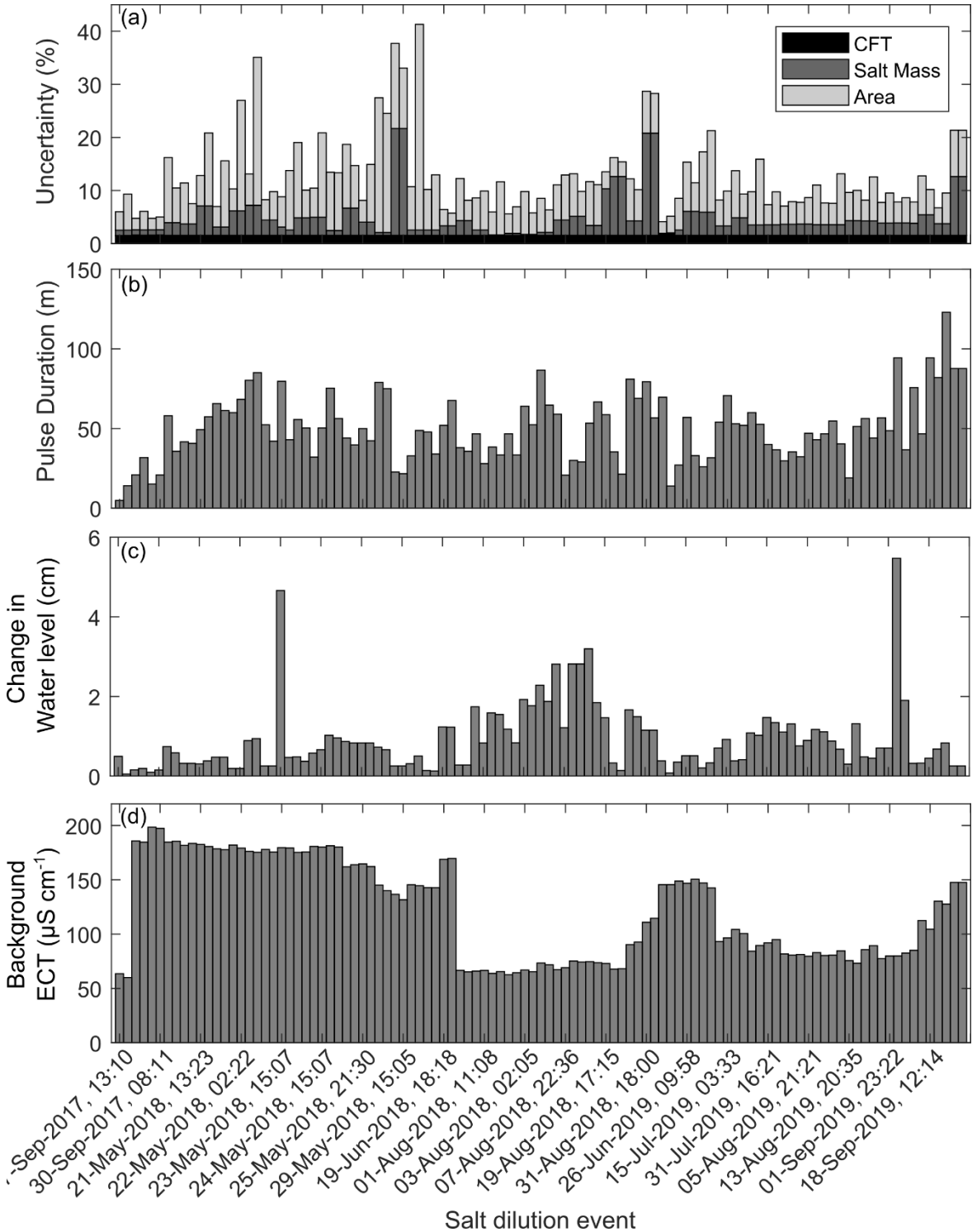

Figure 2.4. Salt dilution measurement uncertainty for the 105 salt dilution measurements, classified as caused by the CF_T calibration factor, the injected salt mass and the salt dilution breakthrough curve (a), with other sources of errors linked to the breakthrough curve duration (b) and water level change (c) and background electrical conductivity (d).

A possible concern during salt dilution measurements is the change in discharge occurring during the salt dilution experiment. This might be particularly concerning for glacier-fed streams which show a strong diurnal change in discharge. In this case, salt dilution breakthrough curves lasted on average 50 minutes, with a standard deviation of 21 minutes (Figure 2.4b). An average change in water level during measurement of 0.9 cm was observed. Out of the 105 measurements, 93 have a change in height of 1.5 cm or less, and only 5 have a change in the water level of 5 cm or more (Figure 2.4c). When looking at the change in water level as a percentage of the measurement water level, 77 out of 105 points have a change of less than 1.5% of the water level, and only two measurements have a water level change corresponding to more than 5% of water level. This indicates that the uncertainty linked with changing water levels during a measurement is not a key area of concern. Moreover, there was only a weak correlation between the average water level measured during the experiment and the change in water level. The uncertainty relating to the water level measurement was set to half the change in water level during the salt dilution breakthrough curves. This uncertainty corresponds to, on average, 1.3% of the measured water level, and consists of the smallest uncertainty source.

An additional possible source of error originates from changing background electrical conductivity. Linked with the quickly changing flow of glacierized basins, the risk of having a changing background electrical conductivity could obscure the change due to the salt dilution. At the Peyto site, a highly variable background electrical conductivity is present over the three monitoring seasons, but the change in background conductivity during measurement is low, at a mean absolute value of 0.42 ± 0.60 µS cm^{-3} (Figure 2.4c). Even though this change in background electrical conductivity is quite low, in cases where the mass of salt injected was also relatively low compared to the flow volume, it can increase uncertainty in the calculation of the salt dilution breakthrough curve.

2.5.3.2. *Suitability of landscape*

Other sources of uncertainty are harder to quantify and are linked to the suitability of the landscape in which the salt system is installed, such as additional water entering the mixing length and the presence of pools and storage in the mixing length. Additionally, another source of uncertainty is the appropriate placement of the electrical conductivity probes: they have to be in a suitable location to record the salt dilution pulse, but also have to be accessible in a safe manner. In a dynamic proglacial landscape, finding and accessing an optimal location for the electrical conductivity probe placements can be difficult, and increases the uncertainty of the salt dilution method. These sources of

uncertainty are mitigated by careful selection of the mixing reach and the placement of the salt dilution system but must be considered.

A key assumption of the salt dilution system is that the discharge between the injection site and the electrical conductivity probe is constant. However, at the onset of the melt season, while streamflow is still low due to the limited melt occurring at higher elevations, low-lying snow patches along the mixing reach, as seen in Figure 2.1e, can add to the basin streamflow. This source of uncertainty is likely negligible once glacier and snowmelt start to increase streamflow, as the contribution from the small and isolated snow patches along the mixing reach contributes limited water compared to the bulk of the sow and ice in the basin.

Even though the volume of water provided by late-lying snow patches is likely a negligible uncertainty source during most of the melt season, the location of this additional meltwater to the stream can have a larger impact. A snow patch providing meltwater to the main river channel near an electrical conductivity probe can prevent reliable mixing at this location. Without *a priori* knowledge of the location of persistent snow patches and their meltwater routing to the main channel, this source of uncertainty is difficult to reduce. This emphasizes the difficulties associated with finding an appropriate placement for the electrical conductivity probes in a heterogeneous proglacial landscape.

The presence of pools and slow flow in the mixing reach complicates discharge measurements using salt dilution. In an ideal case, pools and eddies are avoided in the mixing reach. However, as noted in Hudson and Fraser (2005) this is rarely achieved. When pools are present and relatively large compared to the channel area, the salt stays in the pools and is slower to reach to EC sensor. This results in an extended tail in the EC measurements. However, Hudson and Fraser found that cutting the tail of the salt dilution breakthrough curve results in less than 5% error, but that this error is systematic. At Peyto, the large storage volume between the injection site and the EC probe is likely to entail some error. The possibility of surface-subsurface water mixing in the colluvium proglacial field is likely to increase the source of uncertainty.

2.5.4. Rating curve development

After processing the 105 discharge-rating curve pairs obtained from salt dilution measurements and inspecting the salt dilution breakthrough curve, the discharge-water level curve and the location of the electrical conductivity probes, several measurements form the AT04 sensors were determined

to be anomalous. the anomalous measurements were likely associated with a poor placement of the electrical conductivity probe combined with the presence of a snow patch providing meltwater entering the main channel near the sensor, preventing a reliable mixing at this location. Due to the difficulty of judging which measurements from AT04 were valid and which ones were not, the 46 AT04 measurements were discarded. The other 59 measurements were kept to build the rating curve (Figure 2.5).

The rating curve is set to:

$$Q = 7.65 * (h - 0.2)^{1.58} \quad if\ h < 0.75m \tag{2.2}$$

$$Q = 24.57 * (h - 0.35)^{2.29} \quad if\ h \geq 0.75m \tag{2.3}$$

Where Q is the calculated streamflow (m^3s^{-1}) and h is the water level (m). The rating curve shows stability between the years, suggesting it is appropriate to use the current rating curve for the duration of the SR50 measurements (2013-2020) (Figure 2.6a).

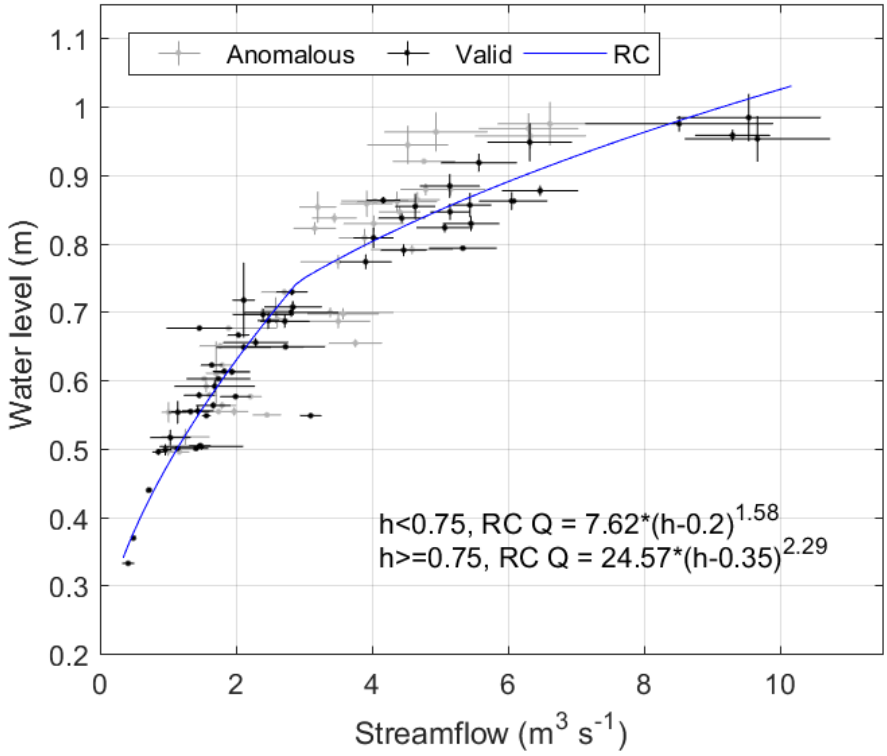

Figure 2.5. Rating curve for the Peyto Glacier Research Basin outlet based on 59 measurements over the 2017-2019 period with associated showing measurement uncertainty.

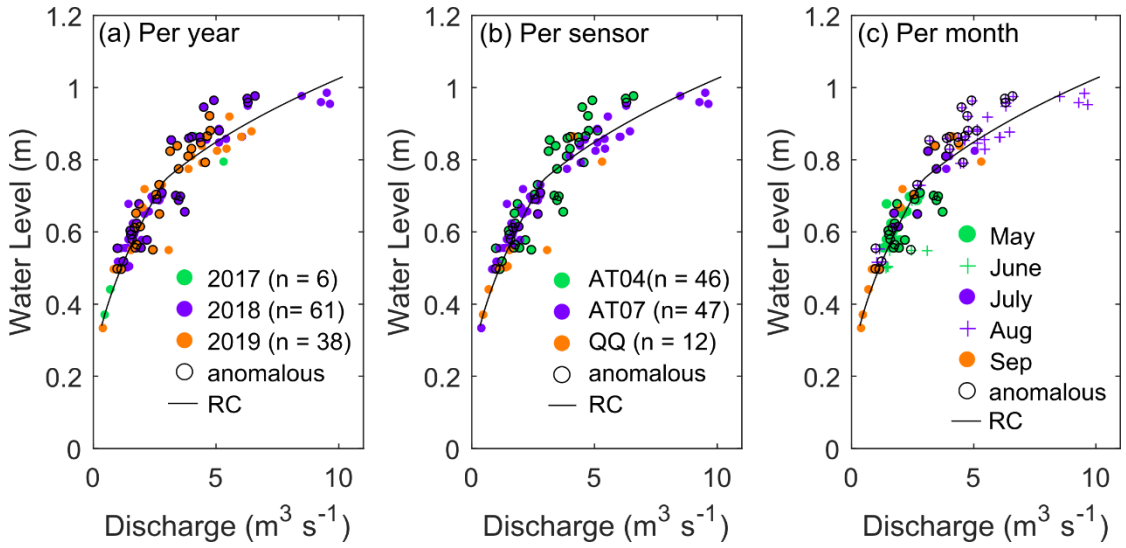

Figure 2.6. Discharge-water level point divided per year (a), instrument type (b) and month (c). Anomalous measurements are shown by a black outline.

2.5.5. Peyto streamflow, 2013-2020

The rating curve calculated from the salt dilution measurements in 2017-2019 was used to determine streamflow discharge for the duration of the SR50 record (2013-2020). The streamflow calculated over the 2013-2020 period shows strong fluctuation within each melt season, with different patterns occurring in different years. High flows associated with rapid melt events followed by a decrease in streamflow as melt rates declined in colder conditions caused large variations in daily streamflow. For example, some years show a quick increase and decrease in streamflow in early June (2015, 2016, 2018, 2020), and other years show a rise and fall in streamflow in the late Fall (2014, 2015). The timing of the annual peak daily streamflow is highly variable between years, ranging from early July (2013) to early September (2017), with streamflow volume between 5.7 $m^3 s^{-1}$ and 10.1 $m^3 s^{-1}$.

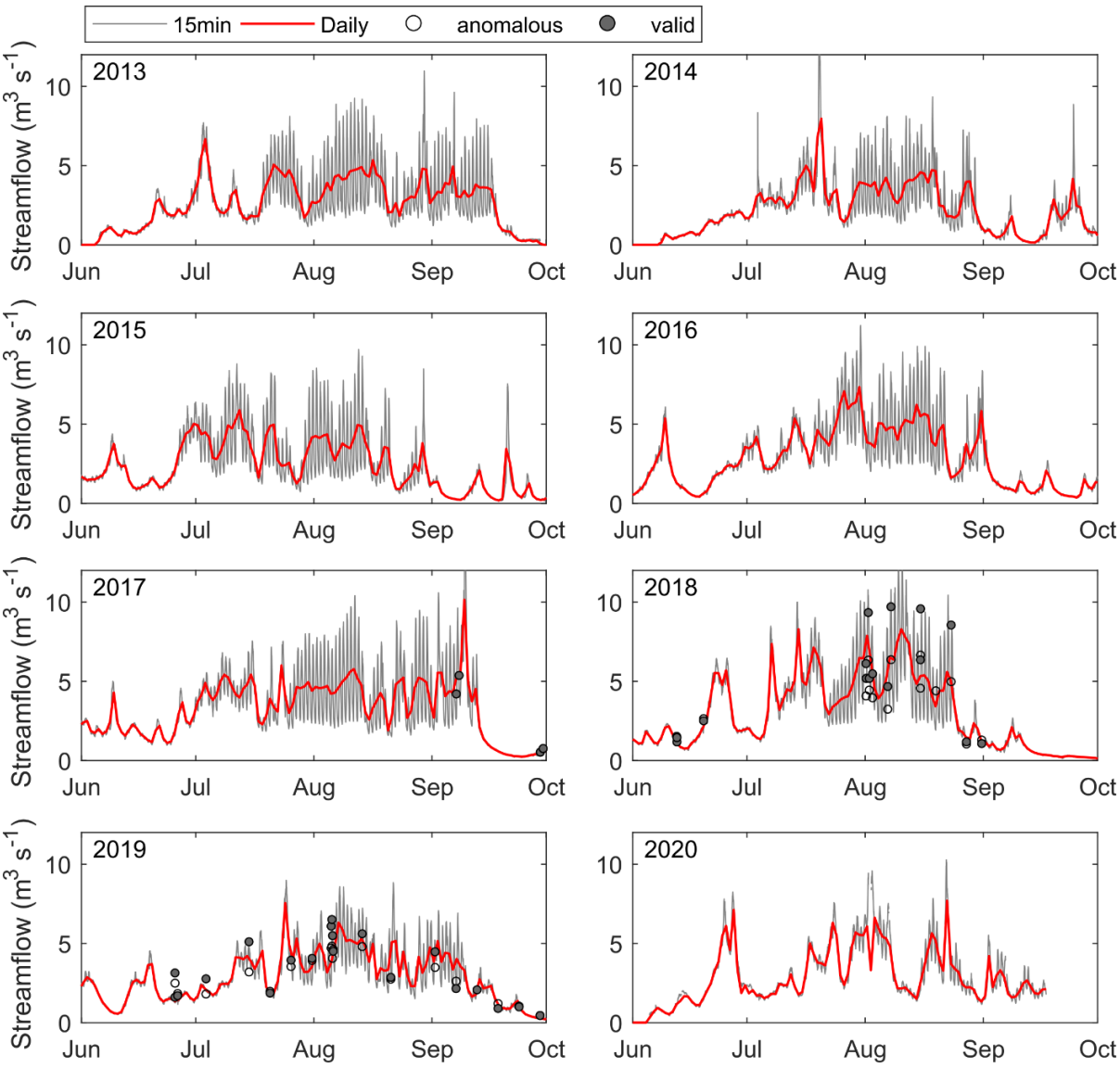

Figure 2.7. Calculated streamflow for the 2013-2020 melt seasons with daily averages (red) and 15-minute values (grey). The empty circles mark the timing of the anomalous measurements, and the full circles show the valid points used in the rating curve development.

2.6. Strengths and possible improvements in using an automated salt dilution system

Using an automated salt dilution system allowed the collection of a higher number of streamflow measurement points during varied conditions. Specifically, the automated salt dilution system allowed measurement of the high flows which are dangerous to survey manually. Additionally, manual flow measurements during field visits can only be done in a limited time window due to the hike-in and out, and therefore do not cover the range of flow conditions induced by the diurnal glacier melt signal.. The AutoSalt system permitted measurements at the varied hours of the day, capturing different sections of the diurnal flow regime.

The high flow volume occurring at Peyto required a high volume of brine to be injected into the stream and therefore, only approximately five measurements could be obtained before a field visit was required to refill the reservoir. This could easily be mitigated by having a larger brine reservoir. The high-frequency refills of the reservoir also meant a large volume of salt had to be carried to the site, which became a heavy load to be carried during field visits. This issue was resolved by bringing a large amount of salt by helicopter, but this is a non-negligible concern when aiming to assess streamflow for larger streams using salt dilution.

To minimize area error, which is the largest part of the uncertainty assessed at the Peyto outlet, having a third electrical conductivity probe above the salt injection location would be beneficial. Additionally, using a higher volume of salt during the injections to obtain a more distinct salt dilution breakthrough curve would reduce this uncertainty.

Overall, the largest source of error at this site was linked with channel characteristics and local snowmelt inputs. Almost half of the streamflow measurements had to be discarded due to the insufficient mixing occurring at the probe AT04. This source of error was mitigated by having a careful assessment of the site before installing the electrical conductivity probe and relying on field expertise in the salt dilution system, but it could not be eliminated. The proglacial landscape at the Peyto outlet is a highly dynamic, quickly changing environment, which renders any measurement type difficult. Even though the site has a large mixing volume and is in theory not an ideal site for salt dilution measurements, salt dilution estimates of streamflow discharge could be measured reliably as determined by a robust assessment of uncertainty.

2.7. Conclusion

The installation of an automated salt dilution system permitted reliable streamflow measurement with a quantifiable uncertainty in a remote, dynamic, unstable and flashy proglacial stream. Using a combination of automated and manual salt injections with water levels measured from a sonic range depth sensor, 105 measurements of streamflow were made over the 2017-2019 melt seasons. This work showcased the importance of careful testing and assessing methodologies when applying them to different environments. Even though salt dilution is a well-used and common method to measure streamflow in turbulent mountain streams, its application to a dynamic proglacial landscape revealed multiple complications that required careful examination. Local field knowledge gained from years of monitoring the Peyto Glacier Research Basin and expertise in streamflow monitoring techniques were instrumental to diagnose and understand the uncertainties in the salt dilution measurements.

Quantifiable streamflow uncertainty averaged 12% of streamflow, ranging between 4 and 41%. The largest source of uncertainty stemmed from the salt dilution breakthrough curve and is associated with high background noise in the stream electrical conductivity associated with underestimation of the required salt mass injections. This could be reduced by careful selection of a provisional rating curve used to calculate the volume of salt to inject, and by adding a third electrical conductivity probe upstream. Overall, the largest source of error, which was unquantifiable, was linked with the problematic positioning of one of the two electrical probes in the channel. This probe was located just downstream of the discharge from a late-lying snow patch and so was placed where mixing was incomplete, which caused all the measurements from this probe to be anomalous and unusable for the rating curve calculation. The usable salt dilution measurements provided the basis for a rating curve for the Peyto outlet and the calculation of streamflow for the 2013-2020 melt seasons. The Peyto streamflow was found to be highly variable, with peak daily flow varying from early July to early September, and a characteristic glacier ice melt diurnal signal occurring from mid-July to early September. Peak streamflow varied between 5.7 m^3s^{-1} and 10.1 m^3s^{-1}.

This streamflow record will be useful for monitoring the changes occurring in this headwater system as it deglaciates as well as to benchmark and evaluate hydrological simulations used to diagnose past changes and predict future ones, and their impact on downstream water resources. Streamflow measurements in heavily glacierized basins such as the one developed in this study are rare but critical. This assessment of the uncertainties associated with salt dilution measurement in a remote, proglacial landscape, as well as suggestions to reduce these uncertainties, can help guide streamflow monitoring efforts in such landscapes.

3. USING GROUND-BASED THERMAL IMAGERY TO ESTIMATE GLACIER DEBRIS THICKNESS: FIELDWORK CONSIDERATIONS TO IMPROVE EFFECTIVENESS

Paper manuscript status: Contents of this chapter have been compiled as manuscript published with the Journal of Glaciology.

> **Aubry-Wake, C.**, Lamontagne-Hallée, P., Baraer, M., McKenzie, J.M., Pomeroy, J.W. (2022b). Using ground-based thermal imagery to estimate glacier debris thickness: fieldwork considerations to improve effectiveness. *Journal of Glaciology*, 1-17. DOI:10.1017/jog.2022.67

Author contribution: Caroline Aubry-Wake conceptualize the study and co-organized and conducted data collection. Caroline Aubry-Wake compiled, organized, and processed the field measurements and wrote the first draft of the manuscript. Pierrick Lamontagne-Halle co-organized and conducted fieldwork, processed the GPS dataset, and provided critical input to the study design. Michel Baraer guided the study design and data analysis. Jeffrey McKenzie contributed equipment and funding to the field campaign. John Pomeroy funded the project, examined moraine thermal modelling physics, helped in evaluating the data and edited the manuscript.

Role in thesis: The debris thickness derived in this chapter are used in the glacio-hydrological models in chapter 6 and 7.

3.1. Abstract

Debris-covered glaciers are an important component of the mountain cryosphere and influence the hydrological contribution of glaciated basins to downstream rivers. This study examines the potential to make estimates of debris thickness, a critical variable to calculate the sub-debris melt, using ground-based thermal infrared radiometry (TIR) images. Over 4 days in August 2019, a ground-based, time-lapse TIR digital imaging radiometer recorded sequential thermal imagery of a debris-covered region of Peyto Glacier, Canadian Rockies, in conjunction with 44 manual excavations of debris thickness ranging from 10 to 110 cm, and concurrent meteorological observations. Inferring the correlation between measured debris thickness and TIR surface temperature as a base, the effectiveness of linear and exponential regression models for debris thickness estimation from surface temperature was explored. Optimal model performance (R^2 of 0.7, RMSE of 10.3 cm) was obtained with a linear model applied to measurements taken on clear nights just before sunrise, but

strong model performances were also obtained under complete cloud cover during daytime or nighttime with an exponential model. This work presents insights into the use of surface temperature and TIR observations to estimate debris thickness and gain knowledge of the state of debris-covered glacial ice and its potential hydrological contribution.

3.2. Introduction

Rock debris are found on 44% of the world's glaciers (Herreid and Pellicciotti, 2020). Debris thickness is one of the key factors that modulate the sub-debris ice melt - a thin layer (less than several centimetres) enhances melt, while a thick layer of debris insulates the underlying ice and reduces melt (Østrem, 1959; Nicholson and Benn, 2006). Generally, debris thickness increases towards a glacier terminus (Anderson and Anderson, 2018), but exhibits a strong small-scale variability, caused by a variety of factors (Nicholson *et al.*, 2018; Shah *et al.*, 2019). Manual excavations (e.g. Reid *et al.*, 2012), observations of debris thickness above exposed ice cliffs (e.g., Nicholson and Benn, 2013) or ground-penetrating radar surveys (e.g. McCarthy *et al.*, 2017; Giese *et al.*, 2021) at a high enough spatial resolution to capture this small-scale variability are both time and labour-intensive. As these methods either apply to limited zones or are highly time consuming, there is a risk of bias in the results linked with the number and distribution of the measurements.

Due to the difficulties in obtaining field-based debris thicknesses, different methods have recently been developed to estimate debris thickness from remotely sensed observations, such as satellite-derived surface temperatures. Two main approaches are used to derive debris thickness from surface temperatures. Both assume that surfaces above thinner debris have cooler temperatures than areas with thicker debris. The first approach is to derive debris thickness from an empirical relationship with surface temperature, but uncertainties remain regarding the best form of empirically-derived relationship to use, with linear (Mihalcea *et al.*, 2008a) or exponential (Mihalcea *et al.*, 2008b; Juen *et al.*, 2014; Minora *et al.*, 2015; Kraaijenbrink *et al.*, 2017; Tarca and Guglielmin, 2022) functions performing best in different studies. This empirical approach, appealing for its simplicity and low amount of required data, works when heat conduction between buried ice and the surface is the predominant surface energy balance term compared to others such as turbulent transfer and net radiation. The performance of these empirical relationships depends on the thermal conductivity of the surface material as well as microscale variations in energy balance terms. Other processes in the debris, such as heat advection in the debris subsurface, complicate the relationship between surface temperature and debris thickness and result in lower empirical model performance. Another key

limitation of empirically-derived models to estimate debris thickness is that their performance is strongly dependent on the availability of well-distributed input data that represent the full range of debris thickness and surface temperature (Boxall *et al.*, 2021).

The second common approach to derive debris thickness from surface temperature is through a physically-based energy-balance model (Foster *et al.*, 2012; Rounce and McKinney, 2013; Schauwecker *et al.*, 2015; Rounce *et al.*, 2018; Stewart *et al.*, 2021). A major challenge for this approach is to obtain reliable meteorological data to accurately quantify the energy fluxes at the debris surface (Foster *et al.*, 2012; Rounce and McKinney, 2013; Rounce *et al.*, 2015). In addition to the difficulties in obtaining the energy fluxes, debris properties, such as the thermal resistance, surface roughness or surface albedo, often have to be estimated across the glacier area and add further uncertainty to the method.

Both the empirical relationships and the energy-balance approach only provide an accurate debris thickness estimate for debris shallower than approximately 0.5m, after which a decoupling between surface temperature and debris thickness is observed (Mihalcea *et al.*, 2008a; Foster *et al.*, 2012; Tarca and Guglielmin, 2022). Rounce *et al.* (2018, 2021) addressed this limitation and obtained robust estimates for debris thicker than 0.5m by combining an inverted sub-debris melt model with calculations of elevation change and flux divergence. This method requires a series of digital elevation models and surface velocity data in addition to the meteorological data and debris parameters of the melt model. Therefore, it faces similar difficulties linked with data and parameter uncertainty.

As pointed out by Rounce *et al*. (2013), a key limitation in using surface temperature from satellite to derive debris thickness, either using empirical models or surface-energy balance, is the poor resolution of the satellite thermal band (typically between 60-100m). At this resolution, local slope and aspect variations, which play an important role in controlling the surface energy balance and therefore the surface temperature, are not captured. Due to the large pixel area of these thermal images, debris, ice cliffs and supraglacial ponds can all appear in a single pixel, resulting in an underestimation of the debris thickness (Rounce *et al.*, 2018; Herreid, 2021). Nicholson *et al*. (2018) showed that ignoring the small-scale variability in debris thickness and using spatially averaged values can have a strong impact on the melt predicted by glacier models, underestimating the ablation rate by 11-30%.

One option to capture surface temperature at a high spatial resolution in glacierized terrain is to use near-surface remote sensing, such as from a plane or uncrewed aerial vehicles (UAVs, Kraaijenbrink *et al*, 2018) or ground-based oblique imagery (Hopkinson *et al.*, 2010; Aubry-Wake *et al.*, 2015; Herreid, 2021; Tarca and Guglielmin, 2022). These instruments offer the possibility to measure surface temperatures from thermal infrared radiometry (TIR) both at a high spatial resolution and with flexible timing to account for different times of the day or variable weather conditions. This increased flexibility in measurement methods enables further investigation of the relationship between surface temperature and debris thickness (Herreid, 2021), but it also facilitates assessments of when and how surface temperature should be measured to optimize debris thickness estimates. For example, Mihalcea *et al.* (2008a) suggested that early morning hours optimized the correlation between surface temperature and debris thickness, while afternoon provided the weakest correlation at the debris-covered Miage glacier in the Alps. Herreid (2021) further examined the optimal time of day at which surface temperature should be collected for the Canwell Glacier in Alaska and found that cold nights provided poor conditions to derive debris thickness from surface temperature, as the debris surface became isothermal. Herreid (2021) suggested that weather conditions play a key role in obtaining suitable thermal infrared imagery to derive debris thickness, with clear days being the least suitable and cloud cover providing optimal conditions. However, obtaining surface temperature from UAV or ground-based TIR imagery presents complications that need further assessment, such as issues related to the radiometer viewing angle, which can cause shifts in emissivity, the distance between the TIR radiometer and the study surface, which increases the atmospheric interference, and small-scale variations in surface emissivity linked with varying surface types (Aubry-Wake *et al.*, 2015; Kraaijenbrink *et al.*, 2018; Baker *et al.*, 2019; Herreid, 2021). Considering the advances in measuring surface temperature using near-surface remote sensing and its widespread potential use in debris thickness reconstructions, there is a need for further experimentation and testing to explore best practices to measure debris surface temperature as a method to estimate debris thickness.

The objective of this paper is to examine how debris thickness over glacial ice can best be estimated using ground-based, oblique TIR imagery. More specifically, this paper explores how the simple empirical models of debris thickness based on TIR surface temperature and debris thickness are influenced by:

a) The empirical regression type

b) The time of day of TIR image acquisition

c) Weather conditions

d) The number and depth distribution of the manual debris thickness measurements

e) The spatial resolution of the images

f) The distance between the region of interest and the TIR camera.

3.3. Study area

The ice-cored lateral moraine of Peyto Glacier (51.676°, -116.554°), a well-studied outlet glacier of the Wapta Icefield in the Canadian Rockies (Pradhananga *et al.*, 2021; Pradhananga and Pomeroy, 2022a), was selected to investigate the relationship between debris surface temperature and debris thickness. This ice-cored moraine used to be connected to the glacier toe, but ongoing glacier retreat has disconnected it from the clean ice glacier. The study area is 100 by 50 m (Figure 3.1) and is predominantly east-facing, with an average slope of 23.5˚, gradually increasing toward the upper ridge, and is located between elevations of 2138 and 2159 m. a.s.l. (Figure A.1). During the TIR surveys, sunrise at the study site above the horizon created by surrounding mountains was around 0800h MDT and sunset was at 1800h, reaching full darkness by 2200h. The mountains surrounding Peyto Glacier are composed of dolomitic limestone rock, which was representative of the debris composing the study area. Two weather stations located in the vicinity of the study area recorded the meteorological conditions during the experiment: $AWS_{moraine}$ located 1.4 km northeast of the study area on the moraine below the glacier toe, and AWS_{ice}, an on-ice station located 415 m east of the study area (Figure 3.1).

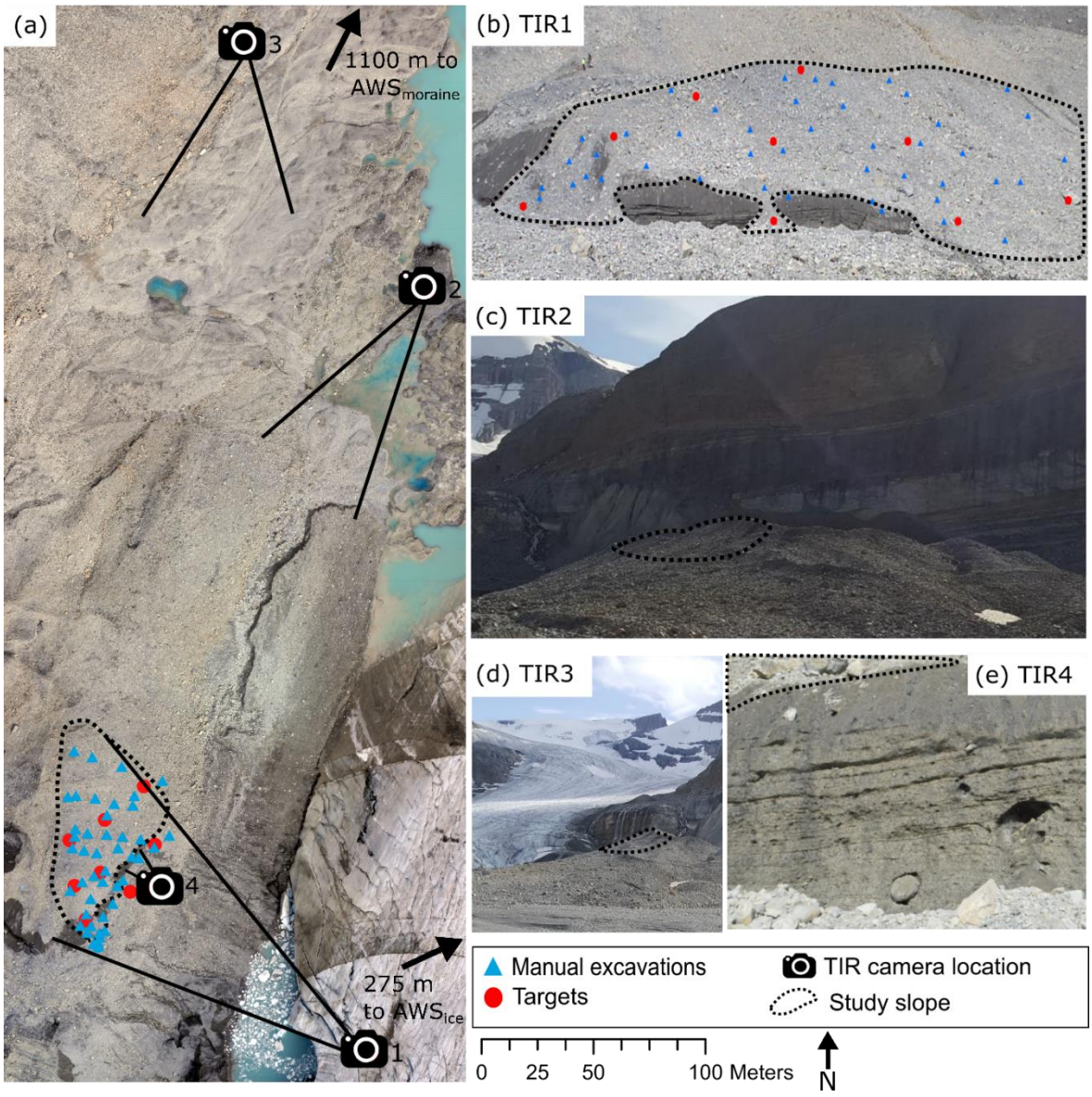

Figure 3.1. Study area (a) showing the location and camera angle from the four thermal infrared imaging radiometer locations and the distance and direction to the AWS_{ice} and $AWS_{moraine}$. The field-of-view from the four locations is shown in (b-e). The blue triangles in (a) and (b) show the manual excavation locations and the red circle shows the control point. In all pictures, the dashed black line delimits the study area. Note that the scale bar and north arrow apply to (a) only.

3.3.1. Data collection and processing

3.3.1.1. *Thermal infrared imagery survey*

Two thermal infrared imaging radiometers were used at four locations to survey the study area and surroundings. A Jenoptik VarioCam HD thermal infrared imaging radiometer was installed on the glacier facing the study area at location TIR1 (Figure 3.1a), and recorded images at 5-minute intervals

from August 5th, 2019, 17:15 to August 9th, 9:00 for a total of 1077 images over 90 consecutive hours. The radiometer's field of view is shown in Figure 3.1b. The field of view of TIR1 is considered the reference frame and is the primary field of view for the analysis.

A second Jenoptik VarioCam Basic thermal imaging radiometer was installed at three locations for intermittent measurements during the experiment. The only difference between the two cameras is the pixel resolution: 1024x768 for the VarioCam HD and 640x480 for the VarioCam Basic. Locations TIR2 and TIR3 (Figure 3.1a) had a survey area larger than TIR1, with a field of view including a side-view of the study area, the toe of Peyto Glacier, mountain cliffs and the sky (Figure 1c and 1d). The fourth location was a close-up view of an ice cliff in the study area (Figure 1e). These three locations also recorded thermal images at 5-min intervals. Details of the image collection timing can be found in Table 3.1.

Both thermal imaging radiometers use an uncooled microbolometer sensor with a spectral range of 7.5 to 14 µm, with a manufacturer-stated accuracy of ±1.5°C. The radiometers were automatically corrected for an emissivity of 1.0, a distance of 10.0 m and an atmospheric temperature of 20.0°C. The emissivity of limestone debris is closer to 0.93 (Salisbury and D'Aria, 1994; Sobrino and Cuenca, 1999; Kraaijenbrink *et al.*, 2018) which means that its reflectance of incoming longwave radiation is 0.07 and it is not a full black body for application of the Stephan-Boltzmann equation. An emissivity of 1.0 is a standard assumption of land surface models and other situations where it is difficult to explicitly account for near-black body emission and reflectance and permits direct application of the Stephan-Boltzmann equation. This assumption results in the total radiation measured by the radiometer and considered in calculating the surface temperature being a combination of the radiation emitted and reflected from the target object and atmospheric radiation emitted along the beam path. To calculate accurate absolute measured surface temperatures, a correction needs to be applied to the total radiation to isolate the radiation emitted from the target (Cardenas *et al.*, 2008; Aubry-Wake *et al.*, 2015). Surface emissivity and longwave irradiance are needed to solve for the surface radiant temperature in this manner, however as discussed by Baker *et al.* (2019), the uncertainty associated with the small-scale variability in surface emissivity and longwave irradiance to the surface due to slope, aspect, sky view, wetness, ice exposure and surface mineral characteristics, coupled with the variability of the radiant temperature of the surface, results in a limited ability to apply these spatially variable corrections accurately to field TIR images. In the field TIR imaging radiometer used, any emissivity correction or atmospheric correction is applied

uniformly across the image and so modifies all surface temperatures equally. Such coarse corrections would not advance this study, which focuses on how observed correlations between TIR imagery observations and debris thickness are influenced by different TIR field data collection procedures. The debris emissivity was therefore assumed to be 1.0 and images were not corrected for atmospheric TIR emission.

Table 3.1. Details of thermal infrared time-lapses. The picture from Figure 3.1 corresponding to the field-of-view for each location is indicated in italic

Location	Scene description	Number of pixels in study area	Start time - End time	Recorded time	Distance to ice cliff (m)	Number of images
TIR1 *Figure 3.1b*	Study area	91408	Aug 5, 17:15 - Aug 6, 9:00	89:45	140	1077
TIR2 *Figure 3.1c*	Ice-cored moraine and cliff	18966	Aug 5, 17:35 - Aug 6, 2:20	8:10	290	98
			Aug 7, 13:55 - Aug 7, 21:20	7:30		90
			Aug 8, 11:40 - Aug 8, 23:35	11:55		143
TIR3 *Figure 3.1d*	Ice-cored moraine and glacier toe	4052	Aug 6, 17:25 - Aug 6, 20:45	3:25	370	41
TIR4 *Figure 3.1e*	Ice cliff close-up	10251	Aug 9, 8:35 - Aug 9, 10:20	1:50	6	22

The TIR images recorded at TIR1 were first co-registered to account for minor position shifts of the camera using an automated, intensity-based image registration algorithm from the MATLAB Image Processing Toolbox (MathWorks, 2017). For TIR1, three groups of images were considered, corresponding to the images recorded between battery changes. Then, the three image groups were registered using manual control-point image registration to account for the sudden shift in the field of view of the camera at battery changes. A similar procedure was followed for locations TIR2, TIR3 and TIR4. For each location, a visual image was also registered using a control-point approach (Figure 3.1b-e).

3.3.1.2. *Manual excavations*

Forty-four manual debris excavations were dug at an array of locations aiming to capture the local debris thickness variability of the study area. The debris layer thickness was measured at each excavation using a measuring tape along the vertical axis. Manual excavations were surveyed with differential GPS to obtain accurate locations.

Even though the aim was to select excavation spots randomly, some bias may have been introduced to their location. First, a debris depth of zero was not recorded, even though some areas showed exposed ice. The steepest slopes of the study area were not sampled for safety reasons. Sparse or thin debris sites, in a region of discontinuous debris on the southern end of the study area (left side of the TIR1 images), were unstable and multiple mass movements were observed during the surveys, meaning that the recorded depth might only be valid in temporal proximity to the measurements. For the rest of the study area, debris cover was continuous and stable throughout the observation period. Manual measurements were not performed under large boulders as it was impossible to displace them. These two factors led to systematic under-sampling of the extremes in debris thickness and bias samples to depths of 10 to 70 cm. The manual excavations were refilled while attempting to recreate the stratigraphic distribution of the debris.

3.3.2. Geospatial localization

During the TIR surveys, nine targets were installed on the study area surface and located with a differential GPS (red circles, Figure 3.1a-b). All nine targets are visible in the registered visual image of the study area, but only six targets, which were partially covered with aluminum foil to create a significantly different emissivity, are visible in the TIR images.

A high-resolution orthomosaic and digital surface model was obtained from an uncrewed aerial vehicle (UAV) survey on Aug 28th, 2019, 18 days after the TIR surveys. A comparison of visual images recorded during the TIR surveys and the UAV flight shows the ice cliff in the study area receded slightly, but only affecting the area immediately adjacent to the ice cliff and not affecting the rest of the study area. The orthomosaic visual imagery is used to select an additional six boulders as tie-in points between the TIR images and the UAV survey to provide 15 ground control points. The control points were used to geolocalize the TIR images, create a local spatial frame of reference and assign spatial coordinates to every pixel in the TIR images. These local spatial frames, in the form of matrices

of latitude and longitude values of the same dimensions as the TIR images, were used to localize the manual excavations in the TIR images.

3.4. Results and discussion

3.4.1. Debris thickness from manual excavations

The manual excavations showed a debris thickness ranging from 5 cm to more than 110 cm (Figure 3.2a). The most common measured depth were between 40-45 cm (n=6), followed by 45-55 cm (n = 10) (Figure 3.2b). Stratigraphy was recorded for every excavation more than 15 cm deep. Most stratigraphy showed a layer of coarse to very coarse debris (average thickness of 15 ± 9 cm) overlaying a layer of sand, typically moist up to approximately 2 cm below the sand/pebble interface, with interspersed boulders (Figure A.2). The bottom of the sand layer, at the ice-debris interface, was water-saturated and ponding was observed at the ice interface in four of the 45 excavated holes. This lack of ponding at the debris-ice interface might be linked to the slope of the study area, promoting quick evacuation of the meltwater, and might be less representative of other debris-covered areas with lower surface slopes (Giese *et al.*, 2020).

The debris thickness measurements were interpolated following a natural neighbour algorithm to estimate distributed debris thickness over the study area (Figure 3.2a). The debris thickness across the slope showed a similar distribution as the measured manual excavation, with debris thickness ranging from 0 to 120 cm with a mode of 35-40 cm. To simplify the image processing, the ice cliffs at the bottom of the study area were not included in the analysis. Since this study focuses on the correlation between debris thickness and surface temperature rather than ice cliff processes or absolute surface temperature analysis, including the ice cliffs in the analysis was considered out of the scope of this current study.

The interpolated debris thickness is used as the reference to which the simulated debris thicknesses are compared. Due to the high density of manual excavations performed to calculate the interpolated debris thickness, it is likely to represent the large-scale spatial patterns occurring on the slope. However, the interpolated debris thickness might miss small-scale spatial patterns that could be reflected by the surface temperature variations. Therefore, the interpolated debris thickness is used as a reference in the comparisons but should not be considered the known debris thickness.

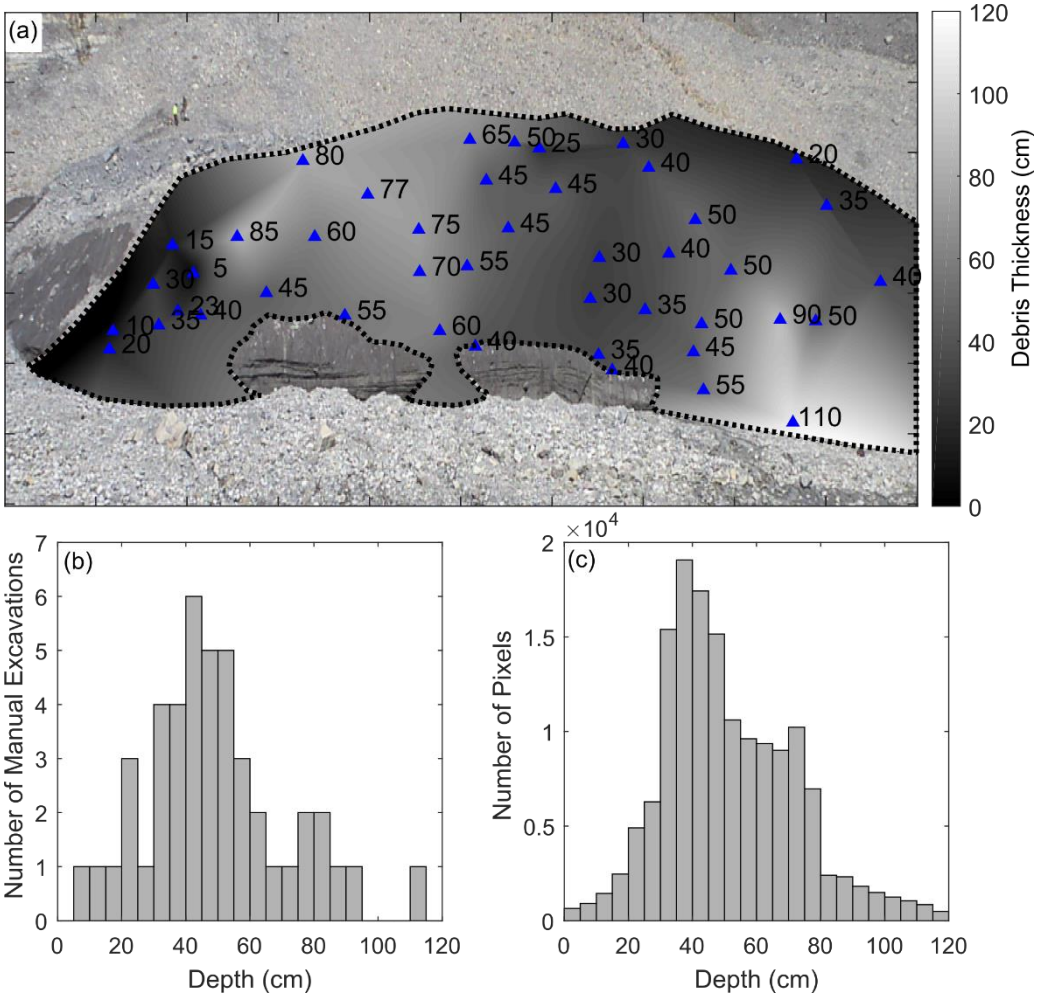

Figure 3.2. Location and depth of manual excavations (blue triangles) and interpolated thickness from point excavation in (a). The dashed line indicates the study area. (b) The distribution of the manual excavations and (c) the distribution of the interpolated debris thickness across the study area.

3.4.2. Measured surface temperature at manual excavation locations

The surface temperature of 2 x 2 pixels (corresponding to 0.12 x 0.4 m) at the location of each manual excavation was extracted from the TIR1 images (Figure 3.3). The manual excavations did not cause detectable thermal anomalies in the surface temperature record. This was assessed by comparing the temperatures at the excavation locations, for the period when the manual excavation was performed, to the retrieved time series for those in the immediate vicinity (Figure A.3). Generally, thicker debris had higher surface temperatures than thinner debris, with the largest differences occurring at peak shortwave irradiance (around 1400-1500h MDT). The surface temperature pattern differs on the first day of the study period, August 6th, from those on the subsequent two days, August 7th and 8th, due to a shift in weather, with the first day being predominantly cloudy, with

rainfall occurring on the evening of August 6th and the following days being sunny. The influence of weather on the surface temperature and debris thickness correlation is further discussed in section 4.1.1. (Figure 3.6). August 6th shows cooler peak surface temperatures, reaching a daily maximum of 21.8 °C compared to 27.3°C and 27.1°C on August 7th and August 8th. Similarly, night temperatures on August 5th-6th only reached lows of -0.11°C, compared to -2.75°C, -2.64°C and -2.30°C for the following nights. The timing of minimum and maximum temperatures also differed between the first day of the study period and subsequent days. On the night of August 5th-6th, the minimum temperature occurred at 0110h MDT, compared to 0555h, 0620h and 0700h MDT for subsequent nights. The variation in surface temperatures observed at the sites of manual excavations reached between 16 and 23°C in the early afternoon, but only 6 °C at the end of the night.

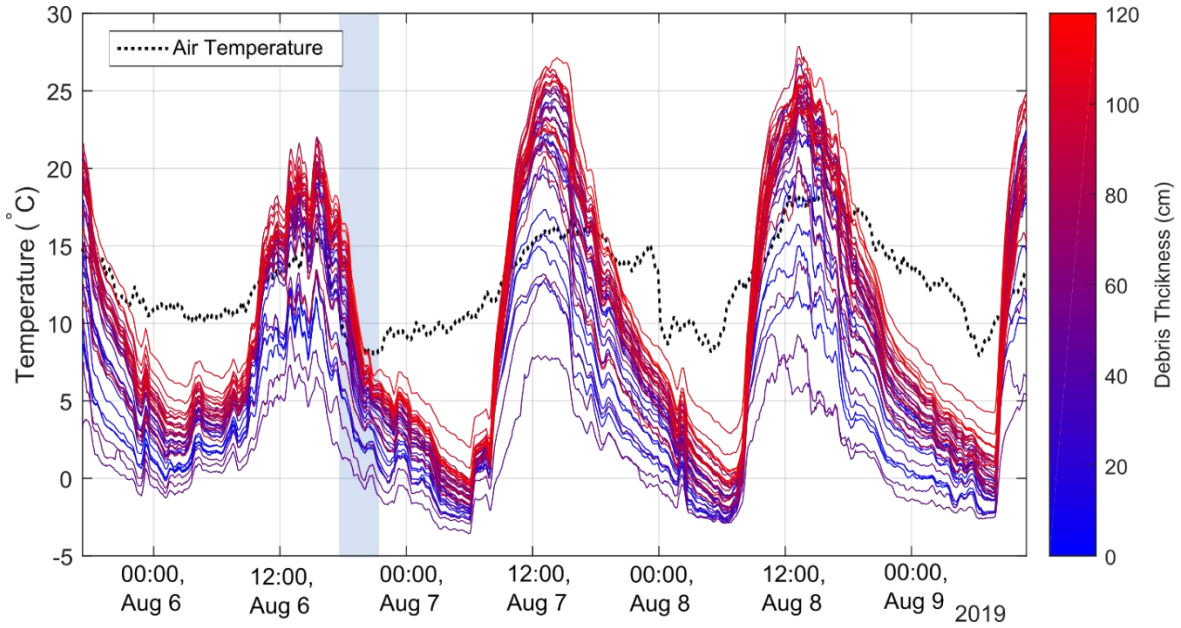

Figure 3.3. TIR1-derived surface temperature at the location of each manual excavation (full line) and air temperature measured at the moraine $AWS_{moraine}$ (dotted line). Blue lines correspond to thin debris and red lines to thicker debris. Lines are smoothed using a 30-minute moving frame for visual clarity. The shaded blue area corresponds to a period of intermitted rain.

3.4.3. Relationship between debris thickness and surface temperature

The 44 manual excavations and corresponding surface temperatures were used to calculate empirical relationships for each TIR1 image (n = 1077). Five regression types were tested with debris thickness as the only control of surface temperature (linear, quadratic, power, exponential, log). Multivariate linear regression models were also tested using slope, aspect and elevation in addition

to surface temperature as possible controls on debris thickness. Slope and aspect are important controls on debris thickness in addition to surface temperature (Rounce and McKinney, 2013). For the simple regression models, the linear and logarithmic empirical regression performed very similarly, and the exponential and power empirical regression also showed comparable performance. The second quadratic fit provided a model performance between the two groups (Figure 3.4a-d). Out of the 1077 time steps analyzed, model performance was improved for 20, 238 and 25 time steps when including either slope, aspect and elevation, respectively, compared to the linear regression model considering surface temperature only, and no improvements were obtained when including a combination of slope, aspect and elevation (Figure 3.4e). These improvements were minor, with an average increase of 0.01 in the adjusted R^2 values compared to the linear regression model. The time steps that showed improvement when including either slope, aspect or elevation in the linear regression models still performed more poorly than the exponential regression model. This limited model improvement is likely caused by the largely uniform slope, aspect and elevation of the study area. As limited improvements were observed when including topographic variables in the linear regression model, and the comparable performance between the varied empirical model tested, only the exponential or linear were selected for further analysis and discussions.

The coefficient of determination, R^2 between surface temperature and debris thickness from both linear and exponential model fit is shown in Figure 3.4a-c for August 8th, 2019 at 12:00 (noon), August 8th, 2019 at 20:00 and August 9th, 2019 at 6:45. These times were selected as reasonable times for fieldwork data collection in remote glacial environments, corresponding to just before sunrise, around sunset, and midday. Additionally, these images show examples of relatively poor, average and good model performances, with the good performances corresponding to R^2 values above the median (0.55 and 0.50 for the exponential and linear model), the average values near the median, and the poor model values corresponding to the bottom 10% of R^2 values.

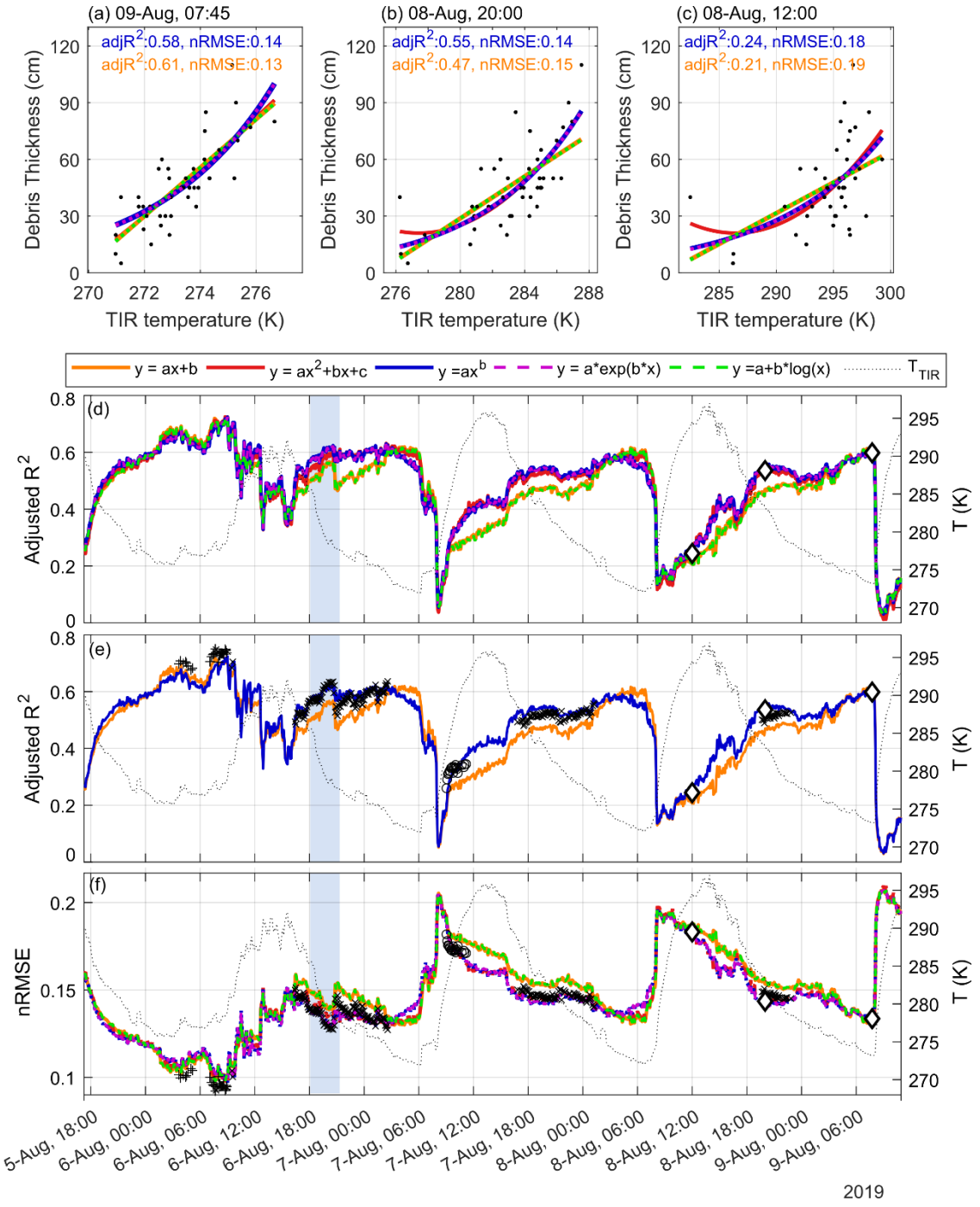

Figure 3.4. Correlation of debris thickness and TIR surface temperature with empirical regression for linear, exponential, quadratic, power and logarithmic fit for three time steps over the study period (a-c). Panel (d) shows the calculated adjusted coefficient of determination R^2 for the five types of regression tested and panel (e) shows the linear and exponential fit in combination with the multiple linear regression model including slope, aspect and elevation. Panel (f) shows normalized Root Mean Square Error (nRMSE) for each TIR image for 5-August to 9-August 2019. The average TIR surface temperature is shown in (d-f) on the right axis. The timing of the (a-c) scatter plots is indicated by the diamond on the (d-f) panels and the blue shading indicates the intermitted rainfall period.

For each regression model, the goodness-of-fit at each manual excavation was assessed by calculating the adjusted coefficient of determination adjR^2 and the root mean square error normalized to the range of observed data (nRMSE) between the measured debris thickness and the modelled debris thickness. The coefficient of determination ranged between 0.09 and 0.70 (Figure 3.4d), with nearly all models showing a significant correlation (with a p-value lower than 0.05). Only three thermal images for the exponential fit and six images for the linear fit, out of 1077, did not have a significant correlation. The nRMSE values range between 0.13 and 0.21 m (Figure 3.4e) for the duration of the study. Both metrics show a strong variation in model performance based on time of day, which is further discussed in section 4.4.2. The coefficients obtained for each linear and exponential model varied with time and are included in Figure 3.5.

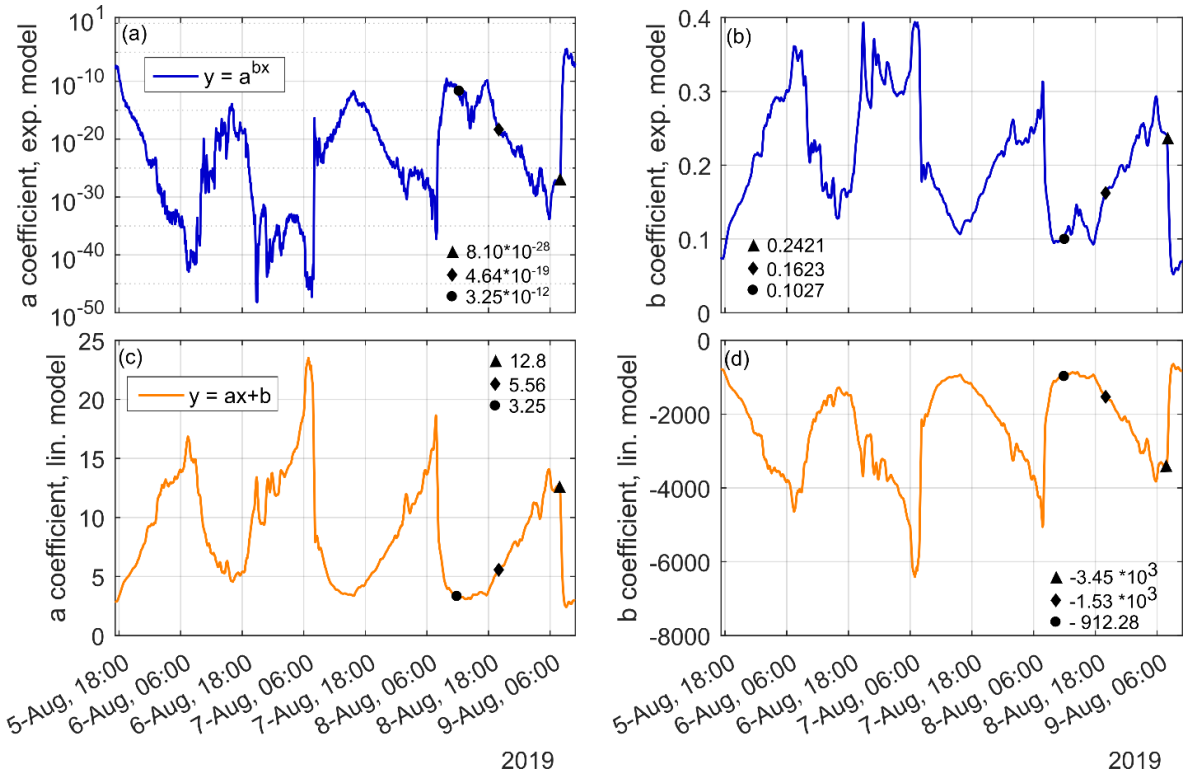

Figure 3.5. Parameter values for both the exponential and linear model. The timing of the scatter plots shown in Figure 3.4a-c is indicated by the triangle (08-Aug-2019 12:00), the diamond (08-Aug-2019 20:00) and the circle (08-Aug-2019 12:00), with the corresponding values for the parameters indicated on the figure.

Under clear conditions from August 7th to 9th, model performance was at the lowest for both models when direct solar radiation first reached the study area, around 8:00 AM. Model performance increased throughout the day, to reach a maximum at late night or very early morning (around 2:00 for exponential fit and 6:00 for linear fit). The performance of both models increased throughout the

night as the negative net longwave radiation gradually cooled the debris and the influence of warming from shortwave net radiation in the previous day decreased relative to heat conduction. This explains why both models perform better late at night or very early in the morning, long after the sun sets behind the mountains at 1800h. When sunlit, the surface energy balance becomes dominated by net shortwave radiation, and the amount of irradiation absorbed by the surface fluctuates at a very small spatial scale due to varying rock albedo, slope, aspect and shading from both individual boulders and surface micro-topography which further decouples the surface temperature from the debris thickness. The simple exponential and linear regression models tested herein could not reliably estimate debris thickness in shortwave radiation-dominated regimes since the surface temperature increase caused by absorption of shortwave radiation is decoupled from subsurface thermal regimes associated with debris thickness over ice, but rather is influenced by many other factors (e.g., partial cloud cover, local slope inclination, shading, multiple reflections, solar elevation), which is in agreement with finding from Herreid (2021). These results suggest that the ideal timing to measure surface temperature for estimating debris thickness over ice using empirical relationships as presented here is late at night or early morning before sunshine hits the study site. Simple relationships ignoring the surface energy-balance processes or not accounting for the strong influences of shortwave radiation on surface temperature, should not be used to estimate debris thickness from surface temperatures measured during daylight, as it is usually done with satellite imagery and UAV applications.

The variation in model performance between the exponential and linear fit also followed a pattern: an exponential curve provides a higher coefficient of determination and a lower RMSE during most of the day, but a linear fit performs better late at night, approximately from 3:00 AM to 8:00 AM. This diurnal pattern between the two models was broken on the first day of data collection (August 6th), when dense clouds, fog and rain occurred over the study area, causing similar high model performance for both the exponential and linear models. This pattern is likely linked to the dual controls on surface temperature occurring throughout the day. During daylight, the solar radiation heats the debris surface, but thin debris stays cool due to the close presence of the underlying ice, creating an exponential fit between the debris thickness and surface temperature. At night, the thermal inertia linked with the presence of the underlying ice dominates, and the correlation between surface temperature and debris thickness is better represented by a linear model.

3.4.4. Factors impacting the surface temperature-debris thickness correlation

Over this study period, the empirical relationships derived between surface temperature and debris thickness showed a high variability both in terms of model performance and parameters values (Figure 3.4, 3.5). In the next section, different factors that influence the surface temperature-debris thickness relationship, and the resulting modelled debris thickness, are investigated. Five environmental and data collection factors were tested: (1) weather conditions, (2) the time of the day at which the TIR images are collected, (3) the number and (4) distribution of the manual excavations, and (5) the spatial resolution of the TIR images.

3.4.4.1. *Weather conditions*

The meteorological conditions observed during the experiment explain some of the measured surface temperature as well as the modelled debris thicknesses. Over the study period, weather was overcast during the first day of the three-day study (August 6th). Intermittent rainfall occurred in the eveningwith 10mm rainfall recorded at the $AWS_{moraine}$ between 6:00 PM and 9:00 PM. Two predominantly sunny days followed on August 7th and 8th. This cloudiness is also discernible in the incoming shortwave and longwave radiation measurements from the two weather stations adjacent to the study area: the moraine and on-ice Peyto weather stations (Figure 3.6b-c). Both meteorological datasets are shown to showcase the variable conditions in the area. The AWS_{ice} is located only 425 m to the study area, and at only 25 m higher, but on a different surface, and the $AWS_{moraine}$ is located 1400 m away, and 90m higher, but on similar moraine sediments.

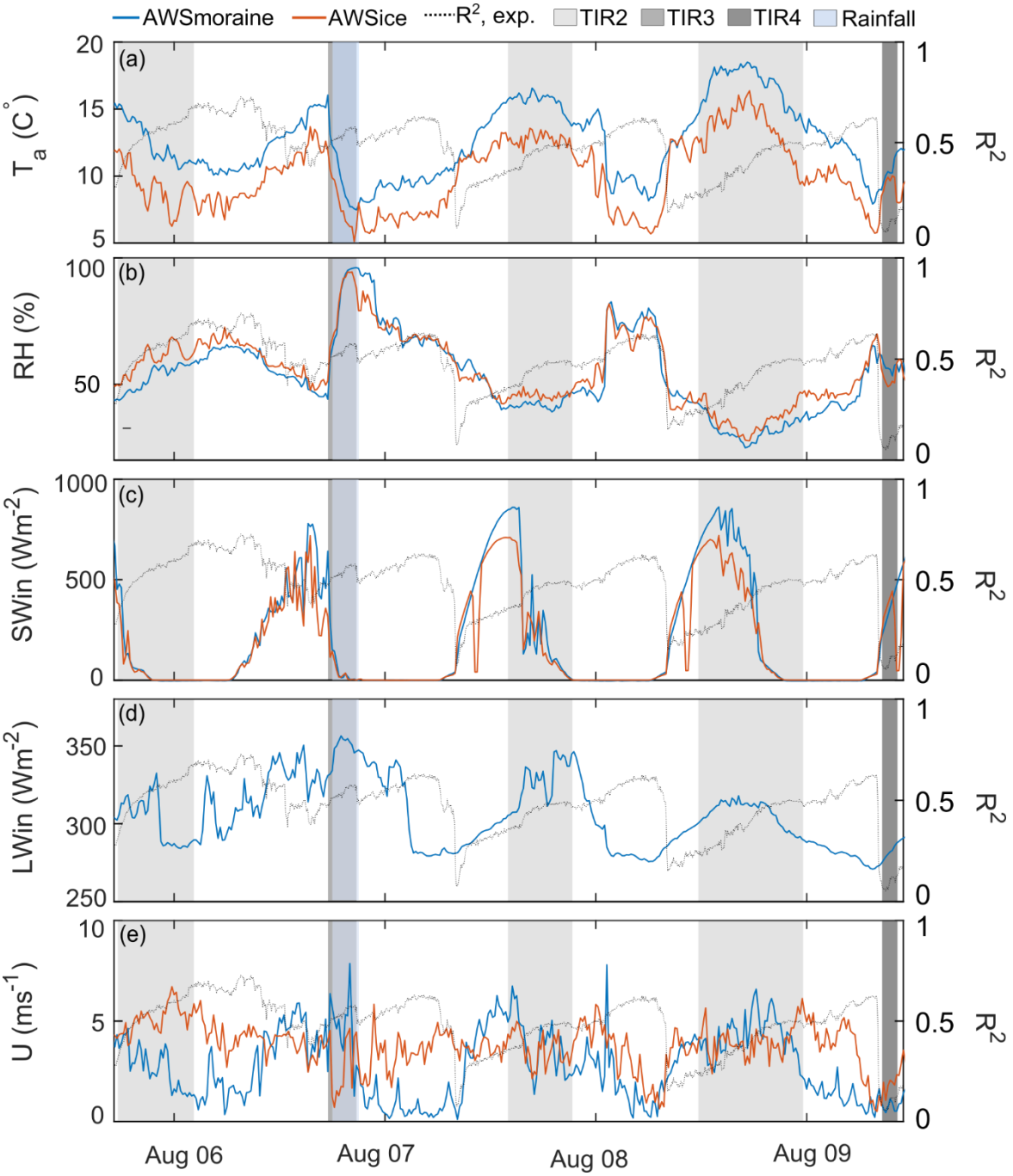

Figure 3.6. Meteorological measurements at the Peyto Moraine and Ice weather stations. The coefficient of determination R^2 for the exponential model between surface temperature and debris thickness (dashed line) is shown on the right axis. The shading represents the periods at which TIR2 to TIR4 were taken while TIR1 was measured during the entirety of the plotted data. The intermittent rainfall period is shaded in blue and is overlapping with the TIR3 measurement period.

Over the three nights analyzed, the best model performance occurs around 0745h MDT during the morning of August 5-6th under cloudy conditions, which contrasts with the following predominantly clear nights, when the highest correlation between surface temperature and debris thickness occurred slightly earlier (before 0700h). Additionally, on August 6th, both the linear and exponential model performances stay relatively high throughout the day compared to the following two days. The high cloudiness on August 6th shifted the incoming radiation regime from one dominated by shortwave radiation with its high spatial variability to one dominated by longwave radiation, which has a lower dependency on slope and aspect of the surface. The cloudiness allowed the conductive heat flux to continue to dominate the observed variability in surface temperature and resulted in better daytime model performance. This suggests that one can reliably obtain reasonable model performance towards the end of the night under clear conditions, but other times may be suitable if a continuous cloud cover is present, which is suitable to ground- or UAV-based surface temperature survey, but not applicable to satellite imagery analysis. These results are in agreement with Herreid (2021), who found optimal timing to use TIR imagery to estimate debris thickness during nighttime or during daytime hours but under cloudy weather, and Mihalcea *et al.* (2008a), who found a stronger correlation between elevation-band averaged surface temperature obtained from thermistor and debris thickness during nighttime.

Low clouds and short intense precipitation occurred between 19:00 and 21:00 on August 6th, likely causing interference between the TIR cameras and the study area and resulting in doubtful temperature measurements. Due to the short distance between TIR1 and the study area (140m) and the short duration of the intermittent rainfall, it was not possible to clearly detect the rainfall events in the TIR1 visible or infrared images. No image appeared obviously blurred from the atmospheric interference, and therefore, all the images were kept in the analysis. TIR3 was also active during the rainfall event, and in this case, due to the wider field of view and longer distance between the study area and the TIR3 camera, the atmospheric interference due to clouds was noticeable above and behind the study area, but not at its exact location, and all images were kept in the analysis. However, the surface temperature and modelled debris thickness obtained during the rainfall event should be treated carefully. Examples of the TIR1 and TIR3 visible and TIR images are shown in Figure A.3. Once the clouds lifted and the atmospheric path between the study area and the camera was clear, the possible presence of rainwater on the debris of the studied area did not seem to significantly affect the correlation between surface temperature and debris thickness, as shown by the relatively high correlation for the images of TIR1 on August 6th from 18:00 to 21:00 in Figure 3.4d, during which the

rainfall occurred. The good empirical performance model performance under wet conditions obtained here are contrasting with results from Herreid (2021), who observed the opposite.

3.4.4.2. *Temporal variation*

The distribution of calculated and interpolated debris thickness is compared for the same times of day as shown in Figure 3.4a-c, selected to represent relatively good (0745h), average (2000h) and poor (1200h) model performance. For each image, the best-fit model was selected. Both examples for the good (0745h, linear) and average (2000h, exponential) model performances provide reasonable estimates of debris thickness (Figure 3.7a-b). Both obtain average debris thicknesses over the study area that are one cm or less from the mean debris thickness interpolated from the manual excavations. However, they show mixed successes in replicating the interpolated debris distribution (Figure 3.7d-e). They can capture the range of measured debris thickness, from 0 to 110 cm thick, and capture the distribution of debris thinner than 30 cm and thicker than 70cm, but do not capture the mode of the measured debris thickness, which occurs at 35 cm for the interpolated debris thickness, but at 55-65 cm for the modelled debris. The “poor” (noon, exponential) model was unable to replicate the measured debris thickness patterns, indicated by a debris thickness strongly centred on 50 cm, strongly missing the presence of debris thinner than 25 cm or thicker than 75 cm (Figure 3.7f). The “poor” model underestimates the average debris thickness across the study area by 7 cm. This suggests that, when using TIR imagery obtained late at night, or under cloudy conditions, when the coupling between surface temperature and debris thickness is the strongest, it is possible to derive debris thickness for thick debris up to 100 cm, beyond the thermal decoupling suggested to occur around 50 cm when the surface temperature was obtained during daytime.

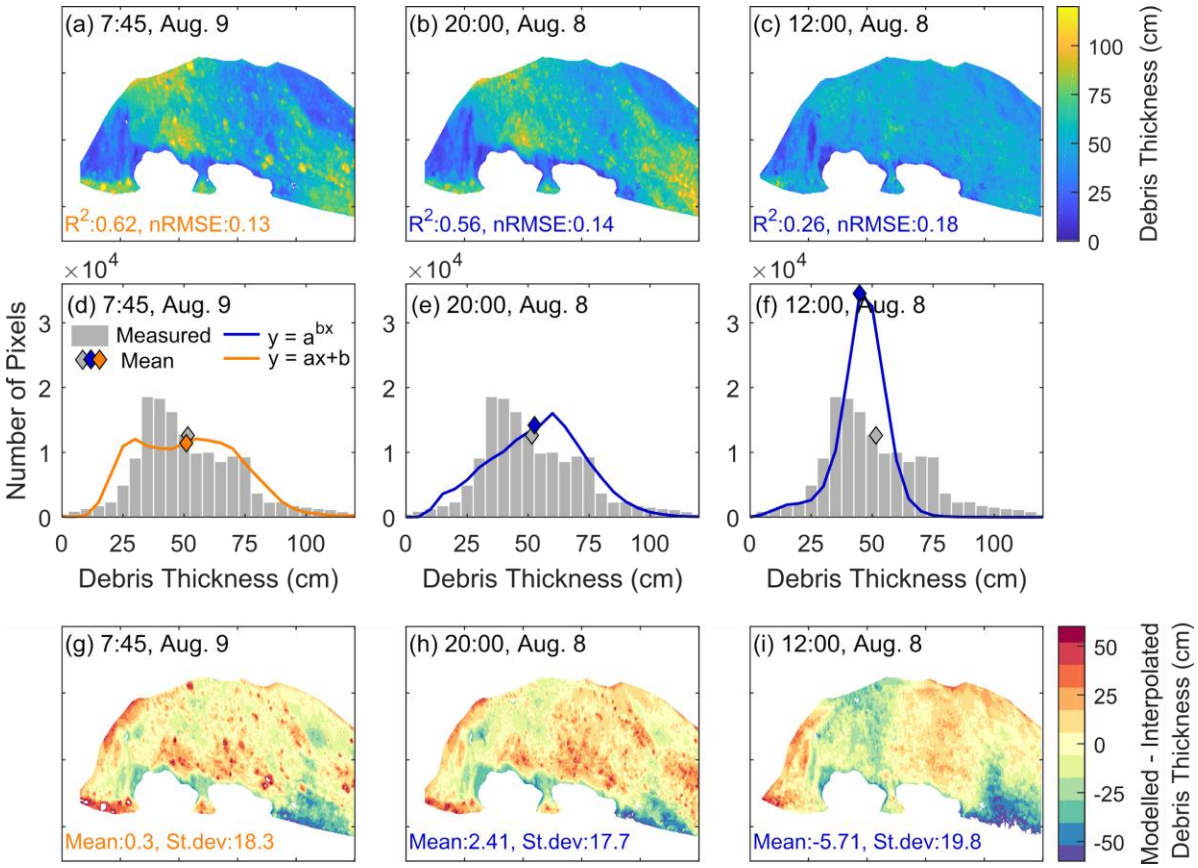

Figure 3.7. Modelled debris-thickness based on the "good" (a), "average" (b) and "poor" (c) model performance and associated debris thickness distribution (d-f). The difference between the modeled debris thickness and the interpolated debris thickness (in Figure 3.2a) is shown in (g-h). Orange refers to the linear model and blue to the exponential model. Note that the measured debris distribution, in (d) – (f) is the same as shown in Figure 3.2c.

The difference between the modelled and interpolated debris thickness is shown in Figure 3.7g-i. All models show an underestimation of debris thickness in the lower right region of the study area, where the thickest debris measurement was located. The difference between the "good" modelled and the interpolated debris thickness (Figure 3.7g) is mainly linked to the presence of large boulders, which are present in the modelled debris thickness but were not well captured but the smooth interpolation of the manual excavations across the study area. The "average" model and the "poor" model both over and underestimate the debris thickness across wider areas of the study area (Figure 3.7h-i). The distribution of the difference between modelled and debris thicknesses is shown in Figure A.5.

The cooling rates at the debris surface were also analyzed to see how they relate to measured debris thickness but using surface temperature change to estimate debris thickness did not provide

stronger model performances than the instantaneous surface temperatures (Figure 3.8). Cooling rates were tested from hourly intervals to daily intervals. For example, using the temperature change between 12:00 (noon) and 15:00 on August 6 as a predictor of debris thickness in the exponential empirical model did not provide a better estimate than only using the surface temperature measured at 15:00. Similarly, using the surface temperature change between 18:00 and 00:00 (midnight) on August 6 showed a similar model performance as using the surface temperature at midnight. These two examples showcase early and late-night cooling rates where a signal linked to the debris thickness might be expected to emerge. Hopkinson *et al.* (2010) found that the active areas of the ice-cored moraine at Peyto Glacier peaked at a cooler temperature during the daytime and presented a more rapid cooling after sunset than the cooling experienced in the stable areas of the moraine and concluded that these cooler areas were indicators of buried ice but did not draw any conclusion on debris thickness. The results presented here suggest that, while the overnight temperature changes can be used to derive empirical models of debris thickness, these models do not provide better model performances than using instantaneous surface temperature. However, this analysis is limited by the lack of correction of the TIR images for atmospheric emissions along the path from target to imaging radiometer, which can change with time and influence the temperature change observed between the images and add noise to the measured temperature change.

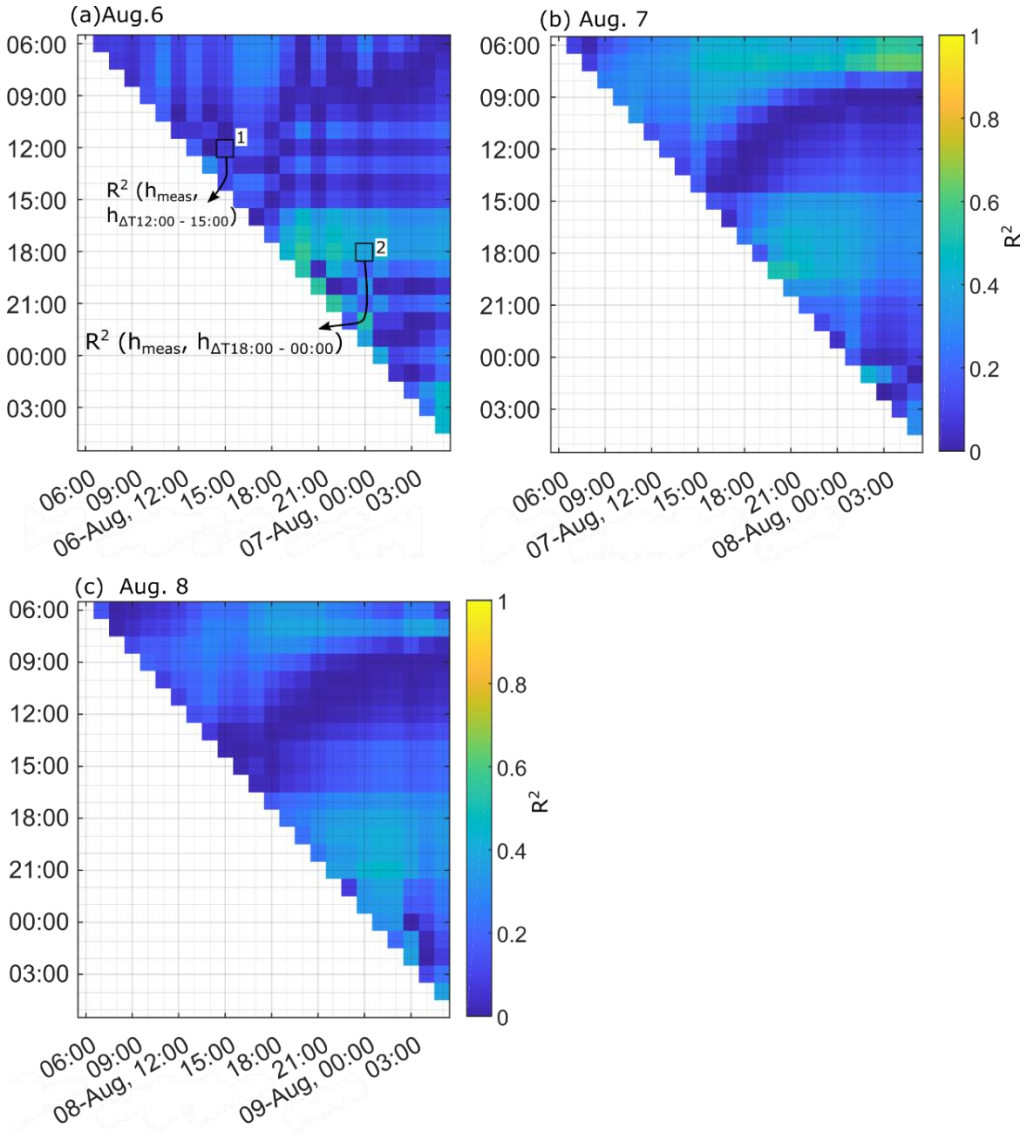

Figure 3.8. Correlation of determination (R^2) between modelled ($h_{\Delta T}$) and measured debris thickness (h_{meas}) with the exponential model, when the empirical model is based on surface temperature change (d-f) for August 6, 7 and 8. The outlined cell (1) shows the R^2 value calculated from the measured debris thickness (h_{meas}) and modelled debris thickness obtained with an exponential empirical model based on a change in temperature between 12:00 (noon), August 6, and 15:00, August 6 ($h_{\Delta T\ 12:00\text{-}15:00}$). The outlined cell (2) shows the R^2 value calculated from the measured debris thickness (h_{meas}) and modelled debris thickness obtained with an empirical model based on the change in surface temperature between 18:00, August 6, and 00:00, August 7 ($h_{\Delta T\ 18:00\text{-}00:00}$).

3.4.4.3. *Number and distribution of the manual excavations*

The number of manual excavations used to determine the correlation of the regression models between surface temperature and debris thickness was varied following two approaches to estimate their effect on the correlation parameters and performances. First, the number of manual excavations was reduced to half and then to a quarter of the available measurements while attempting to conserve the range and distribution of the debris thickness (Figure 3.9a-c). This resulted in using 22 and then 11 measurement points instead of 44. Secondly, the manual excavations used were classified by depth: shallow (<35 cm), medium (35-50 cm) and deep (>50 cm) (Figure 3.9d). The selection of this subset of data aimed to represent fieldwork scenarios when lower resources were available, causing a lower number of manual excavations to be performed and potentially resulting in a bias towards certain debris thicknesses in the empirical models that are developed.

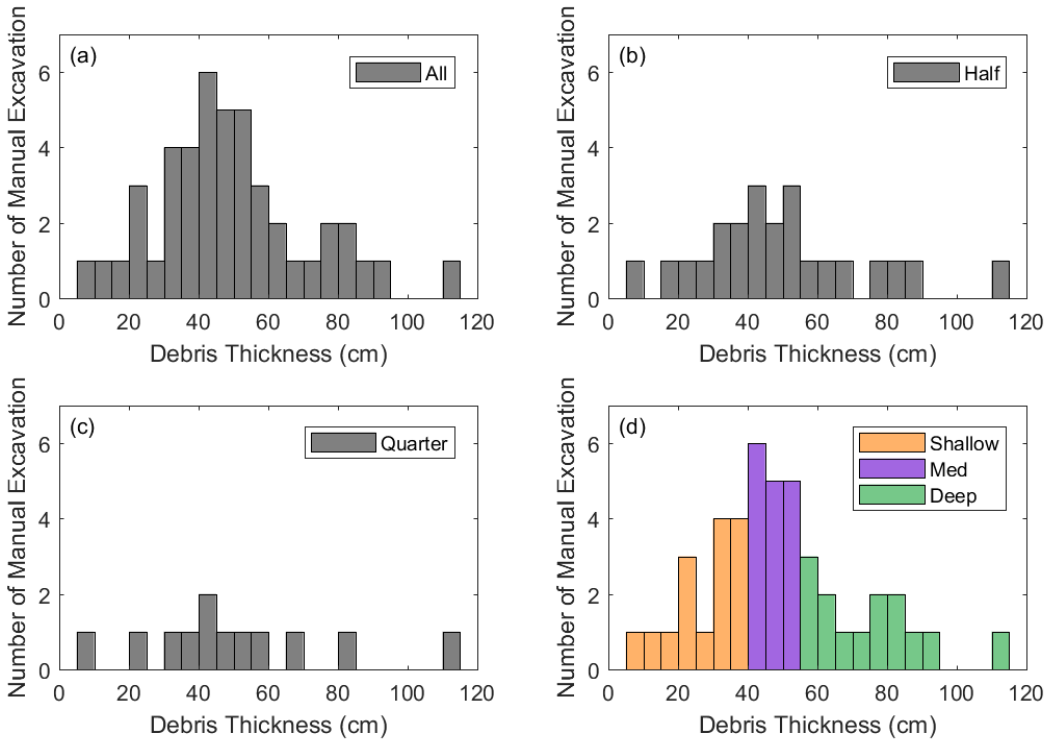

Figure 3.9. Manual excavation distribution used to build the regression models for showing (a) all the validation points (n = 44), (b) half the points (n = 22), (c) a quarter for the points (n = 11) and the shallow, medium and deep validation points (d).

Reducing the number of manual excavations used to derive the empirical model, while keeping a similar depth distribution of the validation points, shows an improvement in the model performance (Figure 3.10a). When only using a quarter of the manual excavations to establish the exponential regression models, the maximum R^2 over the study period improved from 0.73 to 0.91 (Figure 3.10a, Table 3.2). Comparing the three empirical models for August 7th, at 16:50, the coefficient of determination improves from 0.54 to 0.66 and 0.73 when only half and a quarter of the available measurements were used, even though the models are highly similar (Figure 3.10b-d) and provided comparable spatial distribution for the modelled debris thickness (Figure 3.10e-f). However, the models using only one half, and one quarter of the manual excavations overestimated the mean thickness across the study area by 6.14 and 4.33 cm respectively. Those errors are substantially above the mean deviation reached when all the available measurements are used (less than 1cm).

The modelled debris thickness distribution obtained with one quarter and one half of the manual excavations underestimated the presence of very thin debris (<10 cm) and medium thickness debris (30-50cm) but overestimated the presence of thick debris (>75 cm). The TIR images used to derive these modelled debris thicknesses are shown in Figure A.6a-c.

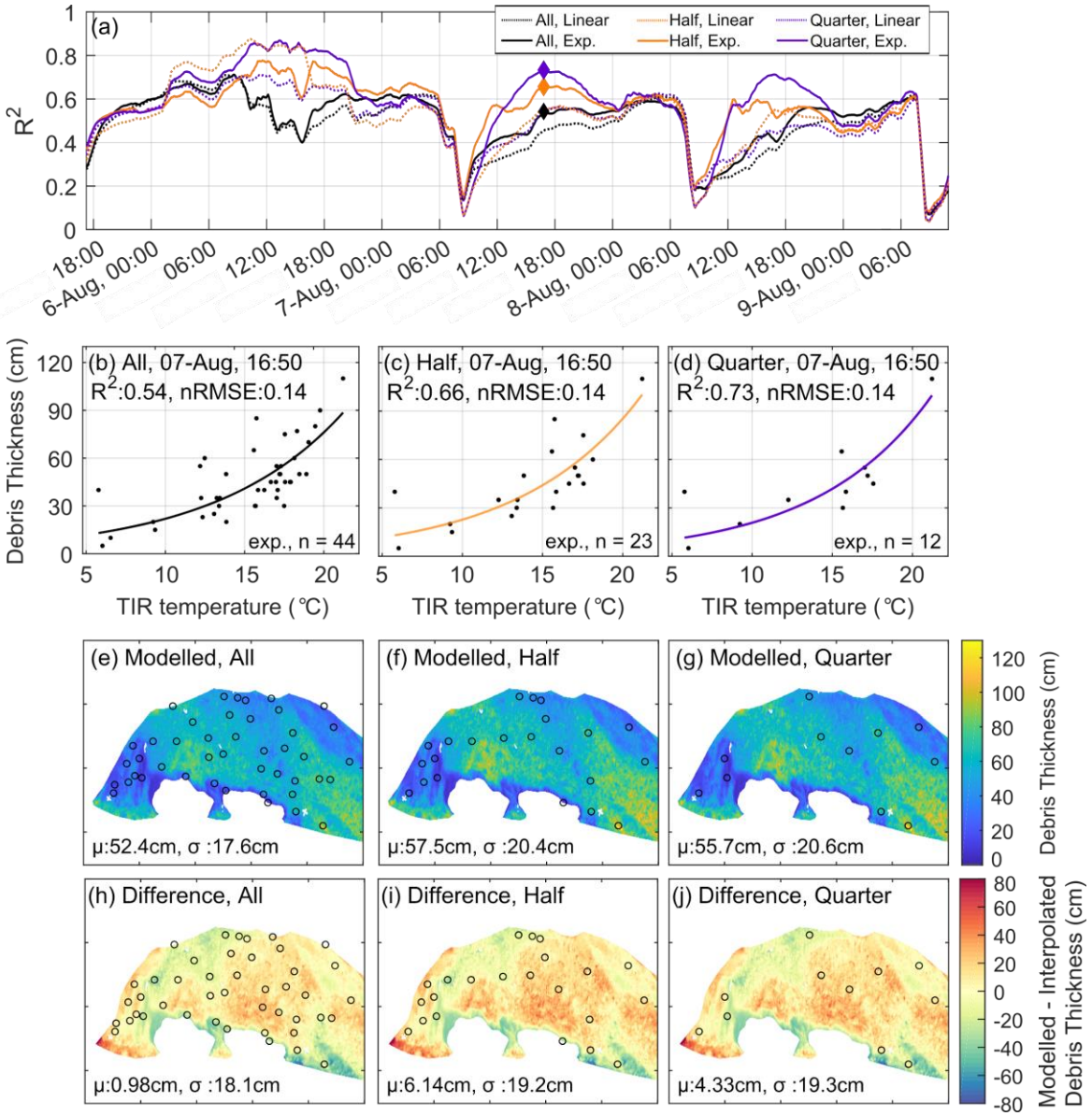

Figure 3.10. Coefficient of determination (R^2) obtained when using all, half or a quarter of the manual excavations in the regression model (a), with the regression models the TIR image taken on 07-Aug, 16:50 showed in (b-d), along with the coefficient of determination and the normalized RMSE. The model type (exponential or linear) and the number of point manual excavations used are shown in the bottom left of the panel. The timing of the (d-e) scatter plots is indicated by the diamond on the (a) panel. The resulting modelled debris thickness for the study area is shown in (e-g) and the difference between the modelled and interpolated debris thickness from the manual excavations is shown in (h-j). For the panels (e-j), the mean and the standard deviation are shown, and the locations of manual excavation used in the regression model are shown as circles.

Using only manual excavations measurements corresponding to shallow, medium or thick debris to derive empirical regression models, shown in Figure 3.9d, lead to very different patterns in model performance (Figure 3.11). When only shallow or medium debris were used in the empirical models, the resulting modelled debris thickness was highly uniform and strongly underestimated the interpolated measurements across the study area (Figure 3.11e-f, h-i). When using only thick debris, the modelled debris thickness showed a higher range of debris with a spatial distribution closer to the interpolated debris measurements, but strongly overestimated the mean debris thickness over the study area (Figure 3.11g, j). The TIR images used to derive these modelled debris thicknesses are shown in Figure A.6d-f. These results illustrate how an apparently strong model performance based on a limited number of ground observations can lead to inaccurate modelled debris thicknesses. For example, strong model performance was obtained when building a regression model on a few measurements, but the modelled variability in the debris thickness was wrong. Similarly, when a bias existed in the measurements used in the regression model, the average depth simulated over the study area was incorrect. This emphasizes the limitations of developing empirical models in highly heterogeneous environments with low numbers of observations and indicates that careful interpretation of statistical analysis is warranted.

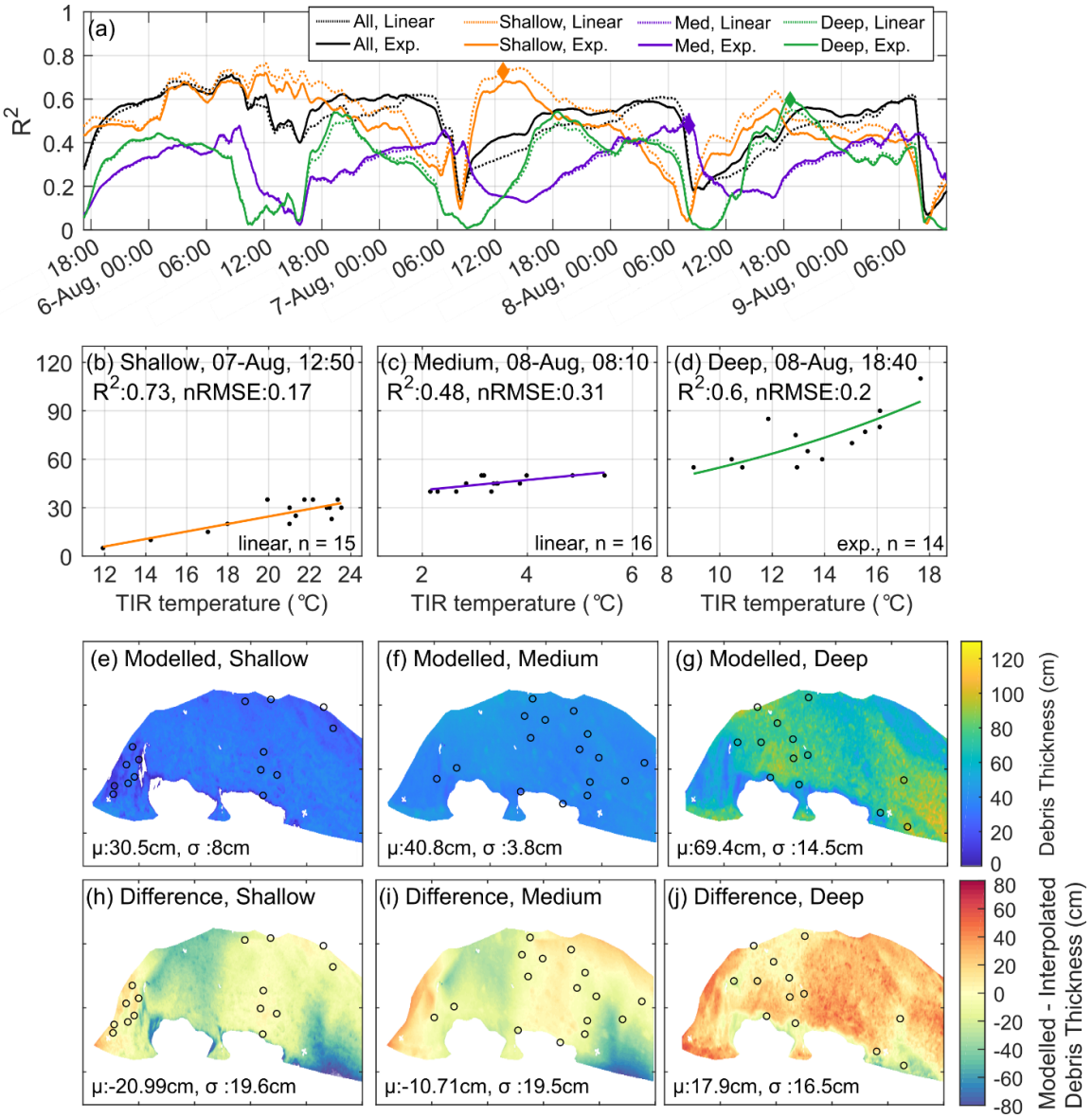

Figure 3.11. Coefficient of determination (R^2) obtained when using only shallow, medium or deep manual excavations in the regression model (a), with an example of good performing models shown in (b-d), along with the coefficient of determination and the normalized RMSE. The model type (exponential or linear) and the number of point manual excavations used are shown in the bottom left of the panel. The timing of the (d-e) scatter plots is indicated by the diamond on the (a) panel. The resulting modelled debris thickness for the study area is shown in (e-g) and the difference between the modelled and interpolated debris thickness from the manual excavations is shown in (h-j). For the panels (e-j), the mean and the standard deviation are shown, and the locations of manual excavation used in the regression model are shown as circles.

3.4.5. Spatial resolution

Variation in the coefficient of determination was also explored by varying the spatial resolution of the surface temperature data. The spatial resolution of the images was artificially degraded to obtain images at resolutions 10, 20 and 30 times lower than the original images from TIR1. The original TIR image provided a pixel resolution of 1000 x 350 over the study area, which was degraded to 36 x 100, 18 x 50 and 12 x 34 pixels. These correspond to pixel sizes of 0.06 x 0.2m (original), 0.6 x 2.0m, 1.2 x 4m and 1.8 x 6m, respectively. Further degrading the spatial resolution was not possible due to the small area covered by the study area and would have led to not having enough points to develop the correlations. Even though these spatial resolutions are higher than the ones available from satellite-based thermal imagery, they are comparable to those from UAV or plane-based instruments. For each degraded resolution, a linear and exponential regression model was fit, and the coefficient of determination was calculated between modelled and measured debris thickness for each image (Figure 3.13a). Changing the spatial resolution of the image caused a moderate decrease in the model performance, but a strong impact on the small-scale variability of the calculated debris thickness. Decreasing the spatial resolution produced a similar overall pattern of debris thickness compared to the high-resolution images, but the debris thickness variability linked to individual clusters of boulders, for example, was not captured (Figure 3.13e-j). This suggests that high-resolution images are not necessary to estimate the overall pattern of debris thickness and that high-resolution images only introduce noise due to microtopography. However, this comparison is limited by the use of the interpolated debris thickness as the reference, as it does not capture small-scale variability in debris thickness and microtopography. The TIR images used to derive these modelled debris thicknesses are shown in Figure A.6g-i. The summary statistics of model performance for the number and distribution of measured debris thickness used in the regression model as well as the spatial resolution of the TIR images are shown in Table 3.2.

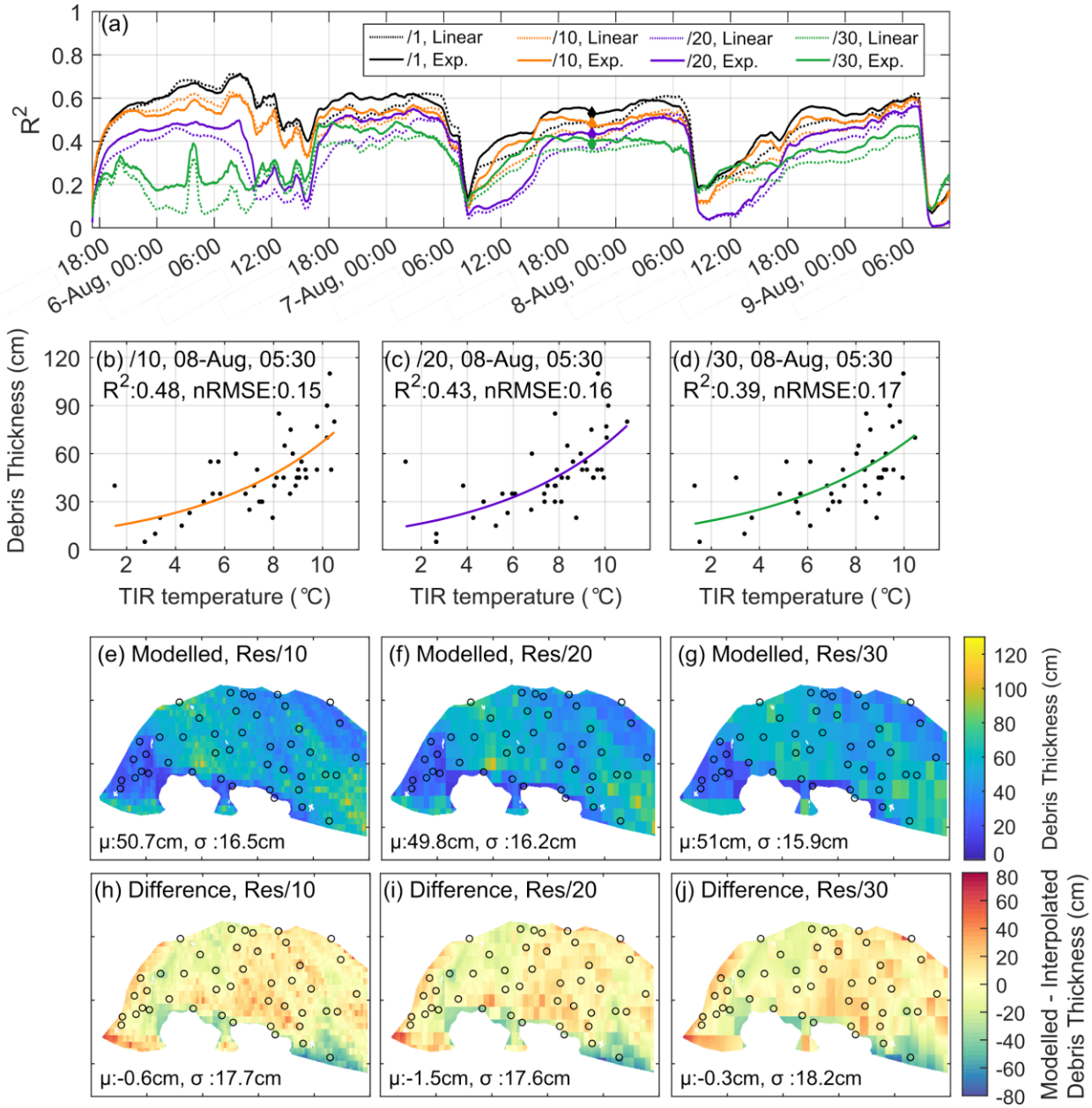

Figure 3.12. Coefficients of determination (R^2) obtained when using all, half or a quarter of the manual excavations in the regression model (a), with the regression models the TIR image taken on 07-Aug, 16:50 showed in (b-d), along with the coefficient of determination and the normalized RMSE. The model type (exponential or linear) and the number of point manual excavations used are shown in the bottom left of the panel. The timing of the (d-e) scatter plots is indicated by the diamond on the (a) panel. The resulting modelled debris thickness for the study area is shown in (e-g) and the difference between the modelled and interpolated debris thickness from the manual excavations is shown in (h-j). For the panels (e-j), the mean and the standard deviation are shown, and the locations of manual excavation used in the regression model are shown as circles.

Table 3.2. Summary of model performance for the number and depth of manual excavations as well as spatial resolution scenarios. Values refer to the exponential model, and values in parenthesis refer to the linear model.

	R^2_{mean}	R^2_{min}	R^2_{max}	$nRMSE_{mean}$	$nRMSE_{min}$	$nRMSE_{max}$
Normal	0.51 (0.48)	0.05 (0.05)	0.73 (0.73)	0.15 (0.16)	0.13 (0.13)	0.21 (0.21)
Half	0.56 (0.51)	0.07 (0.06)	0.8 (0.73)	0.16 (0.17)	0.11 (0.14)	0.23 (0.23)
Quarter	0.58 (0.52)	0.03 (0.02)	0.91 (0.89)	0.18 (0.2)	0.1 (0.12)	0.28 (0.29)
Shallow	0.47 (0.52)	0 (0)	0.76 (0.79)	0.24 (0.23)	0.17 (0.16)	0.33 (0.33)
Medium	0.3 (0.3)	0 (0)	0.65 (0.65)	0.35 (0.36)	0.25 (0.24)	0.42 (0.42)
Deep	0.31 (0.3)	0 (0)	0.61 (0.56)	0.27 (0.28)	0.2 (0.21)	0.38 (0.38)
Resolution/ 10	0.45 (0.43)	0.05 (0.05)	0.64 (0.67)	0.16 (0.17)	0.13 (0.13)	0.24 (0.24)
Resolution/ 20	0.37 (0.32)	0 (0)	0.57 (0.6)	0.18 (0.18)	0.14 (0.13)	0.24 (0.24)
Resolution/ 30	0.33 (0.28)	0.02 (0.02)	0.59 (0.57)	0.18 (0.19)	0.15 (0.16)	0.24 (0.24)

3.4.6. Camera location and angle

Another factor influencing data collection is the distance and angle between the camera and the study area. A camera located further away will cause a decrease in spatial resolution, but other sources of error can appear, such as atmospheric interference along the optical path between the camera and the study area. To assess how this might affect calculated debris thickness, the average measured surface temperature for the study area captured from the different TIR locations was compared. This showed that the surface temperatures obtained by the four camera locations followed a similar pattern with similar average measured temperatures, even though the distance between the study area and the camera, the camera view angle, and the number of pixels of the study area greatly differed amongst the shots (Figure 3.12). TIR1 was located 140m from the study

area, while TIR2 and TIR3 were at 290 and 370 m, and TIR4 was only 6 m from the ice cliffs. These distances were relatively short compared to other oblique imagery applications (945-1145m in Aubry-Wake *et al*., 2015; 10-1000m in Herreid, 2021). Overall, the standard deviations of the surface temperature of continuous debris measured with TIR1, TIR2, and TIR3 were very similar as well. This suggests that TIR imagery is a robust approach to monitor debris surface temperature and does not strongly depend on the distance and view angle, as long as the distance does not allow for significant atmospheric disturbances between the target area and the camera (Aubry-Wake *et al.*, 2015; Herreid, 2021; Baker *et al.*, 2019). This conclusion might be due to the specific atmospheric conditions and short distances of this study site, and more efforts should be put forward to understand the environmental conditions that impact atmospheric emission of TIR along the path from target to imaging radiometer, and how these emissions affect TIR imagery in glacial environments.

Considering that the surface temperature between the different camera locations follows similar patterns of absolute temperature, one could assume that the resulting calculated debris thickness provides similar results. However, this is difficult to assess with the TIR images in this study. Due to the changing camera angle and the increased distances, most validation points and TIR targets were not discernable in the images from TIR2-4. Regression models could not be derived specifically for these images. When the linear and exponential regression equations derived from TIR1 are used on TIR2, TIR3 and TIR4 images, modelled average debris thicknesses over the study area are very different (Figure 3.13b). This emphasizes the limitations of empirical model transferability and their applications outside the specific setting in which they were developed. A future experiment comparing surface temperature from TIR imagery from different perspectives and distances should ensure that the difference in camera location provides a strong overlap in the view of the study area to allow matching geospatial localization. Specifically, the localization targets should be visible from all the camera perspectives. Such an experiment could be used to assess not only average surface temperature but also assess the changes in longwave radiation transmission between the camera and the study area.

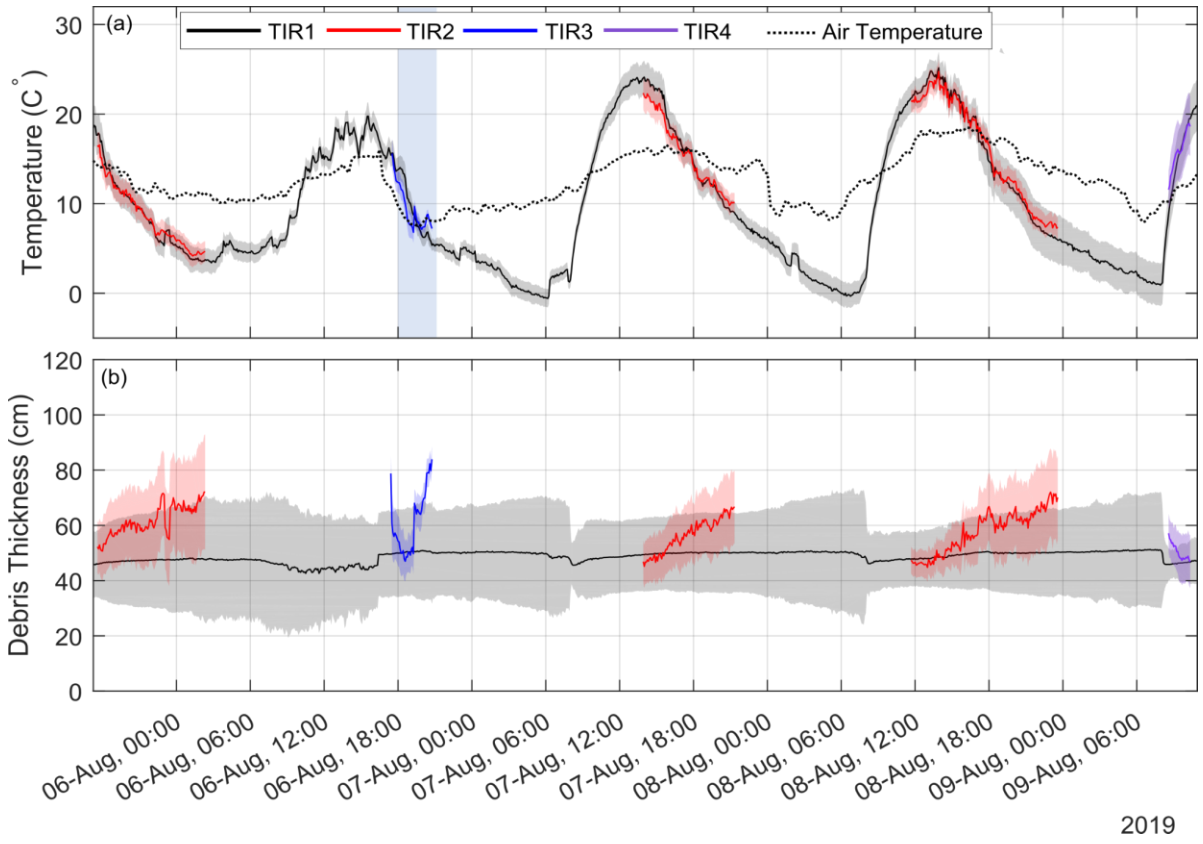

Figure 3.13. TIR-derived average surface temperature for the study area (a) for location TIR1 (grey), TIR2 (red), TIR3 (blue) and TIR4 (purple). The mean temperature is represented by a solid line and the standard deviation is illustrated by the shading. Air temperature is shown as a dotted line for comparison. The modelled debris thickness using the exponential model from the TIR1 location is shown in (b), for the TIR1 (grey), TIR2 (red), TIR3 (blue) and TIR4 (purple) locations.

3.4.7. Debris thermal emissivity

The TIR-derived surface temperatures used in the empirical debris thickness models are radiant temperatures obtained under the assumption that the debris cover has a uniform emissivity of 1.0 and thus behaves as a perfect blackbody. This allows more straightforward processing of the images, and as the TIR-derived temperatures are not analyzed for accuracy of the absolute temperature, but only to derive the relationship with debris thickness, this possible bias in surface temperature due to the lack of emissivity correction cannot influence the results. However, some small-scale variability in surface exitance of longwave radiation linked to the varying lithology, sky view, reflectance, slope and aspect, and reflectance of thermal irradiance is likely, even though this small-scale variability is mitigated by the uniform rock debris cover type analyzed in the study area, as the ice cliffs were removed from the analysis. However, despite the cover type of the study area being uniformly rock debris, it presented varying clast size and specific lithology, which also affects the emissivity

(Salisbury and D'Aria, 1994; Sobrino and Cuenca, 1999). Additionally, emissivity decreases when the view-angle moves further from nadir with the decrease following different curves for varying surface types (Sobrino and Cuenca, 1999). Individual boulders, therefore, present varying viewing slopes relative to the camera, shifting the emissivity. This small-scale variability in emissivity, reflectance, irradiance and hence exitance may have added noise to the correlation between radiant surface temperature and debris thickness. In this study, this was mitigated by having a uniform slope in the area with a small study area with consistent lithology.

It should be noted that given the short distance between the camera and the study area (140 m) and low absolute humidity in the cool, unsaturated air, atmospheric TIR emissions along the path from target to imaging radiometer are likely to be minimal. The distance from the TIR imager to the furthest and closest points in the study area is very close, and therefore, any atmospheric TIR emissions are likely to be relatively uniform for each image. Atmospheric TIR emission can vary over time, but as each image was assessed independently and so this has minimal effect on the analysis.

3.4.8. Suggestions for optimal TIR surveys

Modelled debris thickness was highly sensitive to biases in the range of measured debris thickness used in the empirical models, with a strongly weakened predictive capacity at the study area scale when the regression models were developed using only shallow, medium or thick debris thicknesses. This supports findings by Boxall *et al.* (2021), who drew similar conclusions when using empirical models to estimate debris thickness at the regional scale in High Mountain Asia. When comparing different empirical debris thickness models, Boxall *et al.* (2021) also suggested that optimal model type was related to debris thickness, with linear models performing better for thinner debris, which is observed in this study as well.

The number of debris thickness measurements used in the regression models, as well as the spatial resolution of the TIR images, had a relatively smaller impact on modelled debris thickness. Even when reducing spatial resolution by a factor of three, reasonable modelled debris thickness was obtained despite a decrease in model performance. This suggests spatial resolution, once high enough to capture patterns in slope and angle and resolve features such as ice cliffs, does not need to be a key priority when estimating debris thickness from surface temperature. In this study, a spatial resolution of 0.6 x 2.0 m or 1.2 x 4 m, instead of the original 0.06 x 0.2 m, would have been adequate to capture the debris cover pattern on the study area while smoothing over the microtopography that causes additional noise in the relationship. Similarly, based on this analysis, the temporal resolution used in

this study, with image acquisition occurring every 5 minutes, was superfluous. Images acquired hourly under stable weather conditions, or every 15 to 30 minutes interval during quickly changing weather and around sunrise would have been sufficient, with the added benefit of preserving battery power and allowing longer data collection.

Due to the highly variable model performance that was due to a large range of the factors analyzed here, the empirical models presented in this study have no validity or known performance outside of the four days and the small study area used in their generation. Developing debris thickness empirical models that hold transferability in time or space approaches using the information in the infrared images to constrain the exponential scaling, such as in Kraaijenbrink *et al.* (2018) and Herreid (2021) should be further explored.

3.5. Conclusions

This study explored how the correlation between oblique ground-based TIR-observed surface temperature and debris thickness over ice is influenced by data collection methods and weather conditions in the field. A total of 1478 thermal-infrared images were collected on August 5-9th, 2019 using two TIR imaging radiometers at four locations around a small ice-cored moraine complex at the edge of Peyto Glacier, in the Canadian Rockies. These images were used to produce high spatial and temporal resolution surface temperature maps of the ice-cored moraine. Along with these maps, 44 excavations of the moraine were made to measure debris thickness above the ice and surface temperatures were correlated to debris thicknesses.

This study presents a thorough analysis of the different factors relating to weather conditions and data collection approaches that influence the empirical relationship between surface temperature and debris thickness. High-resolution temperature maps of debris-covered glaciers, such as those processed by Kraaijenbrink *et al.* (2018) and Tarca and Guglielmin (2022), provide a valuable snapshot of surface temperature distribution but only allow limited investigation of how the relationship between surface temperature and debris thickness varies throughout the day. Similarly, previous studies linking surface temperature to debris thickness using empirical relationships were limited both in spatial and temporal resolution by the use of satellite imagery (Mihalcea *et al.*, 2008a, 2008b; Minora *et al.*, 2015). Therefore, this study provides a substantial advance in the understanding of surface temperature and debris-cover variability.

Using 44 debris thickness measurements ranging from 5 to 110 cm, a linear and exponential regression model between debris thickness and surface temperature was generated for each image. A pattern emerged, where an exponential model provided better performance than the linear model throughout the day, but the linear model performed better than the exponential model for a short period in late-night conditions, reaching R^2 values of 0.71 and nRMSE of 0.13 m. Based on these results, the most reliable times to obtain surface temperatures that correlate well to debris thickness are from late at night to just before sunrise under clear conditions or any time of the day or night under cloudy conditions.

The findings of this study have several practical implications for future efforts involving the acquisition of TIR-derived surface temperature. This is of obvious use for debris thickness calculations as presented in this work but can also be of use to a broader range of geophysical investigations using surface temperatures, such as studies in the field of permafrost, soil moisture, surface water-groundwater interactions or volcanology. Beyond presenting practical implications for TIR radiometer data collection, this study provides an initial insight into the small-scale radiative and conductive controls of surface temperature in debris over glacial ice.

4. EVALUATION OF TURBULENT TRANSFER PARAMETERIZATION AND INFLUENCE ON SURFACE MELT FOR TWO MID-LATITUDE GLACIERS IN THE CANADIAN ROCKIES

Paper manuscript status: This chapter has not been submitted for publication.

Author contribution: Caroline Aubry-Wake compiled and analyzed field data, designed and tested the CRHM model implementation and wrote the first draft of the manuscript. Scott Munro collected and processed the Peyto Glacier field data, and provided advice on the data analysis and writing. Jonathan Conway and Warren Helgason collected and processed the Athabasca field data. Logan Fang scripted the Cold Region Hydrological Model modules. John Pomeroy funded the project, participated in both the Peyto and Athabasca experimental design and data collection, provided critical feedback on data processing, and approach and edited the manuscript.

Role in thesis: This chapter introduces a new module implemented in the Cold Region Hydrological Modelling Platform (CRHM) to calculate turbulent transfer to melting glacier ice. It focuses on the implementation of an hourly energy balance with a katabatic parameterization for the turbulent fluxes of sensible and latent heat to ice. Utilizing in-situ data from both the Peyto Glacier and Athabasca glacier, the katabatic parameterization is compared with eddy covariance turbulent fluxes, with the Monin-Obukhov bulk transfer approach, a commonly used turbulent flux parameterization, and with the EBSM daily turbulent flux parameterization already implemented in CRHM. The resulting melt from the different parameterizations is compared with measured surface melt. This model development was essential for the work presented in Chapter 6, for point-balance glacier surface melt modelling, and Chapters 7 and 8 for the Peyto basin CRHM model. This chapter relates to Objective 1 of this thesis.

4.1. Abstract

Melt season meteorological conditions, turbulent fluxes and the resulting surface melt were investigated for the Athabasca Glacier and the Peyto Glacier, both located in the Canadian Rockies. Profiles of air temperature, humidity and wind speed, in addition to turbulent fluxes measured using eddy-covariance systems, a full radiation budget and snow or ice surface lowering were available for 13 days in June 2015 on the Athabasca Glacier and intermittently for 14 days in July and August 2008 on Peyto Glacier. At Peyto Glacier, a katabatic wind was detected in 51% of the measurements, compared with 80% at the profile located downwind, near the terminus, and only in 31% of the

measurements at the Athabasca profile. At both sites, the net radiation (shortwave and longwave) was the largest energy flux, contributing nearly 70% of the energy available for melt. In contrast, the sensible heat flux contributed approximately 30% of the energy available for melt, while the latent heat flux contributed less than 2.5%. The katabatic approach underestimated the turbulent fluxes compared to the eddy covariance measurements, while the bulk transfer approach overestimated them. The katabatic approach provided better RMSE values, and the bulk transfer resulted in higher correlation coefficient values. In all cases, daily flux calculations made using the Energy Budget Snowmelt Model underestimated observed fluxes. Including hourly time steps, process-based parameterizations of the surface energy balance processes with an explicit representation of the effects of the katabatic winds improved the capacity of the Cold Region Hydrological Modelling Platform to simulate the dynamics of glacier melt and estimate glacier melt contributions to streamflow.

4.2. Introduction

Glacierized catchments display a range of complex hydrological processes that affect streamflow generation (Milner *et al.*, 2017). There is a need to include the range of processes occurring in these headwater glacierized catchments to increase the fidelity of hydrological models, or their capacity to reproduce not only streamflow measurements at the catchment outlet but also their internal functioning (Finger *et al.*, 2011; Pellicciotti *et al.*, 2012; MacKay *et al.*, 2018). A common approach for model development is to take an existing hydrological model and add routines to represent the glacier processes (van Tiel *et al.*, 2020b). As more data and knowledge are obtained, the routines for the varied processes should be updated to reflect ongoing scientific advances.

In glacierized alpine catchments, an important streamflow generation process is the melt of ice surfaces, dictated by the surface energy balance (the sum of the energy fluxes in and out of the ice surface). Net radiation, the main energy source to the glacier surface, can be reliably measured and spatially distributed using digital elevation models to replicate shading, slope, and aspect with reasonable accuracy (Munro, 2004). The turbulent fluxes (sensible heat flux Q_h and latent heat flux Q_e) are more difficult to measure. Eddy covariance (EC) systems provide the capacity to directly measure turbulent fluxes in the field (Munro, 1989; Cullen *et al.*, 2007; Litt *et al.*, 2014; Fitzpatrick *et al.*, 2017; Radic *et al.*, 2017; Steiner *et al.*, 2018). These measurements are typically limited in time from a few days to a few weeks due to both the fragility and sensitivity of EC instruments installed in harsh glacier conditions (Fitzpatrick *et al.*, 2017).

The calculation of turbulent fluxes in melt models employs a wide range of approaches. In the commonly used enhanced temperature index models, the surface melt is parametrized based only on air temperature and incoming radiation, and the turbulent fluxes are not explicitly considered (Hock, 1999; Carenzo *et al.*, 2009).

A common method to calculate turbulent fluxes in glaciology is to measure profiles of temperature, wind speed and humidity and to apply the Monin-Obukhov (M-O) similarity theory. The bulk transfer approach with the M-O stability correction relies on a constant flux layer over the vertical gradient of measured air temperature and moisture between a measurement height and the surface to estimate the turbulent fluxes with Eqs. 4.1 and 4.2.

$$Q_{h\,BT} = \rho\, c_p\, C_H u_z\, (T_a - T_s) \tag{4.1}$$

$$Q_{e\,BT} = \frac{\mu \rho L_v}{p}\; C_E u_z\, (e_a - e_s) \tag{4.2}$$

in which ρ is the air density, c_p is the specific heat of air at constant pressure, μ is the gram molecular weight ratio of water to air, L_V is the latent heat of vaporization, p is the air pressure scaled for elevation, T_a is the air temperature, T_s is the surface temperature, u_z is the wind speed, e_a is the water vapour pressure, e_s is the surface water vapour pressure and z is the measurement height for the wind speed.

The bulk transfer coefficients $C_{H,\,E}$ are calculated with Eq. 4.3.

$$C_{H,E} = \frac{k^2}{[ln\,(z/z_0) + \psi_M][ln\,(z/z_{H,E}) + \psi_{H,E}]} \tag{4.3}$$

where k is von Karman constant (0.4), $\psi_{M,\,H,\,E}$ are the stability corrections for momentum, temperature and water vapour, and $z_{0,\,H,\,E}$ are the corresponding surface roughness lengths for momentum, temperature and water vapour.

On a glacier, the surface temperature and humidity are well constrained during the melting season and therefore, a bulk aerodynamic transfer approach requiring only one measurement height is commonly applied. Observations of wind speed and temperature gradients within the lowest few meters of the glacier surface have been made in various locations (Smeets *et al.*, 2000; Munro, 2004; Litt *et al.*, 2014, 2017). These measurements have shown that the applicability of bulk aerodynamic methods used to model turbulent heat fluxes depends on the proximity of a wind speed maximum

to the glacier surface and the extent to which large-scale winds influence the glacier surface boundary layer.

However, the aerodynamic bulk transfer approach does not account for the presence of katabatic winds, sometimes referred to as glacier winds. A katabatic wind, a common glacier feature during the melting season, is a stable, cold air drainage wind with a shallow boundary layer. A key feature of a katabatic wind is the presence of a low-level wind speed maximum. Katabatic winds are caused by the cooling of the near-surface air layer by the colder glacier surface, which results in winds flowing down-glacier along the flow line and modifying the near-surface air temperature distribution (Greuell *et al.*, 1997; Shea and Moore, 2010; Ayala *et al.*, 2015; Carturan, 2016; Shaw *et al.*, 2017; Troxler *et al.*, 2020). This alters the surface energy balance and ultimately the distribution of melt (Petersen and Pellicciotti, 2011). In a katabatic flow regime, wind speed maxima occur near the surface, which leads to a decoupling of the fluxes calculated at a measurement height from those at the surface (Grisogono and Oerlemans, 2001; Oerlemans and Grisogono, 2002b). The bulk aerodynamic approach assumes a constant turbulent flux layer, with vertical changes less than 10%, which is not valid in a katabatic wind layer. For a wind speed maximum at 5 m, the M-O theory would only be valid for the lowest 0.5 m (Denby and Greuell, 2000). One parameterization that has represented fluxes in a katabatic flow in a bulk heat transfer approach is the Oerlemans-Grisogono parameterization, here referred to as the katabatic parameterization (Oerlemans and Grisogono, 2002). This parametrization is based on the temperature deficit at the glacier surface caused by the katabatic forcing, but for simplicity, replaces it with the surface-air temperature gradient and a scaling coefficient K(Eq. 4.4).

$$K_{kat} = K(T_a - T_s)\left(\frac{g}{T_0 \gamma Pr}\right)^{1/2} \tag{4.4}$$

where Pr is the dimensionless turbulent Prandtl number, which relates the eddy diffusivity for heat Kh, and the eddy diffusivity for momentum Km (Pr = Km/Kh) , K is a dimensionless scaling coefficient and γ is the potential temperature lapse rate.

The K_{kat} coefficient (m s^{-1}) replace the wind speed and bulk transfer coefficient in equations (4.1) and (4.2), as shown in Equations (4.5) and (4.6):

$$Q_h = \rho\, c_p\, K_{kat}(T_a - T_s) \tag{4.5}$$

$$Q_e = \frac{\varepsilon \rho L_v}{p}\, K_{kat}\, (e_a - e_s) \tag{4.6}$$

In other cases, the turbulent fluxes are calculated following a range of algorithms at different time steps. For example, the glacier melt module implemented in the Cold Regions Hydrological Modelling platform (CRHM), a process-based, flexible, modular hydrological modelling platform that has been extensively used in mountains in recent years (DeBeer and Pomeroy, 2009; MacDonald *et al.*, 2010; Fang *et al.*, 2013; López-Moreno *et al.*, 2017), includes daily energy-balance calculations with the turbulent fluxes estimated based on daily temperature, wind and humidity measurements, from the Canadian Prairies in the Energy Balance Snow Model (EBSM; Gray and Landine, 1988; Pradhananga and Pomeroy, 2022a):.

$$Q_{h_{ebsm}} = -0.92 + 0.076 * u_{mean} + 0.19 * T_{max} \quad (4.7)$$

$$Q_{e_{ebsm}} = 0.08 * (0.18 + 0.098 * u_{mean}) + (6.11 - ea_{mean} * 10) \quad (4.8)$$

Where Q_h and Q_e are the sensible and latent heat fluxes (MJ day^{-1}), u_{mean} is the mean daily wind speed (m s^{-1}), T_{max} and T_{mean} are the maximum and mean daily temperatures (°C) and ea_{mean} is the daily mean vapour pressure (kPa).

This daily time step might be appropriate in certain settings, but it prevents the investigation of the diurnal evolution of the energy balance, which can be important an important process. For example, to investigate the influence of wildfire smoke on the surface melt of the Athabasca glacier, Aubry-Wake *et al.* (2022) required to correct the shortwave and longwave radiation fluxes at a sub-daily time scale to reflect the variable influence of smoke on atmospheric processes. Munro (1990) compared hourly measurements of surface ablation and simulated melt from hourly energy-balance calculations to gain insights into the diurnal storage and routing delays at the ice meltwater at Peyto Glacier. Hourly surface energy balance and ablation were also essential to investigate the importance of subsurface heat conduction and uncertainties associated with assuming a constant surface temperature at zero degrees (Pellicciotti *et al.*, 2009). As showcased by these examples, energy-balance calculations at the sub-daily time scales are key to understand and quantify certain processes influencing glacier ablation.

In this chapter, turbulent fluxes parametrizations are explored and compared with eddy covariance flux measurements collected during intensive field campaigns under differing meteorological regimes on two glaciers located in the Canadian Rockies. This is addressed through the following objectives:

1) Characterize the temperature, wind and humidity profiles on the Athabasca and Peyto glaciers during the melt season
2) Compare the measured eddy covariance fluxes with calculated turbulent fluxes from different algorithms
3) Investigate the resulting melt from the energy balance from these measured and estimated turbulent fluxes

4.3. Study sites and available data

Turbulent fluxes were calculated from the bulk transfer, katabatic and EBSM approaches and compared with eddy covariance measurements from the Athabasca Glacier, located in Jasper National Park obtained in June 2015, and Peyto Glacier, in Banff National Park, obtained in July and August 2008.

4.3.1. Athabasca Glacier

Athabasca Glacier (52.19 N, 117.25 W) is an outlet glacier of the Columbia Icefield. The upper section of the glacier forms part of the main ice mass of the Columbia Icefield and consists of an extensive plateau at ~2,900 m elevation. Below a series of steep icefalls that step down from the plateau, a relatively flat glacier tongue extends for 3 km. Here, an intensive field experiment was undertaken from mid-June to July 1, 2015 (Conway *et al.*, 2021) where instrumentation placed at 2175 m elevation (Figure 4.1a, b) consisted of an automatic weather station (AWS), and eddy-covariance system and a tower with wind, temperature and humidity sensors to measure profiles between 0.75 and 8 m above the ice surface (Table 4.1).

4.3.2. Peyto Glacier

Peyto Glacier (51.67 N, 116.55 W) is the northernmost outlet glacier of the Wapta Icefield which sits astride the Continental Divide in the Canadian Rockies (Pradhananga *et al.*, 2021). The upper region of Peyto Glacier, reaching 3100 m elevation, forms a semi-circular amphitheatre that converges into a gently sloping glacier tongue at around 2100 m elevation. On the glacier tongue (Figure 4.1c), two profile masts were installed approximately 640 m apart on the ice surface, one closer to the glacier toe (Toe site, Figure 4.1e) and one upwind of the toe (Peyto Upwind site, Figure 4.1f), where micrometeorological observations were recorded for 14 days between July 23 and August 25, 2008. Both sites recorded temperature, wind and wet bulb temperature at 1, 2, 4 and 6 m, with net shortwave and net total radiation at the Peyto Upwind site and an eddy-covariance measurement system 1.8 m above the surface at the Toe site. Additionally, an AWS was installed on supports drilled

into the ice between the profile sites (Figure 4.1d), recording incoming and outgoing shortwave radiation, temperature, relative humidity, wind speed and ablation (Table 4.1).

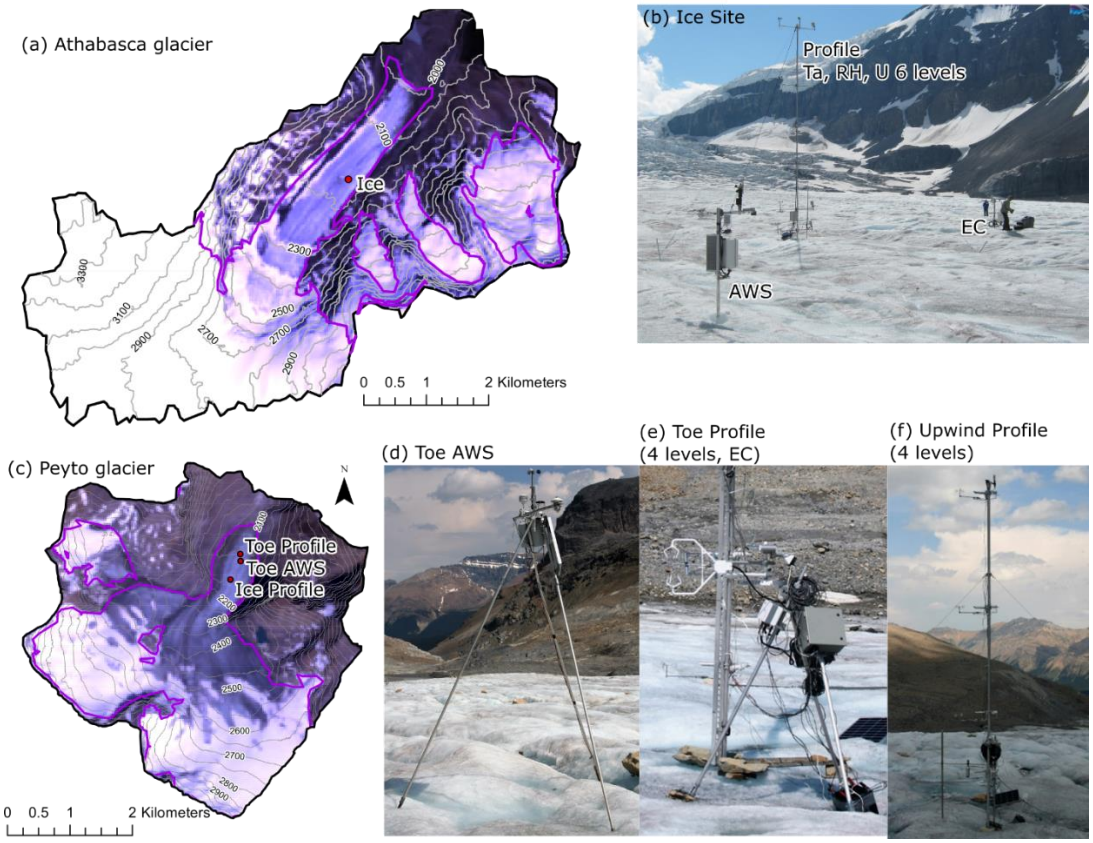

Figure 4.1. Site location. Athabasca glacier (a) was instrumented with an ice station (b) with an eddy covariance system, AWS and a profile mast. Peyto Glacier (c) was instrumented with an AWS near the glacier toe (d), a profile mast near the toe including an eddy covariance system (e) and an upwind profile mast further up the ice (f). Details of the instrumentation can be found in Conway et al. (2021) and Table 4. 1.

Table 4.1. Turbulent fluxes data available for model parameterization evaluation

Athabasca Glacier	Variables	Measurement Height
Ice AWS	Air temperature/ humidity	1.5 m
	Wind speed	2.0 m
	Barometric pressure	1.5 m
	Incoming/outgoing shortwave radiation	1.5 m
	Infrared surface temperature	1.4 m
	Surface height change	1.6 m
Ice Profile	Wind speed	0.75/1.5/3/4.5/6/8 m
	Air temperature/humidity	0.75/1.5/3/4.5/6 m
Ice Eddy-covariance	3-dimensional wind velocity, sonic air temperature	1.5 m
Peyto Glacier	**Variables**	**Measurement Height**
Ice AWS	Air temperature/ humidity	0.4 m above SR50a
	Wind speed	0.7 m above SR50a
	Incoming/outgoing shortwave radiation	0.1 m above SR50a
	Surface-height change (SR50a)	SR50: 1-4 m above ice
Toe Eddy-covariance	3-dimensional wind velocity, sonic air temperature	1.8 m
Toe Profile	Wind speed, Air and Wet-bulb temperature	1/2/4/6 m
Upwind Profile	Wind speed, Air and Wet-bulb temperature	1/2/4/6 m
	Net radiation/net shortwave radiation	2 m

4.4. Turbulent fluxes and surface melt calculation

The turbulent fluxes obtained from the eddy-covariance system at the Peyto and Athabasca sites were compared with fluxes calculated following three approaches: the bulk transfer with Monin-Obukhov (M-O) stability, the OG katabatic parameterization and the EBSM method. For the bulk transfer and the katabatic parameterizations, the calculations were made at an hourly time step, and for EBSM, the calculations were made on a daily time step. To be consistent with the height of the

eddy-covariance measurements, the calculations were made for fluxes at the height of 1.5 m at the Athabasca site, with meteorological data from the AWS station, and 2 m at Peyto Toe site, with the meteorological data of the corresponding height. The turbulent fluxes were used to calculate the surface melt using the energy balance (Eq. 4.9, 4.10):

$$M = \frac{Q_m}{L_v * \rho_w} \tag{4.9}$$

$$Q_m = Q_n + Q_h + Q_e + Q_r + Q_g - \frac{dU}{dt} \tag{4.10}$$

Where M is surface melt (mm w.e.), ρ_w is the density of water and L_v is the latent heat of fusion. Q_m is the energy available for melt, Q_h is the sensible heat and Q_e is the latent heat due to sublimation and evaporation, Q_r is the energy from precipitation, Q_g is the energy conducted into the ice or snow and dU/dt is the change in internal energy of the surface ice layer. For temperate glacier ice, the heat flux is zero except during occasional nocturnal freezing and is thus considered negligible in this situation (Hock, 2005). The surface layer is considered to be of minimal thickness, with changes in the energy fluxes translating to instantaneous changes in energy available for melt and therefore, the change in internal energy is typically considered negligible (Hock, 2005). All fluxes result in the energy available for melt, M (all in W m^{-2}). The fluxes are considered positive when towards the surface and negative when leaving the surface.

The net radiation is the sum of the longwave and shortwave radiation.

$$Q_n = (1 - \alpha)\, SW_{in} + \varepsilon_{ice} * \sigma * T_{ice}^4 + (1 - \varepsilon_{ice}) * LW_{in} \tag{4.11}$$

where α is the surface albedo, SW_{in} is the incoming shortwave radiation, LW_{in} is the incoming longwave radiation, ε_{ice} is the ice surface emissivity (0.985), σ is the Stefan Boltzmann constant (5.67 x10^{-8} kg s^{-3} K^{-4}), T_{ice} is the ice surface temperature (K), assumed to be at the melting point during melting season.

The energy due to precipitation was calculated from Hock (2005).

$$Q_r = \rho_w * c_w * R * (T_{rain} - T_{ice}) \tag{4.12}$$

where ρ_w is the density of water (1000 kg m^{-3}), c_w is the specific heat of water (4.2 kJ kg^{-1} K^{-1}), R is the rainfall rate (m hr^{-1}), T_{rain} is the temperature of the rain and T_{ice} is the ice surface temperature.

4.4.1. Bulk Transfer with Monin-Obukhov stability

The sensible heat flux Q_h and latent heat flux Q_e were calculated with Eqs 4.1-4.2. The surface temperature, T_s and the surface water vapour pressure e_s were set to 0 ˚C and 6.113 hPa for a melting ice surface (Hock, 2005).

In this study, the roughness length for momentum was set a 2.41 mm, based on a micro-relief study at Peyto Glacier (Munro, 1989). This approach based on roughness-element description, was found to have reasonable results when compared with z_0 derived from eddy covariance measurements (Fitzpatrick *et al*., 2017). The roughness length for heat and water vapor, z_H and z_E , were calculated from z_0 using the kinematic viscosity v and the roughness Reynolds number (Andreas, 1987, 2002):

$$Re_* = u_* z_0 / v \tag{4.13}$$

$$ln\left(z_{H,E}/z_0\right) = b_0 + b_1(ln\, Re_*) + b_2(ln\, Re_*)^2 \tag{4.14}$$

Values for b_0, b_1 and b_2 specific to z_H and z_E are tabulated in Andreas (2002).

The stability corrections are based on the Monin-Obukhov length L:

$$L = \frac{\rho c_p u_* T}{kgQ_H} \tag{4.15}$$

L conceptually represents the height above the surface where buoyant forces equal shear forces in the production of turbulence (Stull, 1988). To obtain L, an iterative scheme was used (Munro, 1989; 2004). The parameter z/L was used to define the application of the stability correction, with z/L > 0 implying stability, z/L< 0 implying instability, and z/L = 0 being neutral. The Holtslag and De Bruin (1988) approach was used for stable conditions, following recommendation from Andreas (2002), and following previous applications on glacier surfaces (Munro, 1989; Conway and Cullen, 2013a; Fitzpatrick *et al.*, 2017; Radic *et al.*, 2017). The Dyer (1974) approach was used for unstable conditions. These stability corrections were selected for consistency with previously published literature on turbulent transfer parametrization on glaciers in Western Canada, however, much discussion remains on the proper application of stability corrections in the determination of the turbulent fluxes over glaciers. Radic *et al*. (2017) compared the two main stability parametrizations for the bulk transfer approach, based on the M-O stability criteria, as here, and based on the bulk Richardson number, and found that limited improvements of the turbulent fluxes compared to parametrization without stability corrections. As discussed in Hock (2005), many studies assume that logarithmic vertical profiles of wind speed, temperature and humidity are valid under prevailing

stable conditions, and therefore do not apply stability corrections. Further advances are required to assess the parametrization of turbulent fluxes on sloped glacier surfaces.

4.4.2. Katabatic parameterization

Turbulent transfer with reference to katabatic flows was calculated following Klok and Oerlemans, (2002) and Munro (2004). Theyadded an additional parameter, the background turbulent exchange, K_b, to represent the turbulence generated by large-scale wind field in addition to the turbulence generated by the katabatic wind, which is represented by K_{kat}:

$$Q_h = \rho\, c_p \left(\frac{K_b + K_{kat}}{2}\right) (T_a - T_s) \tag{4.16}$$

$$Q_e = \frac{\varepsilon \rho L_v}{p} \left(\frac{K_b + K_{kat}}{2}\right) (e_a - e_s) \tag{4.17}$$

The inclusion of this K_b (m s^{-1}) acts as an optimizing parameter to fit the turbulent fluxes into to match measured surface melt (Klok and Oerlemans, 2002) or to match independent flux measurements. This parameterization shows that Q_h increases quadratically with the temperature difference between the surface and air temperature, a "heat pump" effect due to the katabatic wind that brings increased turbulence near the surface. The value for background turbulent exchange K_b was set to 0.01, a value found in the application of the katabatic parametrization on the Peyto Glacier (Munro, 2004). The version of the equation including this background turbulent exchange coefficient is preferred as the winds occurring at Peyto glacier and the Athabasca are likely a combination of local katabatic winds and background geostrophic winds that are aligned with the direction of the katabatic flow. The parameters in the calculation of the katabatic factor K_{kat}, described in section 4.2. and equation 4.4., were obtained from Munro (2004), with Pr is 5, K is 0.0004 and γ is 0.005 ˚C m^{-1}.

4.4.3. Performance metric

The Bulk transfer, katabatic and EBSM outcomes were compared with EC data by way of mean values, standard deviations, correlation coefficients (Pearson's r) and the root mean square error (RMSE):

$$RMSE = \sqrt{\frac{\sum_{i=1}^{N} (x_i - \hat{x}_i)^2}{N}} \tag{4.18}$$

$$r = \frac{\sum (x_i - \bar{x})(y_i - \bar{y})}{\sqrt{\sum (x_i - \bar{x})^2 \sum (y_i - \bar{y})^2}} \tag{4.19}$$

Comparisons were performed with hourly values to compare eddy covariance measured fluxes with the bulk transfer and katabatic results, and with daily averages for the EBSM parameterization.

4.5. Results

4.5.1. Characterizing the micrometeorological conditions

A total of 343, 370 and 307 hours of measurements were collected for the Peyto Toe, Peyto Upwind and Athabasca Ice study sites, corresponding to 14, 15 and 13 days. At the Athabasca measurement site, measurements were continuous from 17-June 2015, 15:00 to 30-June 2015, 9:00. For the Peyto sites, the measurements were segmented into five periods lasting 24, 52, 103, 115 and 54 hours for the Toe profile and 24, 55, 103, 121 and 70 hours for the Peyto Upwind profile between 21-Jul 2008 and 25-Aug 2008. Relative humidity at the Peyto profiles was mainly only available at the lower measurement level due to malfunctions of the sensors at 4 and 6 m at both towers.

The five measurement segments at Peyto showed similar meteorological conditions, with the mid-August period showing warmer temperatures than the July ones. The Athabasca condition presents an initially cooler temperature that gradually increases over the measurement period (Figure 4.2-4.4).

Despite their proximity, the Peyto Toe and Upwind profiles showed some key differences in air temperature, humidity and wind speed (Figure 4.5). The air temperature at the Peyto Toe profile was warmer, with a more pronounced air temperature gradient than at the Peyto Upwind profile location. It also showed higher humidity near the surface, with a more pronounced humidity gradient. The high relative humidity at the 1m height is likely a wet-bulb temperature sensor malfunctioning and not drying properly, causing relative humidity to stay unrealistically high for prolonged periods. This is visible in Figure 4.3a-b for 1-m height values. The relative humidity values at 1 m are therefore considered erroneous due to sensor malfunction. Peyto Toe profile showed a consistent wind speed maximum at the 4-m height, while the Peyto Upwind profile showed wind speed increasing with height. The Athabasca Ice profile was similar to the Peyto Upwind profile, but with colder air temperatures and higher wind speeds.

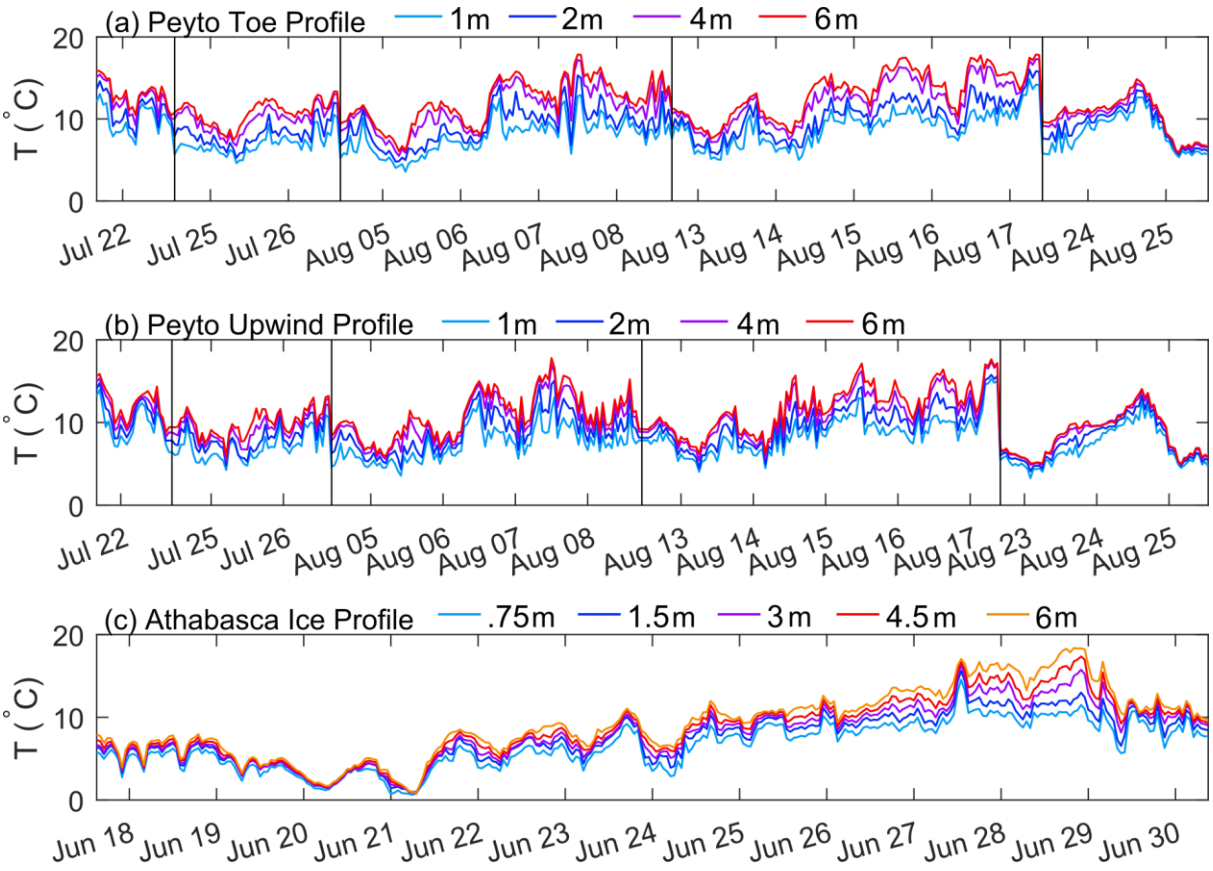

Figure 4.2. Air Temperature for the Peyto Toe profile (a), the Peyto Upwind profile (b) and the Athabasca ice profile (c), for each measurement height.

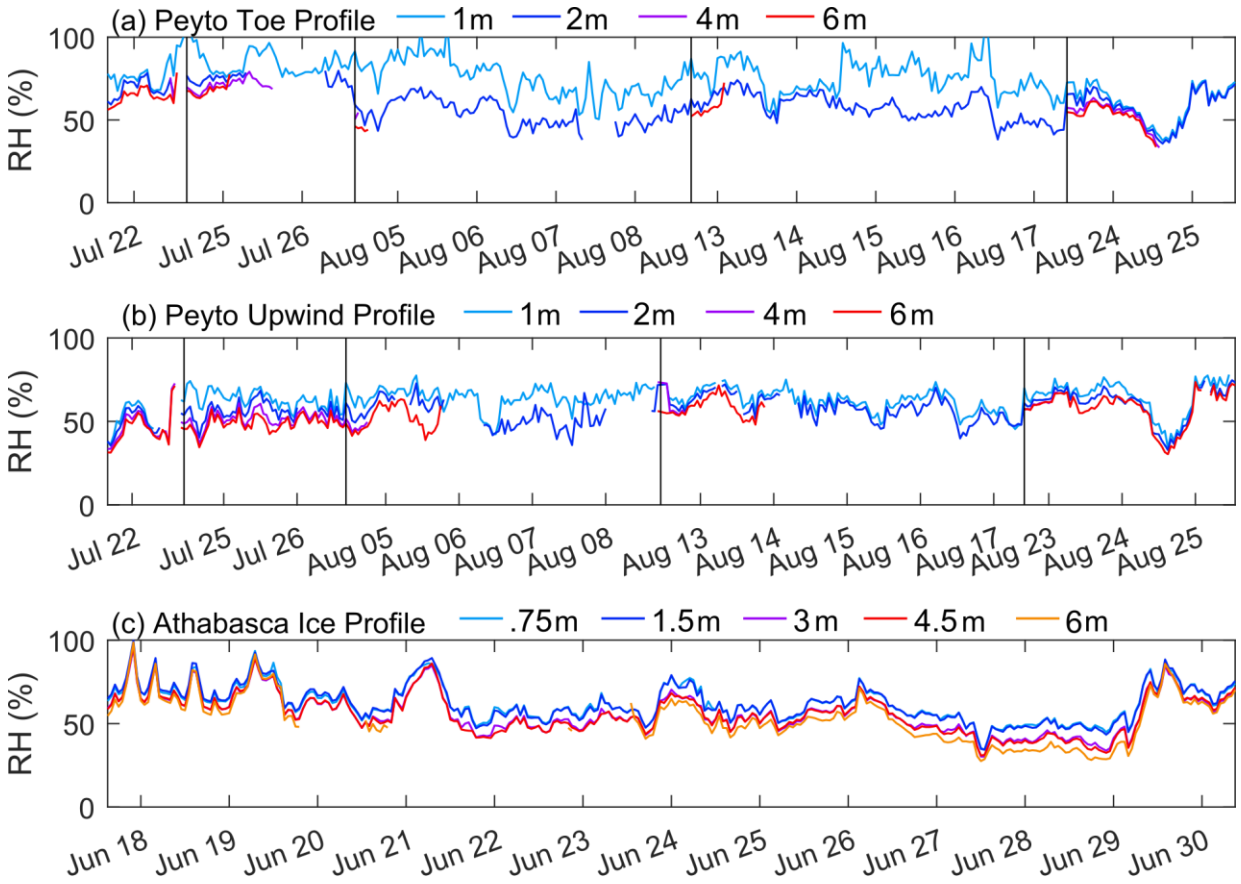

Figure 4.3. Relative humidity for the Peyto Toe profile (a), the Peyto Upwind profile (b) and the Athabasca ice profile (c), for each measurement height.

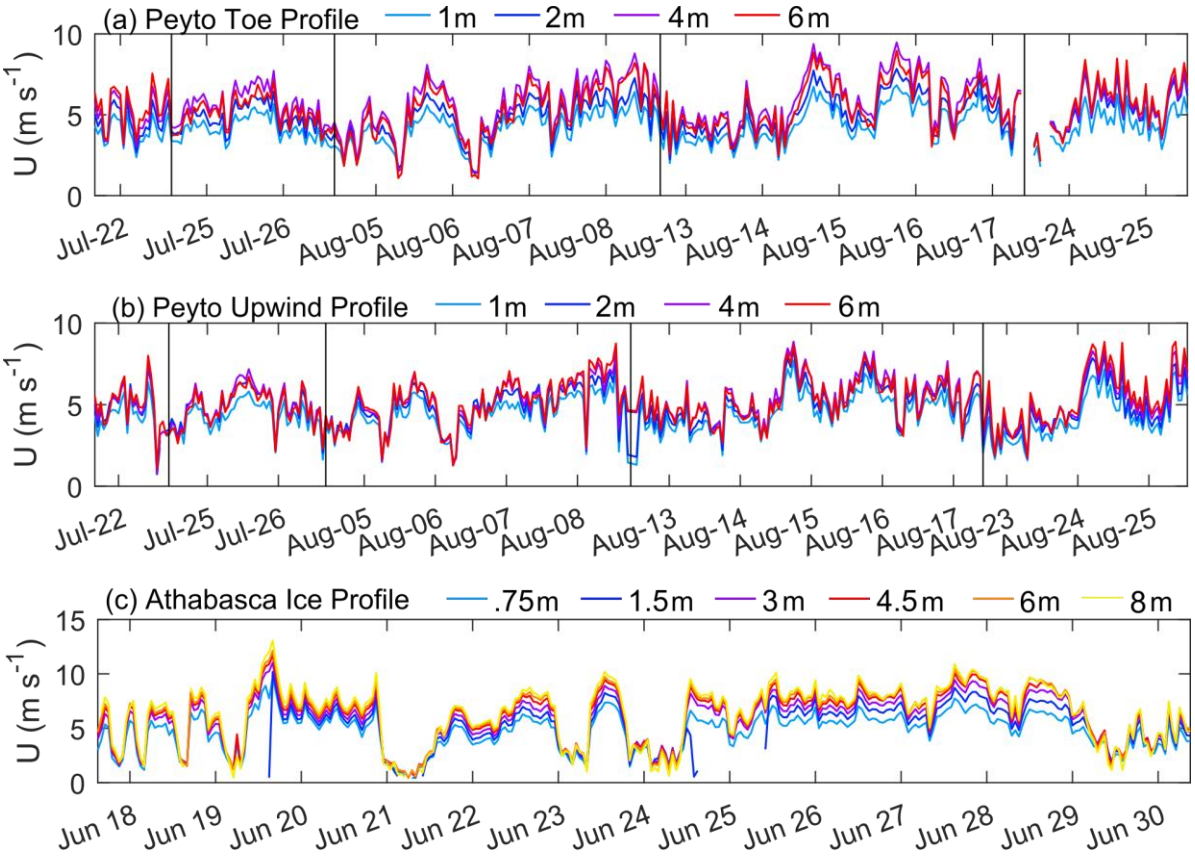

Figure 4.4. Wind speed for the Peyto Toe profile (a), the Peyto Upwind profile (b) and the Athabasca ice profile (c), for each measurement height.

The wind profiles showed that at the Athabasca glacier site, a katabatic wind was present in 31% of the measurements, with a wind speed maximum located below the highest measurement height. At the Peyto Upwind site, katabatic winds were present 51% of the time, and 80% of the time at the Peyto Toe site (Figure 4.6). Under katabatic wind conditions (with a wind speed maximum near the surface), the most common height of wind speed maxima was 4 m for both Peyto sites and 6 m for the Athabasca site. Wind speed maxima within 1 m of the surface were uncommon (less than 5% of the measurements for the Peyto and Athabasca profiles) and occurred under very low wind speeds.

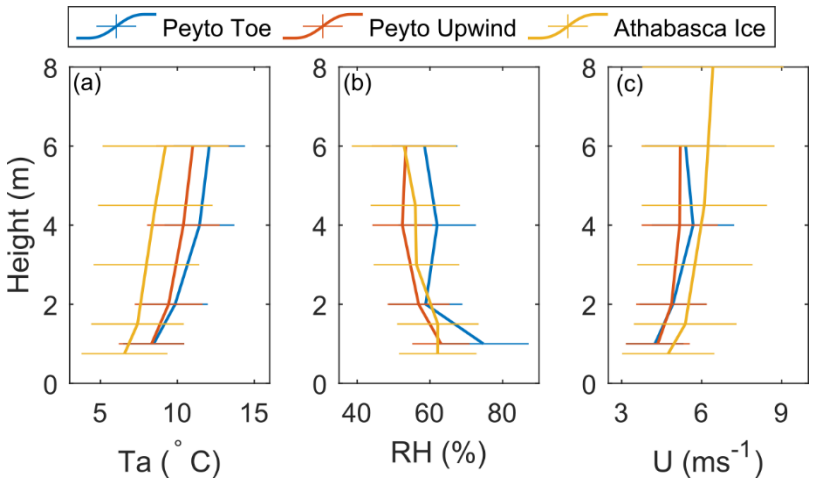

Figure 4.5. Mean temperature (a), relative humidity (b) and wind profile (c) at the Peyto Toe, Peyto Upwind and Athabasca Toe profiles, with the horizontal bars showing one standard deviation for each measurement height.

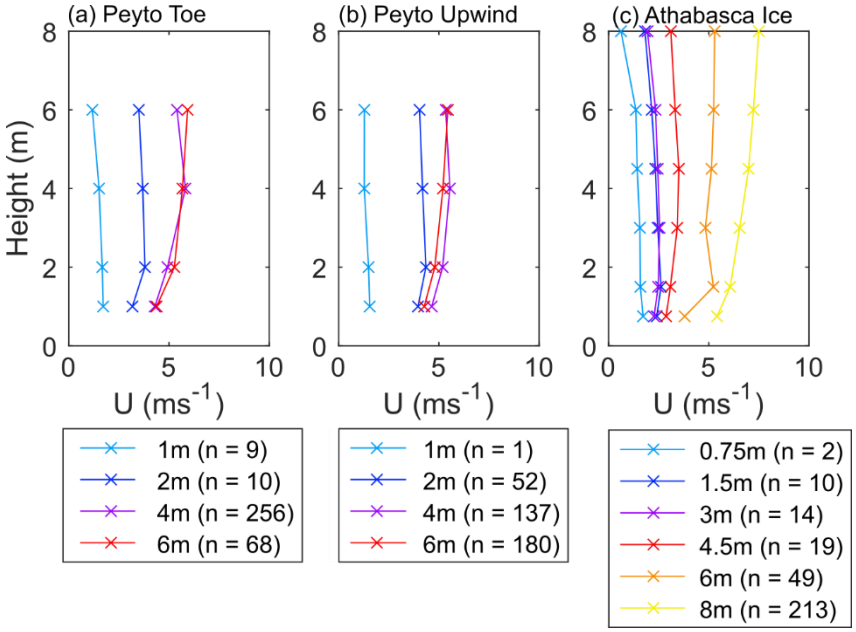

Figure 4.6. Wind profiles grouped by maximum wind speed height at the Peyto Toe (a), Peyto Upwind (b) and Athabasca Toe profile (c).

4.5.2. Evaluating Turbulent fluxes

At Athabasca Ice station, the average EC-measured sensible heat flux was 70 W m^{-2} and varied from -10 to 192 W m^{-2}. In contrast, the latent heat flux was much smaller and more negative, varying between -77 and 55 W m^{-2}, with an average of -1.8 W m^{-2} (Figure 4.7a-b). Both the bulk transfer and the katabatic parameterizations reproduced the measured sensible and latent heat fluxes well, with

the katabatic parametrization underestimating the fluxes and the bulk transfer overestimating them. The daily EBSM parameterization severely underestimated them. For the sensible heat flux, the katabatic parameterization provided mean values close to those observed, with an average of 50 W m^{-2}, but the bulk transfer followed the measured fluctuations more closely, though with a positive bias, being on average 45 W m^{-2} higher than the measured flux. This was more noticeable in the second half of the study period (Figure 4.7a). For the latent heat flux, the katabatic parameterization averaged 1.6 W m^{-2} over the study period, compared with 1.1 W m^{-2} for the bulk transfer approach (Figure 4.7b). The mean, standard deviation, as well as comparison metric between the measured eddy covariance fluxes and bulk transfer, katabatic and EBSM parameterization are available in Table 4.2.

At the Peyto Upwind station, the sensible heat flux provided a similar performance than to the Athabasca Ice Profile, with the bulk transfer slightly overestimating the measured flux, the katabatic parametrization underestimating it, and the EBSM parameterization strongly underestimating the eddy covariance values. For the latent heat flux, the bulk transfer overestimated the measured flux, with an average of 12 W m^{-2}, and the katabatic parameterization underestimated the measured flux, with mean measured values of 8 W m^{-2}, compared with the 6.7 W m^{-2} measured.

Table 4.2. Statistics for the measured and parametrized turbulent fluxes at the Athabasca Site. The parentheses indicate values calculated using daily averages.

	Athabasca	Mean	Max	Min	Standard deviation	R	RMSE
Q_h	EC	70.6	191.6	-10.4	43.2	-	-
	Bulk Transfer	102.8	277.8	0.6	65.3	0.92	44.6
	OG	50.1	125.4	5.1	24.7	0.76	35.6
	EBSM	(1.3)	(2.5)	(0.3)	(0.7)	(0.88)	(76.4)
Q_e	EC	-1.8	55.8	-77.4	20.6	-	-
	Bulk Transfer	1.1	96.8	-70.4	27.5	0.92	12.0
	OG	1.6	64.6	-25.2	14.1	0.85	11.9
	EBSM	(0)	(0.1)	(-0.1)	(0)	(-0.97)	(16.9)
	Peyto	**Mean**	**Max**	**Min**	**Standard deviation**	**R**	**RMSE**
Q_h	EC	82.2	185.5	-6.7	40.1	-	-
	Bulk Transfer	111.4	214.9	3.4	41.4	0.83	37.7
	OG	68.4	132.2	28.8	18.7	0.63	34.6
	EBSM	(1.8)	(3.6)	(1.1)	(0.6)	(0.67)	(81.6)
Q_e	EC	6.7	52.8	-29.7	13	-	-
	Bulk Transfer	12.1	85.8	-67.8	25.4	0.55	21.9
	OG	7.8	78.4	-29.9	14.9	0.51	14
	EBSM	(-0.1)	(0)	(-0.2)	(0.1)	(-0.51)	(13.1)

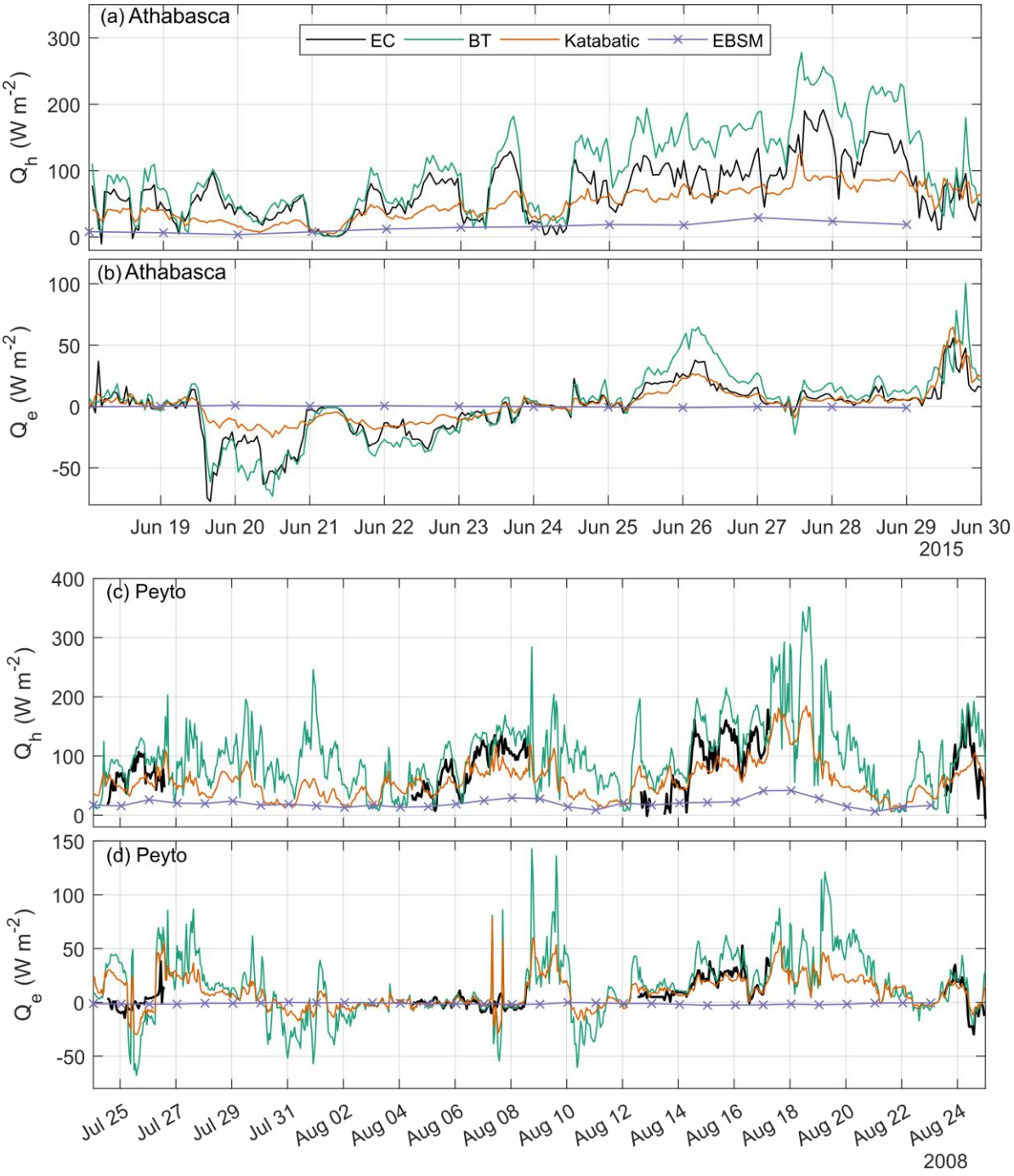

Figure 4.7. Measured and simulated sensible heat (Q_h, a) and latent heat flux (Q_e, b) for the Athabasca Ice site and the Peyto Toe site (c, d). The measured eddy-covariance fluxes (EC), as well as the bulk transfer (BT) and katabatic, are hourly values while the EBSM parameterization provides a daily average.

4.5.3. Melt energy partitioning

For both the Athabasca and Peyto sites, net radiation was the largest contributor to the energy available for melt with 70% and 69% respectively of the energy available for melt for the measurement period (Table 4.3, Figure 4.8). The turbulent sensible heat flux was the second-largest energy flux, contributing 30.5% and 28% to Athabasca and Peyto Glaciers respectively. The turbulent latent heat fluxes were the smallest, between 0.8% and 2% of the total energy available for melt. The main difference between Athabasca and Peyto sites was the direction of latent heat flux, where it was a net negative flux for the Athabasca glacier, but a net positive for the Peyto glacier. This energy partitioning between the variable fluxes is similar to that seen in other mid-latitude glaciers (Hock, 2005; Radic *et al.*, 2017). For example, at the Nordic Glacier in British Columbia, Fitzpatrick *et al*. (2017) reported net radiation and the sensible heat flux contributed 62.5% and 29.7% of the energy available for melt respectively.

Table 4.3. Energy available for melt partitioning between the net radiation (Q_n) the sensible heat flux (Q_h) and the latent heat flux (Q_e). The parenthesis refers to the percentage of the given flux for the total energy available for melt.

	Q_n	Q_h	Q_e
Athabasca	162.5 (69.2)	70.6 (30.0)	-1.79 (0.8)
Peyto	162.4 (69.5)	66.1 (28.3)	5.1 (2.2)

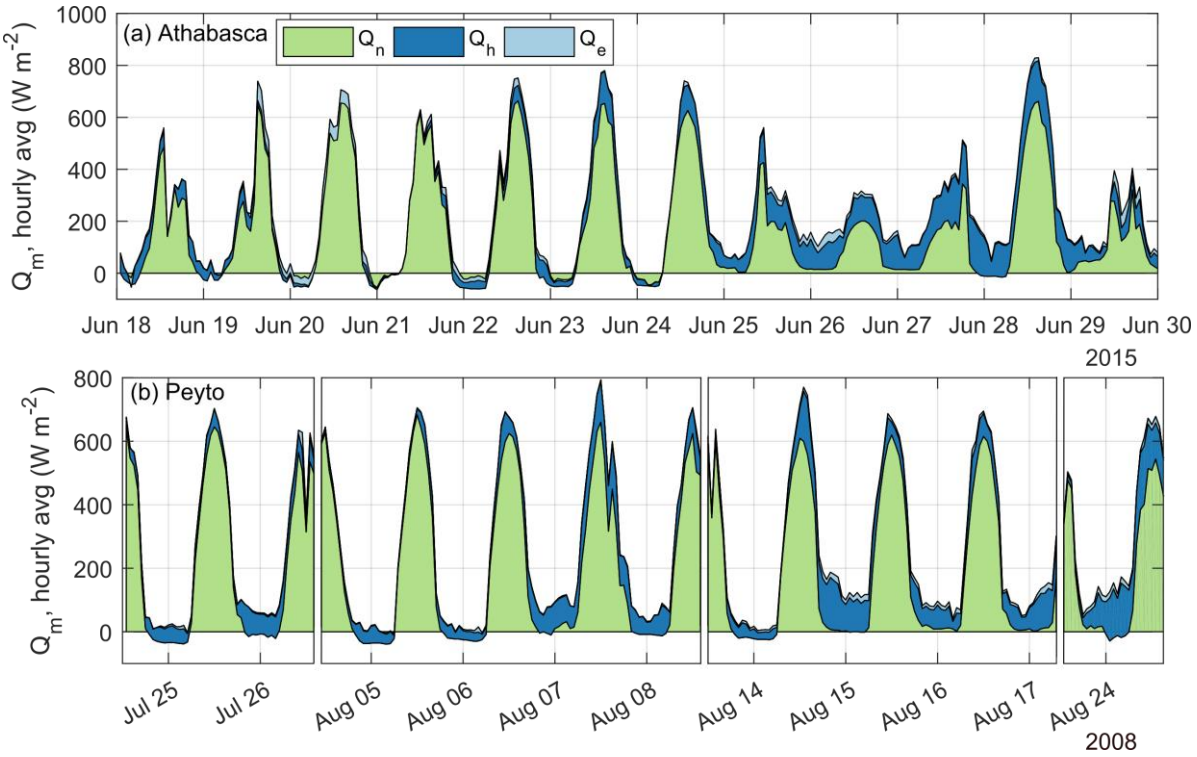

Figure 4.8. Hourly energy available for melt at Athabasca (a) and Peyto Glacier (b), as divided between net radiation (Q_n), sensible heat flux (Q_h) and latent heat flux (Q_e). Note that for Peyto glacier (b), only the period with the functioning eddy covariance system is shown, resulting in four specific periods as shown by the vertical lines.

4.5.4. Evaluating surface melt

The measured and parametrized turbulent fluxes, in combination with measured radiation, were used to simulate surface melt at the Athabasca and Peyto sites. The simulated melt was then compared with the measured melt (Figure 4.9, Table 4. 4). For the Athabasca site, the measured and simulated melt using turbulent flux measurement showed good agreement, with the simulated ice melt using the eddy covariance measurements overestimating melt by 41 mm w.e. (6%) over the 289 hours where measurements were available. The bulk transfer method overestimated melt by 157 mm w.e (22 %), and the katabatic parameterization underestimated melt by 13 mm w.e. (2%). The EBSM strongly underestimated the daily turbulent fluxes by 345 mm w.e. (-47%). For Peyto, considering the four distinct periods together, the simulated melt using eddy covariance turbulent fluxes overestimated melt by 16%, while the bulk transfer and katabatic parameterization

overestimated the surface melt by 30% and 10% respectively. The EBSM parameterization underestimated melt by 52%.

Table 4.4. Measured surface melt from SR50 and simulated melt using the eddy covariance measurements and the parameterization for the turbulent fluxes. Note that for the EBSM parameterization, only the first three periods at Peyto glacier are available.

Athabasca	Measured	EC	Bulk Transfer	Katabatic	EBSM
Total Melt (mm w.e.)	729	770	886	715	384
Difference (mm w.e.)	-	41	157	-13	-345
Difference (%)	-	6	22	-2	-47
Peyto	Measured	EC	Bulk Transfer	Katabatic	EBSM
Total Melt (mm w.e.)	744	865	966	818	316
Difference (mm w.e.)	-	121	221	73	-348
Difference (%)	-	16	30	10	-52

At Athabasca, the hourly melt rates were very similar between the eddy covariance, bulk transfer and katabatic approaches, ranging up to 9.4, 10.2 and 8.6 mm hr^{-1} and hourly melt averages of 2.7, 3.1 and 2.5 mm hr^{-1} (Figure 4.10a). For daily melt, the eddy covariance approach resulted in slightly lower average daily melt rates than the bulk transfer and katabatic approach, averaging 60, 69, 56 mm d^{-1}. The EBSM approach simulated daily melt averaging 32 mm d^{-1} , or 1.33 mm hr^{-1}, over the study period (Figure 4.10b).

At Peyto, the hourly surface melt rate reached 9.04, 11.24 and 9.17 mm hr^{-1} with the eddy covariance turbulent fluxes, the bulk transfer approach and the katabatic approach, and averaged 3.17, 3.15 and 2.62 mm hr^{-1} over the measurement period (Figure 4.10c). When looking at daily surface melt, the eddy covariance, bulk transfer and katabatic approach averaged 72, 73 and 60 mm d^{-1}, while the EBSM approach simulated an average daily melt of 28 mm d^{-1} , or 1.2 mm hr^{-1} (Figure 4.10d).

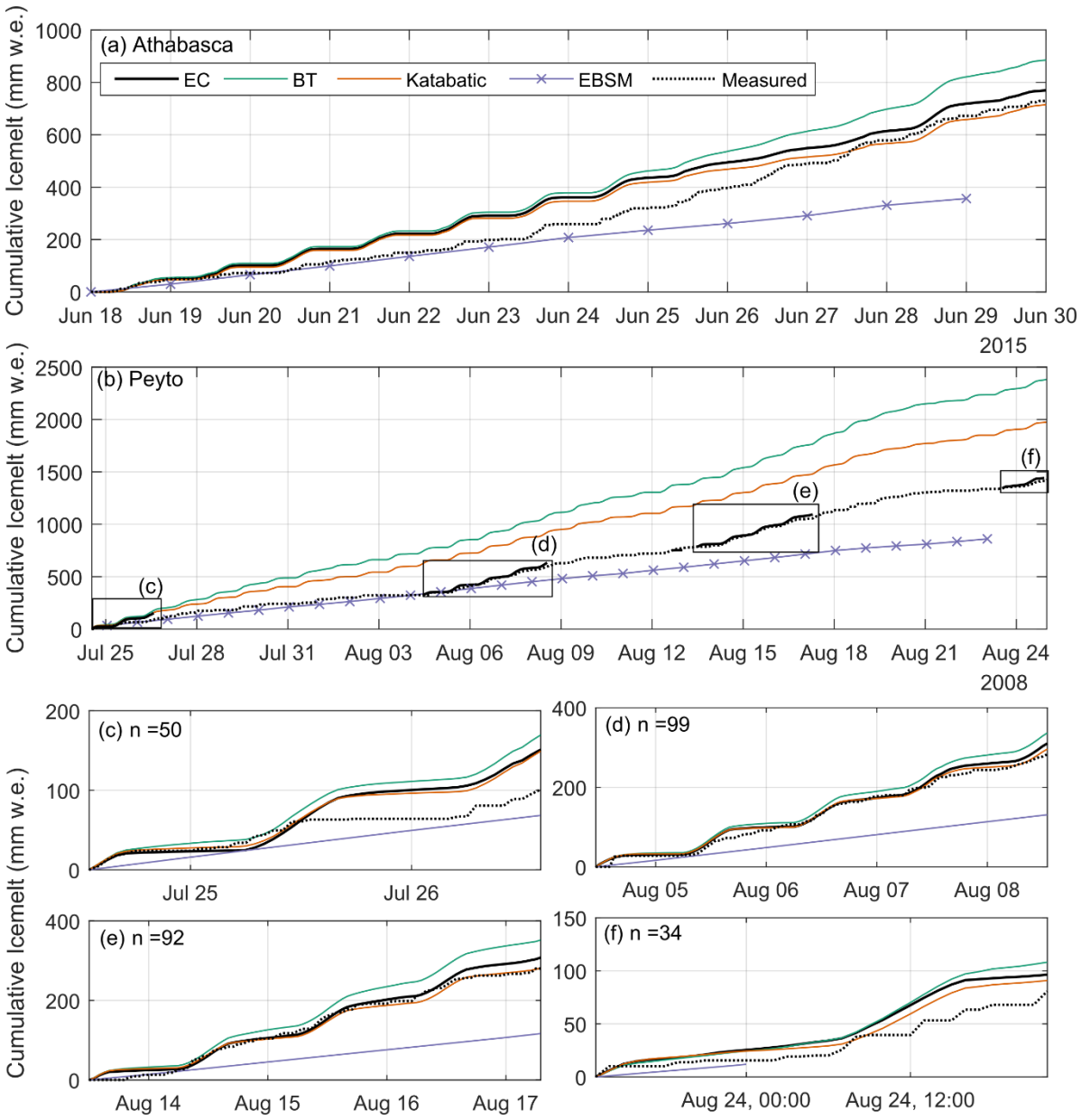

Figure 4.9. Cumulative measured and simulated surface melt at Athabasca station (a) and Peyto Upwind station (b-e). The number of hours for each of the Peyto segments with measurements (c-f) are indicated for each panel.

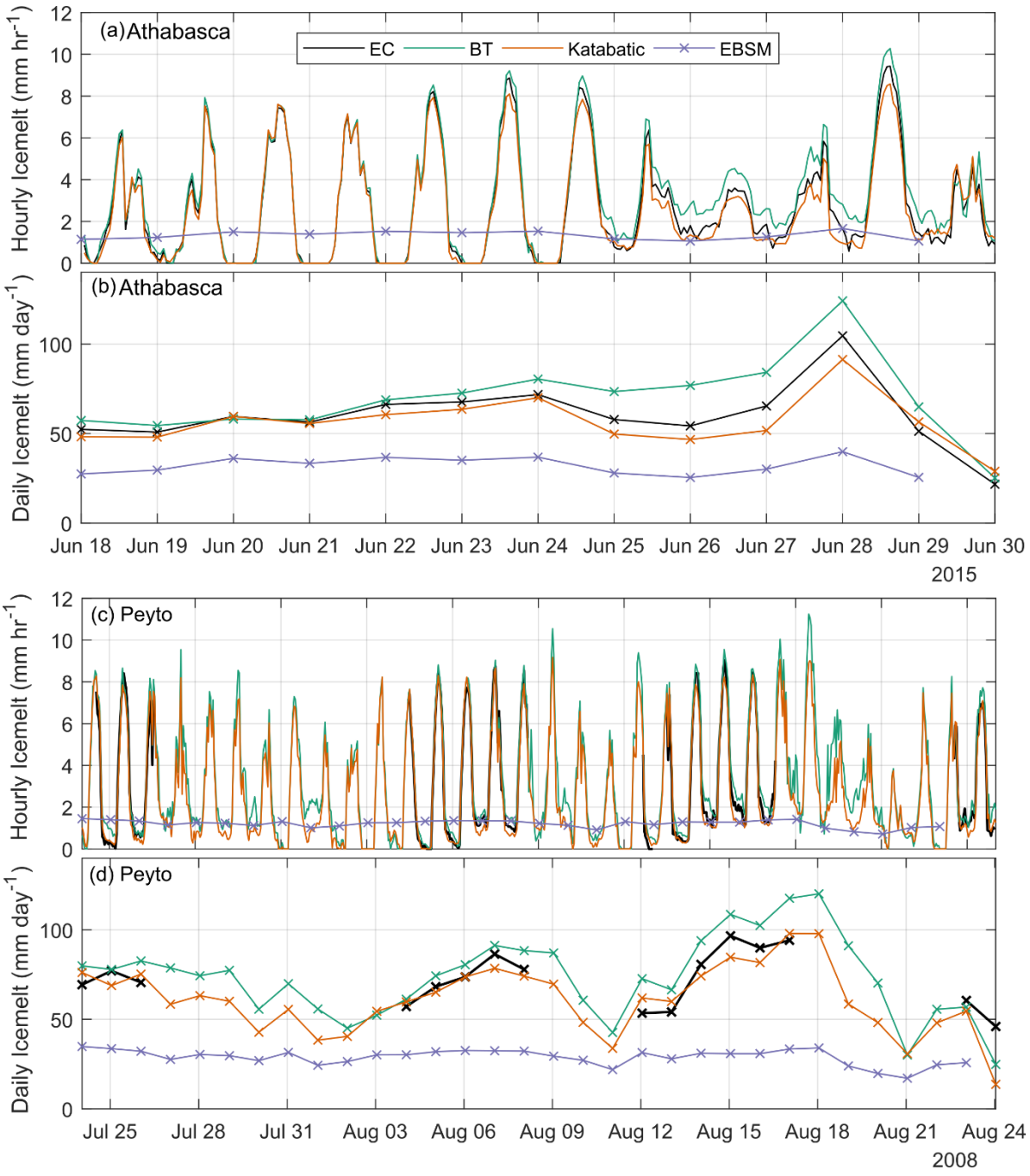

Figure 4.10. Simulated surface melt with measured and simulated turbulent fluxes at Athabasca (a, hourly, b, daily) and for Peyto (c, hourly, and d, daily).

4.6. Discussion

The implementation of hourly energy-balance melt routines in the CRHM modelling framework provides the ability to investigate sub-daily energy-partitioning and melt patterns, which was not possible in the previous EBSM daily parametrization. While this hourly timescale might not be always required, and a daily parametrization might sometimes be more efficient, having the flexibility to investigate energy fluxes and melt patterns at an hourly time scale increases the range of research questions that CRHM can be used in.

The overestimation of the bulk transfer approach during katabatic conditions, as commonly observed at the Peyto toe site, has been attributed to a failure of the Monin-Obukhov similarity theory in the presence of shallow katabatic wind speed maximum (Denby and Greuell, 2000). This was also observed at the Castle Creek Glacier and the Nordic Glacier, located in British Columbia (Fitzpatrick *et al.*, 2017; Radic *et al.*, 2017). In this case, it might also be linked to uncertainties in the roughness height parametrization. The uncertainties and parameterization difficulties associated with the bulk transfer approach have been thoroughly discussed in the literature, particularly those associated with the roughness lengths calculations and the stability corrections (Munro, 1989; Conway and Cullen, 2013b; Fitzpatrick *et al.*, 2017; Litt *et al.*, 2017; Radic *et al.*, 2017; Chambers *et al.*, 2020). In the case of Fitzpatrick *et al*. (2017), a balancing of errors occurred between the surface roughness values and the stability corrections, resulting in strong model performance but with errors in the physical processes. The large variability in the bulk transfer model performance between sites, and the difficulties in obtaining accurate roughness lengths and stability indicate further need to develop and test turbulent fluxes parameterization in glacier environments.

The katabatic and bulk transfer approaches rely on accurate measurement of wind speed, humidity and temperature. As observed at the Peyto sites at the 1m measurement height, measurements such as those from wet-bulb humidity sensors can be flawed, resulting in latent heat fluxes calculation errors. The difficulties associated with obtaining accurate measurements in harsh, remote glacier settings are an ongoing challenge in the discipline, and careful assessment of field measurements is recommended, as measurement errors can result in large biases in the calculated energy fluxes and resulting surface melt.

4.6.1. Sensitivity to parameter selection in the katabatic parametrization

The calculation of the turbulent fluxes with the katabatic approach requires a background turbulent transfer, K_b, and the background temperature lapse rate γ. The K_b value of 0.1 m s^{-1} was obtained by

Munro (2004) by optimizing the sensible heat flux Q_h calculated with the katabatic parametrization to estimates from the bulk transfer approach over three different melt seasons on the Peyto Glacier. Klok and Oerlemans (2002) obtained much a much smaller K_b value of 0.00037 m s^{-1} by optimizing it to surface melt estimates for a glacier in the Austrian Alps. Klok and Oerlemans (2002) tested the sensitivity of the K_b on the surface melt estimates and found that the parameter has a significant influence on the melt, but not as large as the influence of albedo or threshold temperature for liquid and solid precipitation. Radic *et al*. (2017) concluded that the katabatic approach performed adequately without involving K_b in a comparison between multiple flux parameterization on the Castle Creek Glacier, British Columbia when the scaling factor K in Eq. (4.4) was optimized but noted that the lack of information limited a proper application of the model.

The background temperature lapse rate γ was set to 0.005 °C m^{-1}, as in Oerlemans and Grisogono (2002) and Munro (2004). Klok and Oerlemans (2002) used a varying background lapse rate from weather stations in an adjacent, non-glacierized valley, but had to set a minimal lapse rate value of 0.0015 °C m^{-1} to avoid negative lapse rates occurring on warm days. In a study of temperature lapse rates in the Canadian Rockies eastern slopes, Wood *et al.* (2018) found a daily mean temperature lapse rate of 0.0048 °C m^{-1} for the 2005-2018 period, but varying between 0.0031 and 0.0065 °C m^{-1} depending on the month of the year. In the June-August period, inversions rarely occurred (0.4% of the measurements), but were common in the December-February period (21% of measurements). Munro (2004) additionally tested including a diurnal γ value varying between a maximum of 0.0085 °C m^{-1} around 1400h and a minimum of 0.0015 °C m^{-1} occurring 12 hours later. This resulted in an overall decrease in model performance but reduced the systematic error component of the model bias. The sensitivity of K_b and γ on the simulated turbulent fluxes for the Peyto Toe Profile is shown in Figure 4.1, for K_b values ranging from 0.003 to 0.02 m s^{-1} and γ from 0.0015 to 0.006 °C m^{-1}. The change in parameters has an overall small influence on the correlation coefficient between the measured and simulated turbulent fluxes, but a large influence on the RMSE values. This shows the interplay between the coefficients, as multiple combinations of K_b and γ lead to similar model

performances. Figure 4.11 also indicates that no unique parameters for K_b and γ would provide optimal results for Q_e and Q_h.

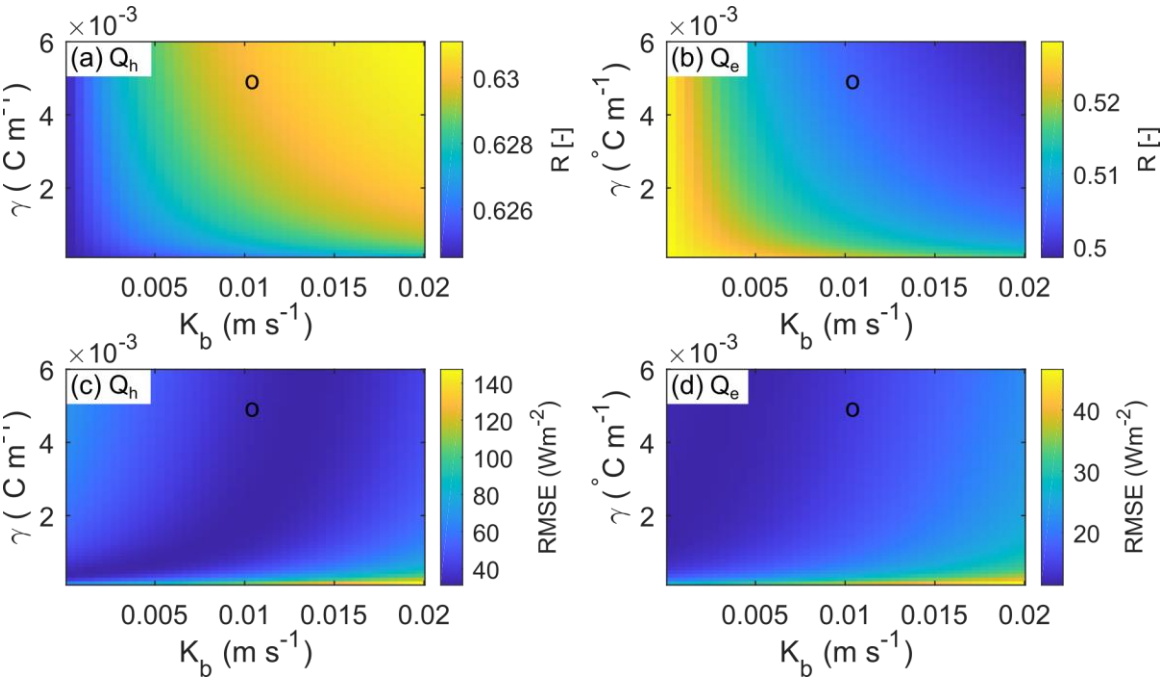

Figure 4.11. Correlation coefficient (Pearson's R) (a, b) and root mean square error (c-d) for modelled turbulent fluxes Q_h (a, c) and Q_e (b, d) and measured fluxes at the location of Peyto Toe Profile location for a range of γ and K_b values. The black circle is the mean flux from the reference simulations (γ = 0.005 °C m^{-1} and K_b = 0.01 m s^{-1}).

4.7. Conclusion

The summer temperature, humidity and wind regime of the Athabasca and Peyto glaciers, both located on the eastern side of the Canadian Rockies, were compared based on field-campaign measurements conducted in 2015 at Athabasca and 2008 at Peyto glaciers. At both sites, the turbulent fluxes using an eddy-covariance system were measured, in addition to multilevel profiles of wind speed, humidity and temperature. At Peyto Glacier, a wind speed maximum below 6 m height is detected 51% of the time at the upwind station, and 80% of the time at a toe station closer to the glacier terminus. As no wind speed was measured above 6 m, there is a possibility that near-surface wind speed maximum might occurs at higher heights but was simply not captured in this experiment. On the Athabasca Glacier, a katabatic wind, with a wind speed maximum below 8 m, is detected only 31% of the time. On the Athabasca Glacier, Conway *et al*. (2021) profiled wind speeds up to 200 m above the surface during the same study period and found slightly increasing or constant wind speed with height in the majority of the measurements, which confirms the rarity of near surface wind speed maximum. The eddy-covariance turbulent fluxes were used in conjunction with net radiation measurement to simulate the surface melt at the sites. At both sites, the net radiation was the largest energy flux, contributing near 70% of the energy available for melt. The sensible heat flux contributed approximately 30% of the energy available for melt, while the latent heat flux contributed less than 2.5%.

The measured turbulent fluxes on the Athabasca and Peyto Glaciers were compared with three distinct parameterizations: the bulk transfer with Monin-Obukhov stability correction, the katabatic parameterization (Munro, 2004; Klok and Oerlemans, 2002; Oerlemans & Grisogono, 2002) and the Energy Balance Snow Model (EBSM, Gray & Landine, 1988). The katabatic parameterization provided a reasonable approach to simulate the turbulent fluxes in a combined katabatic and non-katabatic flow regime. The katabatic approach has the advantage of not requiring surface roughness lengths or a stability correction, which are large sources of uncertainty in the bulk transfer approach. However, the katabatic approach requires some hard-to-measure parameters. Overall, the advantages associated with including the katabatic parametrization in the CRHM modeling platform to calculate hourly melt rates and increase physical representation of glacier microclimates outweighs the uncertainty associated with the details of the katabatic parametrization. The uncertainty in the parametrization of the katabatic approach could be reduced by having measurements of the background temperature lapse rate γ, which could be included as a variable instead of a constant in the simulations, as tested in Munro (2004). This would additionally add

physical realism to the parametrization, as a constant background lapse rate is a simplistic assumption. The reasonable performance of the parameters γ and K_b obtained in the literature and derived at Peyto Glacier to the Athabasca Glacier suggest reasonable transferability, but the comparison is limited due to the similar climate and geographic settings between the two sites. However, in environments where no information is available to estimate the parameters, this katabatic parametrization could be difficult to implement and result in large bias in the resulting turbulent fluxes.

Including process-based parameterization of the surface energy balance processes in the glacio-hydrological framework is needed to simulate the complexities of mountain hydrology. The performance from the katabatic parametrization for the turbulent fluxes presents a similar performance to the commonly used bulk transfer estimate. The main advantage of the inclusion of the katabatic parametrization of the turbulent fluxes in the CRHM glacier module is the capacity to investigate hourly changes in the surface energy and mass balance. While this might not always be necessary, it broadens the applications and possible research questions that can be addressed with the CRHM modelling framework. Future model development could provide more options for turbulent transfer parametrization, such as the bulk transfer approach, to further test and compare the katabatic parametrization. Further improvement of the physical representation of the surface melt processes in mountain basins building upon the development presented here will result in more robust estimates of glacier melt contribution to downstream environments.

FIRE AND ICE: THE IMPACT OF WILDFIRE-AFFECTED ALBEDO AND IRRADIANCE ON GLACIER MELT

Paper manuscript status: Contents of this chapter has been published in the journal Earth's Future:

Aubry-Wake, C., Bertoncini, A., & Pomeroy, J. W. (2022). Fire and Ice: The Impact of Wildfire-Affected Albedo and Irradiance on Glacier Melt. *Earth's Future*, *10*(4). https://doi.org/10.1029/2022EF002685

Author contribution: Caroline Aubry-Wake conceptualized the study, compiled, organized and processed the field measurements, performed data analysis and wrote the first draft of the manuscript. Andre Bertoncini provided remote sensing analysis and contributed to remote sensing components of the conclusions. John Pomeroy proposed the approach, installed the field stations, provided insights on the conceptualization, data processes and modelling approaches, as well as edited the manuscript.

Role in thesis: This chapter presents an analysis of the compensating effects of smoke, attenuating incoming radiation and reducing melt, and surface darkening by the presence of LAIs, reducing albedo and increasing energy absorbed by the surface. Using the Cold region Hydrological Modelling (CRHM) platform, a point energy balance model is developed. This point model is used to run four surface energy-balance scenarios to isolate the impact of these components on ice melt for the melt season 2015-2020. This chapter contributes to objective 1 of this thesis by developing an hourly energy balance approach, a needed component of a process-based glacio-hydrological model, as well as developing a novel methodology to assess the impacts of forest fire smoke on glacier melt. The hourly glacier energy-balance model developed and tested in this chapter is used in the glacio-hydrological models in chapter 6 and 7.

5.1. Abstract

Wildfire occurrence and severity is predicted to increase in the upcoming decades with severe negative impacts on human societies. The impacts of upwind wildfire activity on glacier melt, a critical source of freshwater for downstream environments, were investigated through analysis of field and remote sensing observations and modelling experiments for the 2015-2020 melt seasons at the well-instrumented Athabasca Glacier in the Canadian Rockies. Upwind wildfire activity influenced surface glacier melt through both a decrease in the surface albedo from deposition of soot on the glacier and through the impact of smoke on atmospheric conditions above the glacier.

Athabasca Glacier on-ice weather station observations show that days with dense smoke were warmer than clear, non-smoky days. They sustained a reduction in surface shortwave irradiance of 103 W m^{-2} during peak shortwave irradiance and an increase in longwave irradiance of 10 W m^{-2}, producing an average 15 Wm^{-2} decrease in net radiation. Albedo observed on-ice gradually decreased after the wildfires started, from a summer average of 0.29 in 2015 before the wildfires to as low as 0.16 in 2018 after extensive wildfires and remained low for two more melt seasons without substantial upwind wildfires. Reduced all-wave irradiance partly compensated for the increase in melt due to lowered albedo in those seasons when smoke was detected above Athabasca Glacier. In melt seasons without smoke, the suppressed albedo increased melt by slightly more than 10% compared to the simulations without fire-impacted albedo, increasing melt by 0.42 m. w.e. in 2019 and 0.37 m. w.e. in 2020.

5.2. Introduction

Human-induced climate change, causing warmer spring and summer temperatures and earlier snowmelt, is driving an increase in global forest fire occurrence (Gillett, 2004; Westerling *et al.*, 2006). Predictions of future fire activity under climate change scenarios show an increase in extreme fire danger (Stocks *et al.*, 2003; Kilpeläinen *et al.*, 2010; Bedia *et al.*, 2014; Abatzoglou *et al.*, 2019). Forest fires have a wide-ranging impact on surrounding environments and human activities, impacting air quality, snowmelt and flooding (Burles and Boon, 2011; Pomeroy *et al.*, 2012; Versini *et al.*, 2013; Gleason *et al.*, 2019).

Ongoing climate change is accelerating melt of the mountain cryosphere and threatening downstream water resources (Huss & Hock, 2018). The net radiation received at the glacier surface controls this melt (Hock, 2005). Mountain snow and ice surfaces typically have high albedos and so reflect an extensive amount of solar radiation. However, forest fires upwind of snow and ice covers can affect the melt patterns through the deposition of light-absorbing impurities (LAI). Surface darkening due to LAI results in higher absorption of solar radiation and faster melt (Conway *et al*., 1996; Skiles *et al*., 2019; Warren & Wiscombe, 1980). Keegan *et al*. (2014) linked widespread accelerated melt of the Greenland ice sheet to Northern Hemisphere forest fires, and more recently, Magalhães *et al*. (2019) have shown that forest fires in the Amazon are accelerating the melt of Andean glaciers. Williamson & Menounos (2021) have shown that mountain glacier albedo is declining across North America and the decline is correlated not only with rising temperature but also with forest fire LAI deposition. LAI deposition can feed microbial growth, triggering a feedback

loop that further decreases the surface albedo (Ryan *et al.*, 2018; Cook *et al.*, 2020; Di Mauro *et al.*, 2020). Besides darkening the surface, wildfire smoke reduces incoming shortwave radiation (Stone *et al.*, 2008; McKendry *et al.*, 2019; Sokolik *et al.*, 2019) and can even lead to surface cooling (Kochanski *et al.*, 2019). These two processes, the surface darkening because of LAIs, and the attenuation in incoming solar radiation because of the wildfire smoke, can therefore compensate each other. Even though this has been suggested in the literature (e.g. Stone *et al.*, 2008), it has not previously been quantified.

The objective of this paper is to better understand the roles of several possible processes that link wildfires to ablation of mountain glaciers. To accomplish this objective, the impact of wildfire smoke and LAI deposition on albedo and near-surface meteorology was studied using intensive surface observations, process-based cold regions glacier hydrological modelling, and remote sensing. This study was conducted at the well-instrumented Athabasca Glacier Research Basin, which is part of the Columbia Icefield in the Canadian Rockies, for the 2015-2020 melt seasons.

5.3. Methods

5.3.1. Study Site and data: Athabasca Glacier Research Basin

The Canadian Rockies are the headwaters of some of the largest rivers in North America and provide an important part of the streamflow in late summer for the downstream environments, especially during dry, warm summers (Comeau *et al*., 2009; Jost *et al.*, 2012; Bash and Marshall, 2014; Naz *et al.,* 2014). Within the Canadian Rockies, the Columbia Icefield is the hydrological apex of North America, contributing runoff that ultimately reaches the Arctic, Atlantic and Pacific oceans through the Mackenzie, Saskatchewan and Columbia rivers (Figure 5.1).

Smoke from wildfires occurring in heavily forested British Columbia, just west of the Columbia Icefield, tends to travel eastward along prevailing westerly flows to the Canadian Rockies. In the last five years, fire activity upwind of the Columbia Icefield has been highly variable and includes the two worst fire seasons ever recorded, 2017 and 2018. In 2018 alone, over 1.35 million hectares burned, over 2200 properties were evacuated, and the cost of wildfire suppression reached $615 million (Government of B.C., 2019). Below average fire activity occurred in 2016, 2019 and 2020.

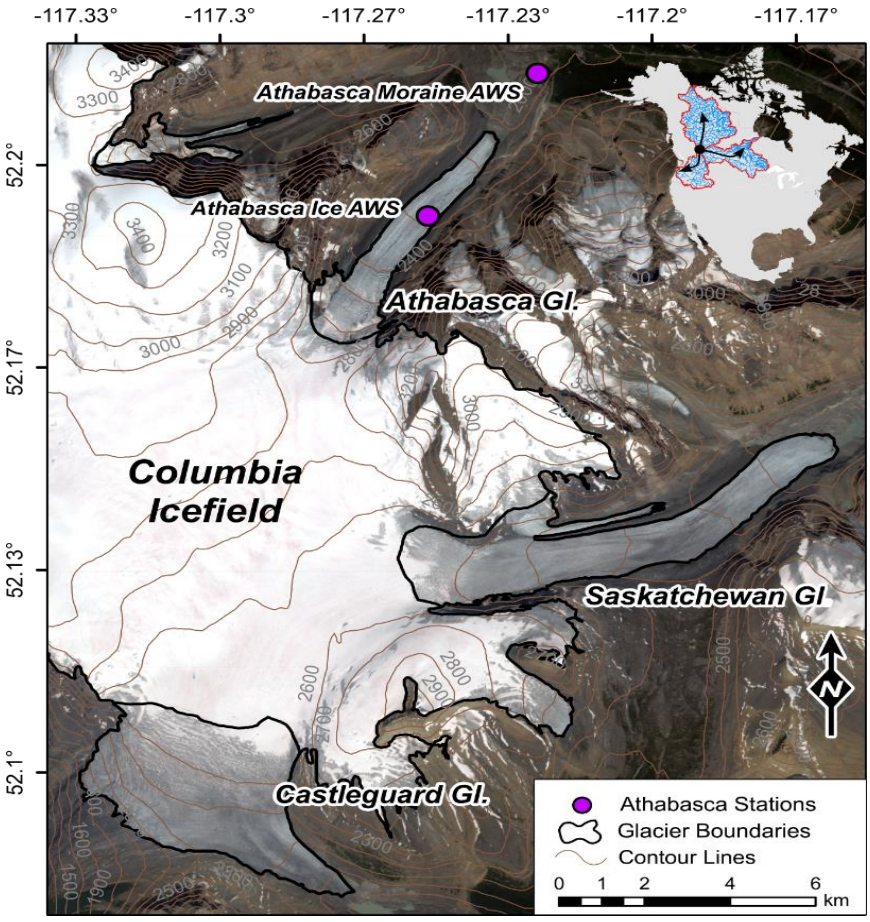

Figure 5.1. Map of the Columbia Icefield with the three main outlet glaciers: Athabasca Glacier, Saskatchewan Glacier and Castleguard Glacier, with the location of the automated weather station (AWS) showed with purple circle. The Columbia Icefield is the headwater of drainage basin reaching the Atlantic, Pacific and Arctic Oceans, as shown by the inset map of North America. The background imagery is from August 8, 2018 obtained from Sentinel-2 and the elevation line are derived from SRTM digital elevation model obtained in February 2000.

Over the same period (2015-2020), two automated weather stations (AWS) operated in Athabasca Glacier Research Basin, which includes an outlet glacier of the Columbia Icefield and its proglacial landscape: AWS_{ice}, on the glacier toe at 2177 m a.s.l., and $AWS_{moraine}$, less than one km from the glacier terminus, at elevation 1966 m a.s.l. (Figure 5.1, Table B.1). The stations observed air temperature (T_a) and relative humidity (RH) using Rotronics temperature and humidity probes, wind speed (U) using RM Young Wind Monitors, incoming and outgoing short (SW) and longwave (LW) radiation using Kipp and Zonen CNR4 net radiometers, and snow depth and ice elevation using Campbell Scientific Canada SR50 ultrasonic depth rangers. Precipitation was observed at $AWS_{moraine}$, using a Meteorological Services tipping bucket rain gauge and an Alter-shielded Geonor weighing precipitation gauge. The precipitation gauge suffered from an instrument malfunction during the

2019 melt season and was infilled with three other stations in the vicinity using an inverse distance weighting interpolation method. A Wingscapes, 8.0-megapixel, time-lapse camera was mounted on the $AWS_{moraine}$ pointed towards the Athabasca Glacier and provided visibility, smoke, precipitation type and cloud observations. The time-lapse camera recorded pictures at 8:00, 13:00 and 16:00 local time.

The seasonal period analysed here, July 1st to September 15th, referred to as the melt season, includes the co-occurrence of the primary glacier melt period and the regional wildfire season. The range of years from 2015 to 2020 includes both high and low wildfire occurrence and cool, wet and warm, dry years.

5.3.2. Defining the characteristic meteorological conditions

Time-lapse images were taken three times a day at the $AWS_{moraine}$ station for the 2015-2020 melt seasons. These were classified manually according to the weather type: predominantly clear sky, a mix of sun and cloud, predominantly cloudy, light smoke or dense smoke (Figure 5.2). Light and dense smoke were selected based on the attenuation of distant visual features in the visual images, such as snow patches, rock outcrops and clouds. In light smoke conditions, these features were still visible, but in dense smoke conditions, it was difficult to discern the clouds and the distant mountain landscape. The resulting time series of Athabasca weather was used to select representative days for each weather type, defined as when two consecutive images out of three show the same weather type. The measured air temperature, relative humidity and incoming shortwave and longwave radiation for these representative days were extracted from the AWS_{ice} record and compiled to obtain average daily meteorological conditions for each of the weather types. These representative meteorological conditions are used to investigate how the presence of smoke affects the atmospheric conditions at the Athabasca glacier.

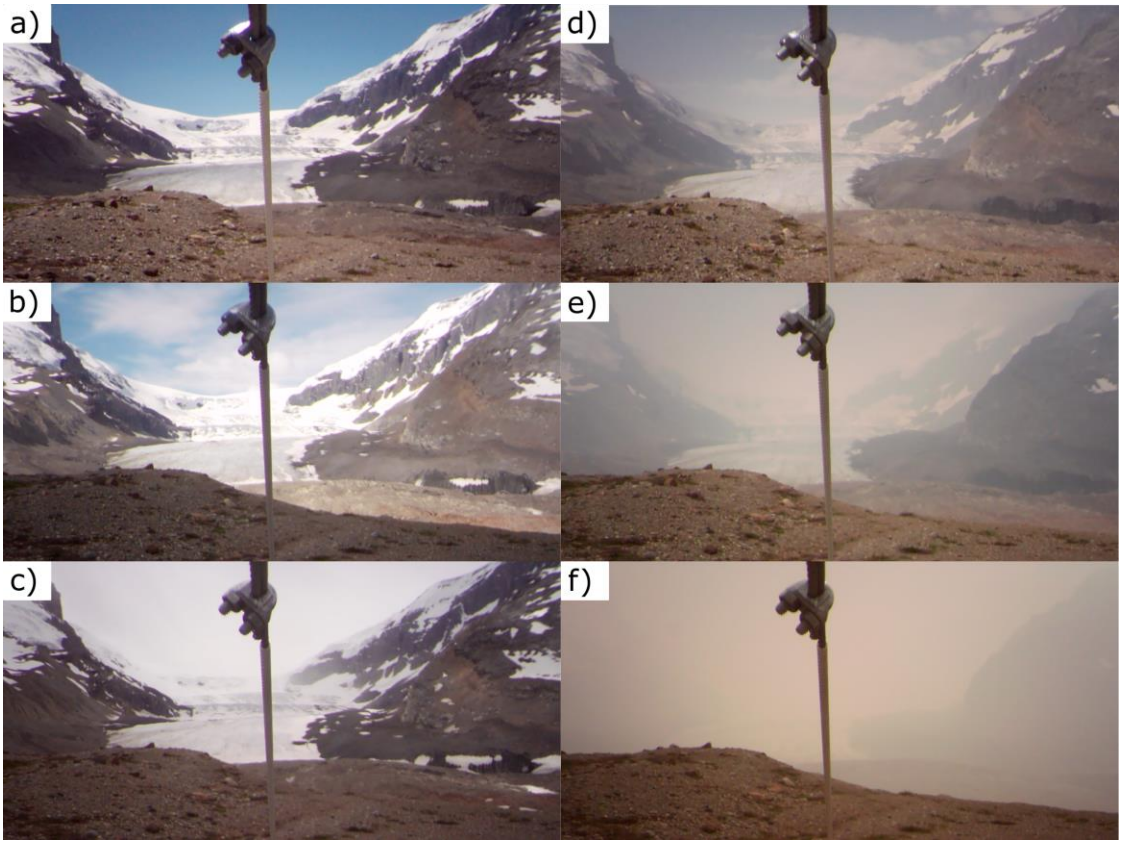

Figure 5.2. Example of time-lapse images for a) clear, b) mix of sun and cloud, c) cloudy, d) light smoke, and e-f) dense smoke, extracted from the 2017 melt season.

5.3.3. Modelling approach: Isolating the impact of smoke and LAI

The impact on the surface melt of both the changes in ice albedo and on short and longwave irradiance was diagnosed using a new point-based surface energy balance model developed in the Cold Region Hydrological Modelling platform (CRHM, Pomeroy *et al*., 2007, 2016) using an hourly energy budget approach (Eq. 5.1):

$$Q_m = SW_{in} (1 - \alpha) + LW_{net} + Q_e + Q_h + Q_p \quad (5.1)$$

Where Q_m is the energy available for melt, SW_{in} is the shortwave irradiance, α is the surface albedo, LW_{net} is net longwave radiation, Q_e is the turbulent latent heat flux, Q_h is the turbulent sensible heat flux and Q_p is the energy advected from precipitation. The turbulent fluxes were calculated using a katabatic wind parametrization from Oerlemans & Grisogono (2002). Model forcings of air temperature, relative humidity, wind speed, albedo, and shortwave and longwave irradiance were observed at the AWS_{ice}, and precipitation at the $AWS_{moraine}$. The model was evaluated using measured surface ablation at AWS_{ice} which was available intermittently during the 2016-2020 melt seasons.

The model was run for the 2015-2020 melt seasons (July 1st - September 15th) following four scenarios to isolate the impact of attenuated irradiance due to smoke and decreased albedo due to LAIs. LAIs are defined as all surface particulates and impurities that contribute to the decrease in surface albedo, including dust, black carbon and microbial growth (Skiles *et al.*, 2019). The four scenarios are shortly described below and in Figure 5.3:

1) No Fire: Removes the impact of fire activity for both the glacier surface and the atmosphere, by using a standard mountain glacier ice albedo of 0.3 and modelled smoke-free irradiance.

2) With Smoke: Isolates the impact of the radiation attenuation due to smoke by using the measured irradiance with the standard ice albedo of 0.3.

3) With LAIs: Isolates the impact of the albedo reduction by LAIs by using measured albedo with modelled smoke-free irradiance.

4) With Fire: Corresponds to observed conditions and combines the measured albedo reduction and the measured irradiance attenuation to simulate fire activity.

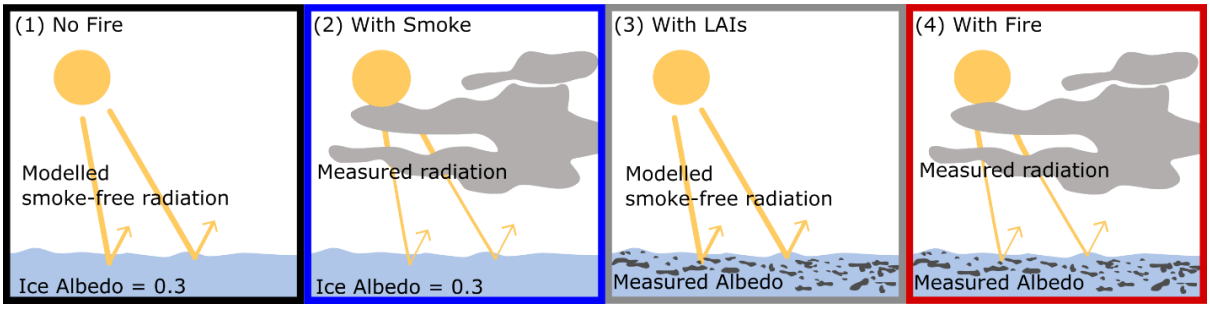

Figure 5.3. Conceptual representation of the four modelling scenarios. The framing colour corresponds to the line colour in Figure 5.8.

Measured albedo was calculated as the ratio of shortwave reflection to irradiance measured from the AWS_{ice}. The no-LAI surface albedo in scenario (1) and (2) was set to a reference value for clean glacier ice, 0.3 (Benn and Evans, 2010). On days when smoke was detected in the time-lapse imagery, the shortwave and longwave irradiance were corrected separately to remove the effects of smoke in scenario (1) and (3). On days when no smoke was detected, measured irradiance was used. Both irradiance corrections used a transmissivity correction. The temperature, relative humidity and wind speed were not adjusted amongst the four scenarios.

The presence of smoke in the atmosphere absorbs shortwave radiation, reducing the irradiance at the surface by decreasing the transmittance (Stone *et al.*, 2008; McKendry *et al.*, 2019). Therefore,

transmissivity on smoky days is lower than on clear days. To simulate smoke-free shortwave irradiance, $SW_{in\ mod}$, the transmissivity of smoky days needs to be increased to a value corresponding to smoke-free days. To achieve this, the clear-sky transmissivity was calculated as the average transmissivity occurring during days classified as clear in the time-lapse imagery classification. Then, the difference in transmissivity between measured smoky days and the average clear-sky transmissivity Δ_τ was calculated (Eq. 2). This difference in transmissivity was used to calculate the missing shortwave irradiance $\Delta_{SW_{in}}$, linked to the presence of smoke (Eq. 3). The missing irradiance was calculated for each smoky day and added to the measured shortwave irradiance to estimate the simulated smoke-free irradiance $SW_{in\ mod}$ (Eq. 4).

$$\Delta_\tau = \tau_{meas\ smoky} - \tau_{\mathrm{clear}} \qquad (5.2)$$

$$\Delta_{SW_{in}} = SW_{in\ meas} * \Delta_\tau \qquad (5.3)$$

$$SW_{in\ mod} = SW_{in\ meas} + \Delta_{SW_{in}} \qquad (5.4)$$

Where $SW_{in\ meas}$ is the shortwave irradiance (Wm^{-2}) measured at the AWS_{ice}, τ_{clear} and $\tau_{meas\ smoky}$ are the average measured clear sky transmissivity and the measured smoky transmissivity, calculated as the ratio of measured shortwave irradiance to the theoretical extraterrestrial incoming shortwave radiation flux – both to horizontal planar surfaces.

To remove the influence of smoke on the longwave irradiance, a factor, f_{lw}, was calculated based on the difference between simulated longwave irradiance with smoky transmissivity and with the average clear-day transmissivity τ_{clear} (Eq. 5). The theoretical simulated longwave irradiance was calculated following Sicart *et al*. (2006, Eq. 6). The measured longwave factor was then used to adjust the measured longwave irradiance to remove the impact of the smoke (Eq. 7).

$$f_{lw} = \frac{LW_{theo_{clear}}}{LW_{theo_{smoky}}} \qquad (5.5)$$

$$LW_{theo} = 1.24 * \left(\frac{e_a}{T}\right)^{\frac{1}{7}} * (1 + 0.44 * RH - 0.18 * \tau) * \sigma T^4 \qquad (5.6)$$

$$LW_{in\ mod} = LW_{in\ meas} * f_{lw} \qquad (5.7)$$

Where e_a is the water vapour pressure (kPa), RH is the hourly relative humidity (%), σ is the Stefan Boltzmann constant ($5.67x10^{-8}$ Wm^{-2} K^{-4}) and T is the air temperature (K) and τ_{meas} is measured transmissivity.

This transmissivity-based approach to simulate smoke-free conditions preserves the daily signature of the measured irradiance. For example, a day with smoke detected in the time-lapse imagery, but also with the low shortwave irradiance associated with cloudy weather, will still have low shortwave irradiance after the impact of the smoke is removed.

5.3.4. Spatial albedo estimates

To upscale the results of the point albedo measured at the AWS_{ice}, the change in albedo over the three largest outlet glaciers of the Columbia Icefield was analyzed using remote sensing imagery over the 2016-2020 melt seasons (Bertoncini *et al*., 2022) For 12 Sentinel-2 images, high-resolution albedo over the glaciers was estimated using MODIS data to model the bidirectional reflectance of snow and ice, following the approach detailed in Bertoncini *et al*. (2022) The spatial variations in albedo across each glacier toe were assessed for each melt season, but also amongst melt seasons.

5.4. Results and Discussion

5.4.1. Seasonal weather types and meteorological conditions

The time-lapse image classification reveals that, for the 2015-2020 melt seasons, the weather at Athabasca glacier was predominantly cloudy, with 50% of images analyzed categorized as cloudy, in contrast to 15% for clear skies, 24% for a mix of sun and clouds, and 5% and 6% for light and dense smoke (Figure 5.4). The presence of smoke differs from year to year. The 2016 and 2019 melt seasons show no presence of smoke. In 2015, smoke was detected in only 7% of the images, concentrated in late August, and in 2020, only 4% of images show smoke, concentrated close to September 15th. The 2017 and 2018 melt seasons have the largest presence of smoke, with 29% and 26% of images showing either light or dense smoke, but with different timing. Detailed numbers of images for each weather type per year can be found in Table S5.2.

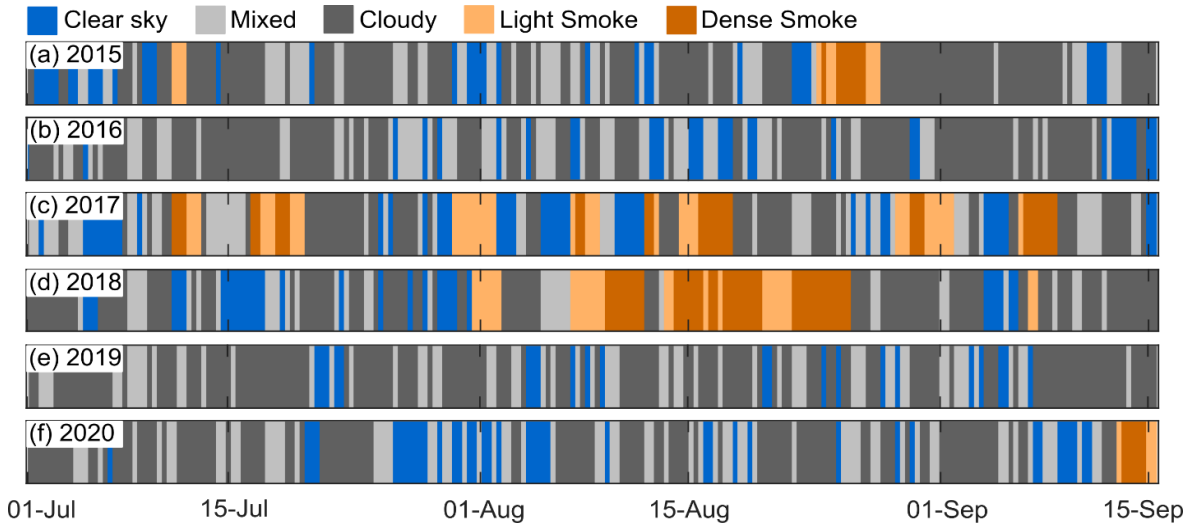

Figure 5.4. Weather type at Athabasca glacier obtained from the time-lapse image classification for the 2015 to 2020 melt seasons.

Meteorological conditions on the glacier in the six melt seasons were not associated with smoke activity, assessed as the number of days with dense or light smoke in a given year (Table 5.1). Mean air temperature over each melt season varied by 1.85°C between the warmest (2017) and the coldest (2016) years. The years with smoke were not consistently warmer than years without smoke. Similarly, even though smoke years (2015, 2017, 2018) were drier than no-smoke years (2016, 2019), the annual smoke activity did not correlate with the humidity of the given year. Precipitation similarly was lower for the intense fire season of 2017 and 2018, but also for 2020 with few fires. The only consistent pattern is for the measured ice surface albedo, which decreased from a summer average of 0.29 in 2015 to 0.20 in 2018, after which it remained low (Figure 5.5). However, the low albedo values in 2020 increased moderately in late August compared to the seasonal progression of albedo in 2018 and 2019, suggesting a partial recovery that may be associated with some surface LAIs being washed away by meltwater. These low ice albedos are similar to what have been measured on other glaciers in the Canadian Rockies during similar forest fire activity, such as on Haig Glacier, where albedo as low as 0.12 were recorded in 2003 and 2017, after summers of high forest fire activity (Ebrahimi & Marshall, Marshall and Miller, 2020). The link between decreasing surface albedo and wildfire activity in the region was also discussed by Williamson and Menounos (2021), who found a strong correlation between glacier albedo decrease over the 2000-2019 period and aerosol optical depth, a proxy for wildfire-generated smoke.

Table 5.1. Seasonal mean meteorological conditions from July 1 to Sept 15, except for albedo which was calculated for July 15-Aug 15, as there were no fresh snowfall event that would influence the calculation of the ice albedo for that period. The glacier surface was snow-free at AWS_{ice} every year in this period. All variables were from AWS_{ice} except precipitation, which was measured at $AWS_{moraine}$.

	2015	2016	2017	2018	2019	2020
Air Temperature (˚C)	6.7	5.9	7.7	6.5	6.6	6.9
Relative Humidity (%)	65	72	61	66	70	64
Shortwave Irradiance (Wm^{-2})	202	192	207	208	206	221
Longwave Irradiance (Wm^{-2})	301	305	297	300	304	302
Wind Speed (ms^{-1})	5.3	4.6	5.6	5.3	5.4	6.4
Total precipitation (mm)	147	144	91	139	126	116
Albedo (minimum)	0.29 (0.24)	0.24 (0.23)	0.26 (0.21)	0.20 (0.16)	0.20 (0.17)	0.20 (0.17)

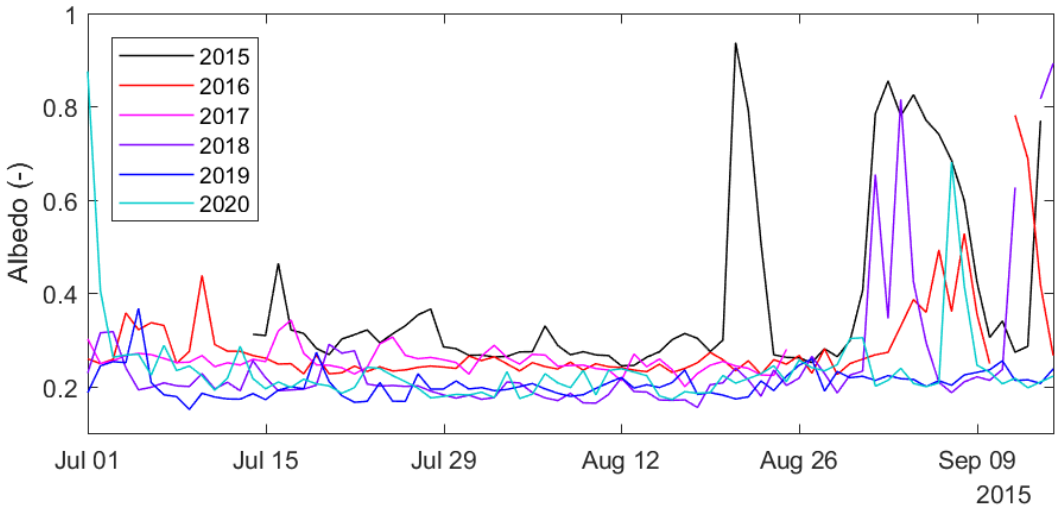

Figure 5.5. Daily measured Athabasca Glacier albedo for the 2015-2020 melt seasons.

5.4.2. Average meteorological conditions per weather type

Meteorological conditions on smoky days contrasted with those on non-smoky days (Figure 5.6). Meteorological conditions were on average warmer on smoky days than cloudy or mixed weather days, with average daily temperatures of 8.0 °C for light smoke and 8.6 °C for dense smoke, compared to 7.6, 7.0 and 5.4 °C for clear, mixed and cloudy weather (Figure 5.6a). Smoky days also underwent a subdued diurnal variation compared to clear days; a variation that was similar to those observed during cloudy weather. This is also visible in the relative humidity (Figure 5.6b), where smoky days were drier than other weather types, and once again with lower diurnal fluctuation.

A clear difference amongst weather types is apparent for the characteristic shortwave irradiance (Figure 5.6c). As expected, the highest shortwave irradiance occurred on clear days, with mean daily peaks of 820 W m^{-2} and SW_{in} on cloudy days was significantly reduced, with the mean daily peak SW_{in} reduced to 433 W m^{-2}. Irradiance on light and dense smoke days was between that on clear and cloudy days, with mean daily peak shortwave irradiance reduced by 225 W m^{-2} for light smoke and 290 W m^{-2} for dense smoke compared to irradiance on clear days.

Longwave irradiance on both light and dense smoke days was between that on clear and cloudy days, with a daily average irradiance of 298 W m^{-2} and 291 W m^{-2}, respectively. Longwave irradiance was higher for cloudy days, averaging 312 W m^{-2}, compared to clear days, on which it averaged 281 W m^{-2} (Figure 5.6d). The average meteorological conditions for each weather type per melt season are presented in Figure B.3.

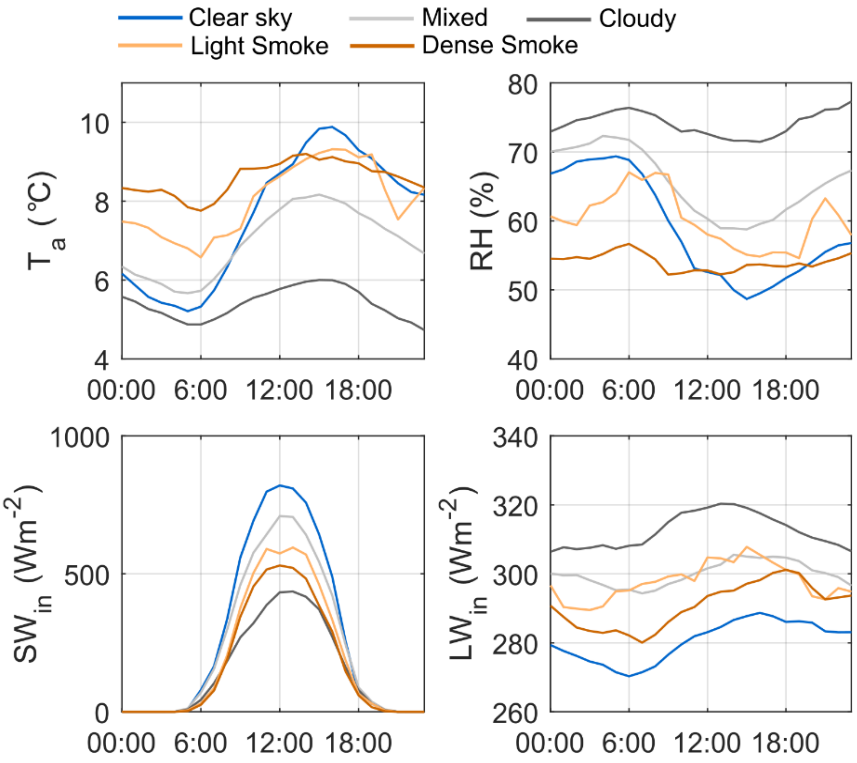

Figure 5.6. Average daily meteorological conditions observed on Athabasca Glacier for the different weather types (clear sky, mixed of sun and clouds, cloudy, light smoke and dense smoke); a) shortwave irradiance, b) longwave irradiance, c) air temperature, d) relative humidity.

5.4.3. Adjusted irradiance based on transmissivity

The transmissivity-based adjustment to the observed irradiance to simulate the removal of the smoke has contrasting effects on the shortwave and longwave irradiance that result in a very small impact on net radiation (Figure 5.7). The smoke-removal adjustment increased shortwave irradiance by, on average, 14 and 21 W m^{-2} for the light and dense smoke conditions respectively, with respective hourly maxima increasing by 193 and 209 W m^{-2} occurring during times of peak irradiance. In contrast, the corresponding smoke-removal adjustment decreased longwave irradiance by, on average, 3.6 and 7.2 W m^{-2} for light and dense smoke respectively, with hourly maxima decreasing by 16 and 23 W m^{-2} respectively. The large decrease in shortwave irradiance due to attenuated transmittance during smoky conditions is partly mitigated by increased longwave irradiance. These irradiance changes result in an average increase in all-wave irradiance of 10 and 13 W m^{-2} when adjusting for light and dense smoke, with hourly maxima increasing by 179 and 195 W m^{-2}, respectively. These adjustments to shortwave and longwave irradiance are consistent with the

observed differences in irradiance between clear and smoky conditions (Figure 5.6c-d), as the presence of smoke reduces shortwave but increases longwave irradiance.

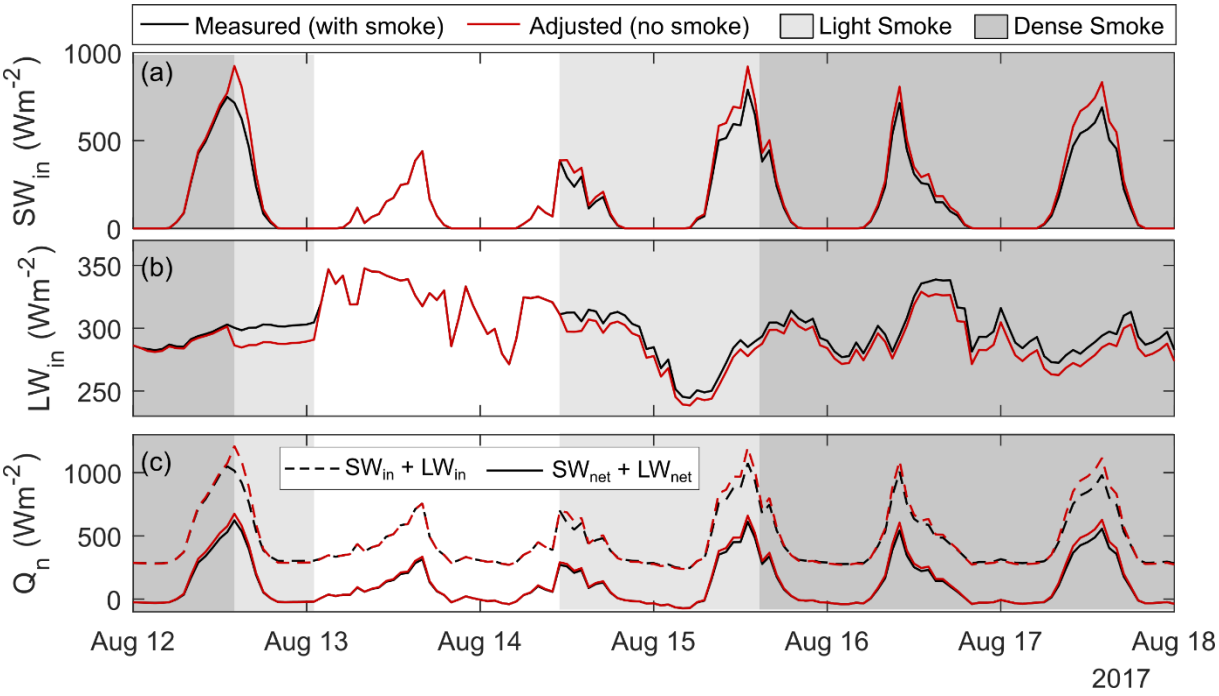

Figure 5.7. Measured (with smoke) and adjusted (no smoke) shortwave (a) and longwave (b) irradiance, with all-wave irradiance (SW_{in} + LW_{in}, dashed) and net radiation (SW_{net} + LW_{net}, full) in c for a selected smoky period in the 2017 melt season.

However it is the absorption of the shortwave and longwave irradiance at the ice surface to form net radiation that determines the impact of smoke on glacier melt. Approximately 99% of longwave irradiance was absorbed by the ice surface assuming an emissivity of 0.99, but only 77% of the shortwave irradiance was absorbed given the average measured ice albedo of 0.22 and 0.24 during light and dense smoke conditions. This difference in absorption reduced the effect of the transmittance attenuation on shortwave irradiance. When considering the changes in shortwave and longwave irradiance and absorption, and using the measured albedo values, the presence of smoke reduces the net radiation at the ice surface by 15 W m^{-2} for both light and dense smoke, with hourly maximal reductions of 107 and 114 W m^{-2}, respectively compared with adjusted, smoke-free conditions. This 15 W m^{-2} average reduction in net radiation due to the presence of smoke results in a reduction in ice melt of less than 4 mm day^{-1} compared to smoke-free conditions. Further examples of the adjusted incoming shortwave and longwave irradiance are available in Figure B.1 and B.2.

5.4.4. Melt model evaluation

Cumulative melt was measured for most of the 2016-2020 melt seasons, with gaps when station maintenance was performed. The CRHM surface melt model predicted observations of surface melt well, with a mean relative error of 3% for all observation periods, ranging between an overestimation of 9% to an underestimation of 4% for individual melt seasons. This corresponds to errors ranging between 6 mm day^{-1} in 2020 to less than 1 mm day^{-1} in 2018. The cumulative melt observed at the AWS_{ice} and melt compiled by the model are presented in Table B.2 and Figure B.4.

Table 5.2. Point melt model evaluation. The number of days used in the model evaluation is indicated in parenthesis in the period column.

Period (number of days)	Observed melt (m)	Modelled melt (m)	Error (m)	Error (%)
July 14 - August 31, 2016 (n = 48)	2.79	2.63	0.15	6
Jul 20 - Aug 6, 2017 (n = 17)	0.9	0.94	-0.04	-4
Jul 1st–Sep 12, 2018 (n = 73)	3.83	3.86	-0.03	-1
Jul 1st – Sep. 15, 2019 (n = 77)	4.24	4.16	0.09	2
Jul 14 – Sep. 6th, 2020 (n = 54)	3.5	3.19	0.32	9
All periods (n = 323)	17.81	17.25	0.56	3

5.4.5. Isolating the effect of smoke and LAI

To illustrate the impact of forest fire activity on the daily melt volume, hourly melt from the four scenarios for days with variable weather conditions is shown in Figure 5.8a-b and Table B.3. These 12 days are representative of the patterns seen throughout the 2015-2020 melt seasons, including smoky days with clouds, smoky days with clear skies (without clouds), and days without smoke. On smoky-cloudy days such as August 14th, 2018, the radiation attenuation ("With Smoke" scenario) and the darker albedo ("With LAIs" scenario) have opposing impacts of similar magnitude on ice melt.

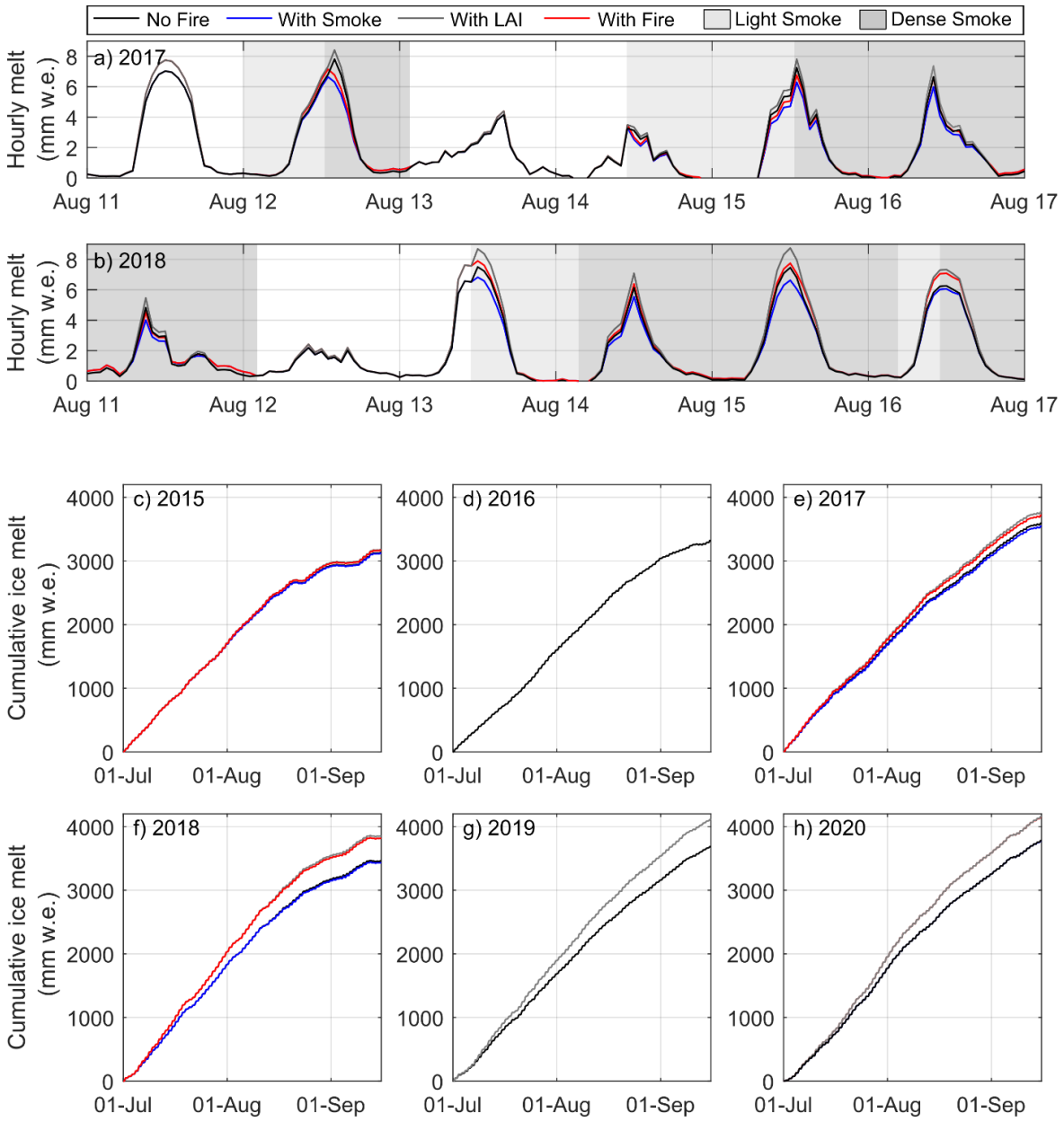

Figure 5.8. Simulated hourly melt for the four scenarios (No Fire, With smoke, With LAIs, With Fire) in a) 2017, and b) 2018, and simulated cumulative seasonal melt for each of the 2015-2020 seasons in c) to h) for the four smoke and LAI scenarios. The days and seasons with only the "No fire" (black) and "No LAIs" (grey) lines correspond to days or seasons with no smoke detected at the Athabasca Glacier.

For example, on August 14th, 2017, the presence of smoke reduced melt by 4 mm, but the darker surface albedo increased melt by 4 mm, resulting in the "No Fire" and the "With Fire" scenario showing the same daily melt. Similarly, the following day, the presence of smoke reduced melt by 2 mm, but the darker albedo increased melt by 3 mm. On smoky-clear days, the impact of the presence of LAI typically outweighed the impact of the presence of smoke. For example, on August 15th, 2018,

the presence of smoke reduced melt by 4 mm, but the presence of LAI increased melt by 9 mm. On the following day, smoke reduced melt by 1 mm, and the LAI increased melt by 8 mm. Therefore, it is important to consider the weather associated with the smoke (smoky and clear or smoky and cloudy), to assess the compensating impacts of reduced atmospheric transmissivity by smoke, affecting both short and longwave irradiance, and albedo reduction by LAIs.

Noting that smoky conditions only occurred during 11% of the 2015-2010 melt seasons, the four simulations show that, at the seasonal time scale, the large increase in melt due to albedo reduction overcomes the small reduction in melt due to reduced atmospheric transmissivity (Figure 5.8c-h, Table S5.4). The compensatory effects of reduced atmospheric transmissivity, which reduces melt, and albedo reduction, which increases melt, are particularly visible in 2017 and 2018. Both these years had smoke detected and low albedo observed on Athabasca Glacier. In 2017, reduced atmospheric transmissivity decreased melt by 1.4% compared to the "No Fire" scenario, but the presence of LAI increased melt by 4.9%, resulting in a total increase in melt of 3.3%. This is equivalent to an increase in melt of 0.12 m w.e. per year. In 2018, the year with the greatest upwind fire activity in historical record, radiation attenuation reduced melt energy by 0.9%, but albedo reduction increased melt by 11.1%, for a net increase in melt of 10.2%, or 0.35 m w.e. per year, compared to the no-fire simulation.

The following year, 2019, no smoke was detected at Athabasca, but the simulations indicate that, with albedo remaining as low as 0.17, the albedo reduction caused an increase in melt of 11.5% (0.42 m w.e. per year.). In 2020, smoke was detected only in the last few days of the melt season, and the reduced albedo simulation shows an increase in melt of 9.6% compared with the no-fire simulation (0.37 m w.e. per year). These two years are very similar and much higher than the 4.5% increase in melt due to albedo reduction reported in Magalhães *et al*. (2019) for the tropical Andes.

This low observed albedo of 0.17, remaining low after two summers of intense fire activity, also indicates that the albedo reduction continues even after fire activity ceases. Even without deposition of new smoke-derived LAIs, and likely some removal of LAIs from the surface meltwater, the albedo remains low. This may be linked with microbial growth on the glacier ice, as carbon deposition on snow and ice surfaces can feed microbial and algal growth, which then causes a further reduction in albedo (Cook *et al*., 2017; Jones *et al*., 2001; Stibal *et al*., 2012; Tedstone *et al*., 2019).

These melt simulations assess how wildfire smoke, through changes to both irradiance and albedo, can influence surface melt. The difference in temperature and humidity between smoky and non-smoky conditions, though observed on site, were not assessed in these melt simulations even though they could influence melt rates. Warmer and less humid conditions can be both a cause and a consequence of wildfire activity, and so untangling the causality between wildfire activity, temperature and humidity in this modelling experiment was considered out of the scope of this study.

Worldwide, glaciers have witnessed an accelerating mass loss since 2000 (Hugonnet *et al*., 2021), and ongoing glacier retreat is well-documented for the Canadian Rockies (DeBeer and Sharp, 2007; Tennant *et al.*, 2012; Tennant and Menounos, 2013; DeBeer *et al.*, 2016). Glacier loss across western North America shows a heterogeneous regional pattern since 1985, with the mass loss rate slowing in the 2000-2009 period and accelerating for the 2009-2018 period, with the regional and temporal variability possibly linked with a shift in regional meteorological conditions from upper level zonal winds (Menounos *et al*., 2019). Glaciers in Western Canada, and specifically in the Canadian Rockies, are expected to be largely ablated by the end of the century (Clarke *et al*., 2015; Huss & Hock, 2018). The increase is surface melt from lowered surface albedo driven by wildfire activity presented in this study provides further insights on the complex mechanism and feedback linking glacier mass balance and climate forcings.

5.4.6. Spatially distributed albedo change from remote sensing

The three outlet glaciers show a range of albedos (Figure 5.9), which demonstrates the importance of complementing point-based analysis with areal estimates. For the Athabasca Glacier, satellite-derived albedo was obtained both for the entire glacier area and for the pixel corresponding to the location of the AWS_{ice}, with a spatial resolution of 20 x 20 m. Glacier-wide albedos for the Athabasca Glacier were higher than at the AWS_{ice} (Figure 5.9a). This difference is likely linked to late summer snow patches lingering at the higher elevation of the glacier area (Figure 5.9b-d). These patches were particularly visible in the 2020 melt season, following a wet and cool spring which caused snowcover to persist into late summer on the Columbia Icefield. The partial recovery in measured surface albedo for the 2020 late melt season is evident in the glacier-wide albedo and for the pixel corresponding to the location of the AWS_{ice}, with the remotely-sensed albedos increasing from 0.293 to 0.327, and 0.186 to 0.233 respectively over the melt season, which suggests the possibility of LAIs being removed from the surface.

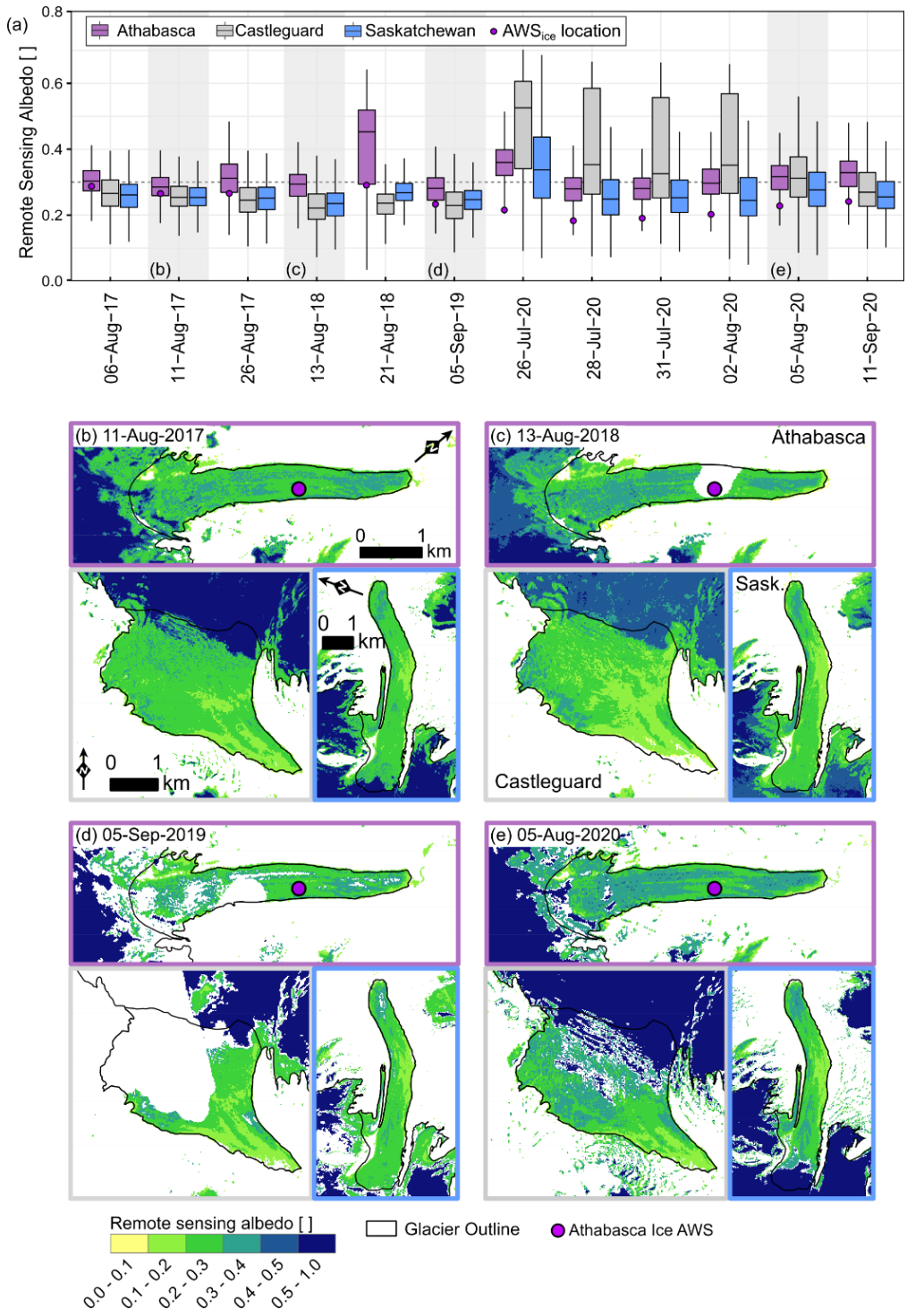

Figure 5.9. Remote sensing albedo for the Athabasca, Castleguard and Saskatchewan Glaciers for 12 dates in the 2017-2020 melt seasons (a), with spatial end-of-summer albedo (dates with the lowest glacier albedo for each season, highlighted in grey) shown in b-e. Please note the change in colour gradation for albedo above 0.5. The location of the Athabasca AWS is shown as a purple dot in b-d. The horizontal grey line in (a) shows the reference albedo of 0.3 and the purple dot corresponds to the albedo for the pixel where the AWSice is located.

The glacier-wide albedo of both the Castleguard and Saskatchewan Glacier show similar trends, with low albedo in 2019 despite the lack of forest fire activity during that melt season, and recovery during the 2020 melt season, with the albedos rising to the more typical clean-ice albedo of 0.3.

The Castleguard and Saskatchewan glaciers showed the largest variability in albedo. For the Castleguard, this is linked to a lingering high-albedo snow patch below the glacier outline, and some dark or debris covered ice with a very low albedo observed near its toe (Figure 5.9b-d). For the Saskatchewan, the variable snowline and a dark ice zone adjacent to low-lying bare soil and rock near the middle of the glacier results in larger spatial variability than the Athabasca.

5.5. Conclusions

The impacts of upwind forest fire activity on glacier melt were investigated through analysis of field observations, modelling experiments and remote sensing imagery for the 2015-2020 melt seasons at Athabasca Glacier and the surrounding Columbia Icefield in the Canadian Rockies of western Canada. At the Athabasca Glacier, upwind forest fire activity influenced surface glacier melt in two ways; firstly, through decreasing the glacier albedo from soot deposition following smoke drifting over the glacier and secondly, through the direct impact of the atmospheric conditions above the glacier on reducing shortwave irradiance, increasing longwave irradiance and reducing net radiation. Days with smoke were warmer and drier, had lower shortwave irradiance and greater longwave irradiance compared to non-smoky, clear days. However, the compensatory impacts of lower shortwave and higher longwave irradiance dampened the reduction in net radiation for smoky days.

The compensatory effects of soot deposits and subsequent microbial growth, which reduced albedo, and smoke in the atmosphere above the glacier, which reduced atmospheric transmissivity, were analyzed using a point-based energy balance model. Even though smoke slightly increased longwave irradiance, the attenuation of the shortwave irradiance is greater, resulting in an overall reduction in all-wave irradiance and a reduction in net radiation of 15 W m^{-2} during smoky conditions, compared to non-smoky conditions. For years when wildfire smoke was detected, reduced all-wave irradiance partly compensated for the effects of reduced albedo on melt energetics, giving a net increase in melt of only 6.75%. However, in years without smoke, the low albedo from antecedent soot deposits increased seasonal ice melt.In 2019, the suppressed albedo resulted in an increased melt of 0.42 m. w.e. per year, or 10.2% of the simulated melt for the July 15-September 15 period compared to when simulated with a standard ice albedo of 0.3. Similarly, in 2020, the simulated melt increased by 0.37 m. w.e. per year, or 8.9% of the simulated melt.

The results from the point-based energy balance model experiment were upscaled by analyzing the areal albedo dynamics using satellite-derived albedos for the three main outlet glaciers of the Columbia Icefield (Athabasca, Saskatchewan and Castleguard glaciers). High-resolution albedo retrievals from 24 Sentinel 2 images, combined with a MODIS snow-kernel used to model the bidirectional reflectance of snow and ice, show that the albedo changes across the three glacier surfaces is consistent with the point-albedo measured on the Athabasca Glacier toe.

This study provides a process-based understanding of the impacts of wildfire activity on the mountain cryosphere. It shows that increased longwave irradiance partly compensates for reduced shortwave irradiance and that reduced net irradiance partly offsetss the reduced albedo on smoky days after soot deposition on glaciers. However, the net effect of wildfires in increasing glacier melt is substantial and long lasting due to the reduced albedo. Considering the expected increase in both climate extremes and forest fire activity, coupled with continued decline in mountain glaciers, understanding the processes at play provides a first step toward improved predictions of runoff from these glaciers and less uncertain assessments of the implications of changing glacier hydrology for downstream water resources and sea level rise.

DIAGNOSING HYDROLOGICAL PROCESS CONTROLS ON CHANGES IN STREAMFLOW GENERATION AND VARIABILITY IN A GLACIERIZED ALPINE HEADWATER BASIN

Paper manuscript status: Contents of this chapter are published in the journal Hydrological Processes.

> Aubry-Wake, C., Pradhananga, D., & Pomeroy, J. W. (2022). Hydrological process controls on streamflow variability in a glacierized headwater basin. Hydrological Processes, 36(10), e14731. https://doi.org/10.1002/hyp.14731

Author contribution: Caroline Aubry-Wake conceptualized the study, compiled, organized and processed the field measurements, set up the glacio-hydrological model and performed the modelling simulation as well as wrote the first draft of the manuscript. Dhiraj Pradhananga provided insights on model development and set-up. John Pomeroy provided insights on the conceptualization, data processes and modelling approaches, developed the CRHM model, as well as edited the manuscript.

Role in thesis: This chapter addresses objective 2 of the thesis. In this chapter, the Cold Region Hydrological Modelling platform is used to build a glacio-hydrological model designed for the Peyto Glacier Research basin. This glacio-hydrological model includes the suite of processes occurring in the basin. The model simulation is run for 1987-2020, using in-situ data. The modelling outputs are used to analyze the hydrological processes at Peyto and their role in causing streamflow variability. The streamflow time series from chapter 2, the debris thickness measurements from chapter 3 and the hourly glacier energy balance from chapter 4 are used the develop and evaluate the modelling approach from this chapter.

6.1. Abstract

Mountain glacierized headwaters are currently witnessing a transient shift in their hydrological and glaciological systems in response to rapid climate change. To characterize these changes, a robust understanding of the hydrological processes operating in the basin and their interactions is needed. Such an investigation was undertaken in the Peyto Glacier Research Basin, Canadian Rockies over 32 years (1988-2020). A distributed, physically based, uncalibrated glacier hydrology model was developed using the modular, object-oriented Cold Region Hydrological Modelling Platform to

simulate both on and off-glacier high mountain hydrological processes and streamflow generation. The model spatial configuration was automatically adjusted during the simulations to represent glacier retreat. Model performance was evaluated with both streamflow and glacier mass balance observations. The hydrological processes that generate streamflow from this cold alpine basin underwent substantial inter-annual variability over the 32 years. Snowmelt runoff always provided the largest fraction of annual streamflow (44% to 89%), with smaller fractional contributions occurring in higher streamflow years. Ice melt runoff provided 10% to 45% of annual streamflow volume, with higher fractions associated with higher flow years. Both rainfall and firn melt runoff contributed less than 13% of annual streamflow. Years with high streamflow were on average 1.43˚C warmer than low streamflow years, and higher streamflow years had lower seasonal snow accumulation, earlier snowmelt and higher summer rainfall than years with lower streamflow. Greater ice exposure in warmer, low snowfall (high rainfall) years led to greater streamflow generation – the converse of that expected for snow dominated non-glacial alpine basins. The understanding gained here provides insight into how future climate and increased meteorological variability may impact glacier meltwater contributions to streamflow and downstream water availability as alpine glaciers continue to retreat.

6.2. Introduction

Glacierized mountain basins provide water to almost one-third of the world's population (Beniston, 2003), but mountain glaciers are retreating quickly and expected to lose 30-80% of their volume by the end of the century (Huss *et al.*, 2017). Their retreat is impacting water resources across the globe, as glaciers have a strong influence on their basin hydrological regime due to their capacity to store water on seasonal to decadal time scales (Jansson *et al.*, 2003). By storing water as snow and ice during cold and wet periods, and releasing it in dry and hot periods, glaciers can modulate streamflow variability via a compensatory effect occurring both at a decadal, seasonal and even weekly timescale (Jansson *et al.*, 2003). For instance, Pradhananga and Pomeroy (2022a) found that increasing glacier ice melt compensated for declining precipitation and snowmelt in two Canadian Rockies glacierized catchments, resulting in increased discharge since the 1960s, showcasing the decadal capacity of the glacier compensation effect. On a weekly timescale, Van Tiel *et al.* (2021) found that glacier and snow melt in glacierized basins with a 5-15% glacier cover could compensate for precipitation deficits and increased evapotranspiration in the European Alps. Even though a glacier coverage of roughly 40% has been suggested to minimize inter-annual variability (and maximize the glacier compensation effect) (Fountain and Tangborn, 1985; Chen and Ohmura, 1990;

Jansson *et al.*, 2003), a recent analysis of streamflow in glacierized basins worldwide was not able to define a universal relationship between glacier coverage and streamflow variability and instead hinted at the range of hydrological processes that can complicate the relationship (van Tiel *et al.*, 2020a). Snow and ice melt in glacierized basins can also overcompensate for weather conditions and cause an increase in streamflow variability (van Tiel *et al.*, 2020a, 2021). In the Canadian Rockies, Hopkinson and Young (1998) showed that glacier meltwater does not always effectively augment streamflow during low flow, dry years. This is in accordance with research showing that during cold years, glacier meltwater can be significantly reduced and induce "glacier melt drought" (Van Loon *et al.*, 2015). For tropical glaciers, glacier meltwater can be the driver of variability in streamflow from hourly to annual timescales (Saberi *et al.*, 2019). These results hint at the complex interactions amongst glacier melt, streamflow generation and seasonal meteorological conditions.

The role alpine glaciers play in modulating inter-annual flow variability is further complicated by their recent and predicted retreat (Radic and Hock, 2014; Shannon *et al.*, 2019; Hugonnet *et al.*, 2021). As currently glaciated mountain headwater basins transition from glacier melt runoff dominated to more rainfall-runoff and snowmelt runoff dominated, they will shift towards a more variable hydrological regimes linked with the decreased capacity of glaciers to provide reliable flow compensation. This shift is already noticeable in the Alps and Pyrenees, where runoff volume is more tightly controlled by seasonal snow accumulation and runoff peaks are more strongly associated with snowmelt and the occurrence of large rainfall volumes than with glacier melt (Milner *et al.*, 2017). López-Moreno *et al.* (2020) have shown that as snowmelt dominated alpine basins warm, their streamflow regimes decouple from snow hydrology regimes, suggesting a progression from glacier-modulated to seasonal snowpack-modulated to rainfall-modulated hydrological regimes as alpine climates warm. There is increasing interannual variability along this progression as hydrological memory times shorten from glaciers to seasonal snowpacks to rainfall. Combining this decrease in the interannual buffering capacity of glacier runoff with an expected increase in extreme weather and hydrological events such as increased heavy precipitation and droughts (Seneviratne *et al.*, 2012), significant changes are expected to occur to the hydrology of mountain glacierized headwater basins around the world.

Analyzing the influence of glacier runoff on headwater basin streamflow is further complicated by the variety of approaches used to define glacier contributions to streamflow. Within the range of methodologies, glacio-hydrological modelling is the most used (Frenierre *et al.*, 2013). Glacio-

hydrological models can be used to increase the understanding of the observed processes in a basin (Verbunt *et al.*, 2003), and can help diagnose the relationship between the different hydrological processes. These glacio-hydrological models are typically adapted from models with either a glaciological or hydrological background, depending on the intended use. Glaciological models typically focus on the ice processes, for example, the representation of ice dynamics (Huss *e*t al., 2010; Clarke *et* al., 2015) or surface mass balance (Hock and Holmgren, 2005), but either ignore or simplify the other hydrological and cryospheric processes (Immerzeel *et al.*, 2010). Hydrological models typically simplify the glacier-specific processes, such as neglecting ice dynamics (Comeau *et al.*, 2009; Jost *et al.*, 2012), but can have more sophisticated representations of the terrestrial hydrological cycle. Both model approaches often use a conceptual approach to parametrize surface melt, using statistical associations to infer mass and energy fluxes, such as the calibrated temperature-index, degree-day melt models (Hock, 2003; Finger *et* al., 2011; Fatichi *et* al., 2014; Ragettli *et* al., 2016; Chernos *et* al., 2020). While this makes them easier to apply in areas with incomplete forcing data, a typical issue for mountain environments, it also makes them more prone to problems such as equifinality (Beven, 2006), which can be reduced by using multi-criteria calibration procedures (Jost *et al.*, 2012; Pellicciotti *et al.*, 2012; Hanzer *et al.*, 2016; van Tiel *et al.*, 2020b). A further concern with these calibrated empirical modelling approaches is their transferability in time (Hock, 1999), especially their ability to simulate conditions outside of the conditions encountered in the calibration period (Duethmann *et al.*, 2020). Some glacio-hydrological model calibration strategies involve using unusual years, such as the hot and dry year of 2003 in the European Alps, to assess model performance under extreme events (Koboltschnig and Schöner, 2011). However, with rapidly changing meteorological conditions and land cover, past conditions are not likely to represent future melt and hydrological events in glacierized alpine basins. Empirically calibrated glacio-hydrological models also increase predictive uncertainty as they are not consistent with the current understanding of glacio-hydrological physical processes. Since shortwave radiation rather than air temperature is the main driver of glacier melt, and snow redistribution is an important control on snow accumulation, the lack of a physical basis for these models is scientifically unsatisfying in that process diagnoses are not possible and predictive uncertainty is high because they are calibrated to past climate and glacier conditions. Models with a more complete range of representations of glacio-hydrological processes do exist (Naz *et al.*, 2014; Frans *et al.*, 2018; Pradhananga and Pomeroy, 2022a, 2022b), but these are still not widely used despite the uptake of models of similar complexity for cold regions hydrological applications (Wheater *et al.*, 2022). To

investigate the inter-annual variability in the hydrology of a glacierized headwater basin and to diagnose the hydrological processes governing this variability requires a physically based model, with a fairly complete representation of both on and off-glacier biophysical processes. Glacierized basins are complex systems, with several hydrological processes on and off the glacier such as snow redistribution, accumulation and ablation, glacier processes, infiltration into seasonally frozen soils, groundwater storage and flow, frozen ground, evapotranspiration and a dynamic land cover. These interconnected processes, driven by complex physical feedbacks, should be included in hydrological assessments of glacierized headwater basins to gain a robust understanding of the sources of hydrological variability occurring in these basins.

The objective of this paper is to assess and characterize the inter-annual hydrological variability of a long-studied alpine glacierized headwater basin in the Canadian Rockies using observations and a physically based glacio-hydrological model, including the full range of processes occurring both on and off the glacier. Specifically, this study investigates the influences of meteorological conditions on hydrological processes, meltwater production, runoff and streamflow variability by addressing the following questions:

- What trends are evident in the hydrometeorological behaviour of the basin in the recent decades?
- How do runoff source and streamflow regime vary with seasonal hydrometeorological conditions?
- How do meteorological conditions, snow dynamics and sources of runoff vary between high and low streamflow years?

6.3. Data and methods

6.3.1. Study site and available data

Peyto Glacier Research Basin (PGRB, Figure 6.1), a small glacierized headwater basin in the Canadian Rockies provided the study site. Peyto Glacier, the northernmost outlet glacier of the Wapta Icefield, ranges between 2100-3190 m.a.s.l. and had an area of 10.2 km^2 in 2016, with a drainage basin of 19.3 km^2 as defined by a stream gauge installed by the University of Saskatchewan's Centre for Hydrology in 2012. Peyto Glacier is one of the few well-monitored glaciers in Western Canada, and has one of the longest time series of measurements in the world, with mass balance observed yearly since 1965, and glacier extent measured since 1896 (Demuth *et al.*, 2006). The rest of the basin is composed of moraine deposits, talus fields, and exposed bedrock, including cliffs (Figure 6.1b).

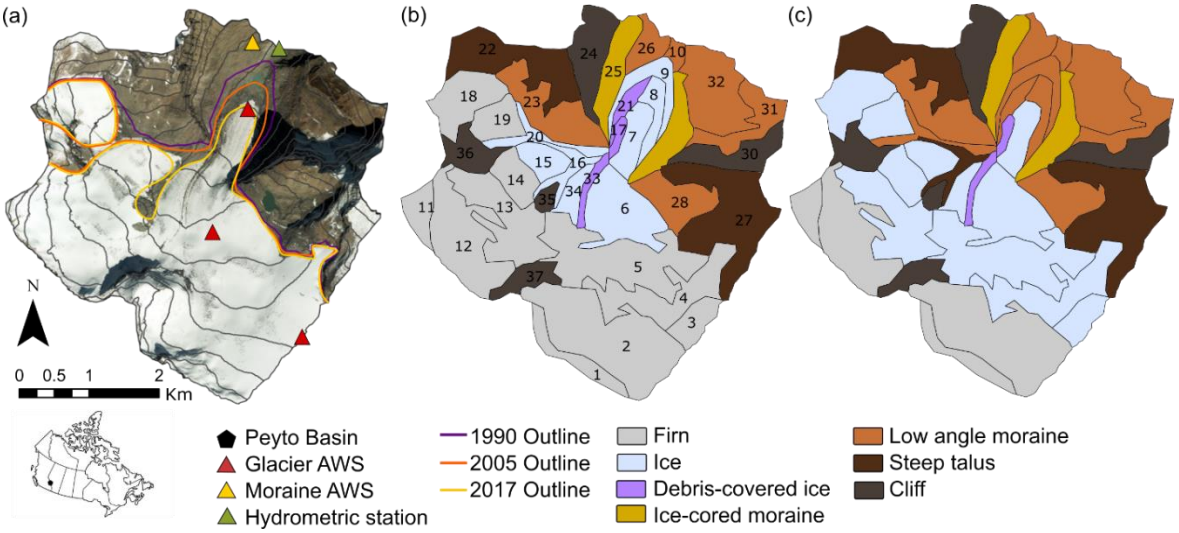

Figure 6.1. Peyto Glacier Research Basin (a) from aerial imagery in 2014. Yellow, red and green triangles indicate locations of the Moraine AWS, Glacier AWS and the Centre for Hydrology hydrometric station. Thin grey lines in (a) are terrain contours at 100 m intervals, from 2100 to 3000 m.a.s.l. The glacier extent, surface cover type and spatial discretization of hydrological response units (HRUs) are shown for (b) 1990 and (c) 2015. The number labels on (b) refer to the table A1 presenting the geomorphic characteristics of the HRUs.

The meteorological data used for model forcing and evaluation in this study has been described in detail in Pradhananga *et al.* (2021) and by Pradhananga and Pomeroy (2022b), but a summary is provided here. An automated weather station (AWS), Peyto Main Old, has recorded sub-hourly to hourly air temperature, relative humidity, incoming solar radiation, incoming longwave and wind speed since 1987, at an altitude of 2240 m.a.s.l. In 2013, a new AWS, Peyto Main, was installed adjacent to the Peyto Main Old AWS. Due to the remote location and harsh conditions found in the basin, gaps are present in the data since the installation. The record from Peyto Main Old between 1987 and 2018 is 94% complete, with few gaps in the 2018 to 2020 period. When data gaps were less than or equal to four hours, they were filled with either linear interpolation, and when gaps were more than 4 hours, they were filled with data from nearby stations using monthly linear regression. When nearby stations were not available to fill the missing data, the gaps were infilled using ERA-Interim data which was bias-corrected and downscaled to the station location using a quantile mapping technique with monthly calibrated parameters from in-situ data (Dee *et al.*, 2011).

Precipitation for the PGRB for 1987-2020 was obtained from the ERA-Interim reanalysis product. The ERA-Interim precipitation data was also corrected using a quantile mapping technique using monthly calibrated factors, but the in-situ data used to derive these factors was obtained from the Alberta

Environment Bow Summit weather station, located 5 km down valley at an elevation of 2030 m. a.s.l., from which a reliable, sheltered-environment hourly precipitation is available since 2008.

Glaciological data are available both as summer and winter point mass balance for the 1993-1995 period (Dyurgerov, 2002) and as stake measurements for the 2003-2017 years. Additionally, glacier surface elevation change was measured intermittently using an ultrasonic depth sensor on the on-ice AWS for the 2011-2020 period, and surface lowering associated with ice melt has been transformed to surface melt water equivalent using an ice density of 900 kg m^{-3}.

In 2013, an ultrasonic depth sensor (SR50) was installed one km below the glacier snout at a bedrock constriction, which acts as a natural notch, providing a reliable water level. Starting in early fall 2017, salt dilution measurements were performed to build a rating curve to relate the water level at the sonic depth sensor to discharge (Sentlinger *et al.*, 2019; Pradhananga *et al.*, 2021, and Chapter 2)). Manual stream width measurements provided values ranging between 8 and 13 m, and a mixing reach of length 420 m was set based on the local geomorphology to constrain the salt measurement between two naturally occurring bedrock notches constricting the flow. 105 salt dilution measurements were conducted between 2017 and 2019 and processed in the Fathom Scientific Salt Portal platform, an online post-processing platform for salt dilution measurements (salt.fathomscientific.com). Of these 105 measurements, 46 were determined to be anomalous due to incomplete mixing associated with the choice of location for the conductivity probe, localized snowmelt runoff, and the high background noise in electrical conductivity. The resulting rating curve, based on 59 measurements with an average uncertainty of 12%, is a power law with an inflection point at depth of 0.75m due to a change in the slope of the bedrock notch walls. The rating curve is stable over the 2017-2019 observations, as expected from the bedrock notch controls on streamflow over the salt dilution mixing reach. This suggests it is appropriate to use the same rating curve for the 2013-2020 melt seasons. Streamflow observations are only possible when the melt channel is sufficiently free of snow that the SR50 sensor can measure open water, which results in streamflow measurement available from mid-May/early June to late September/mid-October.

6.3.2. Modelling approach

The Cold Regions Hydrological Modelling Platform (CRHM, Pomeroy *et al.*, 2007; Pradhananga and Pomeroy, 2022b) was used to investigate the hydrological processes and inter-annual variability in the PGRB. The model was run at an hourly resolution for the period 1987-2020, with the first-year acting as a spin-up period. The modelled period analyzed covers 32 continuous hydrological years

(October 1st – September 31st), starting in October 1988 and ending in September 2020. The model outputs were aggregated into daily values for the analysis. The analysis period was dictated by the availability of in-situ meteorological information in the PGRB (Pradhananga *et al.*, 2021).

CRHM is a process-based, flexible, modular hydrological modelling platform. The user can select processes from an extensive library to assemble a custom hydrological model suited to the complexity, knowledge and available data from the study environment. CRHM has been extensively applied to studies of mountainous regions in the recent years (DeBeer and Pomeroy, 2009; MacDonald *et al.*, 2010; Fang *et al.*, 2013; Rasouli *et al.*, 2014; Zhou *et al.*, 2014; Krogh *et al.*, 2015; López-Moreno *et al.*, 2017) with applications over different terrain and climatic settings and at different spatial scales. A glacier module has recently been developed to represent ice and firn melt and mass balance using an energy balance approach (Pradhananga and Pomeroy, 2022a, Pomeroy *et al*., 2022). This model is selected amongst other models because it has spatially distributed energy balance forcing and a set of modules that represent hydrological processes suitable for the PGRB including blowing snow transport and sublimation, complex terrain wind flow, avalanching, infiltration into seasonally frozen soils and evaporation from soils, vegetation and open water and surface and sub-surface runoff generation.

The modelling work presented here used the CRHM model development from Pradhananga and Pomeroy (2022b) and the PGRB data processing of Pradhananga *et al.* (2021). However, it differed substantially from the CRHM application to the PGRB by Pradhananga and Pomeroy (2022a, 2022b). The study used in-situ forcing data instead of reanalysis and simulated different time period. In addition, the current application used a different energy-balance parametrization for the glacier ice melt, and the model spatial discretization and parametrization was performed independently from these previous studies. In addition, the research goals of this study, specifically to investigate processes resulting in streamflow variability in the PGRB, were different from those of Pradhananga and Pomeroy (2022a, 2022b), and therefore resulted in a different analysis methodology.

6.3.2.1. *Spatial discretization*

The spatial modelling unit in CHRM, the hydrological response unit (HRU), is the spatial extent over which the mass and energy balances are calculated. HRUs are defined as regions with similar hydrological characteristics and common parameters, based on topographic, drainage, vegetation, soil, and hydrometeorological properties. Here, glacier properties were also included in discretizing

the basin into HRUs. PGRB was divided into 36 HRUs that represent the glacier retreat over the 1987-2017 period, as well as the firn line retreat and major land cover types such as moraine, talus, ice-cored moraine, and cliffs (Figure 6.1b, c). The changing land cover types were manually defined using a combination of Landsat imageries for glacier and firn, and field observations for cliffs, moraines and talus characterization. The ice-cored moraine area was defined following Hopkinson *et al.* (2012). For each HRU, parameters such as slope, aspect, elevation, and terrain view factor were then defined using the SRTM digital elevation model. The resulting HRUs, with associated cover-type, can be seen in Figure 6.1b-c, and the elevation, slope, angle aspect and cover-type of each HRU can be found in table C.1.

6.3.2.2. *Physical processes representation and parametrization in CRHM-glacier*

A purpose-built model representing the hydrological processes observed in the PGRB was designed by selecting modules in the CRHM modelling library. Parameters for each module have a physical meaning and can be obtained from field site or remote sensing observations. When parameters specific to the site are unavailable, parameters are obtained following the abduction approach (Pomeroy *et al.*, 2013), meaning they are transferred from studies in similar environments or obtained from compatible hydrological environments described in the scientific literature. In other words, as this CRHM model is based on physical processes, it does not require a parameter calibration scheme based on streamflow observations. The CRHM process representation and parameter estimation approaches are described below.

6.3.2.2.1. ***Distributing meteorological inputs***

The CRHM model created for PGRB distributes the forcing meteorology, namely observations of air temperature, relative humidity, wind, incoming shortwave and longwave radiations and wind speed, spatially and temporally over the basin. The air temperature lapse rate was defined for monthly values, ranging from -0.57 to -0.81°C per 100 m, obtained from three on-ice AWS located on the glacier toe, near the equilibrium line, and in the accumulation area for the years 2010-2013 as in Pradhananga and Pomeroy (2022) (Figure 6.1a). The shallowest temperature elevation lapse rates (slower decrease in temperature with elevation gain) occurred in July and August, with generally steeper temperature elevation lapse rates (faster decrease in temperature with elevation) occurring in Fall and Spring. Monthly values for the temperature lapse rates were fixed throughout the simulation period (i.e. all Januarys had the same lapse rate). The precipitation elevation lapse rate

was derived from the end-of-winter SWE point measurement over the glacier area for two 3-year periods (2003-2005 and 2014-2016) and so integrates the winter snow accumulation season. The same precipitation gradient was used for all seasons, as there was no information available to create a seasonal-lapse rate for this basin. Precipitation phase partitioning was calculated using the psychometric energy balance of a falling hydrometeor based on air temperature and relative humidity (Harder and Pomeroy, 2013). Wind flow acceleration and deceleration over PGRB's complex terrain, an important component to capture blowing snow processes and turbulent transfer calculations, were simulated following a linearized turbulence model (Walmsley *et al.*, 1986). Radiation was adjusted for self-shading and slope-aspect following the formulations of Garnier and Ohmura (1970).

6.3.2.2.2. *Snow redistribution*

CRHM simulates winter snow redistribution from blowing snow with the Prairie Blowing Snow Model module (Pomeroy *et al.*, 1993; Pomeroy and Li, 2000), which was initially developed in the Canadian Prairies but has since then been parameterized for alpine and arctic tundra (Pomeroy *et al.*, 1997), mountainous subarctic terrain (MacDonald *et al.*, 2009) and mountain ridges (MacDonald *et al.*, 2010). The blowing snow sequence follows the dominating westerly wind patterns, from the peaks on the continental divide, east to the glacier toe. Blowing snow redistribution requires a terrain roughness specification, which in the absence of vegetation represents surface undulations and barriers. This was set to between 0.5 and 3 m based on cover type and field observations. Fetch distance was obtained from the length of the HRU in the predominating wind direction.

In high mountain environments, avalanches can redistribute an important part of the snow accumulation (Shea *et al.*, 2015). Avalanches are highly dependent on slope, snow accumulation and meteorological factors (Schweizer *et al.*, 2008; Freudiger *et al.*, 2017). CHRM uses the *SnowSlide* model as a module to represent avalanche redistribution of snow, based on a threshold snow holding depth and slope (Bernhardt and Schulz, 2010; Bernhardt *et al.*, 2012). The minimum threshold depth was set to 500 mm w.e. for most HRU, with a holding capacity of 50 mm w.e. for the HRU with a surface slope angle above 30°, as steep terrain is more likely to avalanche frequently (McClung and Schaerer, 2006).

6.3.2.2.3. *Snow and icemelt*

Snowmelt on- and off-glacier in CRHM is calculated with the SNOBAL module (Marks *et al.*, 1999). This module approximates the snowpack as being composed of two layers: a surface-active layer of fixed thickness and a lower layer representing the remaining snowpack. The module solves for the temperature, liquid water content and the specific mass of each layer for each time step. The point energy balance of the snowpack is expressed as in the following:

$$Q_m = Q_n + Q_h + Q_e + Q_g + Q_p - \frac{dU}{dt} \quad (6.1)$$

where Q_m is the energy available for snowmelt, Q_n is the net radiation composed of both shortwave and longwave components, Q_h, Q_e and Q_g are the sensible, latent and ground heat fluxes, respectively, Q_p is the energy added to the snowpack by precipitation, all in W m^{-2}, and U is the internal energy of the snowpack in Joules. The snow albedo decay function (Essery and Etchevers, 2004) requires a maximum (fresh snow) and a minimum (bare ground) albedo, which in this case was set to 0.85 and 0.17 from regional observations. For glacier and firn, the albedo was set to 0.3 and 0.5 respectively. The snowmelt module was given a surface snow roughness of 0.0055 m based on the observations of Munro (1989) from Peyto Glacier. Turbulent transfer energy fluxes in the module are calculated using a bulk transfer formulation with the Monin-Obukhov stability corrections.

Once the snow is melted, glacier icemelt is calculated using a single layer energy balance model, with the residual of the radiation and turbulent fluxes resulting in energy available for melt (Hock, 2005). The model distinguishes between firn and ice cover for albedo, roughness length and density. The energy balance formulation for the ice and firnmelt uses turbulent energy fluxes calculated following the katabatic parametrization of the bulk transfer method as described by Grisogono and Oerlemans (2001) and tested at Peyto Glacier by Munro (2004) and as presented in Chapter 4. This is an advance over the simpler daily icemelt energy balance parameterization employed in CRHM previously by Pradhananga and Pomeroy, (2022b, 2022a) in that sub-daily fluxes can have important contributions to seasonal melt. If the snowpack is not completely melted by the end of the summer, the snow becomes firn. Firn densification occurs through a 5-layer system, with density increasing from 450 to 850 kg m^{-3}. The densification rate was set to 100 kg m^{-3} yr^{-1} to be consistent with observations.

The presence of debris on the ice surface is a strong modulator the surface melt. For sparse or very thin debris, the increased surface albedo causes increased surface heating and increases surface melt, but under debris more than a few centimeters in thickness, the debris insulate the glacier ice and reduces melt. In both case, debris-covered ice melts at a different rate than adjacent clean ice.

Therefore, in a given basin, the relative importance of debris-covered glacier increases as the clean ice areas retreat faster than the debris covered areas. Ice-cored moraines are another type of debris-covered ice, a common feature in mountain environments (Østrem *et al.*, 1970; Gruber and Haeberli, 2009). In the PGRB, Hopkinson *et al*. (2012) found that runoff from the periglacial areas accounted for 8% of the water losses from basin storage for the period 2000-to 2010.

A melt under debris-cover parametrization was added to the CRHM model following the empirical equation of Carenzo *et al.* (2016).

$$M = TF * T(i - lagT) + SRF * (1 - \alpha) * SW_{in}(i - lagSW_{in}) \quad if\ T \geq T_t \qquad (6.2)$$

$$M = 0 \qquad if\ T < T_t$$

in which M is the melt from the ice surface, T is air temperature (°C), α is albedo (-), SW_{in} is incoming short-wave radiation (W m^{-2}), i is the time step (h), lag T and lag I are lag parameters for energy transfer through the debris layers, and T_t is the threshold temperature above which melt is assumed to occur. Also, there are two empirical parameters: the temperature factor, TF (mm h^{-1} °C^{-1}) and the shortwave radiation factor, SRF (m^2 mm W^{-1} h^{-1}), as shown in Table 6.1. Debris cover thickness in the PGRB was obtained from multiple point measurements over the study area from ice cliffs and manually digging pits during field site visits (Aubry-Wake *et al.,* 2022b).

Table 6.1. Melt under debris parameter values

Debris thickness (m)	lag_T (h)	lag_I (h)	TF (mm h^{-1} °C^{-1})	SRF (m^2 mm W^{-1} h^{-1})
0.05	0	0	0.0984	0.0044
0.1	0	1	0.0660	0.0023
0.2	3	3	0.0456	0.0009
0.23	3	4	0.0438	0.0006
0.3	5	5	0.0392	0.0002
0.4	7	7	0.0334	0.0001
0.5	10	11	0.0265	0

The empirical parameters in the Carenzo model were optimized using melt rates simulated by a physically-based debris energy balance model, which was validated against ablation stakes and surface temperature measurements. The Carenzo model was developed on Miage Glacier, Italy, and

then tested on the Haut Glacier d'Arolla, Switzerland. This formulation was shown to have similar results to an energy-balance approach treating the energy transfer as conductive energy flux, driven by the conductivity of the debris layer and the temperature gradient (Reid and Brock, 2010). However, the model can only be applied for discrete debris thickness, and to a maximum of 0.5 m. The thinnest layer in this parametrization is 0.05cm, which reduces melt. It is therefore not possible to simulate the increased melt linked with very thin debris, patchy debris or very dirty ice explicitly. Instead, increased melt associated with very thin debris could be simulated through a decrease in albedo.

For each glacier HRU, runoff water (rainfall on glacier area and meltwater) is routed vertically through the snow, firn and ice reservoir to the glacier-rock interface using a linear reservoir approach. Once the ice thickness of a glacier HRU reaches zero, the cover type is automatically converted to bare rock without interrupting the simulation. The elevation of the glacier HRUs evolves following the surface melt or accumulation throughout the simulation.

6.3.2.2.4. *Infiltration and subsurface flow and storage*

Once the snow and ice meltwater and rainfall runoff reaches the glacier-rock interface of individual HRUs, the water is routed through the soil module to produce surface runoff, infiltration and subsurface runoff as per Fang *et al.* (2013). Similarly, the snowmelt and rainfall runoff from the non-glacierized HRUs, composed of rock debris and exposed bedrock, is also handled by the soil module. Infiltration into unfrozen soils is calculated following Ayers (1959) and into frozen soils following Gray *et al.* (2001). For unfrozen soil, alpine soil texture parameters were transferred from Marmot Creek Research Basin, further south in the Canadian Rockies (Fang *et al.*, 2013). Frozen and thawed soil moisture initial conditions for storage and moisture content were obtained using a one-year spin-up period (1987).

The soil module is divided into a recharge layer, from which evapotranspiration can occur, a subsurface and a groundwater layer. Each soil layer, for each HRU, has a storage volume and a saturated hydraulic conductivity which dictate the fate of the meltwater and rainfall-runoff for each HRUs: saturation excess water becomes surface runoff routed to another HRU, whilst infiltrated water contributes to subsurface runoff and groundwater flow. Groundwater recharge occurs via percolation from the soil layers and groundwater discharge takes place through horizontal drainage in the groundwater layer. Subsurface discharge occurs via horizontal drainage from either soil layer,

with the lateral flow calculated using Darcy's law for unsaturated flow, as described by Fang *et al.* (2013). Surface runoff forms when melt or rainfall rates exceed the infiltration rate (infiltration excess surface runoff) or when they exceed the subsurface withdrawals from saturated soils (saturation excess surface runoff). The presence of water ponding in surface depressions has been observed in the moraine, the ice-cored moraine and the low angle talus environments. This was represented in the model as a depressional storage capacity set for these HRUs. When depressional storage capacity is present, surface runoff refills this storage before it can contribute to downstream runoff.

The soil module was parametrized based on the cover types in the basin: clean ice, debris-covered ice, steep talus, low angle talus, moraine and cliffs (Table 6.2). For the clean ice HRUs, the glacier was assumed to be sitting on bedrock with minimal subglacial debris, and therefore, was given low storage volume. For the debris-covered glacier HRUs, the subsurface layer storage was set to a volume varying with debris thickness to represent moisture storage in the debris layer. For the talus and moraine non-glacierized HRUs, the recharge soil layer was set to represent the coarse and shallow surface rock debris, and the subsurface layer was set to represent the thicker underlying moraine and talus debris, following field observations. The storage parameters for talus and moraine land cover were based on extensive studies of talus and moraine groundwater flow processes at Lake O'Hara Research Basin in the Canadian Rockies (McClymont *et al.*, 2010; Langston *et al.*, 2011; Muir *et al.*, 2011; Hood and Hayashi, 2015). Moraine deposit HRUs were set to have the largest storage capacity, being composed of coarse to fine sediment size. The storage in steep talus slopes (coarse, irregular rocks with large void space) HRUs was set to small values based on Langston *et al*. (2011), who found talus slopes to have a thin saturated layer (0.01-0.1m) at the bedrock-talus interface, which quickly transmits water to the downslope environment. This low storage capacity increases for low-angle talus HRUs, where micro-topographies can enhance water storage. Minimal soil storage was assumed for the cliff HRUs, as these are bedrock with limited debris moisture storage. The groundwater layer, set to represent the bedrock storage, was set to the same value across the basin and reflects the porous limestone lithology of basins in the region (Fang *et al.,* 2013).

The saturated hydraulic conductivities for talus and moraine sediments were transferred also from Lake O'Hara (Mcclymont *et al.*, 2010; Langston *et al.*, 2011; Muir *et al.*, 2011). Talus fields studied in the Canadian Rockies had a very high hydraulic conductivity (0.01-0.03 ms^{-1}) (McClymont *et al.,*

2010), with similar values obtained by Clow *et al.* (2003) in a talus and rock-glacier dominated basin in the Colorado Rockies.

Table 6.2. Subsurface storage and routing parameters (saturated hydraulic conductivity in m d^{-1} and recharge in mm)

	Moraine	Low Talus	Steep talus	Cliff	Clean ice	Debris cover
Maximum recharge layer storage	1	1	1	1	1	1
Maximum lower layer storage	1050	60	30	1	1	60-150
Maximum groundwater layer storage	1000	1000	1000	1000	1000	1000
Saturated hydraulic conductivity - upper soil layer	0.03	0.03	0.03	0.03	0.03	0.03
Saturated hydraulic conductivity - lower soil layer	0.001	0.01	0.01	6.95 ×10−7	6.95 ×10−7	0.001
Saturated hydraulic conductivity - groundwater layer	6.95 ×10−7	6.95 ×10−7	6.95 ×10−7	6.95 ×10−7	6.95 ×10−7	6.95 ×10−7

6.3.2.2.5. *Routing*

Routing of runoff from the surface and subsurface layers between the HRUs is handled in CRHM by Clark's lag and route algorithm (Clark, 1945). Considering the flashiness of the system, with meltwater reaching the outlet of the basin in a few hours to half a day (Ommanney, 2002; Munro, 2011, 2013), the routing through the basin was assumed to occur within a day, the minimum timestep at which the streamflow was analyzed. To capture this fast routing, the routing parameters for snow and ice melt as well as surface and subsurface flow were set to zero. The groundwater reservoir storage routing was set to 10 days for low-angle HRUs and 5 days for steep HRUs based on the physical understanding of alpine groundwater flow and storage (Hayashi, 2020).

6.3.3. Assessing model performance

Model evaluation is done with a range of metrics as appropriate for each dataset. The Nash Sutcliffe efficiency (NSE, Nash and Sutcliffe, 1970) is calculated as follow:

$$NSE = 1 - \frac{\sum_{t=1}^{t=T}(x_{sim}(t) - x_{obs}(t))^2}{\sum_{t=1}^{t=T}(x_{obs}(t) - \overline{x_{obs}})^2} \quad (6.3)$$

where T is the total number of time steps, $x_{sim}(t)$ the simulated variable at time t, $x_{obs}(t)$ the observed variable at time t, and $\overline{x_{obs}}$ the mean observed discharge. A value of NSE = 1 indicates perfect agreement between simulations and observations while NSE = 0 indicates that the model simulations have the same explanatory power as the mean of the observations, and NSE < 0 indicates that the model is a worse predictor than the mean of the observations (e.g. Schaefli and Gupta, 2007).

The Kling-Gupta Efficiency (KGE, Gupta *et al.*, 2009) is also used to evaluate model performance:

$$KGE = 1 - \sqrt{(r-1)^2 + (\alpha - 1)^2 + (\beta - 1)^2} \quad (6.4)$$

where r is the linear correlation between observations and simulations, α is a measure of the flow variability error, and β relates to the bias. KGE can also be written as:

$$KGE = 1 - \sqrt{(r-1)^2 + \left(\frac{\sigma_{sim}}{\sigma_{obs}} - 1\right)^2 + \left(\frac{\mu_{sim}}{\mu_{obs}} - 1\right)^2} \quad (6.5)$$

where σ_{obs} is the standard deviation in observations, σ_{sim} the standard deviation in simulations, μ_{sim} is the simulation mean, and μ_{obs} is the observation mean. KGE>-0.41 indicates that the simulated variable is performing better than the average of the observations and therefore, the model has predictive power, and a KGE<-0.41 indicates a poor model performance (Knoben *et al.*, 2019). Additionally, the root mean square error (RMSE), the Spearman's rank correlation coefficient (r) and the mean bias (MB) are calculated.

6.3.4. Assessing trends and variability in hydrometeorological conditions

Significant trends (p = 0.05) in annual or seasonal air temperature, precipitation and streamflow are tested using the non-parametric Mann-Kendall significance test, and the magnitude of the detected trends are estimated using Sen's slope (Sen, 1968), which calculates the slope using the median of all pairwise slopes in the data set. The seasons for the trend analysis were defined as fall (SON), winter (DJF), spring (MAM) and summer (JJA).

To gain further information on the variability in the streamflow generation processes in the basin, meteorological conditions and melt patterns in years of high streamflow (HF) were compared to

those of low streamflow (LF). Years with volumes greater than the mean plus one standard deviation were considered to be high flow (1992, 1994, 2006, 2013, 2015, 2016) and years with volumes less than the mean minus one standard were considered to be low flow (1995, 1996, 1997, 2000, 2003, 2008).

6.4. Results

6.4.1. Model evaluation

Using multiple lines of evidence to evaluate model performance is critically important to reduce internal inconsistencies and improve model fidelity (Finger *et al*., 2011; Schaefli and Huss, 2011; Pellicciotti *et al*., 2012; van Tiel *et al*., 2020b). The model was evaluated using four sets of observations relating to snow accumulation and ablation, glacier melt, and streamflow. Snow accumulation and glacier melt across the glacier area were assessed using point mass balance measurements by the Geological Survey of Canada for the period 2005-2018 (Figure 6.2a-b). 240-point measurements for winter and 163 for summer mass balance were made using drilled, surveyed stakes between elevation 2136 and 2760 m. a.s.l. For the years 1989-1995, mass balance per elevation band was used to evaluate model performance. The simulated summer and winter mass balance were extracted for the same date as the recorded measurements, generally corresponding to late April or early May for winter mass balance and late September for summer mass balance surveys.

Linear regression was used to calculate the annual winter balance elevation gradient of the measured mass balance points, and a variability envelope is calculated as the 95% interval (2 standard deviations) around the calculated linear regression values (Figure 6.2a). These variability envelopes are used to assess if the fluctuations from the background elevation gradients are similar between the measured and modelled point mass balance. 77% of the modelled winter mass balances fall within this envelope. In most years, the modelled winter mass balance agrees with the measurements, but for some years, such as 1989, 1994 and 2009, there is minimal agreement between measured and modelled winter mass balance. The calculated and modelled winter mass balance lapse rates were compared for the 19 available years between 1995 and 2017. The average lapse rates are similar, with the calculated lapse rate of 0.14 m.w.e. per 100 m elevation being similar to the modelled lapse rate of 0.13 m.w.e., with an RMSE of 0.04 m.w.e. per 100 m elevation gain and a correlation coefficient of 0.21. The model has a slight tendency to underestimate the measured gradient with a mean bias of -0.07 m.w.e. The largest difference between modelled and measured

winter mass balance occurred at ~2600 m.a.s.l. and was likely due to the influence of avalanching at this elevation. Mass balance observations deliberately avoid avalanche-prone areas and so do not reflect this source of variability, even though avalanche deposits have been noted at this elevation in field observations and historical reports (Young, 1977). Additionally, evaluation of snow accumulation at the highest elevation HRU is restricted by the lack of measurements above the altitude of 2760 m. Considering the variability associated with point winter balance point measurements, which at Peyto Glacier have been reported to be up to vary by up 0.2 m.w.e. (Young, 1977; Demuth and Keller, 2006) at the metre scale due to the uneven surface of the glacier ice, the modelled winter balance is considered to have performed satisfactorily.

For summer mass balance, 92% of the modelled values for the 2007-2013 period, or 97 of the 108 values, fit within the variability envelope of the measured stake balances (Figure 6.2b). Despite most of the modelled values fitting within the range of measured values, the elevation lapse rate for summer mass balance was consistently larger than the measured one, with a mean modelled lapse rate of -0.88 m.w.e. per 100 m elevation gain being larger than the mean modelled rate of -0.54 m.w.e., with an RMSE of 0.39 m.w.e., mean bias of 0.63 m.w.e. and a correlation coefficient of -0.04. The lapse rate standard deviation is larger for the measurements (0.58 m.w.e.) than for the modelled values (0.38 m.w.e.). This suggests that elevation has a greater role in controlling melt in the model than is observed – this could be due to deviations from reality in model parameters such as albedo or lapse rate settings for precipitation and/or temperature and/or other errors.

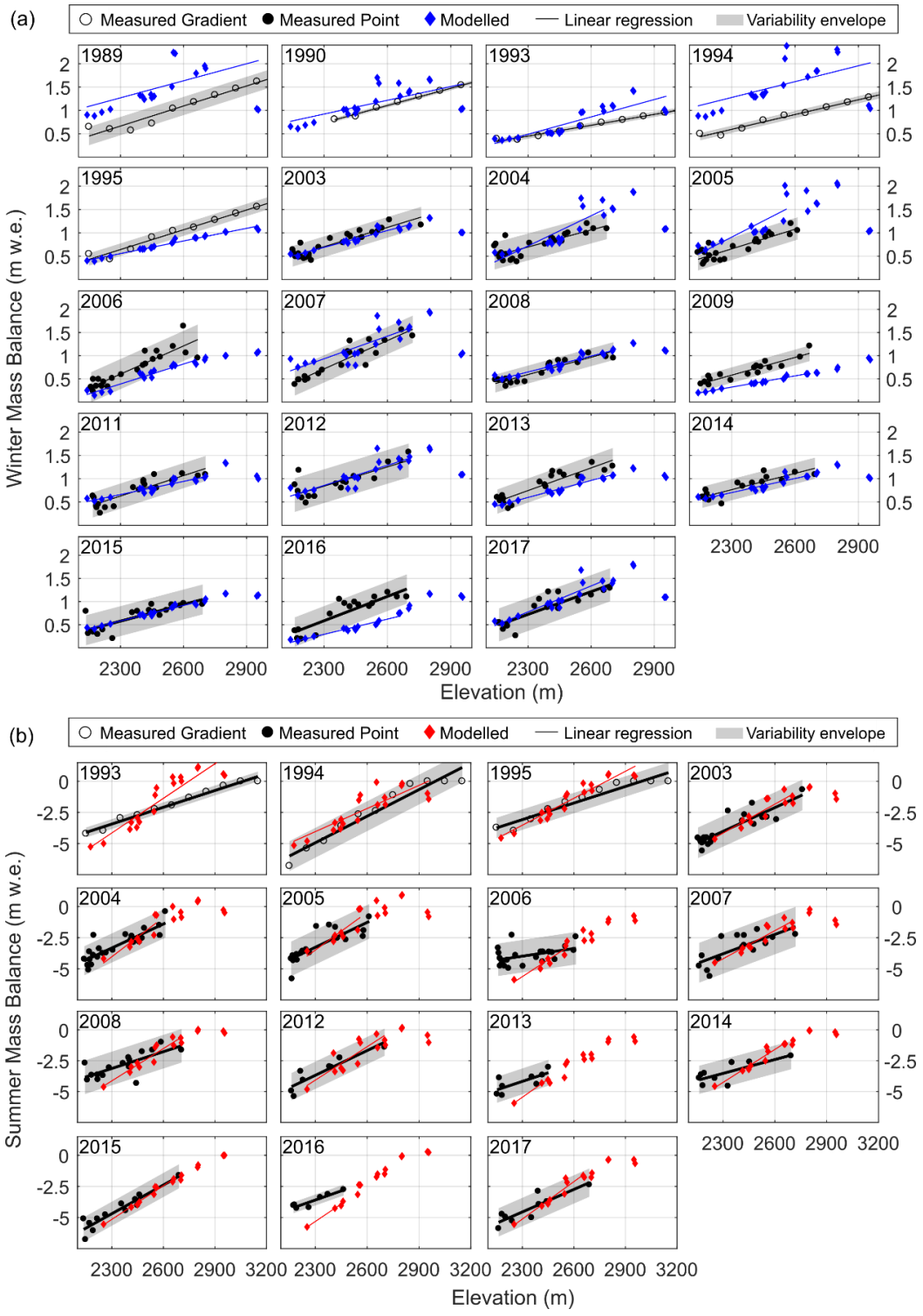

Figure 6.2. Annual measured and modelled point (a) winter and (b) summer mass balance per elevation. The coloured diamonds represent modelled mass balance at individual HRUs, with blue being winter mass balance and red being summer mass balance. The black, filled dots are individual stake measurements, and the empty circles are the measured mass balance gradient.

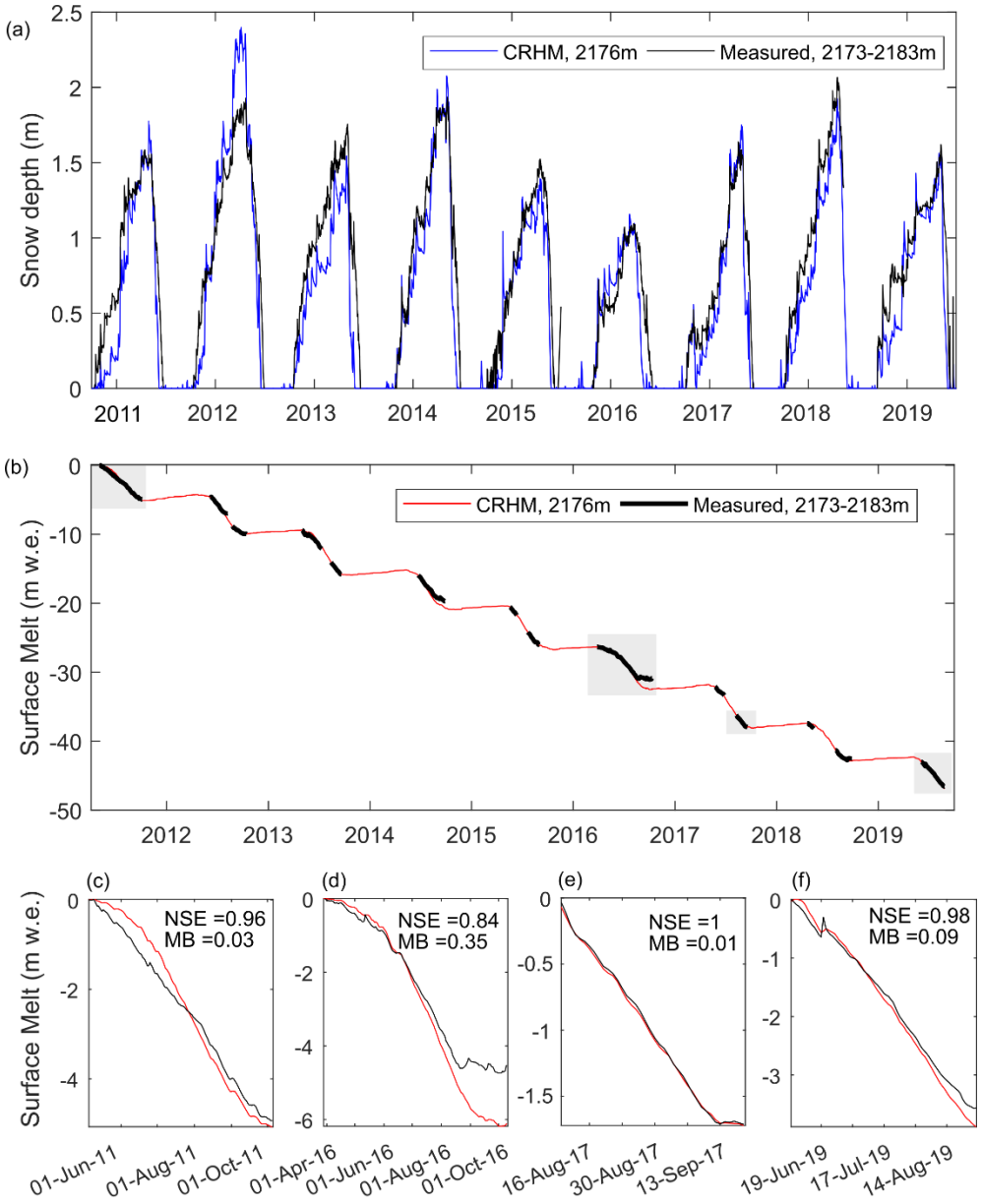

Figure 6.3. Comparison of CRHM model and glacier toe HRU and measurement from the on-ice AWS; (a) snow depth for the 2011-2019 period and (b) cumulative surface melt relative to the start of the observations on May 5th, 2011, with the shaded grey areas shown in detail in (c)-(f) with Nash-Sutcliffe efficiency (NSE) and Mean Bias (MB), also relative to the observation for each period.

To further assess model performance, modelled snow accumulation and depletion for the glacier toe HRU were compared with snow depth measured at the on-ice AWS for the 2011-2020 winters, with a Nash-Sutcliffe efficiency (NSE) ranging between 0.49 and 0.84 and a coefficient of determination (R^2) between 0.62 and 0.98 (Figure 6.3a). For the nine periods with surface melt measurements from the on-ice AWS, which cover a total of 981 days, the correlation coefficient of observations with

modelled ice melt at glacier toe is 0.99, with a mean bias of 0.09 m.w.e., a root mean square error (RMSE) of 0.43 m.w.e. and an NSE of 0.90 (Figure 6.3b-f). Overall, the set of evaluations of modelled snow accumulation and snow and ice ablation shows that the model can appropriately represent snow and ice dynamics on the glacier.

Modelled streamflow at the basin outlet was compared to the measured streamflow for the 2013-2020 melt seasons (Figure 6.4). Streamflow measurement was only available during the snow-free season and did not allow a model evaluation for the earliest and latest seasonal low flow or melt events. For the eight melt seasons, the simulations compared to observations with a NSE of 0.69, with annual results ranging from 0.41 to 0.87. RMSE for the entire period was 0.98 $m^3 s^{-1}$, ranging between 0.66 and 1.2 $m^3 s^{-1}$ and the mean bias ranged from -0.24 to 0.35. The Kling-Gupta efficiency (KGE, Gupta *et al.*, 2009) ranged between 0.09 to 0.45 for individual years and averaged 0.15 for the entire period. When considering the three components of the KGE, the largest values are found for the bias (β) and relativity term (α), with lower values corresponding to the correlation term *r*. Considering that high NSE values are expected for a basin with a strong seasonal cycle (Schaefli *et al.*, 2005; Schaefli and Gupta, 2007; Seibert *et al.*, 2018), the NSE performance of the CRHM model was compared with that of a simple benchmark model calculated as the mean observed discharge for each calendar day (DOY average benchmark model, as discussed in Garrick *et al.*, 1978; WMO, 1986; Schaefli and Gupta, 2007). The DOY average benchmark model performed more poorly than the CRHM model for 7 out of the 8 years available, with its average NSE lower than that of the CRHM model by 0.14, providing further evidence that CRHM can capture both the seasonality of the flow regime and the smaller-time scale fluctuations. Modelled groundwater flow is also shown.

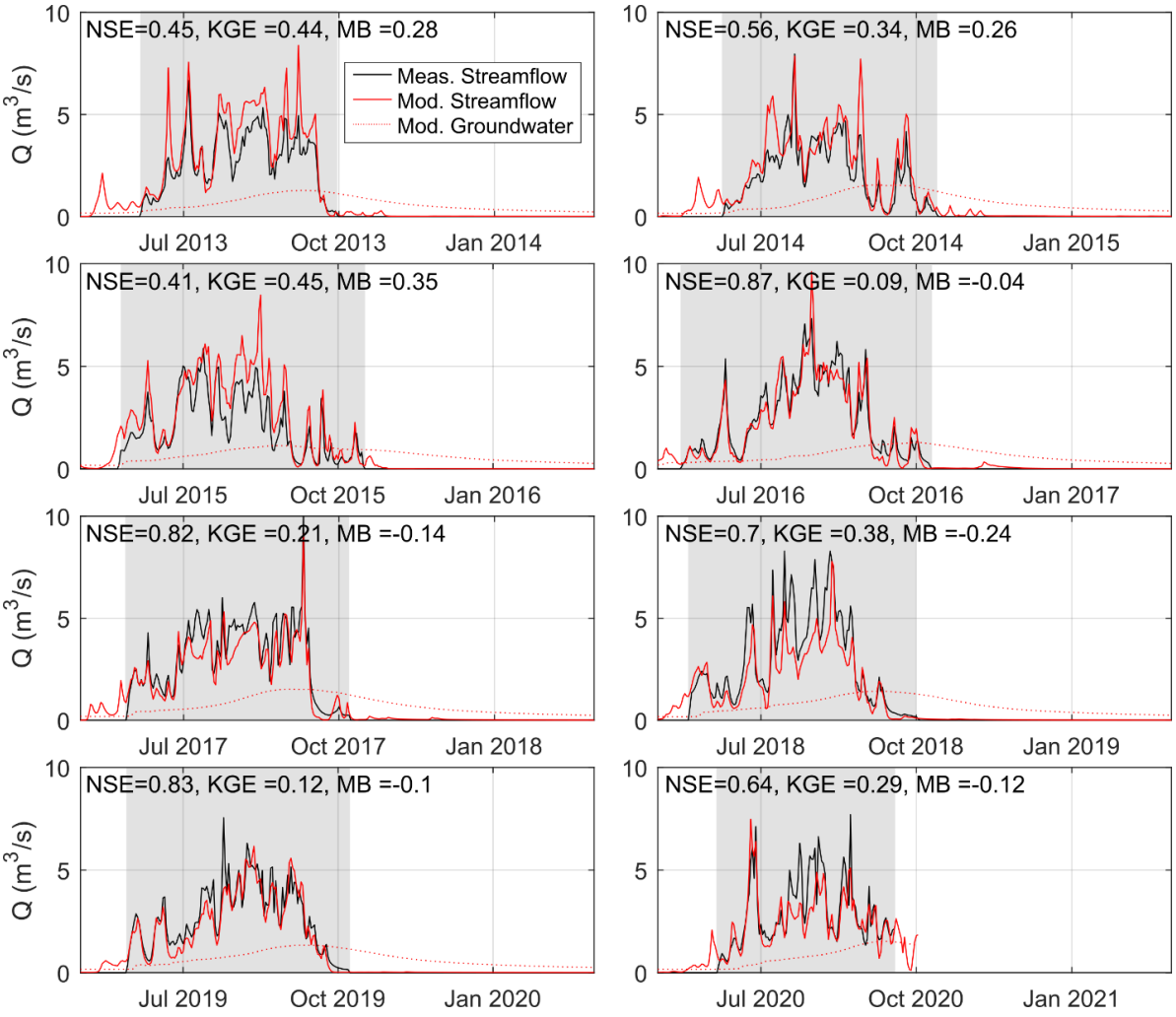

Figure 6.4. Modelled and measured streamflow and simulated groundwater flow for the years 2013-2020. The Nash-Sutcliffe efficiency (NSE), Kling-Gupta efficiency (KG) and the mean bias (MB) value refer to the agreement between measured and modelled streamflow for the given melt season. The gray overlay indicates the period with streamflow measurements.

There is no available dataset to evaluate the melt under-debris parameterization in the PGRB and therefore a comparison between the modelled melt for varied debris thickness is presented and compared with simulated clean ice melt for various albedo, without being evaluated against measured melt (Figure 6.5). Over 5 days of melt, melt under 5 cm of debris was reduced by approximately 45% compared to clean ice. This melt reduction increases to 65, 79, and 83% for debris thickness 10, 20 and 23 cm. For debris thickness 30, 40 and 50 cm and more, melt was reduced by 85% and higher. The presence of debris also shifted the timing of melt and strongly reducing the daily cycle of melt. For clean ice, high melt rates occurred around 11:00-14:00, and near zero or zero melt occurred overnight. For thin debris (0.23 m and less), the daily cycle was still clearly visible in the

surface melt rates, with similar timing of peak melt as with clean ice and decreasing melt rates overnight. However, melt under debris occurred overnight as well, as the energy available for melt has to propagate through the layer of debris before reaching the buried ice. For debris thicker 0.3 m and thicker, the daily cycle of melt was strongly subdued, and peak melt occurred between 20:00 and 3:00 instead. This is in agreement with the physical understanding of the influence of debris thickness on sub-debris melt. Therefore, even if there are no in-situ data to properly evaluate this simulation, and given the low amount of debris-covered ice in the Peyto Glacier Research basin where this module is used, the melt under debris module in the CRHM glacio-hydrological module library is deemed to be reasonable.

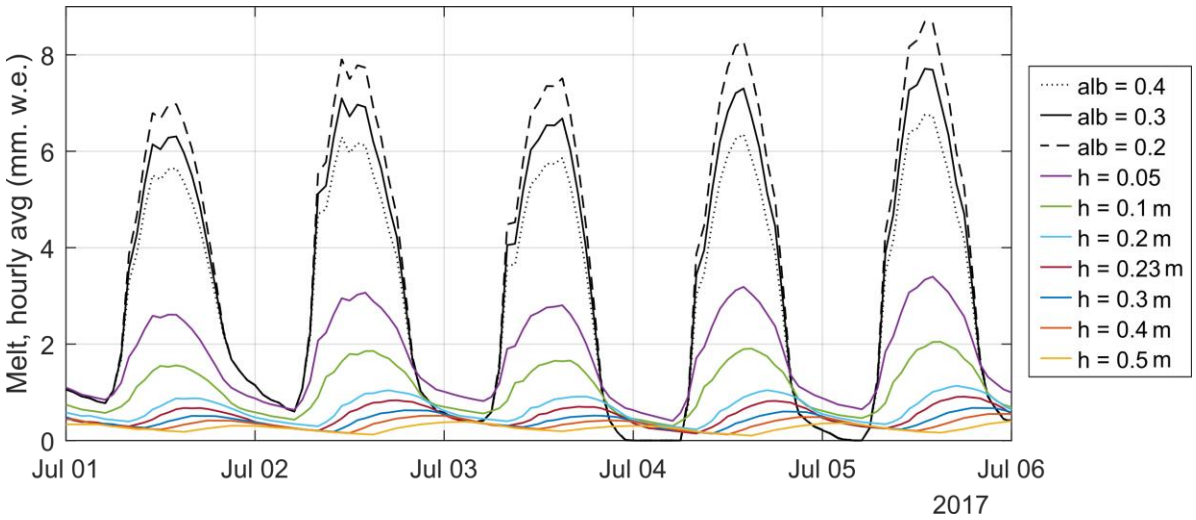

Figure 6.5. Surface melt with varying albedo (alb) and overlying debris thickness (h) simulated for the toe of the Peyto Glacier for five days in July 2017

6.4.2. Basin hydrometeorological variability

6.4.2.1. *Annual conditions and trends*

The basin is in a cold climate, with an annual mean air temperature staying below 0˚C for the whole study period, ranging between -5.0 and -2.3˚C (Figure 6.6a). Only the lowest elevations in the basin, below 2200 m.a.s.l., have an annual mean air temperature above zero, varying from -1.67 to 1.00˚C. Summer temperature in the basin reached up to 23.4˚C during the study interval. The precipitation regime in the basin is dominated by snowfall, which contributes an average of 85% to the total precipitation (Figure 6.6b). This ratio increases to 89% snowfall in the highest elevation of the basin (above 2700 m.a.s.l.) and decreases to 68% in the lowest elevations (below 2200 m.a.s.l.).

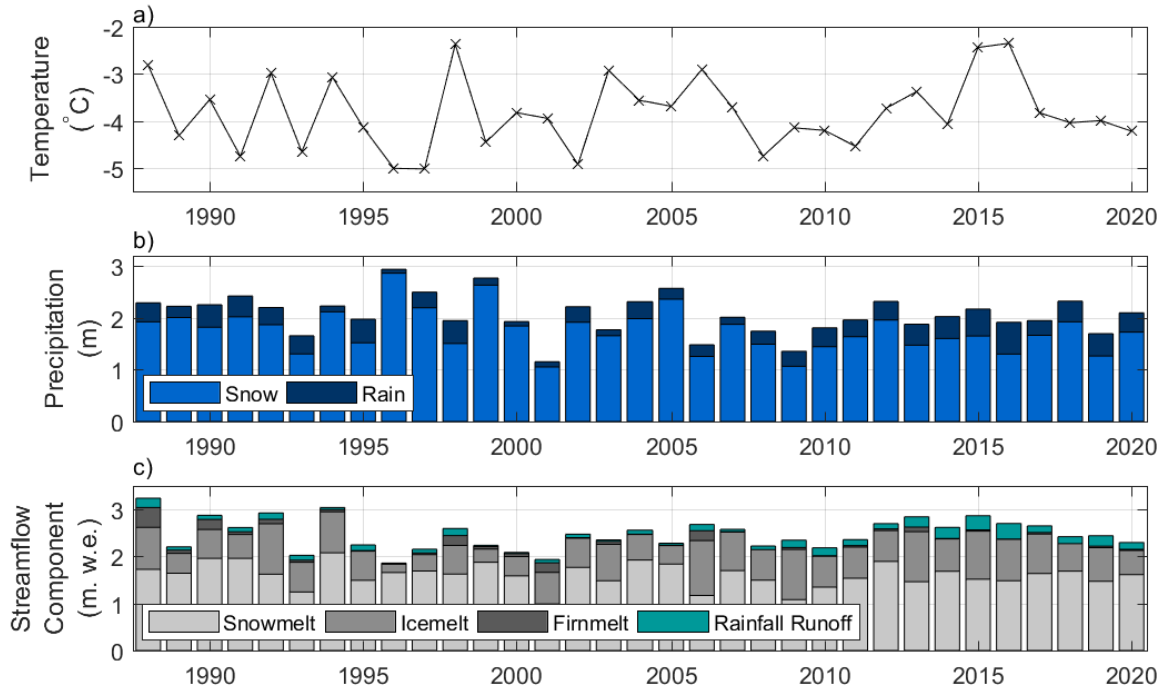

Figure 6.6. Basin area-weighted annual air temperature (a), precipitation (b) and streamflow composition (c), with the total column being annual streamflow in the PGRB for the 1988-2020 period.

As shown in Figure 6.6c, annual area-weighted streamflow expressed as water equivalent depth over the PGRB, also known as specific discharge, varied from 3240 mm yr^{-1}, in 1988, to 1870 mm yr^{-1}, in 1996. On average, snowmelt, both on and off the glacier, contributed the largest volume and fractional contribution, 44-89%, to annual streamflow. Ice melt from the glacier and ice-cored moraine contributed 10-45%. The debris-covered areas of the glacier contributed 2.3 % of the total ice melt, and the ice-cored moraine contributed 3.6 %. Firn melt and rainfall-runoff each contributed 13% or less to annual streamflow, with firn melt ranging from 0-13% and rainfall-runoff and infiltration contributing 1-12% of annual streamflow. Rainfall-runoff represents only rainfall on snow-free surfaces (glacier or bare-ground) as rain-on-snow contributes to the snowpack dynamics including refreezing, melting and discharge from the pack depending on the thermodynamic state and porosity of the snowpack. The modelled streamflow components were calculated before the routing routine was applied and therefore, do not reflect streamflow mixing, but runoff sources in the basin. The snow, firn and ice melt originating from the glacier area, grouped as “glacier runoff”, provide a disproportionate amount of streamflow, as the glacier covers only 56% of the basin area but the glacier runoff provides on average 71% of annual streamflow. Only two out of the 33 years

analyzed showed a positive mass balance. Glacier wastage varied from 6 to 77% of basin yield, with an average of 53%. Glacier wastage was calculated following Comeau *et al.* (2009) and defined as the volume of ice and firn melt exceeding the annual volume of snow accumulation on the glacier and causing an annual net loss of glacier volume. Basin yield was calculated as the combined streamflow at the basin outlet and groundwater discharge leaving the basin. The detailed calculate of wastage and shown in Appendix C.1.

Figure 6.7 shows significant hydrometeorological trends ($p < 0.05$); at the basin scale, summer temperature increases from 3.50 ° C to 4.55 ° C over 1988-2020. Over the same time period, winter snowfall decreased by 286 mm, and summer and annual rainfall increased by 179.6 and 152.1 mm respectively. Despite the trends in precipitation phase favouring rainfall, no trends were found in annual air temperature or annual precipitation depth over 1988-2020.

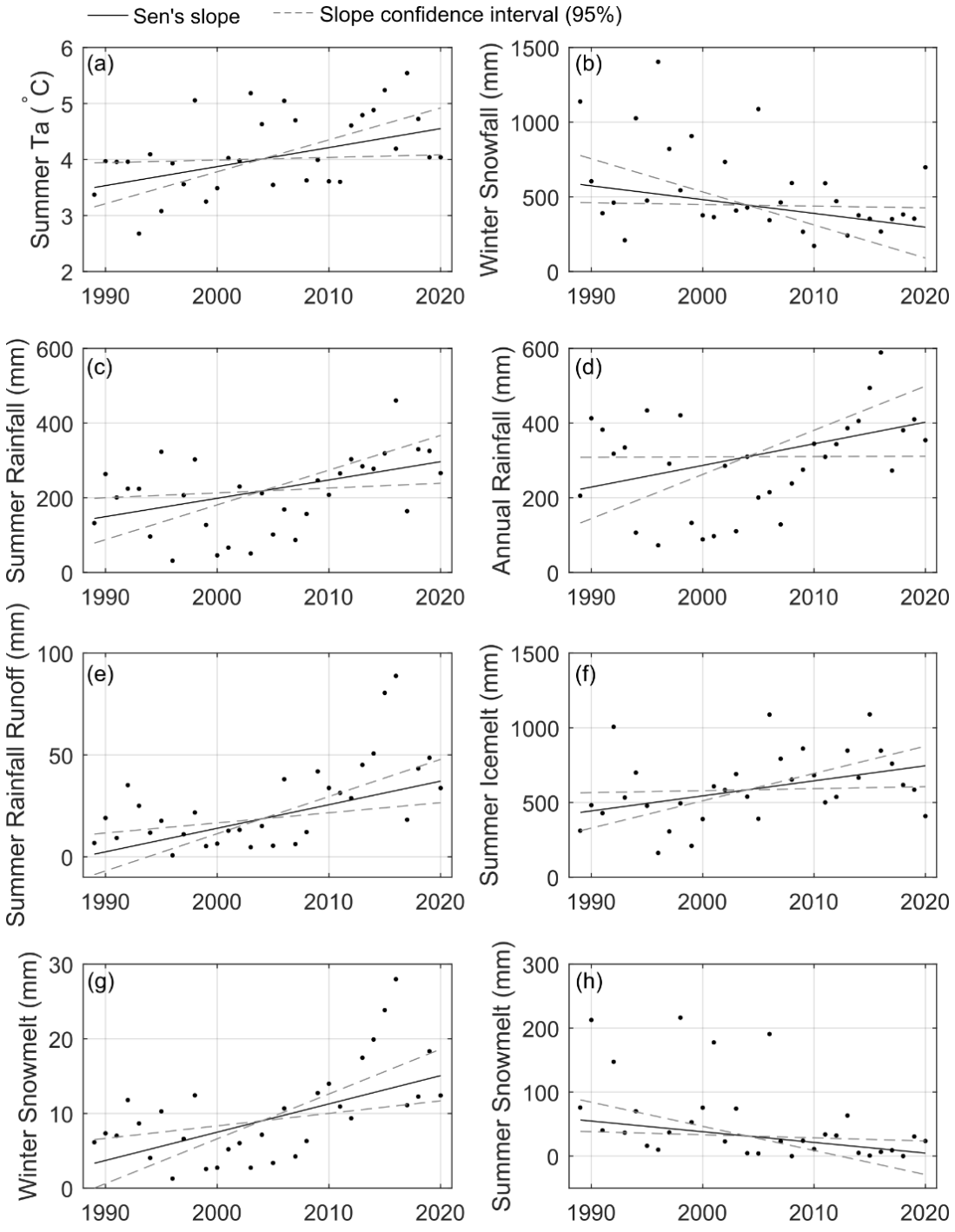

Figure 6.7. Significant trends ($p < 0.05$) for the annual and seasonal basin-averaged hydrometeorological conditions and modelled flow components in the PGRB, calculated for the years 1988-2020. Significant trends were found for summer air temperature, winter snowfall, summer rainfall, annual rainfall, summer rainfall-runoff, summer icemelt, winter snowmelt and summer snowmelt.

6.4.2.2. *Seasonal meteorological conditions and streamflow correlation*

Further analysis determined how forcing meteorological conditions in the basin affected streamflow variability by examining the associations between annual streamflow volume and annual and seasonal meteorological variables (temperature, rainfall, snowfall). Annual, spring and summer temperature, summer rainfall and winter snowfall were the only forcing meteorological variables significantly correlated to annual streamflow (Table 6.3, Figure 6.8). Winter snowfall was negatively correlated with streamflow, the opposite of what would be expected for a snowmelt-dominated non-glacierized basin. Icemelt, firnmelt and rainfall-runoff were the only runoff components significantly correlated to annual streamflow (Table 6.4, Figure 6.8). In addition, the timing of the glacier exposure was strongly negatively correlated with streamflow. The timing of ice exposure was quantified as by the day of year (DOY) by which the winter snowpack has fully melted in the mid- and upper glacier area of the basin, with HRU 3 selected as representative. Icemelt and timing of ice exposure were most strongly correlated to the annual streamflow, followed by the rainfall-runoff and firnmelt. Even though snowmelt provides the greatest fraction of annual streamflow, no significant correlation was found between snowmelt and streamflow. This, combined with the highly significant correlation of streamflow to summer meteorology, suggests that summer hydrometeorological and glaciological conditions play an important role in governing the inter-annual variability of streamflow. This is consistent with results from Europe by Farinotti *et al.* (2012) who analyzed nine alpine glacierized basins in the Alps and found that annual streamflow and precipitation were not significantly correlated for basins with glacierized areas over 40%, but that summer air temperature and annual streamflow were well correlated for basins with a glacierized area above 35%. In the highly glacierized Nordic Creek basin, located 85 km west of the PGRB in the Selkirk Mountains of British Columbia, glacier wastage contributions to streamflow were also found to be highly variable year-to-year (Moore *et al.*, 2020).

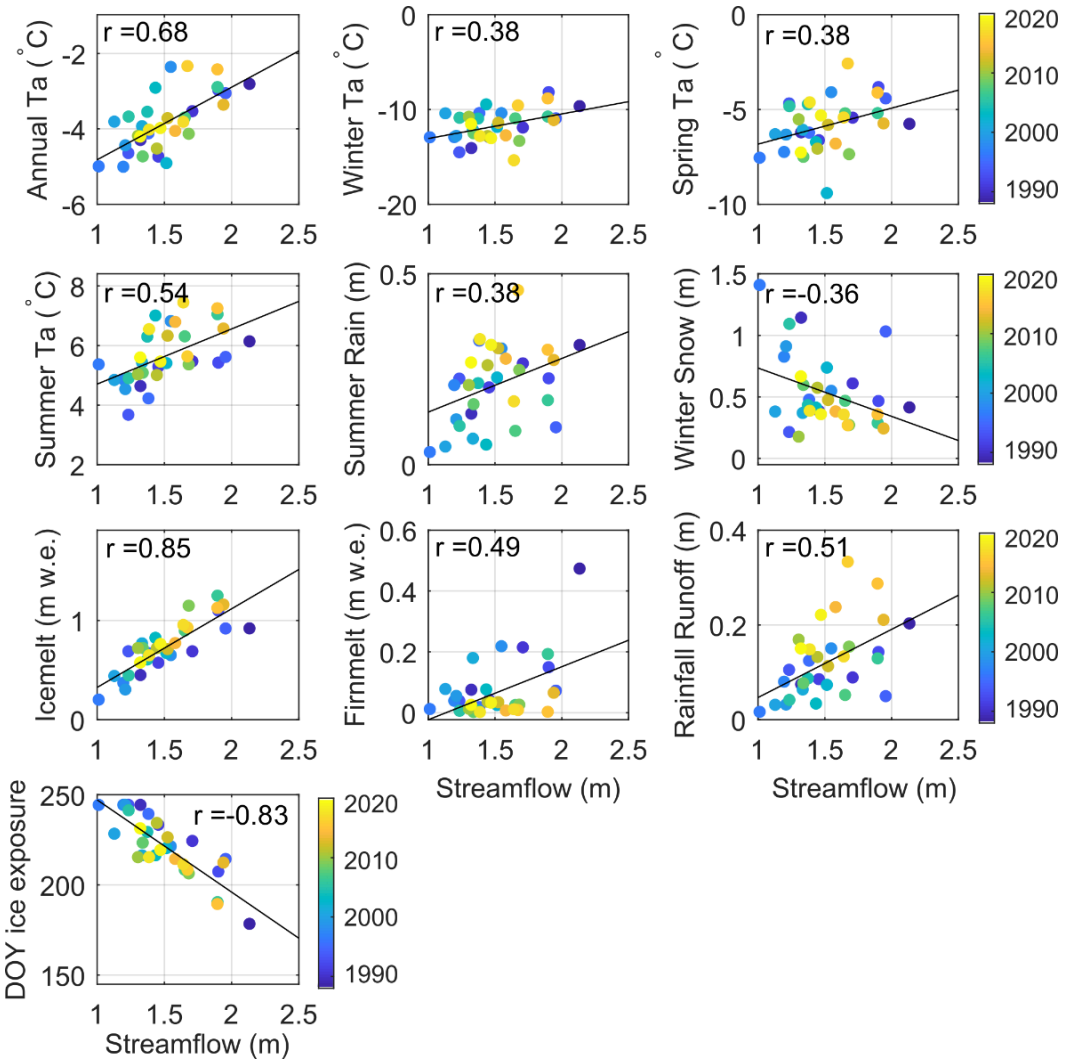

Figure 6.8. Scatterplot for significant associations (shown in bold in Table 2 and 3) between streamflow and meteorological conditions and streamflow components. The colour of the point refers to the year as shown by the colour bar. The Spearman rank correlation coefficient r is shown in each panel.

The influence of winter conditions on streamflow variability was also noticeable through the significant negative correlation of streamflow with winter snowfall and timing of ice exposure rather than snowmelt or peak snow water equivalent. It should be noted that not all snowfall will form snowmelt in high snowfall years and so snowfall is more variable than snowmelt. The negative correlation between winter snowfall and streamflow volume is due to the control that snowfall exerts on the timing of summer ice exposure, as confirmed by the strong negative correlation between timing of ice exposure and streamflow. In low snowfall years, glacier ice is exposed earlier, and due to its lower albedo, the surface melt is enhanced, leading to higher annual streamflow. This

correlation is possible when the additional melt from exposed glacier ice in low snowfall years exceeds the reduction in snowmelt from the glacier and non-glacier fractions of the basin.

Table 6.3. Spearman rank correlation coefficient (r) and significance (p) for streamflow and meteorological associations. Significant associations (p < 0.05) are in bold.

Variable		Annual Streamflow	Fall Streamflow	Winter Streamflow	Spring Streamflow	Summer Streamflow
Ta	r	0.68	0.21	0.43	0.38	0.54
	α	<0.001	0.265	0.013	0.030	0.001
Rainfall	r	0.33	-0.08	0.09	0.13	0.38
	α	0.057	0.677	0.628	0.458	0.03
Snowfall	r	-0.30	-0.21	-0.36	0.06	-0.13
	α	0.085	0.235	0.040	0.718	0.450

Table 6.4. Spearman rank correlation coefficient (r) and significance (p) for annual streamflow and annual snowmelt, ice melt, firn melt, rainfall-runoff, peak SWE, the day of year of the glacier ice exposure at elevation 2701 m. a.s.l. (HRU 3) and the end of summer snow in the previous year associations. Significant associations (p < 0.05) are in bold.

	Annual streamflow	
	r	p
Snowmelt	-0.03	0.860
Ice melt	0.85	<0.001
Firn melt	0.49	0.003
Rainfall Runoff	0.51	0.003
Peak SWE	-0.05	0.779
DOY of ice exposure	-0.83	<0.001
Previous year unmelted snow	0.05	0.784

In 5 of the 33 years analyzed, the snow outside of the glacier area did not completely melt throughout the summer and carried over to the following year. On the glacier, this leftover snow turned to firn, and influenced surface melt in the following summer by having a different albedo and density than either snow or ice. However, the influence of this leftover snow on the following year's streamflow appeared to be minimal in the PGRB as no significant correlation was found between the snow remaining in on and off the glacier basin just before the transition to firn and the following years' streamflow (Table 6.4).

6.4.3. Contrasting high and low streamflow years

High flow years were on average 1.43 ˚C warmer than the years with low flow, with the largest difference in January, March and April (Figure 6.9a). The HF years received 143 mm more rainfall and 295 mm less snowfall than the LF years, (Figure 6.9b-c). The differences in precipitation and temperature are reflected in snowpack ablation (Figure 6.9d). Starting in December, HF and LF snowpack regimes diverge. The HF snowpacks reached a peak SWE of 957 mm in mid-April, whilst the LF snowpacks continued to accumulate until early May when they reached a peak SWE of 1330 mm. Both HF and LF snowpacks follow similar ablation patterns over the melt season and by September 1st, the remaining snowpack starts to transform into firn. In LF years, the remaining snowpack was 213 mm SWE at this transition date, whilst in HF years no snow remained. Using the non-parametric Wilcoxon signed rank test (Gibbons and Chakraborti, 2010), the differences in monthly air temperature, snowfall and SWE (but not monthly rainfall) between HF and LF years were significant at the $p = 0.05$ level.

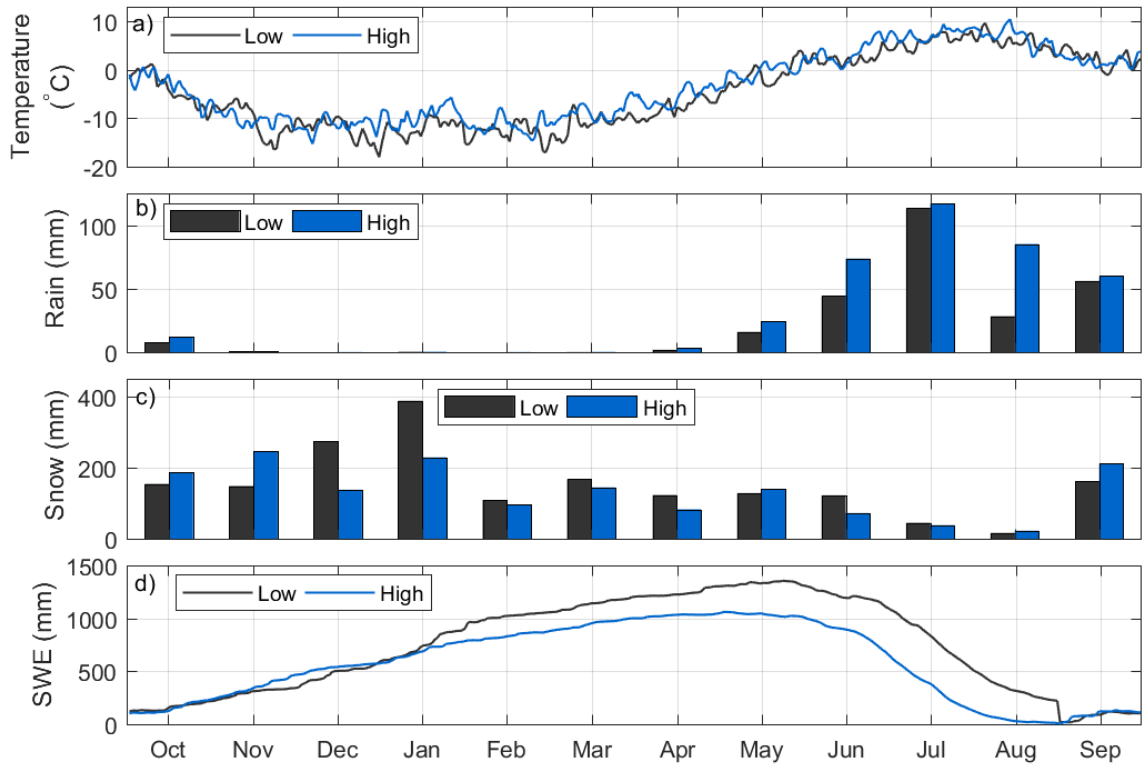

Figure 6.9. Comparison of daily temperature (a), monthly rainfall (b), monthly snowfall (c) and daily snow water equivalent for high streamflow years (light blue) and low streamflow years (dark blue).

Differences in the sources of streamflow were also analyzed between LF and HF years (Figure 6.10). Annual streamflow volumes were 41% greater in HF years than LF years. Snowmelt provided by far the greatest source of streamflow, but its contribution differed by only 1% between LF and HF years and so did not substantially contribute to interannual variability in streamflow volumes. Differences in snow ablation regime between HF and LF years were apparent; snow ablation started 10 days earlier in HF than in LF years, with rapid melt and depletion of snow occurring 15 days earlier, in mid to late summer. The earlier snow ablation in HF years exposed glacier ice earlier and led to a greater ice exposure by late summer, increasing basin-averaged, late summer ice melt rates from 9 mm d^{-1} in LF to 17 mm d^{-1} in HF years (Figure 6.8b). As a result, the volume of ice melt was 103% greater in HF than in LF years. Similarly, the firn melt contribution to streamflow was 162% greater in HF compared to LF years, with nearly double the peak melt rate (2.3 compared to 1.4 mm d^{-1}) and an almost one-month earlier start to firn melt. Consistent with greater rainfall, rainfall-runoff was 145% higher in HF years. Even though firn melt and rainfall-runoff were greater in HF years by a larger fraction than other streamflow sources, their enhancement of streamflow was modest as together they contributed less than 10% of streamflow volume. In contrast, icemelt had smaller fractional increases for HF years, but a much stronger impact on differences in streamflow volumes and timing.

LF years were colder, with higher snowfall and lower rainfall. The deeper LF year snowpack combined with a delayed onset to melt due to colder spring temperatures resulted in snowpacks persisting later in the summer in LF than in HF years. This caused less glacier ice to be exposed and ice exposure to occur later in the melt season, such that its melt contributed less to streamflow. Additionally, LF years received lower rainfall. Initial meteorological forcings, differing snow accumulation and depletion patterns, and resulting rates and durations of rainfall-runoff, snowmelt, icemelt and firnmelt interacted to cause large streamflow volumetric differences between HF and LF years. This result is consistent with the findings of Pradhananga and Pomeroy (2022) who found that with warming conditions from the 1960s to current times, glacierized basin streamflow in the Canadian Rockies was increasing despite declining precipitation and snowmelt, the difference being sustained by greater ice melt.

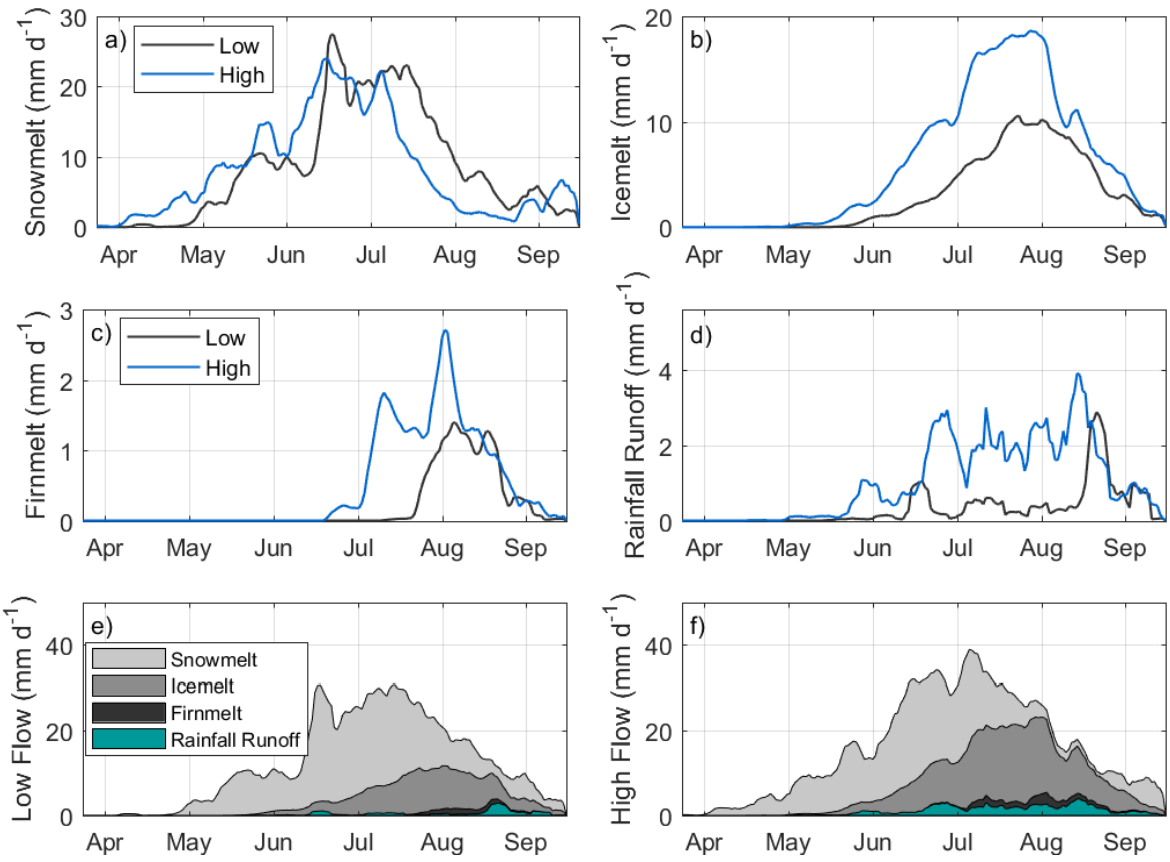

Figure 6.10. Comparison of mean daily basin-averaged streamflow components for high and low streamflow years, with high flow years being the average of 1992, 1994, 2006, 2013, 2015 and 2016 and low streamflow is the average of 1995, 1996, 1997, 2000, 2003, 2008.

6.5. Discussion

6.5.1. Measurements, process representation and parameter uncertainty

The comprehensive processes in the physically based modelling approach used here were included to reduce model uncertainty; these processes were represented with substantial spatial discretization, and process identification and rigorous parametrization were based on extensive fieldwork. In the attempt to comprehensively represent the physical system in the PGRB, it is expected that uncertainty was reduced by selecting appropriate methods and models instead of through more traditional, and sometimes complex, calibration procedures (Kirchner, 2006; Clark *et al.*, 2016). Despite this, model prediction errors can still accrue through inaccuracies in measurements, process-representations and parameters (Beven, 2016). The main elements in the modelling procedure relating to these sources of uncertainty are discussed below.

6.5.2. Limitations of the observational data

A large amount of input data is needed to parametrize and evaluate model simulations but obtaining high-quality observational data from remote glacierized mountain basins is an extraordinary challenge. In the PGRB, the long-term meteorological measurements from the network of on-ice stations are invaluable to investigate the temperature patterns across the basin, but the lack of distributed precipitation observations increases uncertainty. Because of this lack of information on the spatial distribution of precipitation, the end-of-winter SWE elevation gradient is used as a proxy for the precipitation elevation gradient. As the SWE elevation gradient takes into account snow redistribution by wind and gravity, mid-winter melt and sublimation, this approach causes a source of error in the precipitation gradient. Further uncertainty is caused by the use of reanalysis data for precipitation instead of in-situ data. Gridded precipitation datasets are known to be highly uncertain in mountain regions, particularly at high elevations (Lundquist *et al.*, 2015; Henn *et al.*, 2018). Even though the ERA-Interim precipitation was bias-corrected to in-situ observations, ensuring reasonable monthly cumulative volume, the short rainfall events occurring in spring, summer and fall months might have not been adequately captured by the gridded precipitation, resulting in further uncertainty in the model forcing data.

Streamflow information was also limited by the persistence of snowdrifts in the channel, preventing the evaluation of model performance for the early-season and late-season streamflow processes. The uncertainty linked with measuring streamflow in a dynamic, proglacial landscape also increases the uncertainty in developing a robust rating curve, which was mitigated by obtaining several salt-

dilution measurements over three melt seasons and a careful assessment of the measurement quality. The simulated glacier winter and summer mass-balances at the higher elevation in the basin are also not well constrained, as there is a lack of measurements at these altitudes due to the difficult access through avalanche and crevassed terrain.

6.5.3. Limitations in the CRHM process representation

The precipitation gradient used is also fixed in the model, but there is evidence that mountain precipitation gradients vary seasonally and annually based on the processes controlling the precipitation events (Houze, 2012; Pepin *et al.*, 2022). The lack of temporally variable precipitation gradient could explain the variable performance of the simulated end-of-winter snow elevation gradient, with some years failing to capture the measured snow accumulation gradient. However, the lack of information on the variability of the precipitation gradient prevented varying this gradient in the modelling framework.

The lack of soil moisture and groundwater observations in the basin limit the evaluation of surface water-groundwater interaction and prevents a thorough assessment of the possibility of a "leaky catchment" (Fan, 2019). Groundwater contributions and surface water-groundwater interactions could contribute to the bias in simulated streamflow volumes. The fate of groundwater in alpine basins in the Canadian Rockies has been suggested to be mostly limited to local, shallow aquifers in coarse deposits connecting first- and second-order streams (Hayashi, 2020), but some studies have suggested that glacier basin groundwater recharges regional and mountain block aquifers (Castellazzi *et al.*, 2019; Campbell and Ryan, 2021). Considering both possibilities, the water entering the groundwater system in the PGRB simulations could contribute to unmeasured streamflow just downstream of the basin outlet and contribute to the Peyto Lake water budget or form regional flow networks resurfacing further downstream.

6.5.4. Parameter uncertainty

The parameters with the higher uncertainty in the application of the PGRB are the ones associated with non-existent or sparse observations in the basin, preventing the evaluation of these individual processes. This is particularly the case for the surface water-groundwater interactions and the subsurface routing. The surface water-groundwater interactions were parametrized to represent a physical understanding of alpine groundwater systems based on field knowledge from the PGRB and in-depth studies from similar landscapes in the Canadian Rockies, but the lack of direct observations of soil moisture and groundwater storage within PGRB precludes an in-depth evaluation of this

model component. Therefore, the uncertainty associated with these parameters was tested. The storage capacity and routing delays of the different land covers, shown in Table 2, were varied and the resulting change in simulated streamflow was assessed in a scenario-based parameter uncertainty assessment (Table 6.5). Doubling the soil storage decreased streamflow volume by less than 5% and decreasing soil storage by half increased streamflow by 8.8%. However, either doubling or reducing by half the soil storage volume also influenced the groundwater discharge from the basin, changing both the timing and the total volume of groundwater flow by up to 17% compared to the main simulation. When the soil storage increased whilst the groundwater storage decreased, or the converse, the change in groundwater flow timing and volume was limited to below 4%. However, when the total basin subsurface storage either increased or decreased, groundwater flow changed by up to 30% compared with the baseline simulation. Given the sensitivity of basin groundwater to the subsurface storage parametrization and sparse high elevation groundwater observations, further investigations should assess the transferability of storage parameters for groundwater routing in high alpine basins.

Table 6.5. Scenario-based uncertainty assessment for the soil and groundwater storage parameters

Variable	Soil x2, GW x0.5	Soil x0.5, GW x2	Soil x2, GW x2	Soil x0.5, GW x0.5	Soil x0.5	Soil x2
Streamflow Change (%)	-4.5	8.8	-4.5	8.8	8.8	-4.5
Groundwater flow change (%)	-1	3.6	31	-31	-17	-12

6.5.5. PGRB trends and flow composition in context

The absence of temporal trends in annual air temperature and precipitation in this study contrast with most findings in the Canadian Rockies (Harder *et al.*, 2015). DeBeer *et al.* (2016) found a 2˚C increase in air temperature and a 14% precipitation increase in this region for the period 1950-2015. Pradhananga and Pomeroy (2022a) contrasted the hydrology of the PGRB between the 1960s and the 2010s and found an increase of 260 mm (16%) in streamflow with a 226 mm (16%) decrease in precipitation. The difference in trends is most likely due to the different periods analyzed and the methodologies used. However, for 35 basins in the Columbia River headwaters, located southwest

of the PGRB in the adjacent Selkirk and Monashee mountains, Moore *et al*. (2020) did not find significant trends at $p<0.05$ in August air temperature for the 1977-2017 period, but found a significant decreasing trend at $p<0.05$ in August precipitation, which is similar to the trends found for summer rainfall and summer temperature in this study. For streamflow components, significant increasing trends were found for summer rainfall-runoff, summer ice melt, and winter snowmelt, and a decreasing trend was found for summer snowmelt, but no trends were found for seasonal or annual streamflow. This is consistent with Naz *et al*. (2014), who did not find significant trends in streamflow for the years 1981-2007 for the upper Bow River at Lake Louise, a 422 km^2 basin adjacent to the PGRB. These results contrast with findings by Moore *et al* (2020) and Stahl and Moore (2006), who found decreasing trends in August streamflow for glacierized basins in mountain ranges west of the Continental Divide. The difference in these trends might be linked to the different snow accumulation and weather patterns occurring on either side of the Continental Divide; conditions are typically colder and drier on the eastern slopes.

Even if some trends were observed in the summer air temperature, winter snowfall, summer rainfall, and in certain streamflow components in the PGRB, no trends was noticeable in the net annual streamflow volumes. This suggests that, for the period studied, there might be compensating effects amongst the hydrological processes and such that the net flow components generating basin streamflow have been relatively insensitive to environmental change. Harder *et al.* (2015) found evidence for such cold regions compensatory behaviour in the unglacierized Marmot Creek Research Basin in the Canadian Rockies which dampened its streamflow response to changing climate and land cover. Natural climate variability might also have concealed the streamflow trend, as discussed by Fatichi *et al.* (2014), who found that natural climate variability obscured climate-driven changes in streamflow by up ±20% in the Alps.

The flow composition fractions calculated in this study, with snowmelt contributing 44-89% to annual streamflow, ice melt contributing 10-45% and firn melt and rainfall-runoff contributing to 13% or less, are consistent with other studies, even though a comparison of streamflow composition between studies is complicated by the range of methods that can be used to define the streamflow components (Frenierre *et al.*, 2013), by the varying definitions of "glacier runoff" (Radic and Hock, 2014), and the varying temporal and spatial scale investigated. A previous study by Comeau *et al.* (2009), conducted on macro-scale basins located in the Canadian Rockies, showed that July-September glacier runoff (snow and ice melt from the glacier area) contributed 73-83% of the

streamflow in basins with more than 10% glacier cover. For the Peyto Creek basin, corresponding to a slightly larger basin than the one investigated in this study, they additionally found that for the 1973-1977 period, glacier wastage flux (or the net glacier water storage lost from negative mass balance) contributed between 48 and 74% of the July-September streamflow, but did not provide annual values due to the lack of streamflow measurements in other months. For the highly glacierized Nordic Creek basin (58% glacier-cover in 2013), Moore *et al*. (2020), found that the wastage flux contributed from 9-19% of annual water yield, much lower values than calculated in this study. Further comparison can be made with modelling studies of alpine glacierized basin in other mountain ranges, but caution is needed in interpreting these for comparison due to the difference in climate and modelling methodology. In the Alps, Verbunt *et al.* (2003) found that in a 47% glacierized basin, the glacier runoff (snow, and ice melt, but not rainfall on the glacier) contributed 62% of total streamflow, with 20% originating from ice melt, 10% from firn melt and 32% from on-glacier snowmelt, but did not indicate the proportion of off-glacier snowmelt contribution to streamflow and therefore underestimated the contribution of snowmelt at the basin scale. The same study also found that for a basin with 69% glacier cover, the glacier runoff contributed 85% of basin streamflow. Gao *et al.* (2012) found that, in a 44% glacierized basin in Central Asia, 60% of the basin streamflow originated from the glacierized area, which includes firn, snow and ice melt and liquid routed on the glacier surface. These proportions of on-glacier runoff contribution to streamflow are comparable to the results from the PGRB, where 71% of annual runoff originates from the glacier area (including firnmelt, snowmelt, icemelt and rainfall runoff on the glacier), which covers 56% of the basin. In the Andes, Burger *et al.* (2019) found that in a basin with 16% glacier cover, snowmelt on and off the glacier contributed 66-93% of basin streamflow, ice melt formed 3.5-32%, and rainfall-runoff did not exceed 6%. Therefore, the numbers presented here are within the ranges of values obtained in highly glacierized alpine basins, but the different approaches to computing flow compositions and glacier runoff contribution to streamflow preclude deeper comparisons between different studies. To facilitate future comparison between hydrological studies in mountain basins, the glacio-hydrological community should define common and clear metrics to compare runoff components, including both on and off-glacier runoff components and glacier wastage contributions to streamflow.

6.6. Conclusions

Streamflow generation in a glacierized mountain catchment such as the PGRB is caused by a complex interplay of hydrological processes. This study aimed to investigate the key sources of inter-annual

streamflow variability in a highly glacierized basin. To do so, a process-oriented, physically based glacier hydrological model was created in the Cold Regions Hydrological Modelling Platform to represent the full range of processes generating streamflow in a small glacierized Canadian Rockies headwater basin. By using parameters derived from fieldwork, literature values or physical principles, the model was able to capture the basin's snow accumulation, ice and snow melt patterns, and streamflow well. This modelling results emphasise the importance of long-term in-situ observations of meteorological variables in remote, high altitude glacierized basin to guide and evaluate model application.

A comparison of high and low streamflow years showed that streamflow in high flow years was 41% greater than in low flow years. High flow years were warmer (+1.43˚C), rainier (+145 mm) and less snowy (-295 mm w.e.) than low flow years. These differences in temperature and precipitation caused earlier snowmelt (-10 days), enhanced icemelt (+103%) and firnmelt (+162%), and greater rainfall-runoff (+146%). As a result, the predominance of interannual variability in the glacierized basin streamflow was due to hydrometeorological factors that affected ice melt with much smaller impacts from firn melt and rainfall-runoff. Annual streamflow was significantly correlated with annual air temperature, as well as summer rainfall and winter snowfall. The negative correlation with winter snowfall and with timing of ice exposure, concomitant with the lack of association between snowmelt and streamflow indicates that winter conditions play a role in streamflow variability by regulating subsequent summer ice exposure and albedo in the PGRB. Lower snowfall reduces summer albedo on the glacier. Snowmelt, whilst generating a larger fraction of streamflow, was a small source of interannual streamflow variability because high snowfall years were also low ice melt years due to the impact of deep snowpack in covering and protecting glacier ice from melting until late in the summer. Low snowfall years were also warmer and rainier years and so rainfall and firn melt runoff sources also increased with ice melt in these years. High snowfall did not necessarily translate into high snowmelt, as in high snowfall years not all the snow melted. These compensatory feedbacks between snow and glacier runoff processes affected both interannual variability and long-term trends. Even though trends were obtained in select meteorological forcings (summer air temperature, summer and annual rainfall and winter snowfall), these trends did not translate into trends in streamflow or runoff components. This diagnosis of the hydrometeorological conditions resulting in high and low flow years, combined with an analysis of the correlation between meteorological conditions and streamflow and an assessment of trends in the basin, revealed the

key drivers of streamflow variability in the PGRB but also highlighted the complexities of streamflow generation in mountain catchments.

Considering that meteorological extremes are expected to increase in the future, and that glacier retreat enhances flow stochasticity by changing the streamflow regime from ice-dominated to snowmelt and rainfall-runoff dominated, the streamflow in headwater glacierized basins is expected to continue to change in the upcoming decades. Increasingly warm conditions may cause an increase in the frequency of high flow conditions whilst glacier coverage still remains, much as was noted in the shift from the 1960s to recent years by Pradhananga and Pomeroy (2022a). These future changes will be superimposed on the current inter-annual variability that currently dominates the streamflow response in the PGRB. To understand and robustly predict the changing water supply from in glacierized mountain basins, it is crucial to consider the complex interplay of streamflow generation processes.

EXPLORING THE PREDICTED HYDROLOGICAL CHANGES OF A SMALL ALPINE GLACIERIZED BASIN AND ITS SENSITIVITY TO LANDSCAPE EVOLUTION AND METEOROLOGICAL FORCINGS

Paper manuscript status: Contents of this chapter have been compiled as a manuscript submitted to Water Resources Research and under review.

Author contribution: Caroline Aubry-Wake conceptualized the study, compiled, organized and processed the field measurements, set up the glacio-hydrological model and performed the modelling simulation as well as wrote the first draft of the manuscript. John Pomeroy provided insights on the conceptualization, methodology, data processes and modelling approaches, as well as edited the manuscript.

Role in thesis: This chapter addresses Objective 3 of the thesis. In this chapter, the glacio-hydrological model developed in Chapter 5 was used to contrast current (2000-2015) and future (end-of-century under RCP 8.5, approximately 2085-2100) conditions in the Peyto Glacier Research Basin. The model was forced with a dynamically downscaled, convection-permitting, high-resolution WRF atmospheric model. The sensitivity of the PGW simulation was analyzed by developing various scenarios that explore the different possible future landscapes at Peyto (ice cover, surface water storage, subsurface water storage, vegetation cover), and uncertainty linked with temperature and precipitation forcings.

7.1. Abstract

Glacierized mountains are witnessing substantive changes in their streamflow generation processes, influencing their capacity to provide runoff to support downstream water resources and ecosystems. Shifting precipitation patterns, a warming climate, changing snow dynamics and retreating glaciers are occurring simultaneously, driven by atmospheric change. To predict future hydrological behaviour in an examplar glacierized basin, a spatially distributed, physically based cold regions process hydrological model including on and off-glacier process representations was applied to the Peyto Glacier Research Basin, a 21 km^2 alpine basin in the Canadian Rockies. The model was forced with bias-corrected outputs from a high-resolution Weather and Research Forecasting (WRF-PGW) atmospheric simulation for 2000-2015, and under pseudo-global warming for 2085-2100 under a business-as-usual climate change scenario. The simulations show that the end-of-century increase in precipitation nearly compensates for the decreased ice melt associated with almost complete

deglaciation, resulting in a decrease of 7% in annual streamflow. However, the timing of streamflow advances drastically, with peak flow shifting from July to June, and August streamflow dropping by 68%. To examine the sensitivity of future hydrology to possible future landscapes, the end-of-century simulations were run under a range of initial conditions and showed the highest sensitivity to initial ice volume and surface water storage. The high-resolution atmospheric modelling, unprecedented on and off-glacier process representation in a physically-based hydrological simulation and examination of sensitivity to future landscapes and deglaciations provides a comprehensive examination of the water future of a rapidly deglaciating high-mountain environment.

7.2. Introduction

Mountain headwaters worldwide are witnessing a substantial shift in their hydrological and glaciological systems (Huss and Hock, 2018). This shift affects streamflow generation processes as well as downstream environments (Milner *et al.*, 2017). Half of the world's population relies on mountain water, and the reliance on mountain water is expected to increase in the upcoming decades, linked to a decrease in mountain water supply, but also an increase in demand (Beniston, 2003; Schaner *et al*., 2012; Viviroli *et al*., 2007; Viviroli *et al*., 2020).

Hydrological simulations forced with scenarios of future climate help in examining how hydrological responses to climate change might unfold in the upcoming decades and influence future water availability. An ongoing challenge for these hydrological simulations in high mountains is the reliability of the atmospheric forcings used (Addor *et al*., 2014). General circulation models (GCMs) provide simulated atmospheric conditions at coarse scales (50-100 km), which are then downscaled to the study site of interest in a variety of methods (Hay, 2000). However, the coarse spatial resolution of climate models misses the steep topography driving the weather conditions in mountains, resulting in inappropriate temperature and precipitation patterns (Rasmussen *et al.*, 2011; Horvath *et al.*, 2012; Langhans *et al.*, 2013; Prein *et al.*, 2013, 2015; Collier and Immerzeel, 2015). Collier and Immerzeel (2015) found that a 1km simulation of atmospheric forcing in the Himalayas greatly improved temperature lapse rate and moderately improves precipitation. Temperature and precipitation lapse rates are of high importance to appropriately simulate hydrological conditions (Immerzeel *et al.*, 2014a). This high uncertainty in the climate simulations, in particular, that of precipitation dynamics and phase strongly affects hydrological simulations and causes a high uncertainty in future estimates(Ragettli *et al.*, 2013; Addor *et al.*, 2014; Huss *et al.*, 2014; Mackay *et al.*, 2019; Rasouli *et al.*, 2019). The uncertainty in climate conditions affects a range

of processes in the hydrologic simulation. For example, Huss *et al* (2014) discuss the impacts of winter precipitation distribution and accuracy as large sources of uncertainty for predictions of future conditions, which relates to the difficulties of atmospheric models to provide accurate winter precipitation in mountain basins.

In recent years, the increase in modelling capacities has led to convection-permitting models with a horizontal grid spacing of 4 km or less. This high resolution provides a more accurate representation of the underlying surface and topography and explicitly represents deep convection, resulting in more realistic regional-to-local climate simulations (Prein *et al.*, 2015). The main downside of these convection-permitting models is their high computational processing and storage cost, which results in shorter simulations with few realizations (He *et al.*, 2019). A way to balance this need for high-resolution simulations with the long-term climate change impacts is to use the pseudo-global warming approach (PGW) (Rasmussen *et al.*, 2011). The PGW methodology provides high-resolution weather patterns as perturbed by the impact of climate change on regional boundary conditions. It has been recently applied to several hydrological prediction studies in mountain environments (Rasmussen *et al.,* 2014; Musselman *et al*., 2018; Fang and Pomeroy, 2020).

An additional challenge faced when simulating hydrological changes in mountains is the uncertainty associated with the changing landscape. As glaciers retreat, they leave behind a new landscape, with different characteristics and behaviours. For example, glacier retreat often leaves room for pro-glacial development, a change already occurring globally (Shugar *et al.*, 2020). The formation and expansion of pro-glacial lakes are likely to change the storage capacity of the basin, as well as increase the evaporation loss. Vegetation colonization of recently deglacierized areas also changes the hydrological functioning of the basin by increasing evapotranspiration. The primary succession and soil development in the proglacial environment has been well-studied, with multiple case studies in varied glacierized environments (Jones and Henry, 2003; Burga *et al.*, 2010; Schumann *et al.*, 2016; Glausen and Tanner, 2019). These studies reveal the importance of microclimate, micro-topography and altitude in dictating the pattern of plant colonization and soil development. Similarly, relatively little is known about changes in the hydrological properties of newly deglaciated areas in terms of water storage and transmission (Somers and McKenzie, 2020). The uncertain landscape evolution causes difficulties in representing these both for model structure and parametrization. Considering the importance of high mountain headwaters for water security and the ongoing rapid changes observed in these basins, developing hydrological modelling approaches that address both the

challenge at representative high mountain weather in a changing climate and the dynamic landscape evolution is important (Huss *et al.*, 2017; Milner *et al.*, 2017; Immerzeel *et al.*, 2020).

Prior studies have noted the importance of headwater glacierized basin for water resources in the Canadian Rockies (Comeau *et al.*, 2009; Bash and Marshall, 2014; Naz *et al.*, 2014; Anderson and Radic, 2020). Fewer studies look at future conditions. Clarke *et al*. (2015), in a regional estimate of glacier retreat to 2100 for Western Canada, finds the glacier of the southern Canadian Rockies will retreat by up to 95% from their 2005 extent, and cause a strong decrease in glacier-fed flow. Marshall *et al*. (2011) provide an estimate of future glacier contribution to streamflow on the eastern side of the Canadian Rockies using a statistical analysis of past conditions and find a near disappearance of glacier volume, and a strong reduction in late summer flows. Recently, Chernos *et al*. (2020) found a decrease of up to 58% in late summer streamflow by 2100 for the nearby Upper Athabasca River basin.

This study aims to provide a diagnosis of change in the hydrological processes for a glacierized headwater basin in the Canadian Rockies, combining process-based glacio-hydrological modelling with a high-resolution WRF atmospheric product and simulation of landscape change. Specifically,

(1) the ability of the developed model to capture the snow and ice melt regime of the Peyto Glacier basin is evaluated;

(2) the changes in comparing current (2000-2015) with future (2085-2100) hydrological simulations in a PGW approach are diagnosed and;

(3) the sensitivity of the projected changes in the hydrology with changes in the landscape and changes in the atmospheric forcings is explored.

7.3. Methods

7.3.1. Study site

Peyto Glacier, an outlet glacier of the Wapta Icefield in Banff National Park, Alberta, Canada ranges between 2100-3190 m a.s.l. As of 2018, the Peyto glacier had an area of 10.2 km^2 in a 50% glacier-covered drainage basin of 19.3 km^2. The basin has a cold continental climate, with an annual air temperature staying below ranging between -4.2 and -2.2˚C between 1990-2017. Only the lowest elevations in the basin, below 2200 m.a.s.l., have an annual air temperature above zero, varying from -0.8 to 1.2˚C. Summer temperatures in the basin can reach up to 22˚C. Annual precipitation ranges

between 1500-1900 mm, of which on average 76% falls as snow. The basin only has sparse vegetation in the non-glacierized areas, with a few mosses and shrubs colonizing the local depressions in the moraine. It has been the site of multiple glacier- and hydrology-focused studies in the past decades. Peyto Glacier is a headwater of the North Saskatchewan River, which makes its way to the adjacent sub-humid Canadian Prairies and boreal forest, with its water used for ecosystem services, hydropower, and drinking water.

Installed in 1991 and updated in 2013, automated weather stations at the site provide a long-term meteorological record of the area. Since 2013, streamflow monitoring has also been installed about one kilometre below the quickly receding glacier toe. Additionally, mass balance measurements have been conducted since 1965. The compilation of data available from the Peyto Research basin is available from Pradhananga *et al*. (2020).

7.3.2. WRF model

7.3.2.1. *Model overview*

The hydrological simulations were forced with meteorological conditions (temperature, relative humidity, incoming shortwave radiation, incoming longwave radiation and precipitation) from the Weather Research and Forecasting (WRF) model Version 3.4.1 for the grid corresponding to the location of the Peyto weather station (Figure 7.1). The atmospheric forcings consist of two 15-years simulations, one being the control for current conditions (CUR, 2000-2015), and the other obtained following a pseudo-global-warming (PGW) methodology, representing the 2086-2100 period. The CUR-WRF simulation was run with initial and boundary conditions from the 6-hour 0.703˚ ERA-interim reanalysis data (Dee *et al.*, 2011). The PGW simulation takes these same initial and boundary conditions (2000-2015, 6 hours ERA-interim) and adds a seasonal climate perturbation to it. This climate perturbation is derived from a 19-model ensemble mean change from the fifth phase of the Coupled Model Intercomparison Project (CMIP5, Taylor *et al*., 2012) for the business-as-usual scenario, which corresponds to the Representative Concentration Pathway 8.5 (RCP8.5; van Vuuren *et al*., 2011). A detailed description of the WRF model outputs used in this study is provided in Li *et al*., 2019).

7.3.2.2. *Bias correction*

The WRF-CUR and PGW outputs were bias-corrected using observations of air temperature, relative humidity, wind speed, incoming shortwave and longwave radiations from the hydrometeorological

station at Peyto moraine. This hydrometeorological station is located on the lateral moraine about one kilometre east of the retreating glacier toe, at an elevation of 2240 m a.sl (Figure 7.1). Precipitation was observed at an Alberta Environment and Parks meteorological station located further down the valley in a sheltered forest clearing, at Bow Summit, at an elevation of 1080 m a.s.l. Both these datasets are fully described in Pradhananga *et al*. (2021).

Biases in the forcing meteorology from WRF were corrected using a multivariate generalization of quantile mapping (Cannon, 2018) which was shown to outperform univariate quantile delta mapping corrections. This algorithm has the advantage of correcting systematic bias in quantiles of WRF outputs with respect to the observations without changing model projected relative changes in quantile while preserving the interdependence of precipitation and temperature (Meyer *et al.*, 2019). The bias correction was performed for 15 water years (2001-2015) for the current period and the corresponding years (2085-2099) for the pseudo global warming outputs. To assess the performance of the bias-correction WRF product, the bias-corrected WRF current conditions were compared with meteorological observations using the root mean square error (RMSE) and the mean absolute difference (MAE) and correlation coefficient r^2 (Fang *et al.*, 2013; Fang and W. Pomeroy, 2020).

7.3.3. Hydrological model and simulations

7.3.3.1. *The Cold Region Hydrological Model*

The hydrology of the Peyto glacier basin was simulated using the object-oriented, flexible and modular Cold Regions Hydrological Modelling platform (CRHM). CRHM allows the user to select the physical processes to include in the model structure to be appropriate for the basin and to fit the needs of the study. The processes represented are selected from a library of modules of varying complexity. Similarly, the user selects the complexity of spatial discretization by defining hydrological response units depending on the spatial variability of basin attributes. The level of the complexity built in the model by the users is therefore a combination of hydrological understanding, data availability, basin complexity and the objective of the study. CRHM is further described by Pomeroy *et al*. (2007) and Pomeroy *et al*. (2022), with its range of applications in varied environments. It has now been applied in glacierized basins in Western Canada (Pradhananga and Pomeroy, 2022a, b; Anderson, 2017).

Spatial discretization of CRHM applied here to the Peyto glacier basin was based on the concept of hydrological response units (HRUs) defined based on aspect, slope, elevation, cover type and cover type change. This resulted in 37 HRUs across the basin allowing the representation of both the CUR and PGW landscape (Figure 7.1, with the geospatial attributes shown in table D.1 and figure D.1). As the HRU spatial distribution is the same for the control and PGW simulations, the landscape evolution and glacier retreat were represented by changing the cover type and associated model parameters for the changing HRUs. This included updating the cover type, elevation and slope of the HRUs where glaciers disappear. The elevation of the post-glacier HRUs was defined using the global glacier thickness inventory from Farinotti *et al*. (2019).

Observations of air temperature, relative humidity, shortwave and longwave radiation and wind speed and precipitation are distributed to the HRUs while taking into account slope, aspect, elevation and groundcover. Precipitation phase is calculated following Harder and Pomeroy (2013), based on the energy balance of the hydrometeor (Harder and Pomeroy, 2013). Snow is redistributed across the basin by both blowing snow and avalanching (Pomeroy *et al.*, 1993; Pomeroy and Li, 2000; Bernhardt and Schulz, 2010). Melt is calculated based on the energy balance of snow and ice (Marks *et al.*, 1999; Pradhananga and Pomeroy, 2022a, Pomeroy *et al.*, 2022). Once surface melt occurs, the meltwater is routed through a single snow reservoir for non-glacier HRUs and three reservoirs (snow, firn, and ice) for glacier HRUs and discussed in Chapter 6 and in Aubry-Wake *et al.* (2022c). Infiltration is calculated for both frozen and non-frozen soil. Rain and meltwater are then routed through a soil, subsurface and groundwater layer. Flow velocities in the subsurface and groundwater layer are calculated from saturated and unsaturated hydraulic conductivities (Fang *et al.*, 2013). The model parameters are not calibrated from their fit to streamflow or glacier mass balance. Parameters are selected primarily from local and regional observations (e.g., temperature and precipitation lapse rates). The model was initiated by repeating the first year of the simulations. A more detailed model parametrization and description can be found in Chapter 6 and Pradhananga and Pomeroy (2022a).

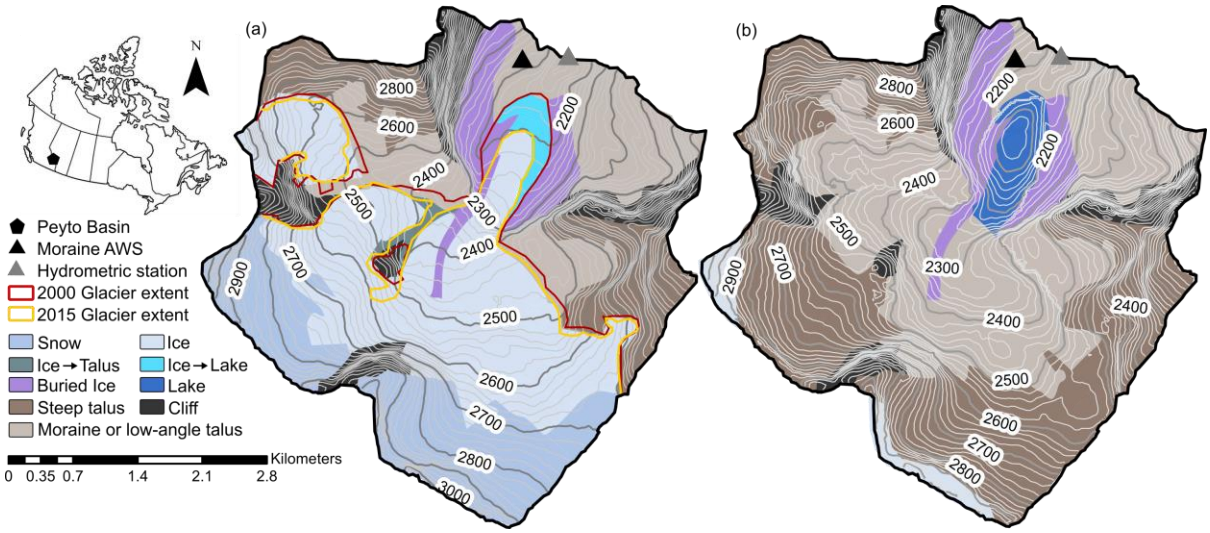

Figure 7.1. Peyto basin with elevation and land cover corresponding to the (a) 2000-2015 and (b) 2085-2100 simulations

7.3.3.2. *Model evaluation*

The CRHM model was evaluated with a combination of winter mass balance, to target snow processes, summer mass balance, to target ice melt processes, and streamflow. For streamflow, the Nash Sutcliffe Efficiency (NSE, Nash and Sutcliffe, 1970) is calculated:

$$NSE = 1 - \frac{\sum_{t=1}^{t=T}(x_{sim}(t) - x_{obs}(t))^2}{\sum_{t=1}^{t=T}(x_{obs}(t) - \overline{x_{obs}})^2} \quad (7.1)$$

where T is the total number of time steps, $x_{sim}(t)$ the simulated variable at time t, $x_{obs}(t)$ the observed variable at time t, and $\overline{x_{obs}}$ the mean observed discharge. A unity value of NSE indicates perfect agreement between simulations and observations while a nil values means that the model simulations have the same explanatory power as the mean of the observations, and NSE < 0 indicates that the model is a worse predictor than the mean of the observations (e.g. Schaefli and Gupta, 2007).

Considering that high NSE values are expected for strongly seasonal basins (Schaefli *et al.*, 2005; Schaefli and Gupta, 2007; Seibert *et al.*, 2018), the NSE performance of this CRHM model was compared with that of a benchmark model consisting of the interannual mean value for every calendar days for the 2016-2018 period (Garrick *et al.*, 1978; WMO, 1986; Schaefli and Gupta, 2007).

For the snow accumulation and ice melt, the simulated and observed mass balance gradient and standard deviation are compared for the 2000-2015 period.

7.3.3.3. *Landscape and forcing scenarios*

To explore the possible impact of different landscape evolution patterns, five sets of simulations were performed in addition to the reference PGW simulation to target four landscape changes: remaining ice volume, water storage in the surface sediments, surface water ponding including lake formation, vegetation colonization, and a combination to create a lush and a bare scenario (Figure 7.2, Table 7.1). A total of 14 simulations regarding landscape evolution scenarios were performed.

The reference PGW scenario was defined based on the current conceptual understanding of the most likely changes in the landscape and associated properties linked to deglaciation (Figure 7.2b). The reference PGW scenario has remaining glacier cover corresponding to 3% of the basin area, located at the highest elevation of the basin. The buried ice, either in the ice-cored moraine or the debris cover section of the glacier, continues to be present in future scenarios. The leftover ice area was set up as an infinite store with a static area over the simulation length. Ice cover over each 15-year simulation period was assumed to be static as the simulations are relatively short duration with relatively small ice masses, and so ice dynamics would be limited. Three additional simulations relating to ice cover were run with 0%, 6% and 9% of the basin area (Figure 7.2c). The exact percentage was dictated by the spatial discretization of the HRU in the simulations. The remaining ice cover is based on a simulation of regional deglaciation in the Canadian Rockies by Clarke *et al.* (2015) who found a range of 0-15% of the 2005 ice coverage in the Canadian Rockies by 2085 under RCP8.5. This is similar to Marshall *et al.* (2011), who suggested that by 2100, only 3% of the 2005 ice coverage would be left in the North Saskatchewan basin under scenario A1B.

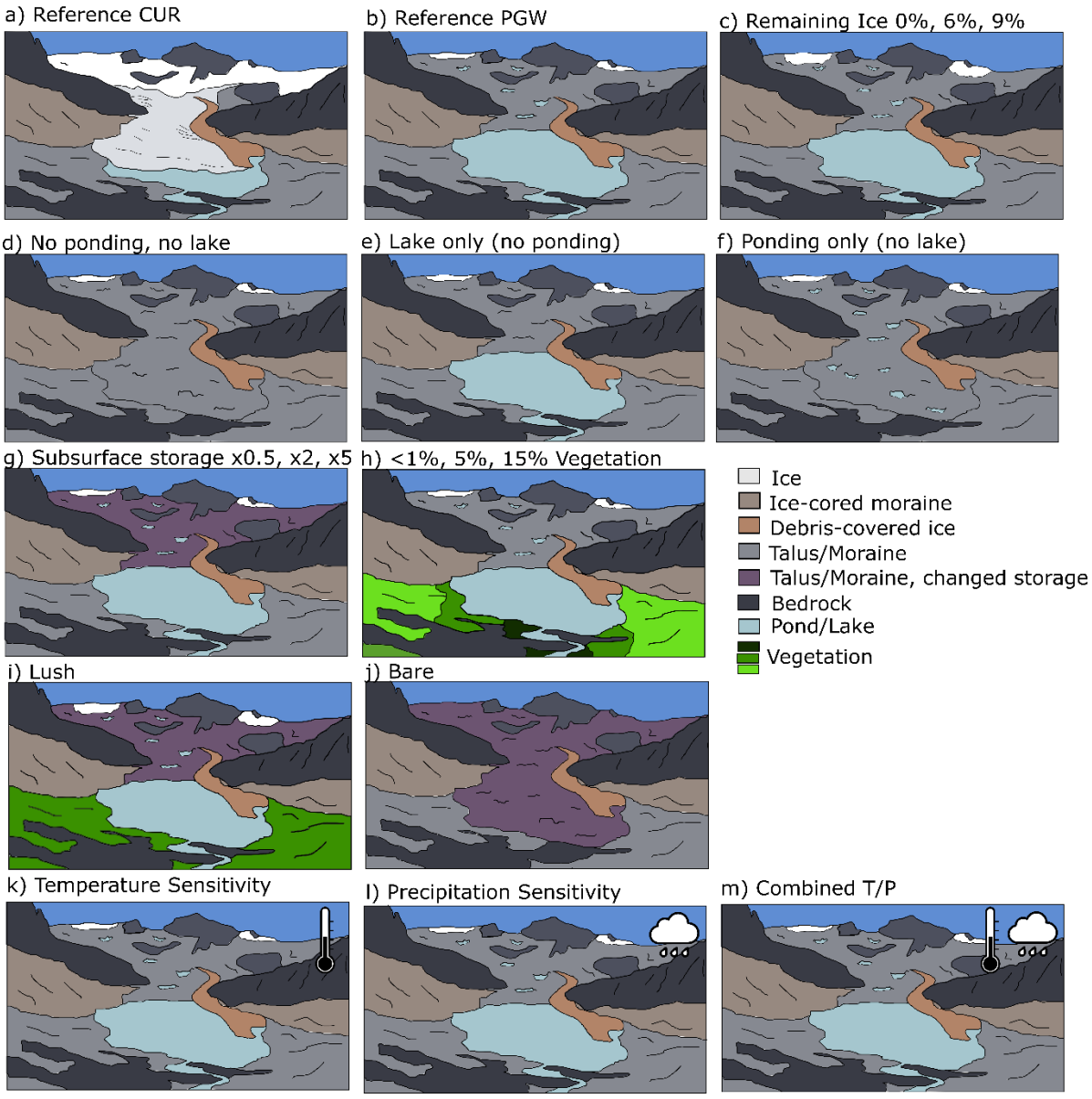

Figure 7.2. Conceptual schematic of landscape evolution scenarios in the Peyto glacier basin

Table 7.1. Overview of simulation for the reference current period (CUR, 2000-2015) and future (PGW, 2085-2100) and the 13 PGW landscape scenarios. The (-) indicates no change from the reference PGW simulation. In the surface water storage scenario, lake refers to the presence of a proglacial lake at the toe of the glacier, ponds refer to the presence of small ponds across the basin and no storage refers to the absence of lake and ponds. Each line refers to a scenario. Letters in italic indicate the corresponding schematic in Figure 7.2.

	Scenario	Glacier cover	Surface water storage	Subsurface storage	Vegetation cover
Reference	CUR (a)	60% in year 2000	Lake	1x CUR	0%
	PGW *(b)*	3%	Ponds and lake	2x CUR	0%
Landscape	Initial ice area *(c)*	0% , 6%, 9%	-	-	-
	Surface water storage *(d-f)*	-	No storage *(c)* Lake *(d)* Ponds *(e)*	-	-
	Subsurface storage *(g)*	-	-	0.5x CUR x1 CUR x5 CUR	-
	Vegetation growth *(h)*	-	-	-	<1%, *(g)* 5% *(h)* 15% *(i)*
	Lush *(i)*	9%	Ponds and Lake	10x CUR	15%
	Bare *(i)*	0%	No storage	1x CUR	0%

To explore the importance of surface water storage on streamflow behaviour, this parameter was manipulated in various scenarios. In the reference PGW scenario, a proglacial lake was placed where the glacier toe used to be, and ponding developed in the deglaciated area to reflect small ponds forming in localized depressions. This type of landscape change can currently be observed in the recently deglaciated areas of the Peyto basin, where both exposed bedrock and sedimentary deposits after glacier retreat create rough topography with a high depressional storage capacity. Similarly, a proglacial lake appeared in the basin in 2006 and is continuing to form as the glacier toe recedes. Three additional scenarios were simulated. The first sets depressional storage at zero, which entails the proglacial lake and all ponds draining (Figure 7.2d). The second permits the formation of the proglacial lake, but no depressional storage in ponds outside of this lake (Figure 7.2f). The third permits the formation of a distributed system of depressional storage in ponds across the deglaciated area, but no proglacial lake (Figure 7.2f).

Glacier retreat could have a variable influence on subsurface storage volume. Glacier retreat could increase subsurface storage, due to increased fracturing, increased debris deposit and possible soil developments. Based on this hypothesis, subsurface water storage was doubled for the deglacierized HRUs in the PGW reference simulation. However, as glacier retreats, the subglacial till layer might erode, and result in reduced subsurface storage. These possible changes have very uncertain volume change with uncertain timing. Three additional landscape changes are explored: cutting the subsurface storage by half, leaving the subsurface storage as in the CUR simulation, and increasing the subsurface storage by a factor of 5 (Figure 7.2g). The subsurface storage increase was limited to no more than the storage in the currently deglaciated moraines.

Future vegetation change in the basin is based on field observations in recently deglaciated parts of the basin as well as regional observations of vegetation encroachment in recently deglaciated landscapes in the Canadian Rockies. For example, the Athabasca Glacier, located approximately 100 km north of the Peyto Glacier, presents an analogous deglaciated terrain. Repeat photographs of land exposed from glacier retreat more than a century ago now show very limited vegetation growth (Mountain Legacy Project, Figure D.2). A recent paper on vegetation change in the Canadian Rockies over the last century shows that deglaciated areas have expressed little change in vegetation type but an increase in the density of existing vegetation (Trant *et al.*, 2020). However, expansion of vegetation cover has been observed in the more temperate Alps which may be an analogue for a future Canadian Rockies (Schumann *et al.*, 2016). Therefore, vegetation was parameterized to cover

an area of low elevation lowin the basin, with scenarios of less than 1%, 10% and 15% of the total basin area (Figure 7.2h).

Finally, the bare and lush scenarios are a combination of the above factors (Figure 7.2i-j). The lush scenario combines the 9% glacier cover, surface water ponding in the form of ponds and a proglacial lake, increased sediment storage (x10), and 15% vegetation growth. The bare scenario is the other end of the combination, with 0% remaining ice, no surface water ponding (no lake and no ponds), no change in subsurface storage, and no vegetation.

To compare the possible landscape evolution pathways in the context of uncertainty in future atmospheric forcings, an additional set of scenarios was designed with changes in temperature and precipitation (Figure 7.2k-m, Table 7.2). An additive bias of -2°C, -1°C, +1°C, and +2°C for temperature and a multiplicative bias of -20%, -10%, +1-% and +2-% in precipitation were applied to the WRF-PGW forcings. A combination of the temperature and precipitation adjustments created wet and cold (+20% precipitation, -2°C), wet and warm (+20% precipitation, +2°C), dry and cold (-20% precipitation, -2°C) and dry and warm (-20% precipitation, +2°C) scenarios.

Table 7.2. Overview of simulation for the 12 forcings sensitivity scenarios. Letters in italic indicate the corresponding schematic in Figure 7.2. The (-) indicates no change from the reference PGW simulation. Letters in italic indicate the corresponding schematic in Figure 7.2.

	Scenario	Temperature	Precipitation
Forcings	Temperature *(k)*	-2, -1, +1, +2 ˚C	-
	Precipitation *(l)*	-	-20%, -10%, +10%, +20%
	Cold and Dry *(m)*	-2˚C	-20%
	Cold and Wet *(m)*	-2˚C	+20%
	Warm and Dry *(m)*	+2˚C	-20%
	Warm and Wet *(m)*	+2˚C	+20%

7.4. Results

7.4.1. WRF-CUR bias correction

The uncorrected WRF-CUR forcings were biased compared to the meteorological observation from the station at the Peyto moraine. The air temperature was negatively biased at colder temperatures. The relative humidity values in the WRF-product reached impossibly high levels, mainly due to oversaturation in wintertime. Incoming shortwave radiation was positively biased and longwave radiation negatively biased, likely linked to the cold temperature bias. The application of the multivariate quantile mapping bias-correction (Cannon, 2018) reduced this bias (Figure 7.3), with bias-corrected data showing marked improvement both in terms of root mean square error and mean absolute bias (Table 7.3). The WRF-simulated precipitation did not well match the interannual variability observed (Figure D.3) For 12 out of 15 years of the simulation, the annual precipitation difference between the bias-corrected WRF and the observation was less than 70 mm. However, for the other three years (2005, 2007, 2012), the annual precipitation was offset by more than 160 mm.

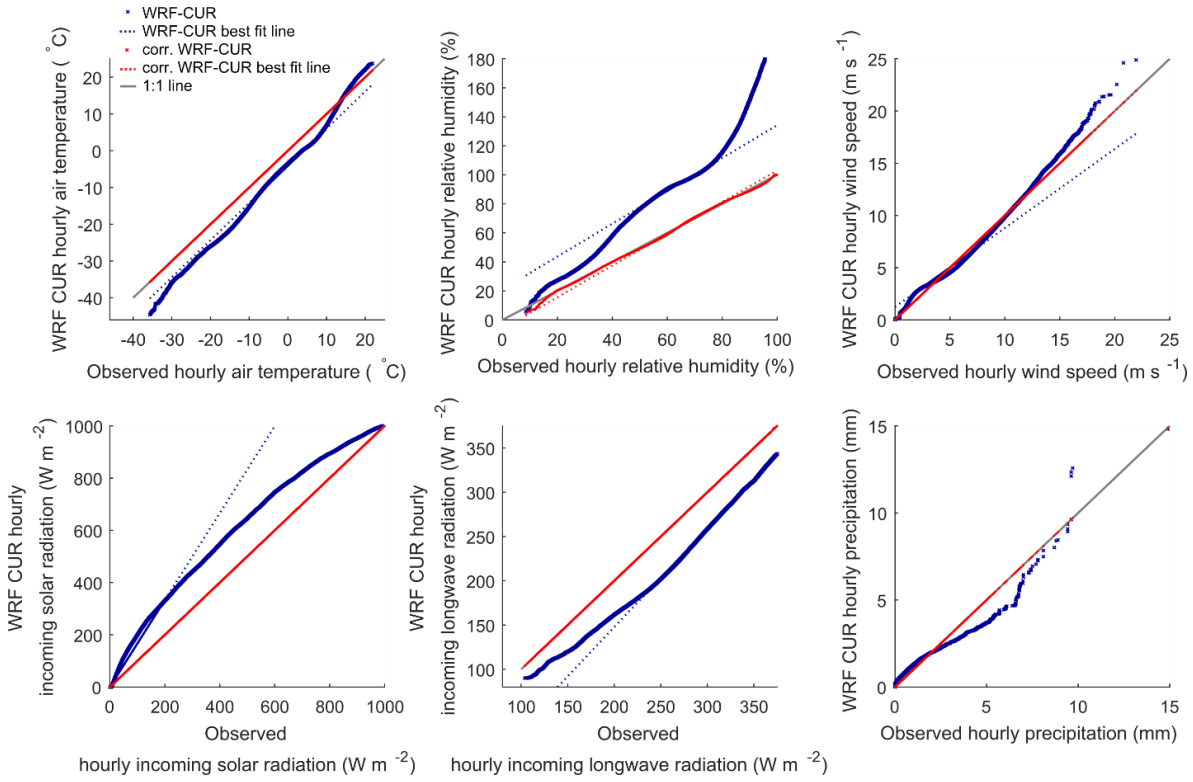

Figure 7.3. Quantile mapping of raw and bias-corrected WRF meteorological forcings

Table 7.3. Correlation coefficient (r^2), root-mean-square error (RMSE) and mean absolute bias (MAE) of the raw and bias-corrected hourly WRF meteorological variables (Temperature T, relative humidity RH, wind speed U, incoming shortwave radiation SW_{in} and incoming longwave radiation LW_{in} and precipitation P) compared with Peyto observations. The value in parenthesis is for the uncorrected WRF-CUR comparison with the Peyto observations.

Variable	r^2	RMSE	MAE
T (°C)	0.93 (0.93)	3.2 (5.4)	2.5 (4.2)
RH (%)	0.39 (0.27)	14 (57)	10 (52)
U ($m^3\ s^{-1}$)	0.45 (0.46)	3.2 (3.2)	2.5 (2.5)
SW_{in} (Wm^{-2})	0.80 (0.81)	145 (170)	81 (96)
LW_{in} (Wm^{-2})	0.74 (0.71)	35 (56)	27 (47)
P (mm)	0.29 (0.33)	0.46 (0.48)	0.12 (0.14)

7.4.2. Hydrological model evaluation

Model performance for streamflow was evaluated with the available streamflow measurement (Pradhananga *et al.*, 2021) for the 2013-2015 melt seasons. Streamflow observations are only available after snow ablates from the melt channel and before freeze-up, which results in streamflow data availability between mid-May/early June and late September/mid-October. This does not allow a model evaluation for early and late low flow or melt events. For the three summers, the simulations had a Nash-Sutcliffe Efficiency (NSE) of 0.61 compared to observed streamflow, with annual NSE of 0.52, 0.58 and 0.70 for 2013, 2014 and 2015 respectively (Figure 7.4a-c; Table 7.4). The model simulated high flow events that were not observed in the streamflow datasets, linked with precipitation events occurring in the WRF forcings or large melt events in the model. These could also be associated with high flow events not being captured in the streamflow observations. During peak flow periods, the high water level in the pond above the bedrock notch where the stream level is calculated causes a small channel to form over the bedrock constriction. It is unclear how much this bypass channel reduces high flow measurements, but it could partially explain the simulated but not observed high flow events.

The simple benchmark model calculated as the mean observed discharge for each calendar day for years 2016-2018 was a poor predictor of the daily average streamflow. In terms of NSE, this

benchmark model achieved a score of only NSE = -0.02. CRHM seemed far more able to capture the temporal and inter-annual variation of the flow regime, giving its score of NSE = 0.61 for the years 2013-2015.

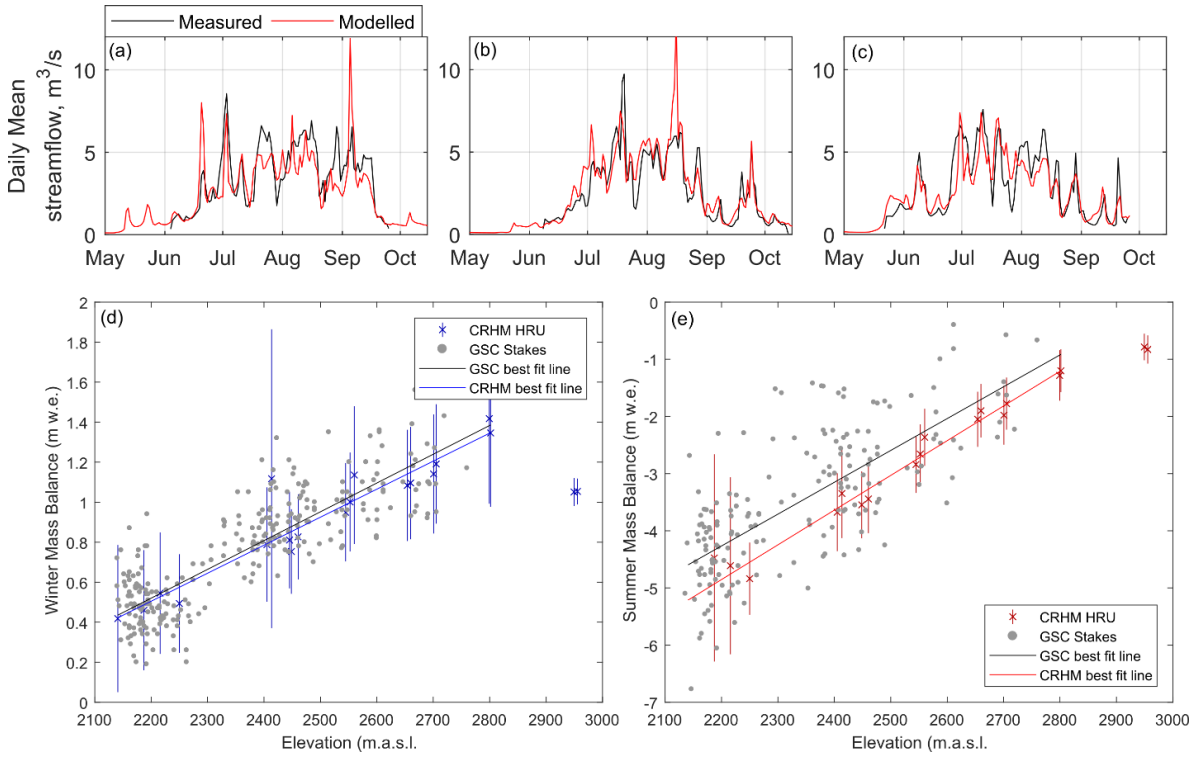

Figure 7.4. Streamflow evaluation for (a) 2013, (b) 2014 and (c) 2015 melt seasons and (d) winter mass balance for the 2003-2015 period and (e) summer mass balance for the 2000-2015 period. The light blue markers in (d) indicate the season with large offsets in the WRF precipitation.

Table 7.4. Model daily streamflow evaluation with the Nash Sutcliffe Efficiency parameter (NSE), the Root mean square error (RMSE), the mean absolute error (MAE) and the correlation coefficient (r^2) for the 2013-2015 period.

	NSE	RMSE	MAE	r^2
All years	0.61	1.23	0.90	0.66
2013	0.52	1.32	0.92	0.59
2014	0.58	1.28	0.92	0.74
2015	0.70	1.07	0.83	0.71

For summer and winter mass balance, point measurements from the stake network were compared with the SWE accumulation and ice melt obtained at the glacier HRUs (Figure 7.4d-e). The stake network provides 234 end-of-winter SWE and 163 end-of-summer melt point measurements between 2003 and 2015 from elevations 2136 and 2760 m a.s.l. These were compared with the clean-ice glacier HRUs (n = 18), for the same 2003-2015 year, for 234 point measurements for both summer and winter mass balance between 2187 and 2955 m a.s.l.

The best-fit lines for both the observed and simulation winter mass balance lapse rate below 2800 m a.s.l. were 0.0014 m w.e/ m elevation. These calculated lapse rates were limited to the lower elevations, as there are no measurements above 2800 m a.s.l. The simulated winter accumulation had a larger variability than the measured winter mass balance. This larger variability is likely attributed to avalanche activity occurring in the basin and the annual precipitation difference between measured precipitation and WRF-CUR modelled precipitations, as outlined in Figure D.3. For the 13 years of winter mass balance available, the largest standard deviation was from an area located at the confluence of the upper glacier tributaries and receiving a combination of avalanche deposits and blowing snow deposits. The lowest standard deviation, 0.06 m.w.e., was at the highest elevation locations in the basin, which avalanches every year and therefore has consistently low snow volume. The simulated HRUs had a standard deviation of 0.44 m w.e., but when not including the WRF years with high precipitation (2005, 2007 and 2012), the standard deviation decreased to 0.34 m w.e. In comparison, the standard deviation of the point measurements across the basin was 0.29 m.w.e.

For summer mass balance, the CRHM results reflect the variability in the stake point measurements. The standard deviation was 1.25 m.w.e. for elevations below 2900 m. The standard deviation of the simulated melt decreased with elevation: the highest standard deviation for summer melt (± 1.81 m w.e.) was found at the lowest glacier HRU, but only ±0.23 m.w.e. for the highest HRU. This is similar to the standard deviation of the stake measurement of ±1.22 m w.e. The lapse rate was also similar (0.0056 for measurements and 0.0061 for the CRHM simulated melt m w.e. m^{-1}). However, CRHM slightly underestimated summer melt conditions, with the best fit lines of the stake measurements and HRU simulated balance showing a mean difference of 0.44 m w.e.

7.4.3. Change in meteorological forcings

The 15-year basin meteorological forcings were warmer and wetter in the PGW compared to the CUR simulation (Figure 7.5). Annual air temperatures increased by 5°C, from -3.8°C to 1.2°C. This

warming reached 8°C in late June. Wintertime experienced less warming but greater variability, with the standard deviation across the 15 years of the simulation averaging 5°C between December and April compared with 2°C in July and August. The day at which air temperature reaches 0°C in the spring moved forward one month, from June 12 in the current period to May 12 in the PGW period. Similarly, the day at which air temperature drops below 0°C in the fall moved from Oct 1 to Oct 26. The PGW simulation also indicates a small decrease in the humidity in May compared with the CUR period, followed by a decrease in the humidity in June with an annual change in relative humidity of -1.8 %. A decrease in summer incoming shortwave radiation is predicted, likely linked with higher cloud cover, causing an annual decrease of -12 Wm^{-2}. Incoming longwave radiation also increased by 29 Wm^{-2}, likely due to increased cloudiness and warmer temperatures. Annual precipitation increased substantially, by 226 mm, from CUR to PGW periods.

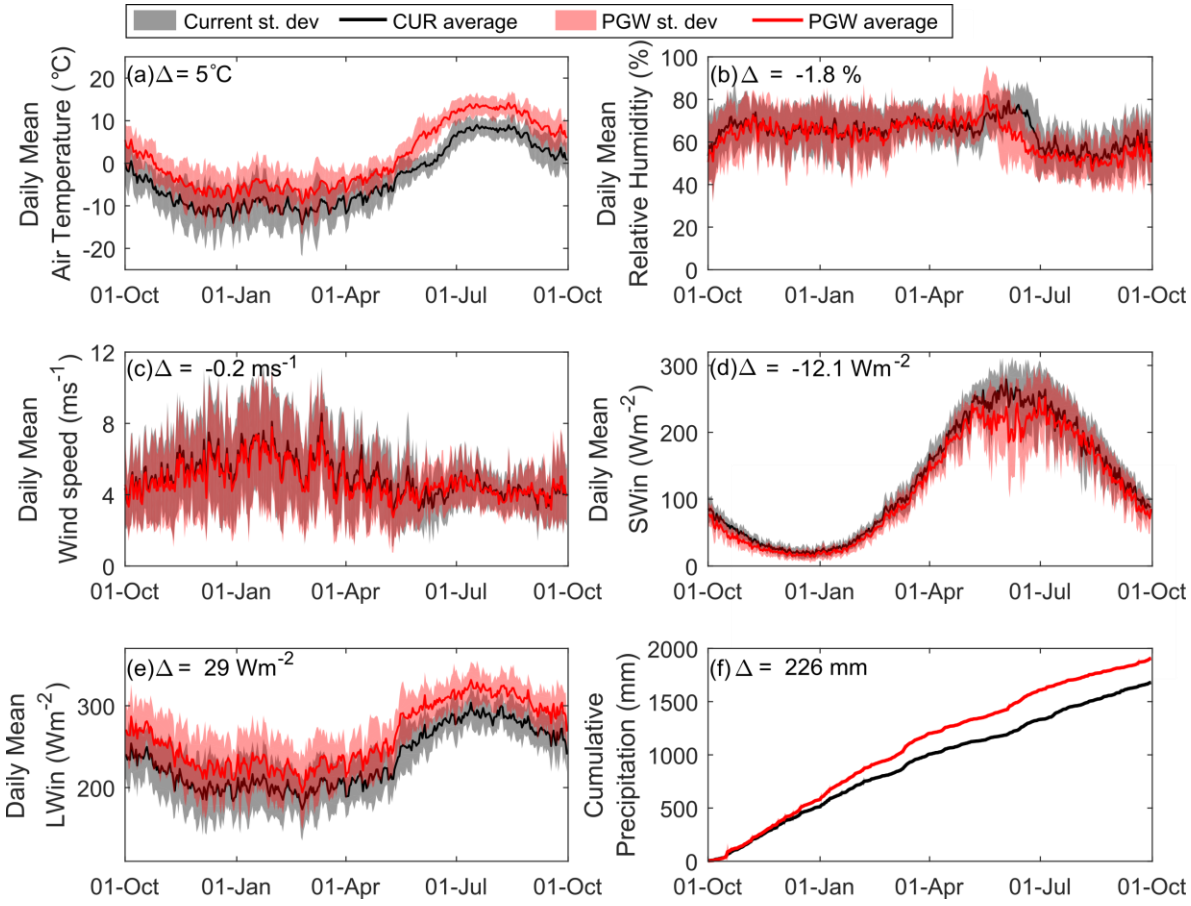

Figure 7.5. Change in basin meteorology for the current (2000-2015) and PGW (2085-2100) period. The thick lines are daily averages with one standard deviation in shade. Precipitation is cumulative.

7.4.4. Changes in hydrological processes

The 15-year average annual streamflow volume decreased 7 % between the CUR and reference PGW simulation period (161 mm, Table 7.5, Figure 7.6a,). PGW streamflow increased substantially in the spring period (+131 and 179 mm in May and June) and dropped substantially in late summer (-301, 271 and 71 mm for July, August and September) compared to the CUR simulation. Winter streamflow increased by 13-17 mm from December to March during a very low flow period (Figure 7.6a, D.4). This shift to earlier streamflow is seen in the centre of mass, the point in time at which 50% of streamflow volume has been discharged, which advanced from July 31st to July 8. The average date of the annual peak flow shifted from August 1st to July 24th, and the average peak of the annual peak flow discharges increased from 37 to 40 mm d^{-1}. Winter streamflow increased in the PGW compared to the CUR simulation. For the January-April period, only 3 days over the 15 years had daily streamflow above 3 mm d^{-1} in the CUR simulation compared to 70 days in the PGW simulations.

Table 7.5. Annual mass fluxes (mm) between the 2000-2015 (CUR) period and the 2085-2085 (PGW) period.

	CUR (mm)	PGW (mm)	Change (mm)	Change (%)
Streamflow	1969	1804	-166	-7
Rainfall	225	506	281	125
Snowfall	1453	1444	-9	-1
Evaporation	1	27	26	2600
Blowing snow sublimation	112	20	-92	-82
Blowing snow transport	244	16	-228	-93
Avalanche	74	162	88	119
Ice melt	706	154	-552	-78
Snowmelt	1377	1509	132	10
Soil moisture	24672	28834	4162	17
Groundwater storage	110287	113933	3646	3

The increase in precipitation observed in Figure 7.5a occurred mainly as an increase in rainfall (+281 mm) across the basin with snowfall decreasing slightly (-9 mm). Increased surface water exposure across the basin due to glacier retreat and the expansion of the proglacial lake increased evaporative

losses from the basin (+26 mm). Blowing snow sublimation and transport both decreased (-92 mm and -228 mm respectively), limited by the impact of increases in winter/spring rainfall and warmer air temperatures in restricting snow erosion by wind through increasing snow particle cohesion at the surface ((Li and Pomeroy, 1997). Avalanche activity increased (+88 mm), as expected by the steepening of the deglaciated headwalls in the high elevation of the basin. The reduction in glacier ice melt is the largest change in the basin (- 552 mm), snowmelt increased slightly (+10 mm) and peak snowmelt occurs one month earlier. The decrease in glacier ice melt can also be expressed in terms of glacier wastage, defined as the volume of ice and firn melt exceeding the annual volume of snow accumulation on the glacier and causing an annual net loss of glacier volume.. In the CUR simulation, glacier wastage corresponded to 60% of the basin yield, compared to 17% in the PGW period. Soil moisture storage remained higher in the winter, linked with increased mid-winter rainfall and melt events, and increased earlier in the spring due to earlier snowmelt. This caused an increase in the average annual soil moisture storage of 17%. Groundwater storage was also recharged earlier but only increased by 3% between the CUR and PGW simulations.

By the end of the century, snowmelt contributes 84% of annual streamflow compared to 70% for the current period. A nival streamflow regime persists, where snow still acts as seasonal storage and releases water late in the spring. This contrasts with warmer alpine glacierized basins, such as in Switzerland, where the glacial-streamflow regime is projected to transition to a rain-dominated regime (Beniston *et al.*, 2018).

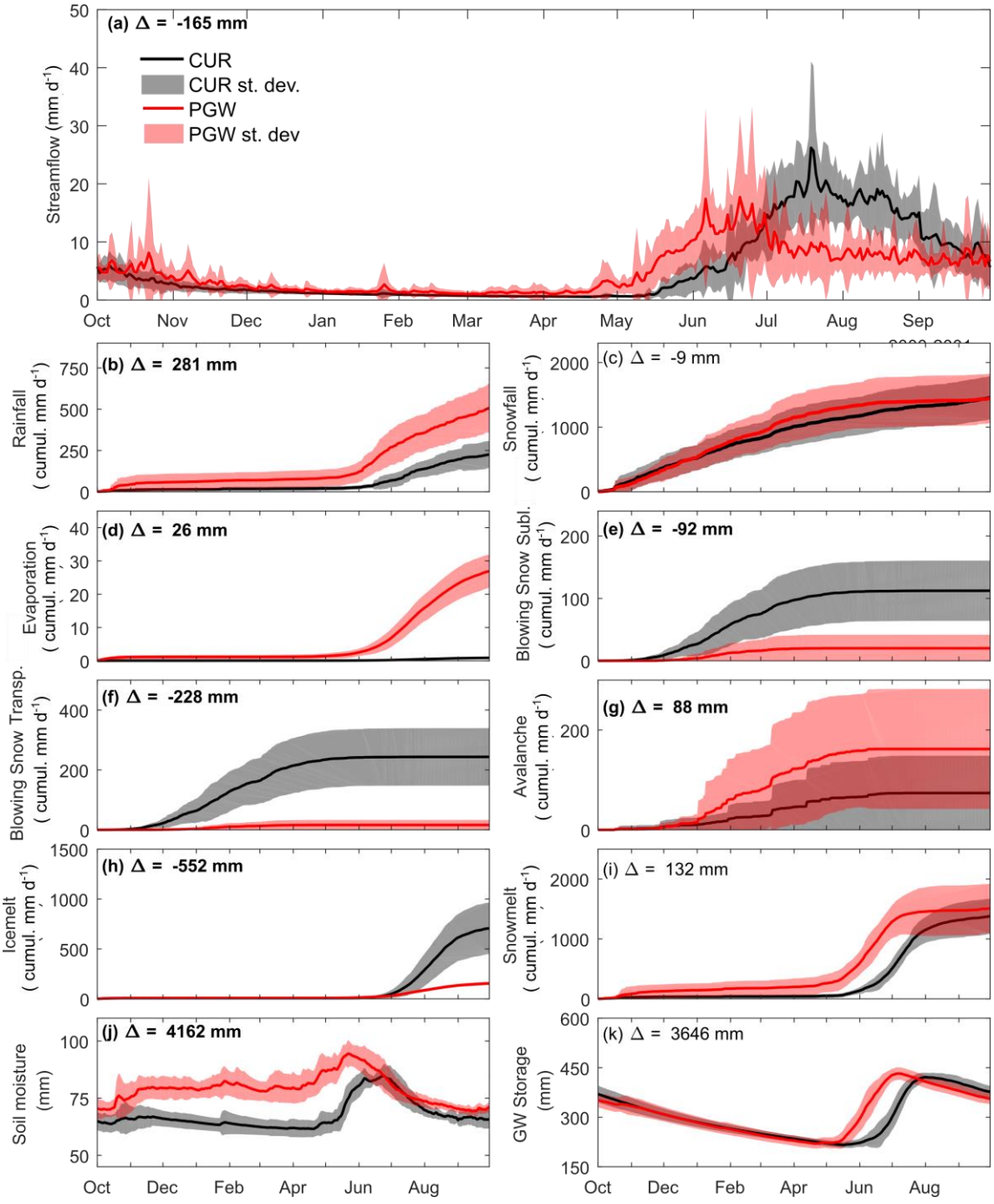

Figure 7.6. Annual basin daily streamflow (a), daily cumulative hydrological processes (b-i) and daily storage volume (j-k) for the current (black) and PGW-reference (red) simulations. The thick line is the 15-year average and the shading is ± 1 standard deviation. Bold fonts are used to indicate significant changes between the two periods. The number for each panel refers to the total change between CUR and PGW.

7.4.5. Streamflow sensitivity

The largest changes in streamflow patterns associated with the landscape simulations were due to variations in the scenarios of the remaining ice, where increased ice volume provided additional meltwater in late summer, and surface water storage, where the removal of depressional storage across the basin increased the flashiness of the streamflow. The variation in the presence of vegetation and subsurface storage through the soil moisture storage capacity had a limited impact on the simulated PGW streamflow (Figure 7.7, Figure 7.8a).

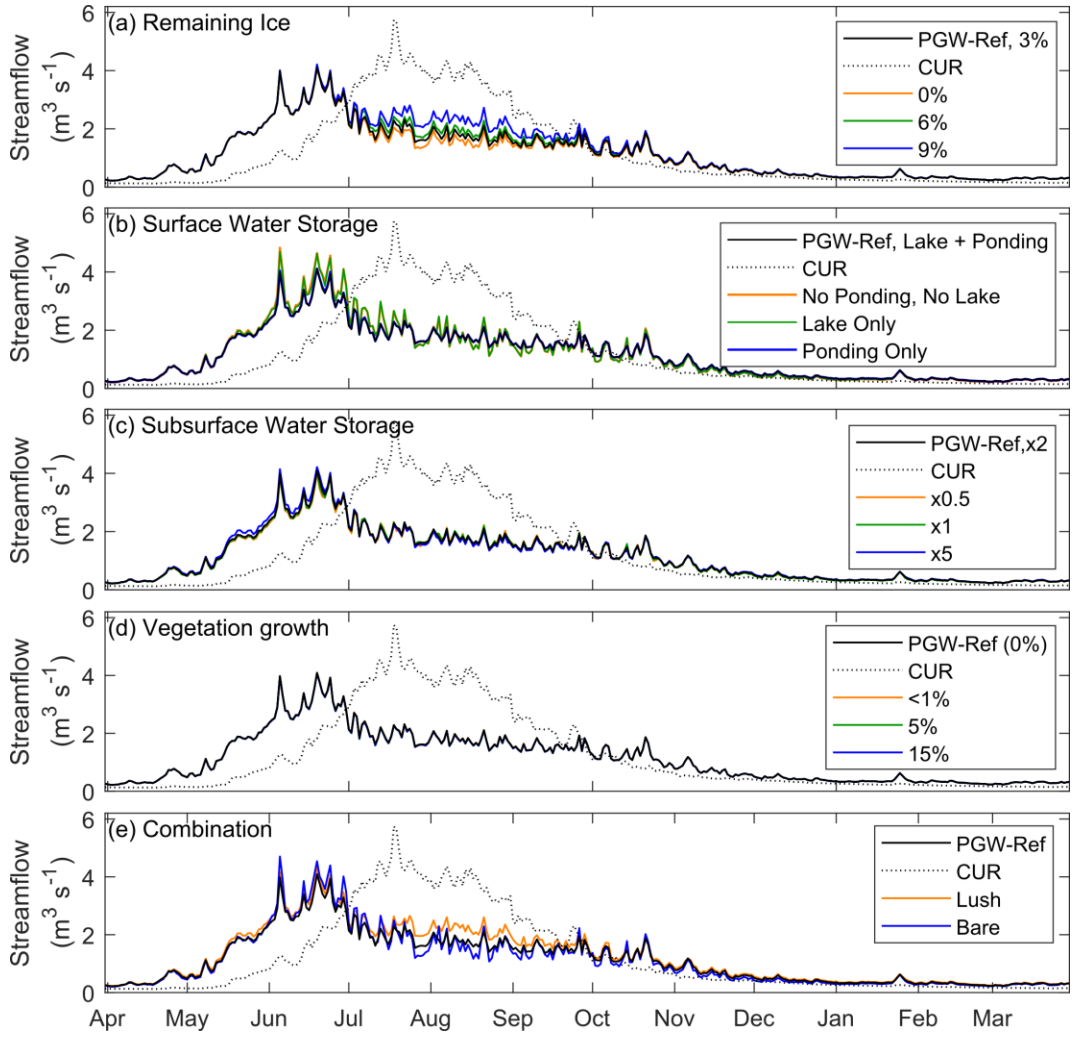

Figure 7.7. Daily streamflow for the different landscape scenarios compared to the reference PGW and CUR simulations for initial glacier area (a), the surface water storage (b), the subsurface water storage(c), the vegetation cover (d) and a combination of the previous scenario (e).

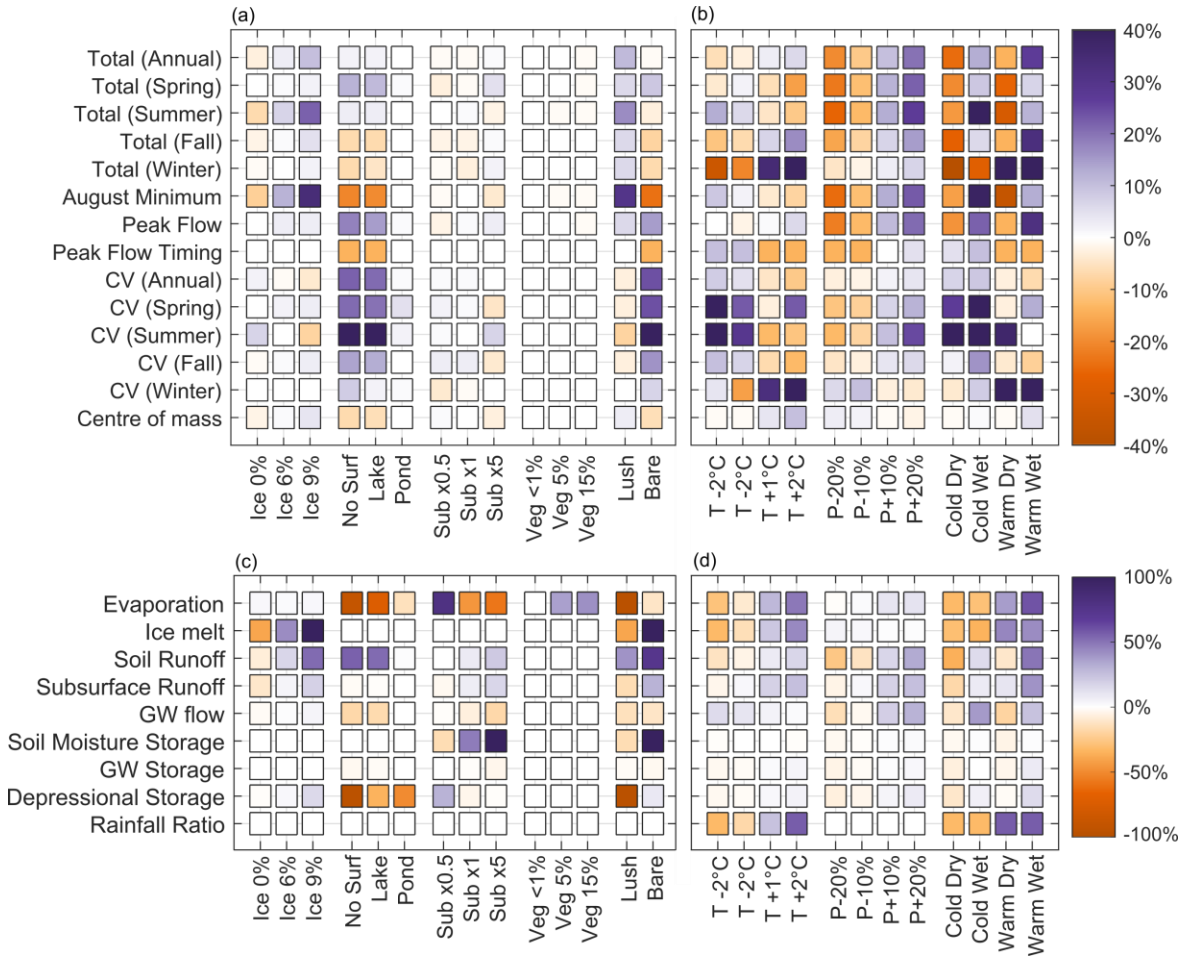

Figure 7.8. Sensitivity to landscape parametrization (a, c) and changes in meteorological forcings (b, d) for the PGW simulation for streamflow signatures (a, b) and hydrological processes (c, d). Note the difference in the colour scale between (a-b) and (c-d).

As the remaining ice volume changed from 3% to 9% glacier coverage, the August low flows increased from -68% to -52% of those simulated under CUR. Similarly, streamflow variability decreased as ice cover increased. The simulations also indicated that a small increase in leftover glacier ice (from 3% to 9% of basin area) could have a large impact on the annual streamflow: in the PGW-reference simulation, the annual streamflow decreased 7% compared to the CUR simulation, but for the 9% glacier cover scenario, streamflow increased by 2%.

The simulations for the scenario without spatially distributed depressional storage (no surface water storage apart from the proglacial lake) had increased streamflow variability, reflected by an increase in the coefficient of variability, compared with the reference PGW scenario. The scenario with spatially distributed depressional storage had a very similar streamflow to the reference simulation. These changes in streamflow variability are caused by the dynamical storage capacity of the pond

system (Figure D.5). Throughout the basin, and especially in the upper reaches of the basin, the depressional storage retained water until reaching maximum capacity, after which streamflow occurred. When no depressional storage was present, melt or rainfall-runoff water predominantly moved downhill as surface runoff. When depressional storage occurred, the ponded water had time to infiltrate and form subsurface and groundwater flow instead of surface runoff. Both this change in the flow pathway and the delayed flow contributed to a smoothed hydrograph. For the scenario with only a pro-glacial lake at the basin outlet, the lake stays nearly full for the entire year, impeding its capacity to provide dynamical storage and smooth the streamflow response. Due to increased evaporation of standing water, the scenario with distributed depressional storage (ponds) resulted in a 3% decrease in annual streamflow compared with the scenarios with either only the proglacial lake or the scenario with no surface water storage (no lake, no ponds) (Figure 7.8c). The two scenarios without distributed surface water storage (with only a proglacial lake and with no surface water storage) also expressed an increase in peak flow value (+17% and +10% compared to reference-PGW).

The increase in subsurface water storage resulted in decreased evaporation, and a decrease in soil moisture, but with a very small net effect on streamflow. Of the five sets of scenarios explored, the presence of vegetation had the lowest overall impact on streamflow. The presence of vegetation in the lower reaches of the basin had a minimal impact on the streamflow volume or timing, reducing streamflow by only 1% when 15% of the basin area had vegetation cover.

The lush and dry scenarios consistently showed larger changes in streamflow behaviour compared to the individual process simulations. The bare scenario only produced a minimal change in annual streamflow (-2%), as the decrease from the absence of glacial ice is somewhat balanced by an increase in streamflow from the lack of surface water storage and reduced evaporation. For the lush scenario, annual streamflow increased 15% compared to the reference PGW simulation, mainly driven by the increased glacier coverage. The bare scenario also presents a 20% increase in streamflow variability, a 16% increase in peak flow values and a 22% decrease in August low flows. The lush scenario, in comparison, decreases streamflow variability by 9% and has a slight increase in peak flow values and a 51% increase in August low flows.

7.4.6. Sensitivity to atmospheric forcings

The streamflow sensitivity to changes in temperature and precipitation is greater than to the changes in the landscape, as it reflects a change in inputs to the basin, and not only the flow and storage within the basin (Figure 7.8b). In comparison with the landscape sensitivity simulations, in which the changes in streamflow could be directly linked to the hydrological processes they impacted, the forcings sensitivity simulations caused shifts distributed across multiple components of the system. As the basin is still snow-dominated in the PGW period, the changes in snowpack accumulation and depletion as well as in streamflow were analyzed to understand the impacts of the forcing sensitivity simulations (Figure 7.9).

The changes in streamflow linked with the temperature sensitivity analysis can be explained by the changes in the snowpack (Figure 7.9a, b). For example, the increase in temperature caused a smaller snowpack accumulation and an earlier depletion, which then resulted in an earlier streamflow onset, peak and recession. The decrease in temperature had the opposite effect: higher snowpack accumulation caused by more precipitation falling as snow and delayed SWE melt resulted in delayed spring streamflow and a larger streamflow peak and recession. The temperature change also resulted in higher winter streamflow; increased temperature caused more melt and rain events in the wintertime and colder temperature resulted in subdued winter flow. The temperature changes do not have a large impact on August-November streamflow, once the snowpack is depleted.

The changes in precipitation caused a similar volume change in the snow accumulation and depletion to the temperature changes: a decrease in precipitation caused a smaller snowpack and an increase in precipitation led to a larger snow accumulation (Figure 7.9c). However, the precipitation perturbation did not shift the timing of SWE accumulation and melt or of streamflow from the PGW-reference simulation (Figure 7.9d). The precipitation perturbation only impacted the volume of streamflow. As the change in precipitation affected both snowfall accumulation and summer rainfall, it caused noticeable changes in the streamflow from April to November.

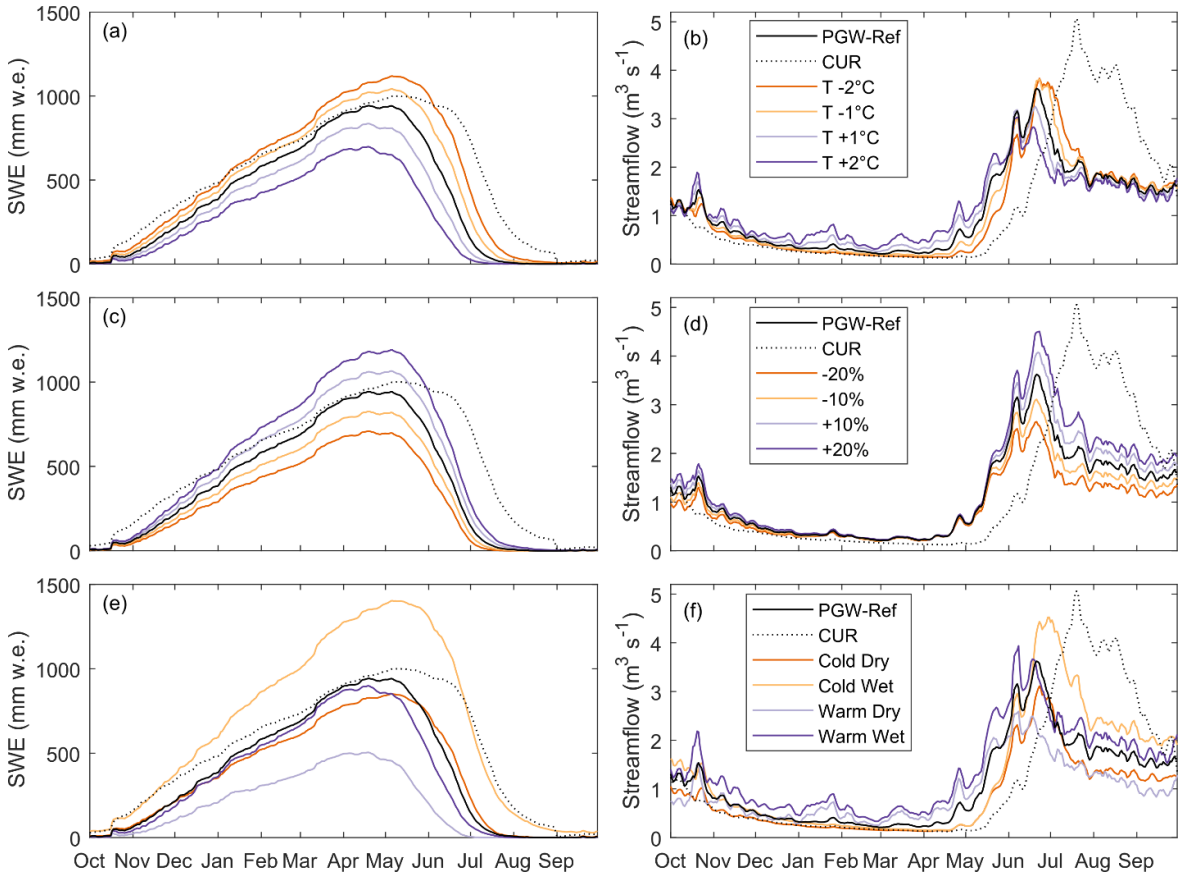

Figure 7.9. Snow water equivalent (a, c, e) and streamflow (b, d, e) for the temperature sensitivity (a, b), precipitation sensitivity (c, d) and combination scenarios (e, f).

The combination of the scenarios clearly shows that the interplay of the precipitation and temperature caused strong changes both in the snowpack and in the streamflow pattern (Figure 7.9e-f). For SWE, as shown in Fig 7.9e, the Cold & Wet scenario produced a high snowpack, with peak SWE 50% higher than the reference PGW simulation. The timing of the snowmelt in the Cold & Wet scenario was similar to the CUR simulation. The Warm & Dry resulted in low snowpack with slower snowmelt depletion, and a complete melt of the snowpack one month earlier than the reference PGW simulation. The Cold & Dry and the Warm & Wet combinations caused smaller changes in the snowpack accumulation and depletion. Both scenarios had slightly smaller peak accumulation than the PGW reference simulation, but the peak SWE for the Warm & Wet occurred three weeks before the peak for the Cold & Dry scenario. The Cold & Dry scenarios resulted in a delayed peak snowpack and snowpack depletion compared to the PGW simulation, while the Warm & Wet scenarios caused an earlier snowpack peak and depletion.

For streamflow, as shown in Figure 7.9f, the four scenarios show distinct changes from the PGW reference simulation. The largest changes are seen in the Cold & Dry and the Warm & Wet (-25% and +27% annual streamflow from the PGW simulation). These two simulations showed a large change in the annual streamflow, but with similar timing as the reference PGW simulation. Both these scenarios showed a consistent increase or decrease over the PGW reference simulation. In contrast, the Cold & Wet scenario and the Warm & Dry scenario resulted in smaller changes in annual streamflow (+13 % and -14% from the reference PGW simulation respectively), but with large changes in timing. For the period June-October, the Warm & Dry scenario averaged a 61% decrease from the PGW reference, while the Cold & Wet scenario was 73% higher than the PGW reference scenario. For the November-April period, the situation reversed, with the Warm & Dry scenario showing an average 10% increase from the PGW reference, while the Cold & Wet scenario was 6% lower than the PGW reference scenario.

7.5. Discussion

7.5.1. WRF and CRHM model performance

The performance of the WRF precipitation product was similar to other studies in high mountains. For example, Collier & Immerzeel (2015) found a correlation coefficient of 0.24 for daily total WRF simulated precipitation at 1-km resolution for the Langtang valley in the Himalayas, and of 0.09 for 5-km resolution. Also using the same WRF product as in this study, Fang & Pomeroy (2020) found an RMSE of 0.6 and 0.43 for two gauges located in an alpine basin on the eastern slopes of the Canadian Rockies after applying a QDM bias correction. The cold air temperature bias for the uncorrected WRF product was an issue already noted in Li *et al*. (2019) and Liu *et al*. (2017)

Comparing model performance for glacio-hydrological studies is difficult due to the wide range of data used in validation, chosen performance metrics and calibration strategies (Van Tiel *et al*., 2020). As few glacio-hydrological studies do not rely on calibration in their model parametrization, it is difficult to draw a definitive model performance comparison to this uncalibrated modelling. One exception is Prasch *et al*. (2013), who also does not calibrate their model for a Himalayan basin and found NSE values for daily runoff of 0.67, 0.70 and 0.73 for the 1996-2000 period at different sub-basins. However, their basin size is 32 800 km^2 with a glacier coverage of only 2% of the basin, which is far less than in the present study (60% glacierized and 24 km^2). Additionally, Prash *et al*. (2013) do not use the seasonal mass balance in their model evaluation, further limiting the model performance comparison. A comparison is possible with other applications of the CRHM in cold regions but

without the presence of glaciers, for which there is comparable streamflow simulation performance. Fang & Pomeroy (2020) used an uncalibrated WRF-CRHM approach to simulate the hydrology of a partially forested alpine basin on the eastern slopes of the Canadian Rockies and obtained an NSE of -33 to 0.72 over 8 years (average of 0.4). For the same basin and model, but forced with observations, Fang *et al*. (2013) obtained NSE ranging from 0.45 to 0.69 over the 2006-2011 period. Krogh *et al*. (2015) simulated the hydrology of two mountainous sub-basins in the Chilean Andes with CRHM and obtained an NSE of 0.53 and 0.32 when run with high-resolution reanalysis data. In a permafrost basin in northern Canada also using the CRHM platform, Krogh and Pomeroy (2019) found an NSE of 0.41 and 0.41 for the validation period and acknowledged that the low model performance may partially be explained by the significant uncertainty in measured streamflow as ice forms in the stream cross-section and snow drifts form in the channel. For the same northern basin but simulated with WRF outputs, Krogh *et al*. (2019) obtained an NSE of 0.45 for the 2002-2012 period.

Model evaluation performed using point mass balance also has a limitation. The HRUs represent the average conditions of an area within the catchment, and therefore, cannot be directly compared with the mass-balance point measurements. These point measurements also have some small-scale variability. For example, Pulwicki *et al*., (2018) found a point scale winter mass balance variability of 0.027 m w.e., 0.035 m w.e. and 0.040 m w.e. for an area of 20 x 20 m for three glaciers in the St. Elias range in Northwest Canada. Similarly, on the Peyto glacier, Young (1981) estimated a measurement error of 0.02, 0.03 and 0.2 m w.e. for zones below 2650, between 2650-2750 and above 2750 m a.s.l. at the metre scale due to the uneven surface of the glacier ice. Considering the limitations linked with the precipitation and snow measurements, the simulated snow accumulation was considered adequate for this study.

7.5.2. Streamflow changes and compensating behaviour in the PGRB

The changes in streamflow between CUR and PGW in the PGRB are in line with finding in other studies of glacierized basins: a strong decrease in summer streamflow combined with an increase in spring flow indicating a shift from glacial and glacio-nival to a nivo-pluvial regime (Hanzer at al., 2018; Huss et Hock, 2018; Addor *et al*., 2014). However, the magnitude of the change in annual streamflow varies between studies, linked to both the modelling approach used and the characteristic of the basins investigated, as discussed in Huss and Hock (2018). For example, in the heavily glacierized Rofental basin, in the Otzal Alps, Hanzer *et al*. (2018) found a decrease of up to 39% in annual streamflow under RCP 8.5 by 2100, but in their case, annual precipitation did not have a clear signal

between the various GCMs used. For the Upper Athabasca River basin, with a drainage area of 9720 km², of which 2.8% is glacier cover, summer streamflow at the end of the century has been predicted to be only a third of the 1981-2010 baseline, despite a predicted increase in precipitation (Chernos *et al.*, 2020). In six basins in the Pacific Northwest, Frans *et al.* (2018) found that an increase in air temperature and precipitation between 1960-2010 and 2080-2099 combined with a strong glacier retreat resulted in a strong decrease in August and September streamflow.

For the PGRB, the annual streamflow only decreased by 7% despite large changes in glacier extent and weather forcing that occurred between the CUR and PGW simulations. This change in streamflow between CUR and PGW is linked to many interconnected processes, with many of these processes compensating for each other and dampening the streamflow response. For example, the small decrease in snowfall in the PGW simulation was more than compensated by a near-complete cessation of the blowing snow sublimation and associated winter blizzards. Similarly, increased precipitation was partly compensated by increased evapotranspiration. The largest example of this compensation in the PGRB is the increase in precipitation (+281 mm) compared to the decrease in ice melt (-552 mm). This suggests that the changes in annual streamflow would be more pronounced if the increase in rainfall was not able to compensate for some part of the loss of the glacier ice in the basin. A compensating behaviour has also been observed in the PGRB by Pradhananga and Pomeroy (2022b) but in a reverse direction. They found that glacier ice melt compensated for declining precipitation and snowmelt, resulting in increased discharge between the 1960s and the 2010s. Glaciers are known to have a compensating effect on streamflow (van Tiel *et al.*, 2020a, 2021). Even with very low glacier coverage in a basin, glacier melt can increase late summer flow and smooth out variability (Hock *et al*., 2005; Huss *et al*., 2018). In the PGRB, the leftover glacier volume had a large influence on the end-of-century streamflow response. These end-of-century estimates are based on regional estimates from Clarke *et al*. (2015) but carry a reasonable uncertainty. Further assessments of glacier retreat rates in the eastern slopes of the Canadian Rockies are needed to better constrain estimates of end-of-century water supply from headwater basins.

Further compensation is noticed in the sensitivity of SWE and streamflow to changes in precipitation and temperature. The Cold & Dry and the Warm & Wet scenarios have compensating mechanisms resulting in small overall changes in SWE: the Cold & Dry received reduced snowfall but had limited snowmelt throughout the winter. The Warm & Wet received higher precipitation, but more of it as rainfall and had more melt events throughout the winter season. In contrast, the Cold & Wet and

the Warm & Dry scenarios showed drastic changes in SWE. For these two scenarios, the precipitation and temperature amplified the response in snow accumulation and melt. However, the large changes in SWE did not directly translate to large changes in streamflow. The two scenarios that showed minimal changes in SWE, the Warm & Wet scenario and the Cold & Dry scenario, had the largest changes in annual streamflow. For example, in the Warm & Wet scenario, increased temperature and increased precipitation compensated for each other to limit the changes in SWE, but the streamflow response was amplified, with higher rainfall and higher melt throughout the year.

7.5.3. Advantages and limitations of the WRF-CRHM Peyto model

The hydrological modelling approach presented here, combining high-resolution WRF atmospheric forcing for two 15-year periods with a semi-distributed, process-oriented, uncalibrated hydrological model with a multi-objective model evaluation, provided a suitable methodology to look into possible futures in a remote, glacierized basin. As discussed in Ragettli *et al*. (2014), using a physically-based model in glacio-hydrological studies with a strong physical representation of processes depends less on calibration and thus is less subject to compensation of errors through different model components. They found when comparing a simple model and an enhanced temperature index model that, even though both models had skill in reproducing historical conditions, the simple model was prone to compensating error for a potentially warmer future climate, which results in different predictions in simulated melt and runoff. This is consistent with the argument from Pomeroy *et al* (2007) that "a *purpose-built physically based model based on a good understanding of the principles and characteristics of hydrology in a basin with an appropriate structure and appropriate spatial resolution and parameter selection should have a good chance of simulating the hydrological cycle".* Therefore, considering its reasonable performance for both streamflow, winter accumulation and summer melt, the WRF-CRHM model developed for the Peyto basin was considered fit for purpose for this analysis despite the relatively short duration of the streamflow measurement for evaluation purposes.

WRF-CUR was able to reproduce the near-surface driving meteorology in the Peyto basin. It could run at a higher resolution, which may provide more realistic temperature and precipitation patterns. However, higher-resolution WRF simulations would require greater computational capacity. The 4km simulation provides an appropriate middle ground: high enough resolution to explicitly represent convection processes and steep topography, but still manageable for large spatial coverage for multiple years. It was therefore considered a good option to assess future climate change (Prein *et*

al., 2015; Liu *et al.*, 2017; Warscher *et al.*, 2019). One key limitation of this approach is its use of only one climate trajectory (RCP 8.5). This only allows the investigation of a possible "worst-case" scenario instead of presenting possible differences due to climate mitigation actions linked to other pathways scenarios. However, the trade-off between high spatial resolution with dynamically downscaled forcings and multiple scenarios was considered justified in this study. Additionally, WRF-PGW does not allow for changes in intensity or frequency of teleconnections such as ENSO, which is known to affect snow distribution over the Western Cordillera (Moore and Demuth, 2001; Demuth and Keller, 2006) or storm tracks due to climate change, as it is initialized with current ERA data, as discussed in Prein *et al*. (2017).

7.6. Conclusions

An approach merging process-oriented glacio-hydrological modelling covering the range of processes acting on a high mountain basin with high resolution with state-of-the-art atmospheric modelling forcings was presented for the PGRB in the Canadian Rockies. Changes in the atmospheric forcings, such as an increase of 16% in precipitation and a 5˚C in annual air temperature, resulted in an annual decrease of 7% in streamflow by the end of the century. This decrease was combined with a strong shift in seasonality, with a 93% increase in June streamflow and a 53% decrease in July-August flow. Peak flow shifted one month earlier and decreased by 30%. Additionally, winter flow events started to occur in the end-of-century simulation. Overall, the Peyto basin changed from a glacial regime to a nival regime, with the snow contribution to streamflow increasing from 70% to 84%. To the author's knowledge, this is the first process-based, hydrological modelling assessment of future glacierized basin conditions for the Canadian Rockies mountain range. This assessment brings valuable knowledge of the possible evolution of the PGRB basin and can provide insights into the future hydrological conditions of the headwaters of the large river systems crossing interior Canada.

Glaciers are expected to almost disappear from the Peyto basin, leaving behind new landscapes with potentially differing hydrological capacities. To assess the uncertainty linked to the future landscape parametrization, 14 landscape change scenarios were designed. Results showed that annual flow volume was most sensitive to the remaining ice cover and that changes in surface water storage had a strong impact on flow variability. Vegetation growth had a low impact on future streamflow as these cold, harsh environments with limited water availability for plant use do not seem to be conducive to plant colonization in the upcoming decades. Plant colonization might be important for

longer-term studies. When comparing this landscape sensitivity analysis to an atmospheric forcings sensitivity analysis, changes in temperature and precipitation had an overall larger impact on end-of-century streamflow, as they strongly impacted both snow accumulation and melt, the dominating mass flux in the basin, and summer precipitation. Based on these sensitivities, two areas of future research are suggested: continued efforts to improve atmospheric forcings for high mountain basins, as the snow and streamflow responses were highly sensitive to the changes in temperature and precipitation; and further consideration of future landscape change in deglacierized basin.

While this study was limited to one modelling approach, in a single location and with one atmospheric prediction, it highlighted the importance of including more than glacier retreat in assessments of future water supply in mountain landscapes. Mountain headwater basins display a complex mosaic of processes, which can compensate for each other and dampen the net response in streamflow. To capture the dynamic interactions between these processes and obtain a comprehensive knowledge of predicted changes in mountain water supply, glacio-hydrological simulations should include a range of processes and be built upon a robust conceptual and physical understanding of mountain hydrology. Similar projects should be conducted with different glacio-hydrological model approaches and forcings to obtain further insights into the influence of landscape change on the hydrological processes and streamflow generation in rapidly changing mountains.

SYNTHESIS AND CONCLUSION

8.1. Closing the research gap

Mountain water reaches populations far away from the mountains and besides supporting aquatic and terrestrial ecosystems, it is used by humans for hydropower, agriculture, irrigation and drinking water. These headwater mountain systems are changing quickly with complex interconnected processes that can result in contrasting and compensating behaviour. Understanding the processes, how they contribute to changing the water availability in headwater systems, and how to include them in hydrological models, is needed to improve predictions and adaptation capacities both in mountain environments and downstream.

The primary research goal this thesis aimed to address was the lack of existing comprehensive glacio-hydrological modelling approaches to assess the complex changes occurring in glacierized basins. This lack of appropriate modelling approaches, coupled with the disconnect between the physical understanding of individual mountain hydrological processes and their representation in basin hydrological assessment, results in limited or uncertain diagnosis and prediction of water resources in mountains. By developing a modelling framework focused on glacio-hydrological processes, this thesis completed a first and significant step towards filling this research gap. This modelling framework started by investigating individual processes, targeting specific processes that were either not included or had limited representation in glacio-hydrological models, or had high uncertainty. The individual processes investigated were streamflow, specifically its measurement uncertainty, melt under debris, specifically measuring the debris thickness, and the glacier surface energy balance, specifically the impact of forest fire smoke and soot on the surface melt. Algorithms for melt-under debris and hourly energy balance with katabatic wind parametrization were developed, tested, and included as modules in the CRHM library. Once an adequate library of processes was available, a glacio-hydrological model developed purposefully for the Peyto glacierized basin was designed and tested. The CRHM-Peyto model was used to investigate current (1987-2020) conditions, using measured meteorology, with a specific focus on the causes of inter-annual variability. The CRHM-Peyto model was then adapted to compare current (2000-2015) and future conditions (2085-2100, RCP 8.5 following a pseudo-global warming approach) using dynamically downscaled, bias-corrected WRF atmospheric outputs. In this current-future comparison, a specific

emphasis was given to assessing how changing hydrological processes result in a shift in streamflow and to understanding the sensitivities to changing landscape and meteorology.

The main findings of each chapter are summarized below.

- The installation of an automated salt dilution system permitted relatively reliable streamflow measurement with quantifiable uncertainty in a remote, dynamic, unstable and flashy proglacial stream. Streamflow uncertainty averaged 12% of streamflow, ranging between 4 and 41%. The Peyto Glacier Research Basin streamflow is highly variable, with peak flow varying from early July to early September, and a characteristic glacier melt diurnal signal occurring from mid-July to early September. Peak streamflow varies between 5.7 m^3s^{-1} and 10.1 m^3s^{-1}.
- The thickness of the debris-covered area at the edge of Peyto glacier was estimated by developing a correlation between surface temperature and debris thickness. The variation in the correlation between surface temperature and debris cover-thickness was thoroughly investigated for weather and data collection factors. The analysis showed that a reliable time to obtain surface temperature correlating to debris thickness is a few hours before sunrise or under cloudy conditions. Modelled debris thickness was strongly sensitive to biases in the range of measured debris thickness for the measurements used in the empirical models, with a strongly reduced capacity to reproduce observed debris thickness occurring when the regression models are developed using only shallow, medium or deep measured debris thickness.
- The impacts of forest fire activity on glacier melt were investigated through field-data analysis, modelling experiment and remote sensing analysis for the 2015-2020 melt season at Athabasca Glacier. Forest fire activity was shown to influence surface glacier melt through both a decrease in the surface albedo following smoke drifting over the glacier surface and through impact on the atmospheric conditions above the glacier. Days with smoke were warmer and drier, with reduced incoming shortwave radiation compared to non-smoky, clear days. For the period 2015-2020, the radiation attenuation from smoke partly compensated the increase in the melt due to reduced albedo for years when smoke is detected at the Athabasca. In years when no smoke drifted over the glacier, the low albedo increased seasonal melt by more than 10%.

- A CRHM glacio-hydrological model was developed and tested for the Peyto basin to diagnose hydrological behaviour, with a focus on streamflow generating processes. Model results showed that for the 1990-2020 period, inter-annual variability dominated the streamflow, leading to variable annual streamflow and streamflow composition. Snowmelt always provided the largest volume to annual streamflow (44-89%), with lower snowmelt contributions occurring in high streamflow years. Ice melt provided between 10-45% of total streamflow, with a higher contribution associated with high flow years. Both rainfall-runoff and firn melt contribute less than 13% each of annual streamflow. Years with high streamflow were on average 1.43˚C warmer than low streamflow years, and high streamflow years had lower winter snow accumulation, earlier snowmelt and higher summer rain than years with low streamflow.
- Annual precipitation depth increased 16% and annual air temperature increased 5˚C from current (2000-2015) to future (2085-2100, RCP8.5, under a PGW approach) climates in the Peyto Glacier Research Basin. These atmospheric changes reduced annual streamflow volumes by 7%, with a strong shift in seasonality resulting in a 93% increase in June streamflow and a 53% decrease in July-August flow. Peak daily streamflow timing advanced one month and peak daily discharges decreased by 30%. Additionally, winter flow events started to occur in the PGW simulation. To assess the uncertainty linked to the future landscape parametrization in the Peyto basin, 14 landscape change scenarios targeting the remaining glacier area in the basin, the surface water storage, subsurface water storage and vegetation growth were designed. Annual flow volume was most sensitive to the remaining ice cover and changes in surface water storage had a strong impact on flow variability. Comparing this landscape sensitivity analysis to an atmospheric forcings sensitivity analysis showed that changes in temperature and precipitation have an overall larger impact on end-of-century streamflow, as they strongly influence both snow accumulation and melt, the dominating mass flux in the basin, and summer precipitation.

8.2. Pushing the glacio-hydrological modelling discipline forward

Beyond the conclusions of each individual chapter, this thesis pushes forward four shifts in mountain glacio-hydrological modelling: (1) applying the *peak water* concept to estimate streamflow changes at the basin scale is inadvisable, (2) assessing changes in melt or streamflow based on individual processes is likely to mask compensatory behaviour, (3) the role of glaciers in buffering inter-annual

streamflow variability should be further discussed, and (4) physical understanding gained from spending time in glacierized basins provides significant advantages to apply glacio-hydrological models. Itshould not be neglected as remote sensing capacities and computational capabilities increase.

This thesis demonstrated that assessing changes in hydrology in mountain headwater systems based only on the glacier response, in the typical *peak water* approach, does not provide a complete picture. While this concept of *peak water* is a robust concept to evaluate the response of glacier wastage in a warming climate, it should not be used to evaluate changes in the water supply of mountain systems. That is, drawing conclusions of streamflow changes at the micro- to macro-basin scale based only on the shifts in glacier cover, as is often done with *peak water* studies, provides an incomplete and potentially misleading picture. While glacier wastage is an important component of the streamflow generation in mountain systems, other shifts, such as precipitation, temperature and routing of water in the basin, can be equally or more important depending on what aspect of the streamflow is more relevant to a specific study. This is showcased in the landscape evolution and climate change sensitivity simulations in chapter 7. For example, for late summer flow in the Peyto Glacier Research Basin, increasing glacier cover from 3 to 9% of the basin increased flow volume by 22%, but increasing predicted precipitation by 20% increased summer flow by 27%. In that case, climate change and glacier retreat had a similar influence on the streamflow response. However, for flow variability, the volume and distribution of surface water storage in the basin had the largest influence on streamflow and were more important than the amount of glacier ice left in the basin or precipitation change. Another landscape change that has been discussed to be an important influence on future mountain hydrology is vegetation growth. For example, Somers *et al.* (2019) found that while groundwater discharge could compensate for the decrease in glacier meltwater in the Tropical Andes, increasing evapotranspiration of mountain vegetation would eventually lead to a decrease in water availability. In snow-dominated northern landscapes, shrubification can also cause a large shift in blowing snow transport, snow accumulation and subsequent melt (Krogh and Pomeroy, 2019). However, in the Peyto Glacier Research Basin, the simulated increase in vegetation only has a minimal influence on future streamflow, as future vegetation would have little water available for evapotranspiration in late summer under future climate. This vegetation would also have a limited influence on the blowing snow transport, as it would already be limited due to the warmer conditions. Assuming that either climate change, glacier change or landscape change is the most important aspect to predict mountain hydrology and that the other two can either be ignored

or highly simplified is a flawed approach. While there is an ongoing need to improve the understanding and parametrization of individual processes, such as in Chapters 2-4, this focus on individual processes has to occur in concert with the understanding of the system and the connections between the processes. Reducing mountain hydrological changes to only glacier change, as is often done with the *peak water* concept, might explain why this elusive regime shift is often not discernable in actual mountain streamflow.

Another way in which the complexity of the mountain system was revealed in this thesis was through the compensatory behaviour showcased at multiple scales. While the influence of surface darkening and albedo change on snow and ice melt is well-documented in the literature (Skiles et al., 2019), and the influence of wildfire soot on surface albedo has previously been discussed (Magalhães *et al.*, 2019), the compensating influence of smoke on the radiation reaching the glacier surface had not previously been quantified. This compensatory behaviour between the atmospheric transmissivity attenuation and the darkening surface albedo is nuanced and operates at multiple levels. First, the transmissivity change in the atmosphere due to the presence of smoke had opposite effects on the longwave and the shortwave irradiance, diminishing the net change in irradiance. If one only considered the influence of smoke on the shortwave irradiance, and use only shortwave irradiance to assess the melt response, as is done in some enhanced temperature index models, the influence of smoke on melt would be assumed to be larger than it is. Then, compensatory behaviour is also noticeable between the reduced all-wave irradiance and the reduced albedo. If one only used albedo decrease to assess the change in melt and ignored the change in irradiance received at the glacier surface, the influence of wildfire activity on glacier melt would be overestimated (Aubry-Wake *et al*., 2022a). At the basin-scale, compensatory behaviour was seen between the various streamflow components in the glacio-hydrological modelling outputs of the Peyto Glacier Research Basin, as trends in individual seasonal components of the headwater system did not translate to trends in the annual streamflow. Individuals processed in the basin interacted to compensate for the response in streamflow. For example, low snowfall years resulted in high streamflow years, as earlier glacier ice exposure increased the glacier melt contribution to streamflow. This interaction and compensation between individual processes are also seen in the end-of-century simulations, with the decrease in snowfall being balanced by the near cessation of blowing snow sublimation and mitigating the net changes in the hydrology in the basin. This assessment of compensating behaviour in glacierized catchment hydrology pushes forward the importance of analyzing individual processes and their

interactions instead of focusing on only one or a few processes to conclude on changes in the hydrology of glacierized basins.

Glaciers are known to buffer inter-annual streamflow variability and to compensate for hot and dry periods at the seasonal to decadal timescale (Jansson *et al.*, 2003; van Tiel *et al.*, 2021; Pradhananga and Pomeroy, 2022b). However, the relationship between glacier melt and streamflow variability is not straightforward, as discussed by van Tiel *et al.* (2020). The work presented in this thesis further advanced this understanding by showing that in the Peyto Glacier Research Basin, icemelt was most highly correlated to streamflow, followed by the timing of ice exposure on the glacier, even though snowmelt accounted for the largest contribution to annual streamflow. This provides insights into the subtleties of the interactions between snow dynamics, glacier wastage and streamflow generation and suggests that the understanding of the hydrological role of glaciers should be assessed in more detail. Carefully distinguishing between and comparing on and off glacier snow accumulation and melt, glacier melt and wastage, as well as assessing the influence of the glacier storage at varying spatial and temporal scales is needed to assess the cryospheric influence on streamflow variability.

Expertise in field methods and knowledge of the physical environment is crucial to accurately collect, understand and process data into products usable for modelling. Field data in remote mountain settings is difficult to collect and comes with limitations and uncertainties. To properly use this data in modelling approaches, one has to be aware and careful to respect these limitations to avoid using this field data in inappropriate ways and drawing flawed conclusions. This was showcased in Chapter 2, where field knowledge was shown to be essential to characterize the uncertainties of the salt dilutions measurements associated with the location of the electrical conductivity probes, and again in Chapters 7 and 8, where a strong conceptual understanding of the landscape based on multiple observations and field visits was used to guide model development and parametrization. In this thesis, spending time in, and carefully observing, the mountain landscape was instrumental in developing the modelling approach and having confidence in its application. Given the limited data available to assess model performance, having an intuitive understanding of the mountain system allowed errors in the analysis, such as typos in the modelling codes, to be noticeable as they would give results that violated the wealth of local knowledge gained through fieldwork. While field data collection is time-consuming and expensive, it is essential not only to obtain the data to force and

parametrize hydrological models but also to develop knowledge of mountain landscapes to guide the research process.

8.3. Recommendation for future analysis

Glacier retreat in mountain systems has wide-ranging consequences on human systems, from agriculture, hydropower, potable water, recreation, spirituality and demography. Furthering the process understanding and prediction capacities in mountains is primordial to ensure communities can adapt to the ongoing changes. Future work should extend the modelling framework developed and tested with CRHM in the Peyto Glacier Research Basin to other glacierized headwaters with different climate conditions, such as the Alps, the Himalayas or the Andes, to test the transferability robustness of the CRHM modelling approach developed in this thesis.

An ongoing challenge in mountain hydrology is the availability and reliability of hydrometeorological data for model parametrization and evaluation. Even in well-studied basins such as the Peyto Glacier Research Basin, large gaps in observations exist, which impede efforts to develop robust understanding and prediction capacities in headwater systems. Continuing and expanding the monitoring of mountain hydrological processes is primordial to ensure a reliable assessment of current and future water availability. Focused field campaigns to target the processes with the highest uncertainties in their parametrization, such as end-of-winter snowpack linked with snow redistribution processes, and subsurface water storage and flow, should also occur. One approach could be to enhance monitoring efforts in a collaborative approach in well-studied glacierized basins across different mountain ranges.

One key process that has not yet been implemented in the CRHM-glacier modules is ice-flow dynamics. Implementing an ice flow routine, or developing a coupling with the existing routine, is needed to simulate the evolution of glacierized basins. Ice cover was shown to be a strong factor in the future streamflow regime of the Peyto Glacier Research basin, and therefore, further research is needed to reduce the uncertainty in estimating the remaining ice cover over the upcoming decades in the Canadian Rockies and inform glacio-hydrological simulations. Another process that would be interesting to further develop and test in the CRHM glacier modules would be linked to water temperature, an important variable for downstream ecology.

The alpine glacierized basin monitoring and modelling advances should be conducted in a collaborative, open-science framework following the FAIR principles. Furthermore, these physical

hydrology developments should be conducted in respectful collaboration with and inclusion of stakeholders and Indigenous Peoples when possible.

REFERENCES

Abatzoglou JT, Williams AP, Barbero R. 2019. Global Emergence of Anthropogenic Climate Change in Fire Weather Indices. *Geophysical Research Letters* **46** (1): 326–336 DOI: 10.1029/2018GL080959

Addor N, Rössler O, Köplin N, Huss M, Weingartner R, Seibert J, Cha Y, Park SS, Kim K, Byeon M, et al. 2014. Robust changes and sources of uncertainty in the projected hydrological. *Water Resources Research* **50** (10): 7541–7562 DOI: 10.1002/2013WR014979.Reply

Anderson ER. 2017. Modelling changes in multi-decadal streamflow contributions - Bologna glacier, Selwyn mountains, NWT, Canada.University of Saskatchewan.

Anderson LS, Anderson RS. 2018. Debris thickness patterns on debris-covered glaciers. *Geomorphology* **311**: 1–12 DOI: 10.1016/j.geomorph.2018.03.014

Anderson S, Radic V. 2020. Identification of local water resource vulnerability to rapid deglaciation in Alberta. *Nature Climate Change* DOI: 10.1038/s41558-020-0863-4

Andreas EL. 1987. A theory for the scalar roughness and the scalar transfer coefficients over snow and sea ice. *Boundary-Layer Meteorology* **38** (1–2): 159–184 DOI: 10.1007/BF00121562

Andreas EL. 2002. Parameterizing scalar transfer over snow and ice: A review. *Journal of Hydrometeorology* **3** (4): 417–432 DOI: 10.1175/1525-7541(2002)003<0417:PSTOSA>2.0.CO;2

Annandale JG, Jovanovic NZ, Benadé N, Allen RG. 2002. Software for missing data error analysis of Penman-Monteith reference evapotranspiration. *Irrigation Science* **21**: 57–67 DOI: 10.1007/s002710100047

Aubry-Wake C, Baraer M, McKenzie JM, Mark BG, Wigmore O, Hellström R, Lautz LK, Somers LD. 2015. Measuring glacier surface temperatures with ground-based thermal infrared imaging. *Geophysical Research Letters* **42** (20): 8489–8497 DOI: 10.1002/2015GL065321

Aubry-Wake C, Bertoncini A, Pomeroy JW. 2022a. Fire and Ice: The Impact of Wildfire-Affected Albedo and Irradiance on Glacier Melt. *Earth's Future* **10** (4): e2022EF002685 DOI: 10.1029/2022EF002685

Aubry-Wake C, Lamontagne-Hallée P, Baraer M, McKenzie JM, Pomeroy JW. 2022b. Using ground-based thermal imagery to estimate glacier debris thickness: fieldwork considerations to improve effectiveness. Journal of Glaciology, 1-17. DOI:10.1017/jog.2022.67

Aubry-Wake C, Pradhananga D, Pomeroy JW. 2022c. Diagnosing Hydrological Process Controls in Streamflow Generation and Variability in a Glacierized Alpine Headwater Basin. Hydrological Processes. Accepted Author Manuscript e14731. https://doi.org/10.1002/hyp.14731

Ayala A, Pellicciotti F, MacDonell S, McPhee J, Burlando P. 2017. Patterns of glacier ablation across North-Central Chile: Identifying the limits of empirical melt models under sublimation-favorable conditions. *Water Resources Research* **53** (7): 5601–5625 DOI: 10.1002/2016WR020126

Ayala A, Pellicciotti F, Shea JM. 2015. Modeling 2m air temperatures over mountain glaciers: Exploring the influence of katabatic cooling and external warming. *Journal of Geophysical*

Research **120** (8): 1–19 DOI: 10.1002/2015JD023137.Received

Ayers HD. 1959. Influence of Soil Profile and Vegetation Characteristic on Net Rainfall Supply to Runoff. In *Spillway Design Floods: Proceeding of Hydrology Symposium No. 1, National Research Council of Canada*198–205.

Baker EA, Lautz LK, McKenzie JM, Aubry-Wake C. 2019. Improving the accuracy of time-lapse thermal infrared imaging for hydrologic applications. *Journal of Hydrology* **571**: 60–70 DOI: 10.1016/j.jhydrol.2019.01.053

Ban N, Caillaud C, Coppola E, Pichelli E, Sobolowski S, Adinolfi M, Ahrens B, Alias A, Anders I, Bastin S, et al. 2021. The first multi-model ensemble of regional climate simulations at kilometer-scale resolution, part I: evaluation of precipitation. *Climate Dynamics* **57** (1–2): 275–302 DOI: 10.1007/S00382-021-05708-W/FIGURES/11

Bandyopadhyay A, Bhadra A, Raghuwanshi NS, Singh R. 2008. Estimation of monthly solar radiation from measured air temperature extremes. *Agricultural and Forest Meteorology* **148** (11): 1707–1718 DOI: 10.1016/j.agrformet.2008.06.002

Baraer M, Mark BG, McKenzie JM, Condom T, Bury J, Huh KI, Portocarrero C, Gómez J, Rathay S. 2012. Glacier recession and water resources in Peru's Cordillera Blanca. *Journal of Glaciology* **58** (207): 134–150 DOI: 10.3189/2012JoG11J186

Baraer M, Mckenzie J, Mark BG, Gordon R, Bury J, Condom T, Gomez J, Knox S, Fortner SK. 2015. Contribution of groundwater to the outflow from ungauged glacierized catchments: A multi-site study in the tropical Cordillera Blanca, Peru. *Hydrological Processes* **29** (11): 2561–2581 DOI: 10.1002/hyp.10386

Barnett TP, Adam JC, Lettenmaier DP. 2005. Potential impacts of a warming climate on water availability in snow-dominated regions. *Nature* **438** (7066): 303–309 DOI: 10.1038/nature04141

Bartelt P, Lehning M. 2002. A physical SNOWPACK model for the Swiss avalanche warning. *Cold Regions Science and Technology* **35** (3): 123–145 DOI: 10.1016/S0165-232X(02)00074-5

Bash EA, Marshall SJ. 2014. Estimation of glacial melt contributions to the Bow River, Alberta, Canada, using a radiation–temperature melt model. *Annals of Glaciology* **55** (66): 138–152 DOI: 10.3189/2014AoG66A226

Bedia J, Herrera S, Camia A, Moreno JM, Gutiérrez JM. 2014. Forest fire danger projections in the Mediterranean using ENSEMBLES regional climate change scenarios. *Climatic Change* **122** (1–2): 185–199 DOI: 10.1007/s10584-013-1005-z

Beniston M. 2003. Climatic change in mountain regions: A review of possible impacts. *Climatic Change* **59** (1–2): 5–31 DOI: 10.1023/A:1024458411589

Beniston M, Farinotti D, Stoffel M, Andreassen LM, Coppola E, Eckert N, Fantini A, Giacona F, Hauck C, Huss M, et al. 2018. The European mountain cryosphere: a review of its current state, trends, and future challenges. *The Cryosphere* **12**: 759–794 DOI: 10.5194/tc-12-759-2018

Benn DI, Evans DJA. 2010. *Glaciers and Glaciation*. Routledge: London.

Bernhardt M, Schulz K. 2010. SnowSlide: A simple routine for calculating gravitational snow transport. *Geophysical Research Letters* **37** (11) DOI: 10.1029/2010GL043086

Bernhardt M, Schulz K, Liston GE, Zängl G. 2012. The influence of lateral snow redistribution processes on snow melt and sublimation in alpine regions. *Journal of Hydrology* **424**–**425**: 196–206 DOI: 10.1016/j.jhydrol.2012.01.001

Bertoncini A, Aubry-Wake C, & Pomeroy JW. 2022. Large-area high spatial resolution albedo retrievals from remote sensing for use in assessing the impact of wildfire soot deposition on high mountain snow and ice melt. Remote Sensing of Environment, 278, 113101. DOI: 10.1016/J.RSE.2022.113101

Beven K. 2016. Facets of uncertainty: Epistemic uncertainty, non-stationarity, likelihood, hypothesis testing, and communication. *Hydrological Sciences Journal* **61** (9): 1652–1665 DOI: 10.1080/02626667.2015.1031761

Beven K. 2021. Issues in generating stochastic observables for hydrological models. *Hydrological Processes* **35** (6): e14203 DOI: 10.1002/HYP.14203

Birsan MV, Molnar P, Burlando P, Pfaundler M. 2005. Streamflow trends in Switzerland. *Journal of Hydrology* **314** (1–4): 312–329 DOI: 10.1016/j.jhydrol.2005.06.008

Bliss A, Hock R, Radic V. 2014. Global response of glacier runoff to twenty-first century climate change. *Journal of Geophysical Research: Earth Surface* **119**: 717–730 DOI: 10.1002/2013JF002931

Bolch T, Menounos B, Wheate R. 2010. Landsat-based inventory of glaciers in western Canada, 1985-2005. *Remote Sensing of Environment* **114** (1): 127–137 DOI: 10.1016/j.rse.2009.08.015

Boxall K, Willis I, Giese A, Liu Q. 2021. Quantifying Patterns of Supraglacial Debris Thickness and Their Glaciological Controls in High Mountain Asia. *Frontiers in Earth Science* **9**: 504 DOI: 10.3389/feart.2021.657440

Bristow KL, Campbell GS. 1984. On the relationship between incoming solar radiation and daily maximum and minimum temperature. *Agricultural and Forest Meteorology* **31**: 159–166

Burga CA, Krüsi B, Egli M, Wernli M, Elsener S, Ziefle M, Fischer T, Mavris C. 2010. Plant succession and soil development on the foreland of the Morteratsch glacier (Pontresina, Switzerland): Straight forward or chaotic? *Flora: Morphology, Distribution, Functional Ecology of Plants* **205** (9): 561–576 DOI: 10.1016/j.flora.2009.10.001

Burger F, Ayala A, Farias D, Shaw TE, MacDonell S, Brock B, McPhee J, Pellicciotti F. 2019. Interannual variability in glacier contribution to runoff from a high-elevation Andean catchment: understanding the role of debris cover in glacier hydrology. *Hydrological Processes* **33** (2): 214–229 DOI: 10.1002/HYP.13354

Buri P, Miles ES, Steiner JF, Ragettli S, Pellicciotti F. 2021. Supraglacial Ice Cliffs Can Substantially Increase the Mass Loss of Debris-Covered Glaciers. *Geophysical Research Letters* **48** (6): e2020GL092150 DOI: 10.1029/2020GL092150

Burles K, Boon S. 2011. Snowmelt energy balance in a burned forest plot, Crowsnest Pass, Alberta, Canada. *Hydrological Processes* **25** (19): 3012–3029 DOI: 10.1002/hyp.8067

Campbell ÉMS, Ryan MC. 2021. Nested Recharge Systems in Mountain Block Hydrology: High-Elevation Snowpack Generates Low-Elevation Overwinter Baseflow in a Rocky Mountain River. *Water* **13** (16): 2249 DOI: 10.3390/W13162249

Cannon AJ. 2018. Multivariate quantile mapping bias correction: an N-dimensional probability density function transform for climate model simulations of multiple variables. *Climate Dynamics* **50** (1–2): 31–49 DOI: 10.1007/s00382-017-3580-6

Cardenas MB, Harvey JW, Packman AI, Scott DT. 2008. Ground-based thermography of fluvial systems at low and high discharge reveals potential complex thermal heterogeneity driven by flow variation and bioroughness. *Hydrological Processes* **22** (7): 980–986 DOI: 10.1002/hyp.6932

Carenzo M, Pellicciotti F, Rimkus S, Burlando P. 2009. Assessing the transferability and robustness of an enhanced temperature-index glacier-melt model. *Journal of Glaciology* **55** (190): 258–274 DOI: 10.3189/002214309788608804

Carey M, Molden OC, Rasmussen MB, Jackson M, Nolin AW, Mark BG. 2017. Impacts of Glacier Recession and Declining Meltwater on Mountain Societies. *Annals of the American Association of Geographers* **107** (2): 350–359 DOI: 10.1080/24694452.2016.1243039

Carturan L. 2016. Replacing monitored glaciers undergoing extinction: A new measurement series on la Mare Glacier (Ortles-Cevedale, Italy). *Journal of Glaciology* **62** (236): 1093–1103 DOI: 10.1017/jog.2016.107

Casassa G, López P, Pouyaud B, Escobar F. 2009. Detection of changes in glacial run-off in alpine basins: examples from North America, the Alps, central Asia and the Andes. *Hydrological Processes* **23** (1): 31–41 DOI: 10.1002/hyp.7194

Castellazzi P, Burgess D, Rivera A, Huang J, Longuevergne L, Demuth MN. 2019. Glacial Melt and Potential Impacts on Water Resources in the Canadian Rocky Mountains. *Water Resources Research* **55** (12): 10191–10217 DOI: 10.1029/2018WR024295

Cazorzi F, Dalla Fontana G. 1996. Snowmelt modelling by combining air temperature and a distributed radiation index. *Journal of Hydrology* **181** (1–4): 169–187 DOI: 10.1016/0022-1694(95)02913-3

Chambers JR, Smith MW, Quincey DJ, Carrivick JL, Ross AN, James MR. 2020. Glacial Aerodynamic Roughness Estimates: Uncertainty, Sensitivity, and Precision in Field Measurements. *Journal of Geophysical Research: Earth Surface* **125** (2): e2019JF005167 DOI: 10.1029/2019JF005167

Chen J, Ohmura A. 1990. Estimation of Alpine glacier water resources and their change since the 1870s. In *Hydrology in Mountainous Regions, I - Hydrological Measurements; the Water Cycle*Proceedings of two Lausanne Symposium, IAHS Publ. no. 193; 127–135.

Chernos M, MacDonald RJ, Nemeth MW, Craig JR. 2020. Current and future projections of glacier contribution to streamflow in the upper Athabasca River Basin. *Canadian Water Resources Journal* **45** (4): 324–344 DOI: 10.1080/07011784.2020.1815587

Clark MP, Hendrikx J, Slater AG, Kavetski D, Anderson B, Cullen NJ, Kerr T, Örn Hreinsson E, Woods RA. 2011. Representing spatial variability of snow water equivalent in hydrologic and land-surface models: A review. *Water Resources Research* **47** (7): 7539 DOI: 10.1029/2011WR010745

Clark MP, Wilby RL, Gutmann ED, Vano JA, Gangopadhyay S, Wood AW, Fowler HJ, Prudhomme C, Arnold JR, Brekke LD. 2016. Characterizing Uncertainty of the Hydrologic Impacts of Climate Change. *Current Climate Change Reports* **2** (2): 55–64 DOI: 10.1007/S40641-016-0034-

X/FIGURES/1

Clarke GKC, Jarosch AH, Anslow FS, Radic V, Menounos B. 2015. Projected deglaciation of western Canada in the twenty-first century. *Nature Geoscience* **8** (5): 372–377 DOI: 10.1038/NGEO2407

Clow DW, Fleming AC. 2008. Tracer gauge: An automated dye dilution gauging system for ice-affected streams. *Water Resources Research* **44** (12) DOI: 10.1029/2008WR007090

Clow DW, Schrott L, Webb R, Campbell DH, Torizzo A, Dornblaser M. 2003. Ground Water Occurrence and Contributions to Streamflow in an Alpine Catchment, Colorado Front Range. *Ground Water* **41** (7): 937–950 DOI: 10.1111/j.1745-6584.2003.tb02436.x

Cogley JG. 2009. A more complete version of the World Glacier Inventory. *Annals of Glaciology* **50** (53): 32–38 DOI: 10.3189/172756410790595859

Collier E, Immerzeel WW. 2015. High-resolution modeling of atmospheric dynamics in the Nepalese Himalaya. *Journal of Geophysical Research* **120** (19): 9882–9896 DOI: 10.1002/2015JD023266

Comeau L, Pietroniro A Al, Demuth MN. 2009. Glacier contribution to the North and South Saskatchewan Rivers. *Hydrological Processes* **23** (18): 2640–2653 DOI: 10.1002/hyp

Conway H, Gades A, Raymond CF. 1996. Albedo of dirty snow during conditions of melt. *Water Resources Research* **32** (6): 1713–1718 DOI: 10.1029/96WR00712

Conway JP, Cullen NJ. 2013a. Constraining turbulent heat flux parameterization over a temperate maritime glacier in New Zealand. *Annals of Glaciology* **54** (63): 41–51 DOI: 10.3189/2013AOG63A604

Conway JP, Cullen NJ. 2013b. Constraining turbulent heat flux parameterization over a temperate maritime glacier in New Zealand. *Annals of Glaciology* **54** (63): 41–51 DOI: 10.3189/2013AoG63A604

Conway JP, Helgason WD, Pomeroy JW, Sicart JE. 2021. Icefield Breezes: Mesoscale Diurnal Circulation in the Atmospheric Boundary Layer Over an Outlet of the Columbia Icefield, Canadian Rockies. *Journal of Geophysical Research: Atmospheres* **126** (6): e2020JD034225 DOI: 10.1029/2020JD034225

Cook JM, Hodson AJ, Gardner AS, Flanner M, Tedstone AJ, Williamson C, Irvine-Fynn TDL, Nilsson J, Bryant R, Tranter M. 2017. Quantifying bioalbedo: A new physically based model and discussion of empirical methods for characterising biological influence on ice and snow albedo. *Cryosphere* **11** (6): 2611–2632 DOI: 10.5194/tc-11-2611-2017

Cook JM, Tedstone AJ, Williamson C, McCutcheon J, Hodson AJ, Dayal A, Skiles M, Hofer S, Bryant R, McAree O, et al. 2020. Glacier algae accelerate melt rates on the south-western Greenland Ice Sheet. *Cryosphere* **14** (1): 309–330 DOI: 10.5194/tc-14-309-2020

Cooper M. 2010. Advanced Bash-Scripting Guide An in-depth exploration of the art of shell scripting Table of Contents. *Okt 2005 Abrufbar uber httpwww tldp orgLDPabsabsguide pdf Zugriff 1112 2005* **2274** (November 2008): 2267–2274 DOI: 10.1002/hyp

Cooper R, Hodgkins R, Wadham J, Tranter M. 2011. The hydrology of the proglacial zone of a high-Arctic glacier(Finsterwalderbreen, Svalbard): Sub-surface water fluxes and complete water budget. *Journal of Hydrology* **406** (1–2): 88–96 DOI: 10.1016/j.jhydrol.2011.06.008

Cullen NJ, Mölg T, Kaser G, Steffen K, Hardy DR. 2007. Energy-balance model validation on the top of Kilimanjaro, Tanzania, using eddy covariance data. *Annals of Glaciology* **46**: 227–233 DOI: 10.3189/172756407782871224

Daly SF, Davis R, Ochs E, Pangburn T. 2000. An approach to spatially distrubuted snow modelling of the sacramento and San Joaquin basins, California. *Hydrological Processes* **14** (18): 3257–3271 DOI: 10.1002/1099-1085(20001230)14:18<3257::AID-HYP199>3.0.CO;2-Z

Day TJ. 1977. Observed mixing lengths in mountain streams. *Journal of Hydrology* **35** (1–2): 125–136 DOI: 10.1016/0022-1694(77)90081-6

DeBeer CM, Pomeroy JW. 2009. Modelling snow melt and snowcover depletion in a small alpine cirque, Canadian Rocky Mountains. *Hydrological Processes* **23** (18): 2584–2599 DOI: 10.1002/hyp.7346

DeBeer CM, Sharp MJ. 2007. Recent changes in glacier area and volume within the southern Canadian Cordillera. *Annals of Glaciology* **46** (1): 215–221 DOI: 10.3189/172756407782871710

DeBeer CM, Wheater HS, Carey SK, Chun KP. 2016. Recent climatic, cryospheric, and hydrological changes over the interior of western Canada: a review and synthesis. *Hydrol. Earth Syst. Sci* **20** (4): 1573–1598 DOI: 10.5194/hess-20-1573-2016

Dee DP, Uppala SM, Simmons AJ, Berrisford P, Poli P, Kobayashi S, Andrae U, Balmaseda MA, Balsamo G, Bauer P, et al. 2011. The ERA-Interim reanalysis: Configuration and performance of the data assimilation system. *Quarterly Journal of the Royal Meteorological Society* **137** (656): 553–597 DOI: 10.1002/qj.828

Demuth MN, Keller R. 2006. An assessment of the mass balance of Peyto glacier (1966-1995) and its relation to Recent and past-century climatic variability. In *Peyto Glacier: One Century of Science*, Demuth, M.N. DSM and GJY (ed.).National Hydrology Research Institute Science Report 8; 83–132.

Demuth MN, Munro DS, Young GJ. 2006. *Peyto Glacier : one century of science*. Environment Canada.

Denby B, Greuell W. 2000. The use of bulk and profile methods for determining surface heat fluxes in the presence of glacier winds. *Journal of Glaciology* **46** (154): 445–452

Déry SJ, Stahl K, Moore RD, Whitfield PH, Menounos B, Burford JE. 2009. Detection of runoff timing changes in pluvial, nival, and glacial rivers of western Canada. *Water Resources Research* **45** (4) DOI: 10.1029/2008WR006975

Dingman SL. 1978. *Physical hydrology*. Waveland Press, Incorporated, 2015: Upper Saddle River N.J.

Duethmann D, Bloschl G, Parajka J. 2020. Why does a conceptual hydrological model fail to correctly predict discharge changes in response to climate change? *Hydrology and Earth System Sciences* **24** (7): 3493–3511 DOI: 10.5194/HESS-24-3493-2020

Duethmann D, Menz C, Jiang T, Vorogushyn S. 2016. Projections for headwater catchments of the Tarim River reveal glacier retreat and decreasing surface water availability but uncertainties are large. *Environmental Research Letters* **11** (5) DOI: 10.1088/1748-9326/11/5/054024

Dyer AJ. 1974. A review of flux-profile relationships. *Boundary-Layer Meteorology* **7** (3): 363–372 DOI: 10.1007/BF00240838

Dyurgerov MB. 2002. Glacier mass balance and regime: data of measurement and analysis. Institute of Arctic and Alpine Research. *Occasional Paper 55, University of Colorado, Boulder* **55**: 1–268

Ebrahimi S, Marshall SJ. 2015. Parameterization of incoming longwave radiation at glacier sites in the Canadian rocky mountains. *Journal of Geophysical Research* **120** (24): 12,536-12,556 DOI: 10.1002/2015JD023324

Essery R, Etchevers P. 2004. Parameter sensitivity in simulations of snowmelt. *Journal of Geophysical Research* **109** (D20111): 1–15 DOI: 10.1029/2004JD005036

Fan Y. 2019. Are catchments leaky? *WIREs Water* **6** (6) DOI: 10.1002/wat2.1386

Fang X, W. Pomeroy J. 2020. Diagnosis of future changes in hydrology for a Canadian Rockies headwater basin. *Hydrology and Earth System Sciences* **24** (5): 2731–2754 DOI: 10.5194/hess-24-2731-2020

Fang X, Pomeroy JWW, Ellis CR, MacDonald MK, DeBeer CM, Brown T. 2013. Multi-variable evaluation of hydrological model predictions for a headwater basin in the Canadian Rocky Mountains. *Hydrol. Earth Syst. Sci* **17** (4): 1635–1659 DOI: 10.5194/hess-17-1635-2013

Farinotti D, Huss M, Fürst JJ, Landmann J, Machguth H, Maussion F, Pandit A. 2019. A consensus estimate for the ice thickness distribution of all glaciers on Earth. *Nature Geoscience* DOI: 10.1038/s41561-019-0300-3

Farinotti D, Usselmann S, Huss M, Bauder A, Funk M. 2012. Runoff evolution in the Swiss Alps: projections for selected high-alpine catchments based on ENSEMBLES scenarios. *Hydrological Processes* **26** (13): 1909–1924 DOI: 10.1002/hyp.8276

Fatichi S, Rimkus S, Burlando P, Bordoy R. 2014. Does internal climate variability overwhelm climate change signals in streamflow? The upper Po and Rhone basin case studies. *Science of the Total Environment* **493**: 1171–1182 DOI: 10.1016/j.scitotenv.2013.12.014

Finger D, Pellicciotti F, Konz M, Rimkus S, Burlando P. 2011. The value of glacier mass balance, satellite snow cover images, and hourly discharge for improving the performance of a physically based distributed hydrological model. *Water Resources Research* **47** (7) DOI: 10.1029/2010WR009824

Fitzpatrick N, Radić V, Menounos B. 2017. Surface energy balance closure and turbulent flux parameterization on a mid-latitude mountain Glacier, Purcell mountains, Canada. *Frontiers in Earth Science* **5** DOI: 10.3389/feart.2017.00067

Foster LA, Brock BW, Cutler MEJ, Diotri F. 2012. A physically based method for estimating supraglacial debris thickness from thermal band remote-sensing data. *Journal of Glaciology* **58** (210): 677–691 DOI: 10.3189/2012JoG11J194

Fountain AG, Tangborn W V. 1985. The Effect of Glaciers on Streamflow Variations. *Water Resources Research* **21** (4): 579–586 DOI: 10.1029/WR021i004p00579

Fowler HJ, Blenkinsop S, Tebaldi C. 2007. Linking climate change modelling to impacts studies: recent advances in downscaling techniques for hydrological modelling. *International Journal of Climatology* **27** (12): 1547–1578 DOI: 10.1002/joc.1556

Fowler HJ, Ekstrom M, Kilsby CG, Jones PD. 2005. New estimates of future changes in extreme rainfall

across the UK using regional climate model integrations. 1. Assessment of control climate. *Journal of Hydrology* **300** (1–4): 212–233 DOI: DOI 10.1016/j.jhydrol.2004.06.017

Frans C, Istanbulluoglu E, Lettenmaier DP, Clarke G, Bohn TJ, Stumbaugh M. 2016. Implications of decadal to century scale glacio-hydrological change for water resources of the Hood River Basin, OR U.S.A. *Hydrological Processes* **30** (23): 4314–4329 DOI: 10.1002/hyp.10872

Frans C, Istanbulluoglu E, Lettenmaier DP, Fountain AG, Riedel J. 2018. Glacier Recession and the Response of Summer Streamflow in the Pacific Northwest United States, 1960–2099. *Water Resources Research* **54** (9): 6202–6225 DOI: 10.1029/2017WR021764

Frei C, Christensen JH, Deque M, Jacob D, Jones RG, Vidale PL. 2003. Daily precipitation statistics in regional climate models: Evaluation and intercomparison for the European Alps. *Journal of Geophysical Research-Atmospheres* **108** (D3) DOI: 10.1029/2002JD002287

Frei C, Schöll R, Fukutome S, Schmidli J, Vidale PL. 2006. Future change of precipitation extremes in Europe: Intercomparison of scenarios from regional climate models. *Journal of Geophysical Research Atmospheres* **111** (6) DOI: 10.1029/2005JD005965

Frenierre JL La, Mark BG, La Frenierre J, Mark BG, Frenierre JL La, Mark BG. 2013. A review of methods for estimating the contribution of glacial meltwater to total watershed discharge. *Progress in Physical Geography* **38** (2): 173–200 DOI: 10.1177/0309133313516161

Freudiger D, Kohn I, Seibert J, Stahl K, Weiler M. 2017. Snow redistribution for the hydrological modeling of alpine catchments. *Wiley Interdisciplinary Reviews: Water* **4** (5): e1232 DOI: 10.1002/wat2.1232

Frey H, Haeberli W, Linsbauer A, Huggel C, Paul F. 2010. A multi-level strategy for anticipating future glacier lake formation and associated hazard potentials. *Natural Hazards and Earth System Science* **10** (2): 339–352 DOI: 10.5194/nhess-10-339-2010

Fyffe CL, Potter E, Fugger S, Orr A, Fatichi S, Loarte E, Medina K, Hellström R, Bernat M, Aubry-Wake C, et al. 2021. The Energy and Mass Balance of Peruvian Glaciers. *Journal of Geophysical Research: Atmospheres* **126** (23): e2021JD034911 DOI: 10.1029/2021JD034911

Fyffe CL, Reid T, Brock BW, Kirkbride MP, Diolaiuti G, Smiraglia C, Diotri F. 2014. A distributed energy-balance melt model of an alpine debris-covered glacier. *Journal of Glaciology* **60** (221): 587–602 DOI: 10.3189/2014JoG13J148

Gao H, He X, Ye B, Pu J. 2012. Modeling the runoff and glacier mass balance in a small watershed on the Central Tibetan Plateau, China, from 1955 to 2008. *Hydrological Processes* **26** (11): 1593–1603 DOI: 10.1002/hyp.8256

Gardner A, Moholdt G, Cogley JG, Wouters B, Arendt CA, Wahr J, Berthier E, Hock R, Pfeffer WT, Kaser G, et al. 2013. A reconciled estimate of glacier contributions to sea level rise: 2003 to 2009. *Science* **340** (6134): 852–857 DOI: 10.1126/science.1234532

Garnier B, Ohmura A. 1970. The Evaluation of Surface Variations in Solar Radiation Income. *Solar Energy* **13**: 21–34

Garrick M, Cunnane C, Nash JE. 1978. A criterion of efficiency for rainfall-runoff models. *Journal of Hydrology* DOI: 10.1016/0022-1694(78)90155-5

Gibbons JD, Chakraborti S. 2010. *Nonparametric statistical inference*. Chapman and Hall/CRC. DOI: 10.5005/jp/books/10313_14

Giese A, Arcone S, Hawley R, Lewis G, Wagnon P. 2021. Detecting supraglacial debris thickness with GPR under suboptimal conditions. *Journal of Glaciology* **67** (266): 1108–1120 DOI: 10.1017/JOG.2021.59

Giese A, Boone A, Wagnon P, Hawley R. 2020. Incorporating moisture content in surface energy balance modeling of a debris-covered glacier. *Cryosphere* **14** (5): 1555–1577 DOI: 10.5194/TC-14-1555-2020

Gillett NP. 2004. Detecting the effect of climate change on Canadian forest fires. *Geophysical Research Letters* **31** (18): L18211 DOI: 10.1029/2004GL020876

Giorgi F. 2019. Thirty Years of Regional Climate Modeling: Where Are We and Where Are We Going next? *Journal of Geophysical Research: Atmospheres* **124** (11): 5696–5723 DOI: 10.1029/2018JD030094

Glausen TG, Tanner LH. 2019. Successional trends and processes on a glacial foreland in Southern Iceland studied by repeated species counts. *Ecological Processes* **8** (1): 11 DOI: 10.1186/s13717-019-0165-9

Gleason KE, McConnell JR, Arienzo MM, Chellman N, Calvin WM. 2019. Four-fold increase in solar forcing on snow in western U.S. burned forests since 1999. *Nature Communications* **10** (1): 2026 DOI: 10.1038/s41467-019-09935-y

Gordon R, Lautz LK, McKenzie JM, Mark BG, Chavez D, Baraer M. 2015. Sources and pathways of stream generation in tropical proglacial valleys of the Cordillera Blanca, Peru. *Journal of Hydrology* **522**: 628–644 DOI: 10.1016/J.JHYDROL.2015.01.013

Government of B.C. 2019. Wildfire Season Summary - Province of British Columbia Available at: https://www2.gov.bc.ca/gov/content/safety/wildfire-status/about-bcws/wildfire-history/wildfire-season-summary [Accessed 4 May 2021]

Granger RJ, Gray DM, Dyck GE. 1984. Snowmelt infiltration to frozen Prairie soils. *Canadian Journal of Earth Sciences* **21** (6): 669–677 DOI: 10.1139/e84-073

Gray DM, Landine PG. 1988. An energy-budget snowmelt model for the Canadian Prairies. *Canadian Journal of Earth Sciences* **25** (8): 1292–1303 DOI: 10.1139/e88-124

Gray DM, Toth B, Zhao L, Pomeroy JW, Granger RJ. 2001. Estimating areal snowmelt infiltration into frozen soils. *Hydrological Processes* **15** (16): 3095–3111 DOI: 10.1002/hyp.320

Greuell W, Knap WH, Smeets PC. 1997. Elevational changes in meteorological variables along a midlatitude glacier during summer. *Journal of Geophysical Research Atmospheres* **102** (22): 25941–25954 DOI: 10.1029/97jd02083

Grisogono B, Oerlemans J. 2001. A theory for the estimation of surface fluxes in simple katabatic flows. *Quarterly Journal of the Royal Meteorological Society* **127** (578): 2725–2739 DOI: 10.1002/qj.49712757811

Grotch SL, MacCracken MC. 1991. The Use of General Circulation Models to Predict Regional Climatic Change. *Journal of Climate* **4** (3): 286–303 DOI: 10.1175/1520-

0442(1991)004<0286:tuogcm>2.0.co;2

Gruber S, Haeberli W. 2009. Mountain Permafrost. In *Permafrost Soils*Springer Berlin Heidelberg: Berlin, Heidelberg; 33–44. DOI: 10.1007/978-3-540-69371-0_3

Gupta H V, Kling H, Yilmaz KK, Martinez GF. 2009. Decomposition of the mean squared error and NSE performance criteria: Implications for improving hydrological modelling. *Journal of Hydrology* **377** (1–2): 80–91 DOI: 10.1016/j.jhydrol.2009.08.003

Gutmann ED, Rasmussen RM, Liu C, Ikeda K, Gochis DJ, Clark MP, Dudhia J, Thompson G. 2012. A Comparison of Statistical and Dynamical Downscaling of Winter Precipitation over Complex Terrain. *Journal of Climate* **25** (1): 262–281 DOI: 10.1175/2011JCLI4109.1

Hanzer F, Helfricht K, Marke T, Strasser U. 2016. Multilevel spatiotemporal validation of snow/ice mass balance and runoff modeling in glacierized catchments. *Cryosphere* **10** (4): 1859–1881 DOI: 10.5194/TC-10-1859-2016

Harder P, Pomeroy JW. 2013. Estimating precipitation phase using a psychrometric energy balance method. *Hydrological Processes* **27** (May): 1901–1914 DOI: 10.1002/hyp.9799

Harder P, Pomeroy JW, Westbrook CJ. 2015. Hydrological resilience of a Canadian Rockies headwaters basin subject to changing climate, extreme weather, and forest management. *Hydrological Processes* **29** (18): 3905–3924 DOI: 10.1002/hyp.10596

Hay LE, Clark MP. 2003. Use of statistically and dynamically downscaled atmospheric model output for hydrologic simulations in three mountainous basins in the western United States. *Journal of Hydrology* **282** (1–4): 56–75 DOI: 10.1016/S0022-1694(03)00252-X

Hayashi M. 2020. Alpine Hydrogeology: The Critical Role of Groundwater in Sourcing the Headwaters of the World. *Groundwater* **58** (4): 498–510 DOI: 10.1111/GWAT.12965

He C, Chen F, Barlage M, Liu C, Newman A, Tang W, Ikeda K, Rasmussen R. 2019. Can Convection-Permitting Modeling Provide Decent Precipitation for Offline High-Resolution Snowpack Simulations Over Mountains? *Journal of Geophysical Research: Atmospheres* **124** (23): 12631–12654 DOI: 10.1029/2019JD030823

Henn B, Newman AJ, Livneh B, Daly C, Lundquist JD. 2018. An assessment of differences in gridded precipitation datasets in complex terrain. *Journal of Hydrology* **556**: 1205–1219 DOI: 10.1016/J.JHYDROL.2017.03.008

Herreid S. 2021. What Can Thermal Imagery Tell Us About Glacier Melt Below Rock Debris? *Frontiers in Earth Science* **9**: 738 DOI: 10.3389/feart.2021.681059

Herreid S, Pellicciotti F. 2020. The state of rock debris covering Earth's glaciers. *Nature Geoscience* **13** (9): 621–627 DOI: 10.1038/s41561-020-0615-0

Hersbach H, Bell B, Berrisford P, Hirahara S, Horányi A, Muñoz-Sabater J, Nicolas J, Peubey C, Radu R, Schepers D, et al. 2020. The ERA5 global reanalysis. *Quarterly Journal of the Royal Meteorological Society* **146** (730): 1999–2049 DOI: 10.1002/QJ.3803

Hock R. 1999. A distributed temperature-index ice- and snowmelt model including potential direct solar radiation. *Journal of Glaciology* **45** (149): 101–111 DOI: 10.1017/S0022143000003087

Hock R. 2003. Temperature index melt modelling in mountain areas. *Journal of Hydrology* **282** (1–4):

104–115 DOI: 10.1016/S0022-1694(03)00257-9

Hock R. 2005. Glacier melt: A review of processes and their modelling. *Progress in Physical Geography* **29** (3): 362–391 DOI: 10.1191/0309133305pp453ra

Hock R, Rasul G, Adler C, Cáceres B, Gruber S, Hirabayashi Y, Jackson M, Kääb A, Kang S, Kutuzov S, et al. 2019. High Mountain Areas. In *IPCC Special Report on the Ocean and Cryosphere in a Changing Climate [H.-O.*, H.-O. Pörtner, D.C. Roberts, V. Masson-Delmotte, P. Zhai, M. Tignor, E. Poloczanska, K. Mintenbeck, A. Alegría, M. Nicolai, A. Okem, J. Petzold, B. Rama NMW (ed.).Cambridge University Press: Cambridge, UK and New York, NY, USA; 131–202. DOI: https://doi.org/10.1017/9781009157964.004

Hood E, Battin TJ, Fellman J, O'neel S, Spencer RGM. 2015. Storage and release of organic carbon from glaciers and ice sheets. *Nature Geoscience* **8** (2): 91–96 DOI: 10.1038/ngeo2331

Hood JL, Hayashi M. 2015. Characterization of snowmelt flux and groundwater storage in an alpine headwater basin. *Journal of Hydrology* **521**: 482–497 DOI: 10.1016/j.jhydrol.2014.12.041

Hopkinson C, Young GJ. 1998. The effect of glacier wastage on the flow of the Bow River at Banff, Alberta, 1951-1993. *Hydrological Processes* **12** (10–11): 1745–1762 DOI: 10.1002/(SICI)1099-1085(199808/09)12:10/11<1745::AID-HYP692>3.0.CO;2-S

Hopkinson C, Barlow J, Demuth MN, Pomeroy JW. 2010. Mapping changing temperature patterns over a glacial moraine using oblique thermal imagery and lidar. *Canadian Journal of Remote Sensing* **36**: S257–S265 DOI: 10.5589/m10-053

Hopkinson C, Demuth MN, Sitar M. 2012. Hydrological implications of periglacial expansion in the Peyto Glacier catchment, Canadian Rockies. In *IAHS-AISH Publication*IAHS Publ; 341–344.

Horton P, Schaefli B, Mezghani A, Hingray B, Musy A. 2006. Assessment of climate-change impacts on alpine discharge regimes with climate model uncertainty. *Hydrological Processes* **20** (10): 2091–2109 DOI: 10.1002/hyp.6197

Horvath K, Koracin D, Vellore R, Jiang J, Belu R. 2012. Sub-kilometer dynamical downscaling of near-surface winds in complex terrain using WRF and MM5 mesoscale models. *Journal of Geophysical Research Atmospheres* DOI: 10.1029/2012JD017432

Houze RA. 2012. Orographic effects on precipitating clouds. *Reviews of Geophysics* **50** (1): 1001 DOI: 10.1029/2011RG000365

Hudson AJ, Ferguson RI. 1999. Fluvial suspended sediment transport from cold and warm-based glaciers in Svalbard. *Earth Surface Processes and Landforms* **24** (11): 957–974 DOI: 10.1002/(SICI)1096-9837(199910)24:11<957::AID-ESP19>3.0.CO;2-J

Hugonnet R, McNabb R, Berthier E, Menounos B, Nuth C, Girod L, Farinotti D, Huss M, Dussaillant I, Brun F, et al. 2021. Accelerated global glacier mass loss in the early twenty-first century. *Nature* **592** (7856): 726–731 DOI: 10.1038/s41586-021-03436-z

Huss M. 2011. Present and future contribution of glacier storage change to runoff from macroscale drainage basins in Europe. *Water Resources Research* **47** (7) DOI: 10.1029/2010WR010299

Huss M, Hock R. 2018. Global-scale hydrological response to future glacier mass loss. *Nature Climate Change* DOI: 10.1038/s41558-017-0049-x

Huss M, Bookhagen B, Huggel C, Jacobsen D, Bradley RSS, Clague JJJ, Vuille M, Buytaert W, Cayan DRR, Greenwood G, et al. 2017. Toward mountains without permanent snow and ice. *Earth's Future* **5** (5): 418–435 DOI: 10.1002/2016EF000514

Huss M, Farinotti D, Bauder A, Funk M. 2008. Modelling runoff from highly glacierized alpine drainage basins in a changing climate. *Hydrological Processes* **22** (19): 3888–3902 DOI: 10.1002/hyp.7055

Huss M, Jouvet G, Farinotti D, Bauder A. 2010. Future high-mountain hydrology: A new parameterization of glacier retreat. *Hydrology and Earth System Sciences* **14** (5): 815–829 DOI: 10.5194/hess-14-815-2010

Huss M, Zemp M, Joerg PC, Salzmann N. 2014. High uncertainty in 21st century runoff projections from glacierized basins. *Journal of Hydrology* **510**: 35–48 DOI: 10.1016/j.jhydrol.2013.12.017

Immerzeel WW, van Beek LPH, Bierkens MFP. 2010. Climate Change Will Affect the Asian Water Towers. *Science* **328** (5984): 1382–1385 DOI: 10.1126/science.1183188

Immerzeel WW, van Beek LPH, Konz M, Shrestha AB, Bierkens MFP. 2012. Hydrological response to climate change in a glacierized catchment in the Himalayas. *Climatic Change* **110** (3–4): 721–736 DOI: 10.1007/s10584-011-0143-4

Immerzeel WW, Kraaijenbrink PDA, Shea JM, Shrestha AB, Pellicciotti F, Bierkens MFP, De Jong SM. 2014a. High-resolution monitoring of Himalayan glacier dynamics using unmanned aerial vehicles. *Remote Sensing of Environment* **150**: 93–103 DOI: 10.1016/j.rse.2014.04.025

Immerzeel WW, Lutz AF, Andrade M, Bahl A, Biemans H, Bolch T, Hyde S, Brumby S, Davies BJ, Elmore AC, et al. 2020. Importance and vulnerability of the world's water towers. *Nature* **577** (7790): 364–369 DOI: 10.1038/s41586-019-1822-y

Immerzeel WW, Pellicciotti F, Bierkens MFP. 2013. Rising river flows throughout the twenty-first century in two Himalayan glacierized watersheds. *Nature Geoscience* **6** (9): 742–745 DOI: 10.1038/ngeo1896

Immerzeel WW, Petersen L, Rafaj P, Pellicciotti F. 2014b. The importance of observed gradients of air temperature and precipitation for modeling runoff from a glacierized watershed in the Nepalese Himalayas. *Water Resources Research* **50** (3): 2212–2226 DOI: 10.1002/2013WR014506

Jansson P, Hock R, Schneider T. 2003. The concept of glacier storage: A review. *Journal of Hydrology* **282** (1–4): 116–129 DOI: 10.1016/S0022-1694(03)00258-0

Jarosch AH, Schoof CG, Anslow FS. 2013. Restoring mass conservation to shallow ice flow models over complex terrain. *Cryosphere* **7** (1): 229–240 DOI: 10.5194/tc-7-229-2013

Jeelani G, Feddema JJ, Van Der Veen CJ, Stearns L. 2012. Role of snow and glacier melt in controlling river hydrology in Liddar watershed (western Himalaya) under current and future climate. *Water Resources Research* **48** (12) DOI: 10.1029/2011WR011590

Jones GA, Henry GHR. 2003. Primary plant succession on recently deglaciated terrain in the Canadian High Arctic. *Journal of Biogeography* **30** (2): 277–296 DOI: 10.1046/j.1365-2699.2003.00818.x

Jones HG, Pomeroy JW, Walker DA, Hoham RW. 2001. *Snow Ecology: An Interdisciplinary Examination of Snow-Covered Ecosystems*. Cambridge University Press: Cambridge, England.

Jost G, Moore RD, Menounos B, Wheate R. 2012. Quantifying the contribution of glacier runoff to streamflow in the upper Columbia River Basin, Canada. *Hydrology and Earth System Sciences* **16** (3): 849–860 DOI: 10.5194/hess-16-849-2012

Juen I, Kaser G, Georges C. 2007. Modelling observed and future runoff from a glacierized tropical catchment (Cordillera Blanca, Perú). *Global and Planetary Change* **59** (1–4): 37–48 DOI: 10.1016/j.gloplacha.2006.11.038

Juen M, Mayer C, Lambrecht A, Han H, Liu S. 2014. Impact of varying debris cover thickness on ablation: A case study for Koxkar Glacier in the Tien Shan. *Cryosphere* **8** (2): 377–386 DOI: 10.5194/tc-8-377-2014

Kaser G, Cogley JG, Dyurgerov MB, Meier MF, Ohmura A. 2006. Mass balance of glaciers and ice caps: Consensus estimates for 1961-2004. *Geophysical Research Letters* **33** (19) DOI: 10.1029/2006GL027511

Kattel DB, Yao T. 2018. Temperature–topographic elevation relationship for high mountain terrain: an example from the southeastern Tibetan Plateau. *International Journal of Climatology* **38**: e901–e920 DOI: 10.1002/JOC.5418

Keegan KM. 2014. Radiative forcing by light-absorbing particles in snow. **8** (11): 964–971 DOI: 10.1038/s41558-018-0296-5

Khanal S, Lutz AF, Kraaijenbrink PDA, van den Hurk B, Yao T, Immerzeel WW. 2021. Variable 21st Century Climate Change Response for Rivers in High Mountain Asia at Seasonal to Decadal Time Scales. *Water Resources Research* **57** (5): e2020WR029266 DOI: 10.1029/2020wr029266

Kilpeläinen A, Kellomäki S, Strandman H, Venäläinen A. 2010. Climate change impacts on forest fire potential in boreal conditions in Finland. *Climatic Change* **103** (3): 383–398 DOI: 10.1007/s10584-009-9788-7

Kirchner JW. 2006. Getting the right answers for the right reasons: Linking measurements, analyses, and models to advance the science of hydrology. *Water Resources Research* **42** (3) DOI: 10.1029/2005WR004362

Kite G. 1989. An extension to the salt dilution method of measuring streamflow. *International Journal of Water Resources Development* **5** (1): 19–24 DOI: 10.1080/07900628908722408

Kite G. 1993. Computerized streamflow measurement using slug injection. *Hydrological Processes* **7** (2): 227–233 DOI: 10.1002/hyp.3360070212

Klok EJ, Oerlemans J. 2002. Model study of the spatial distribution of the energy and mass balance of Morteratschgletscher, Switzerland. *Journal of Glaciology* **48** (163): 505–518 DOI: 10.3189/172756502781831133

Knoben WJM, Freer JE, Woods RA. 2019. Technical note: Inherent benchmark or not? Comparing Nash-Sutcliffe and Kling-Gupta efficiency scores. *Hydrology and Earth System Sciences* **23** (10): 4323–4331 DOI: 10.5194/hess-23-4323-2019

Koboltschnig GR, Schöner W. 2011. The relevance of glacier melt in the water cycle of the Alps: the example of Austria. *Hydrology and Earth System Sciences* **15** (6): 2039–2048 DOI: 10.5194/hess-15-2039-2011

Kochanski AK, Mallia D V., Fearon MG, Mandel J, Souri AH, Brown T. 2019. Modeling Wildfire Smoke Feedback Mechanisms Using a Coupled Fire-Atmosphere Model With a Radiatively Active Aerosol Scheme. *Journal of Geophysical Research: Atmospheres* **124** (16): 9099–9116 DOI: 10.1029/2019JD030558

Kouwen N. 1988. WATFLOOD: a Micro-Computer Based Flood Forecasting System Based on Real-Time Weather Radar. *Canadian Water Resources Journal* **13** (1): 62–77 DOI: 10.4296/cwrj1301062

Kraaijenbrink PDA, Bierkens MFP, Lutz AF, Immerzeel WW. 2017. Impact of a global temperature rise of 1.5 degrees Celsius on Asia's glaciers. *Nature* **549** (7671): 257–260 DOI: 10.1038/nature23878

Kraaijenbrink PDA, Shea JM, Litt M, Steiner J, Treichler D, Koch I, Immerzeel WW. 2018. Mapping Surface Temperatures on a Debris-Covered Glacier With an Unmanned Aerial Vehicle. *Frontiers in Earth Science* **6**: 64 DOI: 10.3389/feart.2018.00064

Krogh SA, Pomeroy JW. 2019. Impact of future climate and vegetation on the hydrology of an Arctic headwater basin at the tundra-taiga transition. *Journal of Hydrometeorology* **20** (2): 197–215 DOI: 10.1175/JHM-D-18-0187.1

Krogh SA, Pomeroy JW, Marsh P. 2017. Diagnosis of the hydrology of a small Arctic basin at the tundra-taiga transition using a physically based hydrological model. *Journal of Hydrology* **550**: 685–703 DOI: 10.1016/j.jhydrol.2017.05.042

Krogh SA, Pomeroy JW, McPhee J. 2015. Physically Based Mountain Hydrological Modeling Using Reanalysis Data in Patagonia. *Journal of Hydrometeorology* **16** (1): 172–193 DOI: 10.1175/JHM-D-13-0178.1

Kuhn M. 2003. Redistribution of snow and glacier mass balance from a hydrometeorological model. *Journal of Hydrology* **282** (1–4): 95–103 DOI: 10.1016/S0022-1694(03)00256-7

Langhans W, Schmidli J, Fuhrer O, Bieri S, Schar C. 2013. Long-term simulations of thermally driven flows and orographic convection at convection-parameterizing and cloud-resolving resolutions. *Journal of Applied Meteorology and Climatology* DOI: 10.1175/JAMC-D-12-0167.1

Langston G, Bentley LR, Hayashi M, Mcclymont AF, Pidlisecky A. 2011. Internal structure and hydrological functions of an alpine proglacial moraine. *Hydrological Processes* **2982** (May): 2967–2982 DOI: 10.1002/hyp.8144

Langston G, Hayashi M, Roy JW. 2013. Quantifying groundwater-surface water interactions in a proglacial moraine using heat and solute tracers. *Water Resources Research* **49** (9): 5411–5426 DOI: 10.1002/wrcr.20372

Lencioni V, Jousson O, Guella G, Bernabò P. 2015. Cold adaptive potential of chironomids overwintering in a glacial stream. *Physiological Entomology* **40** (1): 43–53 DOI: 10.1111/phen.12084

Leroux NR, Pomeroy JW. 2017. Modelling capillary hysteresis effects on preferential flow through melting and cold layered snowpacks. *Advances in Water Resources* **107**: 250–264 DOI: 10.1016/J.ADVWATRES.2017.06.024

Leroux NR, Marsh CB, Pomeroy JW. 2020. Simulation of Preferential Flow in Snow With a 2-D Non-

Equilibrium Richards Model and Evaluation Against Laboratory Data. *Water Resources Research* **56** (9): e2020WR027466 DOI: 10.1029/2020WR027466

Leung R, Mearns LO, Giorgi F, Wilby RL. 2003. Regional climate research:Needs and opportunities. *Bulletin of the American Meteorological Society* **84** (1): 89–95 DOI: 10.1175/BAMS-84-1-89

Li L, Pomeroy JW. 1997. Probability of occurrence of blowing snow. *Journal of Geophysical Research: Atmospheres* **102** (D18): 21955–21964 DOI: 10.1029/97JD01522

Li R, Wang SY, Gillies RR. 2016. A combined dynamical and statistical downscaling technique to reduce biases in climate projections: an example for winter precipitation and snowpack in the western United States. *Theoretical and Applied Climatology* **124** (1–2): 281–289 DOI: 10.1007/s00704-015-1415-0

Li Y, Li Z, Zhang Z, Chen L, Kurkute S, Scaff L, Pan X. 2019. High-resolution regional climate modeling and projection over western Canada using a weather research forecasting model with a pseudo-global warming approach. *Hydrology and Earth System Sciences* DOI: 10.5194/hess-23-4635-2019

Litt M, Sicart JE, Helgason W, Wagnon P. 2014. Turbulence Characteristics in the Atmospheric Surface Layer for Different Wind Regimes over the Tropical Zongo Glacier (Bolivia, 16S). *Boundary-Layer Meteorology* **154** (3): 471–495 DOI: 10.1007/s10546-014-9975-6

Litt M, Sicart JE, Six D, Wagnon P, Helgason WD. 2017. Surface-layer turbulence, energy balance and links to atmospheric circulations over a mountain glacier in the French Alps. *Cryosphere* **11** (2): 971–987 DOI: 10.5194/TC-11-971-2017

Liu C, Ikeda K, Rasmussen R, Barlage M, Newman AJ, Prein AF, Chen F, Chen L, Clark MP, Dai A, et al. 2017. Continental-scale convection-permitting modeling of the current and future climate of North America. *Climate Dynamics* **49** (1–2): 71–95 DOI: 10.1007/s00382-016-3327-9

Van Loon AF, Ploum SW, Parajka J, Fleig AK, Garnier E, Laaha G, Van Lanen HAJ. 2015. Hydrological drought types in cold climates: Quantitative analysis of causing factors and qualitative survey of impacts. *Hydrology and Earth System Sciences* **19** (4): 1993–2016 DOI: 10.5194/hess-19-1993-2015

López-Moreno J-I, Gascoin S, Herrero J, Sproles EA, Pons M, Alonso-González E, Hanich L, Boudhar A, Musselman KN, Molotch NP, et al. 2017. Different sensitivities of snowpacks to warming in Mediterranean climate mountain areas. *Environmental Research Letters* **12** (7): 74006 DOI: 10.1088/1748-9326/aa70cb

López-Moreno J-I, Pomeroy JW, Alonso-González E, Morán-Tejeda E, Revuelto-Benedí J, Revuelto J. 2020. Decoupling of warming mountain snowpacks from hydrological regimes. *Environmental Research Letters* **15** (11): 114006 DOI: 10.1088/1748-9326/abb55f

Lundquist JD, Hughes M, Henn B, Gutmann ED, Livneh B, Dozier J, Neiman P. 2015. High-Elevation Precipitation Patterns: Using Snow Measurements to Assess Daily Gridded Datasets across the Sierra Nevada, California. *Journal of Hydrometeorology* **16** (4): 1773–1792 DOI: 10.1175/JHM-D-15-0019.1

Lutz AF, Immerzeel WW, Kraaijenbrink PDA, Shrestha AB, Bierkens MFP. 2016. Climate change impacts on the upper indus hydrology: Sources, shifts and extremes. *PLoS ONE* **11** (11) DOI: 10.1371/journal.pone.0165630

Lutz AF, Immerzeel WW, Shrestha AB, Bierkens MFP. 2014. Consistent increase in High Asia's runoff due to increasing glacier melt and precipitation. *Nature Climate Change* **4** (7): 587–592 DOI: 10.1038/nclimate2237

MacDonald MK, Pomeroy JW, Pietroniro A. 2009. Parameterizing redistribution and sublimation of blowing snow for hydrological models: Tests in a mountainous subarctic catchment. *Hydrological Processes* **23** (18): 2570–2583 DOI: 10.1002/hyp.7356

MacDonald MK, Pomeroy JW, Pietroniro A. 2010. On the importance of sublimation to an alpine snow mass balance in the Canadian Rocky Mountains. *Hydrology and Earth System Sciences* **14** (7): 1401–1415 DOI: 10.5194/hess-14-1401-2010

Mackay JD, Barrand NE, Hannah DM, Krause S, Jackson CR, Everest J, Aoalgeirsdóttir G, Black AR, Aðalgeirsdóttir G, Black AR, et al. 2019. Future evolution and uncertainty of river flow regime change in a deglaciating river basin. *Hydrology and Earth System Sciences* **23** (4): 1833–1865 DOI: 10.5194/hess-23-1833-2019

MacKay JD, Barrand NE, Hannah D, Krause S, Jackson CR, Everest J, Aoalgeirsdóttir G. 2018. Glacio-hydrological melt and run-off modelling: Application of a limits of acceptability framework for model comparison and selection. *Cryosphere* **12** (7): 2175–2210 DOI: 10.5194/tc-12-2175-2018

Magalhães N de, Evangelista H, Condom T, Rabatel A, Ginot P. 2019. Amazonian Biomass Burning Enhances Tropical Andean Glaciers Melting. *Scientific Reports* **9** (1) DOI: 10.1038/s41598-019-53284-1

Magnusson J, Kobierska F, Huxol S, Hayashi M, Jonas T, Kirchner JW. 2014. Melt water driven stream and groundwater stage fluctuations on a glacier forefield (Dammagletscher, Switzerland). *Hydrological Processes* **28** (3): 823–836 DOI: 10.1002/hyp.9633

Marks D, Domingo J, Susong D, Link TE, Garen D. 1999. A spatially distributed energy balance snowmelt model for application in mountain basins. *Hydrological Processes* **13** (12–13): 1935–1959 DOI: 10.1002/(SICI)1099-1085(199909)13:12/13<1935::AID-HYP868>3.0.CO;2-C

Marks D, Kimball J, Tingey D, Link T. 1998. The sensitivity of snowmelt processes to climate conditions and forest cover during rain-on-snow: a case study of the 1996 Pacific Northwest flood. *Hydrological Processes* **12** (10–11): 1569–1587 DOI: 10.1002/(SICI)1099-1085(199808/09)12:10/11<1569::AID-HYP682>3.0.CO;2-L

Marsh CB, Pomeroy JW, Spiteri RJ. 2012. Implications of mountain shading on calculating energy for snowmelt using unstructured triangular meshes. *Hydrological Processes* **26** (12): 1767–1778 DOI: 10.1002/hyp.9329

Marsh CB, Pomeroy JW, Spiteri RJ, Wheater HS. 2020a. A Finite Volume Blowing Snow Model for Use With Variable Resolution Meshes. *Water Resources Research* **56** (2): e2019WR025307 DOI: 10.1029/2019WR025307

Marsh CB, Pomeroy JW, Wheater HS. 2020b. The Canadian Hydrological Model (CHM) v1.0: a multi-scale, multi-extent, variable-complexity hydrological model - design and overview. *Geoscientific Model Development* **13** (1): 225–247 DOI: 10.5194/GMD-13-225-2020

Marsh P, Woo M -K. 1984. Wetting front advance and freezing of meltwater within a snow cover: 1. Observations in the Canadian Arctic. *Water Resources Research* **20** (12): 1853–1864 DOI: 10.1029/WR020I012P01853

Marshall SJ, White E, Demuth MN, Bolch T, Wheate R, Menounos B, Beedle MJ, Shea JM. 2011. Glacier Water Resources on the Eastern Slopes of the Canadian Rocky Mountains. *Canadian Water Resources Journal* **36** (2): 109–134 DOI: 10.4296/cwrj3602823

MathWorks. 2017. *MATLAB and the Image Processing Toolbox, version 9.2.0 (R2017a)*. The MathWorks Inc.: Natick, Massachusetts, United States.

Di Mauro B, Garzonio R, Baccolo G, Franzetti A, Pittino F, Leoni B, Remias D, Colombo R, Rossini M. 2020. Glacier algae foster ice-albedo feedback in the European Alps. *Scientific Reports* **10** (1): 1–9 DOI: 10.1038/s41598-020-61762-0

McCarthy M, Pritchard H, Willis I, King E. 2017. Ground-penetrating radar measurements of debris thickness on Lirung Glacier, Nepal. *Journal of Glaciology* **63** (239): 543–555 DOI: 10.1017/jog.2017.18

McClung DM, Schaerer PA. 2006. *The avalanche handbook*. Mountaineers Books. DOI: 10.5860/choice.31-3797

Mcclymont AF, Hayashi M, Bentley LR, Muir D, Ernst E. 2010. Groundwater flow and storage within an alpine meadow-talus complex. *Hydrology and Earth System Sciences* **14** (6): 859–872 DOI: 10.5194/hess-14-859-2010

McKendry IG, Christen A, Lee SC, Ferrara M, Strawbridge KB, O'Neill N, Black A. 2019. Impacts of an intense wildfire smoke episode on surface radiation, energy and carbon fluxes in southwestern British Columbia, Canada. *Atmospheric Chemistry and Physics* **19** (2): 835–846 DOI: 10.5194/acp-19-835-2019

Meier MF, Tangborn W V. 1961. Distinctive characteristics of glacier runoff. *U.S. Geological Survey Professional Paper* **424**-**B**: 14–16

Mernild SH, Lipscomb WH, Bahr DB, Radić V, Zemp M. 2013. Global glacier changes: A revised assessment of committed mass losses and sampling uncertainties. *Cryosphere* **7** (5): 1565–1577 DOI: 10.5194/tc-7-1565-2013

Meyer J, Kohn I, Stahl K, Hakala K, Seibert J, Cannon AJ. 2019. Effects of univariate and multivariate bias correction on hydrological impact projections in alpine catchments. *Hydrology and Earth System Sciences* **23** (3): 1339–1354 DOI: 10.5194/hess-23-1339-2019

Meza F, Varas E. 2000. Estimation of mean monthly solar global radiation as a function of temperature. *Agricultural and Forest Meteorology* **100**: 231–241 DOI: 10.1016/S0168-1923(99)00090-8

Mihalcea C, Brock BW, Diolaiuti G, D'agata C, Citterio M, Kirkbride MP, Cutler MEJ, Smiraglia C. 2008a. Using ASTER satellite and ground-based surface temperature measurements to derive supraglacial debris cover and thickness patterns on Miage Glacier (Mont Blanc Massif, Italy). *Cold Regions Science and Technology* **52** (3): 341–354 DOI: 10.1016/j.coldregions.2007.03.004

Mihalcea C, Mayaud C, Diolaiuti G, D'agata C, Smiraglia C, Lambrecht A, Vuillermoz E, Tartari G. 2008b. Spatial distribution of debris thickness and melting from remote-sensing and meteorological data, at debris-covered Baltoro glacier, Karakoram, Pakistan. In *Annals of Glaciology*49–57. DOI: 10.3189/172756408784700680

Miles ES, Pellicciotti F, Willis I, Steiner J, Buri P, Arnold N. 2016. Refined energy-balance modelling of

a supraglacial pond, Langtang Khola, Nepal. *Annals of Glaciology* **57** (71): 29–40 DOI: 10.3189/2016AoG71A421

Miles ES, Willis I, Buri P, Steiner J, Arnold N, Pellicciotti F. 2018. Surface Pond Energy Absorption Across Four Himalayan Glaciers Accounts for 1/8 of Total Catchment Ice Loss. *Geophysical Research Letters* **45** (19): 10,464-10,473 DOI: 10.1029/2018GL079678

Milner AM, Brittain JE, Castella E, Petts GE. 2001. Trends of macroinvertebrate community structure in glacier-fed rivers in relation to environmental conditions: A synthesis. *Freshwater Biology* **46** (12): 1833–1847 DOI: 10.1046/j.1365-2427.2001.00861.x

Milner AM, Khamis K, Battin TJ, Brittain JE, Barrand NE, Füreder L, Cauvy-Fraunié S, Gíslason GM, Jacobsen D, Hannah DM, et al. 2017. Glacier shrinkage driving global changes in downstream systems. *Proceedings of the National Academy of Sciences of the United States of America* **114** (37): 9770–9778 DOI: 10.1073/pnas.1619807114

Minder JR, Mote PW, Lundquist JD. 2010. Surface temperature lapse rates over complex terrain : Lessons from the Cascade Mountains. *Journal of Geophysical Research: Atmospheres* **115** (D14): 1–13 DOI: 10.1029/2009JD013493

Minora U, Senese A, Bocchiola D, Soncini A, D'agata C, Ambrosini R, Mayaud C, Lambrecht A, Vuillermoz E, Smiraglia C, et al. 2015. A simple model to evaluate ice melt over the ablation area of glaciers in the Central Karakoram National Park, Pakistan. *Annals of Glaciology* **56** (70): 202–216 DOI: 10.3189/2015AoG70A206

Mizukami N, Clark MP, Gutmann ED, Mendoza PA, Newman AJ, Nijssen B, Livneh B, Hay LE, Arnold JR, Brekke LD. 2016. Implications of the Methodological Choices for Hydrologic Portrayals of Climate Change over the Contiguous United States: Statistically Downscaled Forcing Data and Hydrologic Models. *Journal of Hydrometeorology* **17** (1): 73–98 DOI: 10.1175/JHM-D-14-0187.1

Moore RD. 2004. Introduction to salt dilution gauging for streamflow measurement Part 1. *Streamline Watershed Management Bulletin* **7** (4): 1–6

Moore RD. 2005. Introduction to salt dilution gauging for streamflow measurement Part 3: Slug injection using salt in solution. *Streamline* **8** (4): 1–6

Moore RD, Demuth MN. 2001. Mass balance and streamflow variability at Place Glacier, Canada, in relation to recent climate fluctuations. *Hydrological Processes* **15** (18): 3473–3486 DOI: 10.1002/hyp.1030

Moore RD, Fleming SW, Menounos B, Wheate R, Fountain AG, Stahl K, Holm K, Jakob M. 2009. Glacier change in western North America: influences on hydrology, geomorphic hazards and water quality. *Hydrological Processes* **23** (1): 42–61 DOI: 10.1002/hyp.7162

Moore RD, Pelto B, Menounos B, Hutchinson D. 2020. Detecting the Effects of Sustained Glacier Wastage on Streamflow in Variably Glacierized Catchments. *Frontiers in Earth Science* **8** (May): 136 DOI: 10.3389/feart.2020.00136

Mott R, Lehning M. 2010. Meteorological Modeling of Very High-Resolution Wind Fields and Snow Deposition for Mountains. *Journal of Hydrometeorology* **11** (4): 934–949 DOI: 10.1175/2010JHM1216.1

Mott R, Vionnet V, Grünewald T. 2018. The Seasonal Snow Cover Dynamics: Review on Wind-Driven

Coupling Processes. *Frontiers in Earth Science* **6**: 197 DOI: 10.3389/feart.2018.00197

Muir DL, Hayashi M, Mcclymont AF. 2011. Hydrological storage and transmission characteristics of an alpine talus. *Hydrological Processes* **25** (19): 2954–2966 DOI: 10.1002/hyp.8060

Munro DS. 1989. Surface Roughness and Bulk Heat Transfer on a Glacier: Comparison with Eddy Correlation. *Journal of Glaciology* **35** (121): 343–348 DOI: 10.3189/S0022143000009266

Munro DS. 1990. Comparison of melt energy computations and ablatometer measurements on melting ice and snow. *Arctic & Alpine Research* **22** (2): 153–162 DOI: 10.2307/1551300

Munro DS. 2004. Revisiting bulk heat transfer on Peyto Glacier, Alberta, Canada, in light of the OG parameterization. *Journal of Glaciology* **50** (171): 590–600 DOI: 10.3189/172756504781829819

Munro DS. 2011. Delays of supraglacial runoff from differently defined microbasin areas on the Peyto Glacier. *Hydrological Processes* **25** (19): n/a-n/a DOI: 10.1002/hyp.8124

Munro DS. 2013. Creating a Runoff Record for an Ungauged Basin: Peyto Glacier, 2002-2007. In *Putting Prediction in Ungauged Basins into Practice*197–204.

Musselman KN, Pomeroy JW, Essery RLH, Leroux N. 2015. Impact of windflow calculations on simulations of alpine snow accumulation, redistribution and ablation. *Hydrological Processes* **29** (18): 3983–3999 DOI: 10.1002/hyp.10595

Nakawo M, Young GJ. 1982. Estimate of glacier ablation under a debris layer from surface temperature and meteorological variables. *Journal of Glaciology* **28** (98): 29–34 DOI: 10.1017/S002214300001176X

Naz BS, Frans C, Clarke G, Burns P, Lettenmaier DP. 2014. Modeling the effect of glacier recession on streamflow response using a coupled glacio-hydrological model. *Hydrol. Earth Syst. Sci* **18**: 787–802 DOI: 10.5194/hess-18-787-2014

Nicholson L, Benn DI. 2006. Calculating ice melt beneath a debris layer using meteorological data. *Journal of Glaciology* **52** (178): 463–470 DOI: 10.3189/172756506781828584

Nicholson L, Benn D. 2013. Properties of natural supraglacial debris in relation to modelling sub-debris ice ablation. *Earth Surface Processes and Landforms* **38** (5): 490–501 DOI: 10.1002/esp.3299

Nicholson L, McCarthy M, Pritchard HD, Willis I. 2018. Supraglacial debris thickness variability: impact on ablation and relation to terrain properties. *The Cryosphere* **12** (12): 3719–3734 DOI: 10.5194/tc-12-3719-2018

Nolin AW, Phillippe J, Jefferson A, Lewis SL. 2010. Present-day and future contributions of glacier runoff to summertime flows in a Pacific Northwest watershed: Implications for water resources. *Water Resources Research* **46** (12) DOI: 10.1029/2009WR008968

Oerlemans J, Grisogono B. 2002a. Glacier winds and parameterisation of the related surface heat fluxes. *Tellus, Series A: Dynamic Meteorology and Oceanography* **54** (5): 440–452 DOI: 10.1034/j.1600-0870.2002.201398.x

Oerlemans J, Grisogono B. 2002b. Glacier winds and parameterization of the related surface heat fluxes. *Tellus* **54A** (5): 440–452 DOI: 10.1034/j.1600-0870.2002.201398.x

Olson M, Rupper S. 2019. Impacts of topographic shading on direct solar radiation for valley glaciers in complex topography. *The Cryosphere* **13**: 29–40 DOI: 10.5194/tc-13-29-2019

Ommanney CSL. 2002. Glaciers of North America — Glaciers of Canada: Glaciers of the Canadian Rockies in: Williams, R.S., Ferrigno, J.G. (Eds.). In *Satellite Image Atlas of Glaciers of the World*J199–J289.

Østrem G. 1959. Ice Melting under a Thin Layer of Moraine, and the Existence of Ice Cores in Moraine Ridges. *Geografiska Annaler* **41** (4): 228–230 DOI: 10.1080/20014422.1959.11907953

Østrem G, Arnold K, Ostrem G. 1970. Ice-Cored Moraines in Southern British Columbia and Alberta, Canada. *Geografiska Annaler. Series A, Physical Geography* **52** (2): 120 DOI: 10.2307/520605

Papalexiou SM. 2018. Unified theory for stochastic modelling of hydroclimatic processes: Preserving marginal distributions, correlation structures, and intermittency. *Advances in Water Resources* **115**: 234–252 DOI: 10.1016/J.ADVWATRES.2018.02.013

Papalexiou SM, Koutsoyiannis D, Montanari A. 2011. Can a simple stochastic model generate rich patterns of rainfall events? *Journal of Hydrology* **411** (3–4): 279–289 DOI: 10.1016/J.JHYDROL.2011.10.008

Pellicciotti F, Buergi C, Immerzeel WW, Konz M, Shrestha AB. 2012. Challenges and Uncertainties in Hydrological Modeling of Remote Hindu Kush–Karakoram–Himalayan (HKH) Basins: Suggestions for Calibration Strategies. *Mountain Research and Development* **32** (1): 39–50 DOI: 10.1659/MRD-JOURNAL-D-11-00092.1

Pellicciotti F, Carenzo M, Helbing J, Rimkus S, Burlando P. 2009. On the role of subsurface heat conduction in glacier energy-balance modelling. *Annals of Glaciology* **50** (50): 16–24 DOI: 10.3189/172756409787769555

Pepin N, Bradley RS, Diaz HF, Baraer M, Caceres EB, Forsythe N, Fowler HJ, Greenwood G, Hashmi MZ, Liu XD, et al. 2015. Elevation-dependent warming in mountain regions of the world. *Nature Climate Change* **5** (5): 424–430 DOI: 10.1038/nclimate2563

Pepin NC, Arnone E, Gobiet A, Haslinger K, Kotlarski S, Notarnicola C, Palazzi E, Seibert P, Serafin S, Schöner W, et al. 2022. Climate Changes and Their Elevational Patterns in the Mountains of the World. *Reviews of Geophysics* **60** (1) DOI: 10.1029/2020rg000730

Petersen L, Pellicciotti F. 2011. Spatial and temporal variability of air temperature on a melting glacier: Atmospheric controls, extrapolation methods and their effect on melt modeling, Juncal Norte Glacier, Chile. *Journal of Geophysical Research Atmospheres* **116** (23): 23109 DOI: 10.1029/2011JD015842

Pichelli E, Coppola E, Sobolowski S, Ban N, Giorgi F, Stocchi P, Alias A, Belušić D, Berthou S, Caillaud C, et al. 2021. The first multi-model ensemble of regional climate simulations at kilometer-scale resolution part 2: historical and future simulations of precipitation. *Climate Dynamics* **56** (11–12): 3581–3602 DOI: 10.1007/S00382-021-05657-4/FIGURES/11

Pomeroy JW, Gray DM. 1990. Saltation of snow. *Water Resources Research* **26** (7): 1583–1594 DOI: 10.1029/WR026i007p01583

Pomeroy JW, Li L. 2000. Prairie and arctic areal snow cover mass balance using a blowing snow model. *Journal of Geophysical Research: Atmospheres* **105** (D21): 26619–26634 DOI:

10.1029/2000JD900149

Pomeroy JW, Male DH. 1992. Steady-state suspension of snow. *Journal of Hydrology* **136** (1–4): 275–301 DOI: 10.1016/0022-1694(92)90015-N

Pomeroy JW, Fang X, Ellis C. 2012. Sensitivity of snowmelt hydrology in Marmot Creek, Alberta, to forest cover disturbance. *Hydrological Processes* **26** (12): 1891–1904 DOI: 10.1002/hyp.9248

Pomeroy JW, Fang X, Marks D. 2016. The cold rain-on-snow event of June 2013 in the Canadian Rockies — characteristics and diagnosis. *Hydrological Processes* **2914** (June 2013): 2899–2914 DOI: 10.1002/hyp.10905

Pomeroy JW, Brown T, Fang X, Shook KR, Pradhananga D, Armstrong R, Harder P, Marsh C, Costa D, Krogh SA, Aubry-Wake C, Annand H, Lawford P, He Z, Kompanizare M, Lopez-Moreno JI. (2022). The Cold Regions Hydrological Modelling Platform for hydrological diagnosis and prediction based on process understanding. accepted in Journal of Hydrology. Manuscript ID: HYDROL46207R1Pomeroy JW, Fang X, Shook K, Whitfield PH. 2013. Predicting in Ungauged Basins Using Physical Principles Obtained Using the Deductive, Inductive, and Abductive Reasoning Approach. In *Putting Predictions in Ungauged Basins into Practice.* 41–62.

Pomeroy JW, Gray DM, Brown T, Hedstrom NR, Quinton WL, Granger RJ, Carey SK. 2007. The cold regions hydrological model: A platform for basing process representation and model structure on physical evidence. *Hydrological Processes* **21** (19): 2650–2667 DOI: 10.1002/hyp.6787

Pomeroy JW, Gray DMM, Landline PG, Landine PG. 1993. The Prairie Blowing Snow Model: characteristics, validation, operation. *Journal of Hydrology* **144** (1–4): 165–192 DOI: 10.1016/0022-1694(93)90171-5

Pomeroy JW, Marsh P, Gray DM. 1997. Application of a distributed blowing snow model to the Arctic. *Hydrological Processes* **11** (11): 1451–1464 DOI: 10.1002/(SICI)1099-1085(199709)11:11<1451::AID-HYP449>3.0.CO;2-Q

Potter ER, Orr A, Willis IC, Bannister D, Salerno F. 2018. Dynamical Drivers of the Local Wind Regime in a Himalayan Valley. *Journal of Geophysical Research: Atmospheres* **123** (23): 13,186-13,202 DOI: 10.1029/2018JD029427

Pouyaud B, Zapata M, Yerren J, Gomez J, Rosas G, Suarez W, Ribstein P. 2005. On the future of the water resources from glacier melting in the Cordillera Blanca, Peru. *Hydrological Sciences Journal* **50** (6): 999–1022 DOI: 10.1623/hysj.2005.50.6.999

Pradhananga D, Pomeroy JW. 2022a. Diagnosing changes in glacier hydrology from physical principles using a hydrological model with snow redistribution, sublimation, firnification and energy balance ablation algorithms. *Journal of Hydrology* **608**: 127545 DOI: 10.1016/j.jhydrol.2022.127545

Pradhananga D, Pomeroy JW. 2022b. Recent hydrological response of glaciers in the Canadian Rockies to changing climate and glacier configuration. *Hydrol. Earth Syst. Sci* **26**: 2605–2616 DOI: 10.5194/hess-26-2605-2022

Pradhananga D, Pomeroy JW, Aubry-Wake C, Munro DS, Shea JM, Demuth MN, Kirat NH, Menounos B, Mukherjee K. 2020. Hydrometeorological, glaciological and geospatial research data from the Peyto Glacier Research Basin in the Canadian Rockies. *Federated Research Data Repository (FRDR)* DOI: 10.20383/101.0259

Pradhananga D, Pomeroy JW, Aubry-Wake C, Munro DS, Shea J, Demuth MN, Kirat NH, Menounos B, Mukherjee K. 2021. Hydrometeorological, glaciological and geospatial research data from the Peyto Glacier Research Basin in the Canadian Rockies. *Earth System Science Data* **13** (6): 2875–2894 DOI: 10.5194/essd-13-2875-2021

Prasch M, Mauser W, Weber M. 2013. Quantifying present and future glacier melt-water contribution to runoff in a central Himalayan river basin. *Cryosphere* **7** (3): 889–904 DOI: 10.5194/tc-7-889-2013

Prein AF, Gobiet A, Suklitsch M, Truhetz H, Awan NK, Keuler K, Georgievski G. 2013. Added value of convection permitting seasonal simulations. *Climate Dynamics* **41** (9–10): 2655–2677 DOI: 10.1007/s00382-013-1744-6

Prein AF, Langhans W, Fosser G, Ferrone A, Ban N, Goergen K, Keller M, Tölle M, Gutjahr O, Feser F, et al. 2015. A review on regional convection-permitting climate modeling: Demonstrations, prospects, and challenges. *Reviews of Geophysics* **53** (2): 323–361 DOI: 10.1002/2014RG000475

Pulwicki A, Flowers GE, Radic V, Bingham D. 2018. Estimating winter balance and its uncertainty from direct measurements of snow depth and density on alpine glaciers. *Journal of Glaciology* **64** (247): 781–795 DOI: 10.1017/jog.2018.68

Rabatel A, Francou B, Soruco A, Gomez J, Cáceres B, Ceballos JL, Basantes R, Vuille M, Sicart JE, Huggel C, et al. 2013. Current state of glaciers in the tropical Andes: a multi-century perspective on glacier evolution and climate change. *The Cryosphere* **7**: 81–102 DOI: 10.5194/tc-7-81-2013

Radic V, Hock R. 2014. Glaciers in the Earth's Hydrological Cycle: Assessments of Glacier Mass and Runoff Changes on Global and Regional Scales. *Surveys in Geophysics* **35** (3): 813–837 DOI: 10.1007/s10712-013-9262-y

Radic V, Menounos B, Shea J, Fitzpatrick N, Tessema MA, Déry SJ. 2017. Evaluation of different methods to model near-surface turbulent fluxes for a mountain glacier in the Cariboo Mountains, BC, Canada. *Cryosphere* **11** (6): 2897–2918 DOI: 10.5194/tc-11-2897-2017

Ragettli S, Pellicciotti F. 2012. Calibration of a physically based, spatially distributed hydrological model in a glacierized basin: On the use of knowledge from glaciometeorological processes to constrain model parameters. *Water Resources Research* **48** (3) DOI: 10.1029/2011WR010559

Ragettli S, Cortés G, Mcphee J, Pellicciotti F. 2014. An evaluation of approaches for modelling hydrological processes in high-elevation, glacierized Andean watersheds. *Hydrological Processes* **28** (23): 5674–5695 DOI: 10.1002/hyp.10055

Ragettli S, Immerzeel WW, Pellicciotti F. 2016. Contrasting climate change impact on river flows from high-altitude catchments in the Himalayan and Andes Mountains. *Proceedings of the National Academy of Sciences* **113** (33): 9222–9227 DOI: 10.1073/pnas.1606526113

Ragettli S, Pellicciotti F, Bordoy R, Immerzeel WW. 2013. Sources of uncertainty in modeling the glaciohydrological response of a Karakoram watershed to climate change. *Water Resources Research* **49** (9): 6048–6066 DOI: 10.1002/wrcr.20450

Ragettli S, Pellicciotti F, Immerzeel WW, Miles ES, Petersen L, Heynen M, Shea JM, Stumm D, Joshi S, Shrestha A. 2015. Unraveling the hydrology of a Himalayan catchment through integration of high resolution in situ data and remote sensing with an advanced simulation model. *Advances in Water Resources* **78**: 94–111 DOI: 10.1016/j.advwatres.2015.01.013

Rahimikhoob A. 2010. Estimating global solar radiation using artificial neural network and air temperature data in a semi-arid environment. *Renewable Energy* **35** (9): 2131–2135 DOI: 10.1016/j.renene.2010.01.029

Rasmussen R, Ikeda K, Liu C, Gochis D, Clark MP, Dai A, Gutmann E, Dudhia J, Chen F, Barlage M, et al. 2014. Climate change impacts on the water balance of the Colorado headwaters: High-resolution regional climate model simulations. *Journal of Hydrometeorology* **15** (3): 1091–1116 DOI: 10.1175/JHM-D-13-0118.1

Rasmussen R, Liu C, Ikeda K, Gochis D, Yates D, Chen F, Tewari M, Barlage M, Dudhia J, Yu W, et al. 2011. High-resolution coupled climate runoff simulations of seasonal snowfall over Colorado: A process study of current and warmer climate. *Journal of Climate* **24** (12): 3015–3048 DOI: 10.1175/2010JCLI3985.1

Rasouli K, Pomeroy JW, Janowicz JR, Carey SK, Williams TJ. 2014. Hydrological sensitivity of a northern mountain basin to climate change. *Hydrological Processes* **28** (14) DOI: 10.1002/hyp.10244

Rasouli K, Pomeroy JW, Marks D. 2015. Snowpack sensitivity to perturbed climate in a cool mid-latitude mountain catchment. *Hydrological Processes* **29** (18): 3925–3940 DOI: 10.1002/hyp.10587

Rasouli K, Pomeroy JW, Whitfield PH. 2019. Hydrological Responses of Headwater Basins to Monthly Perturbed Climate in the North American Cordillera. *Journal of Hydrometeorology* **20** (5): 863–882 DOI: 10.1175/JHM-D-18-0166.1

Reid T, Brock BW. 2010. An energy-balance model for debris-covered glaciers including heat conduction through the debris layer. *Journal of Glaciology* **56** (199): 903–916 DOI: 10.3189/002214310794457218

Reid T, Carenzo M, Pellicciotti F, Brock BW. 2012. Including debris cover effects in a distributed model of glacier ablation. *Journal of Geophysical Research Atmospheres* **117** (17): 1–15 DOI: 10.1029/2012JD017795

Richardson M, Moore RD (Dan., Zimmermann A. 2017a. Variability of tracer breakthrough curves in mountain streams: Implications for streamflow measurement by slug injection. *Canadian Water Resources Journal* **42** (1): 21–37 DOI: 10.1080/07011784.2016.1212676

Richardson M, Sentlinger G, Moore RDD, Zimmermann A. 2017b. Quantifying the Relation Between Electrical Conductivity and Salt Concentration for Dilution Gauging Via Dry Salt Injection. *Confluence: Journal of Watershed Science and Management* **1** (2) DOI: 10.22230/jwsm.2017v1n2a1

Roe GH. 2005. OROGRAPHIC PRECIPITATION. *Annual Review of Earth and Planetary Sciences* **33** (1): 645–671 DOI: 10.1146/annurev.earth.33.092203.122541

Rolland C. 2003. Spatial and seasonal variations of air temperature lapse rates in alpine regions. *Journal of Climate* **16** (7): 1032–1046 DOI: 10.1175/1520-0442(2003)016<1032:SASVOA>2.0.CO;2

Rounce DR, McKinney DC. 2013. Debris thickness of glaciers in the Everest area (Nepal Himalaya) derived from satellite imagery using a nonlinear energy balance model. *Cryosphere* **8** (4): 1317–1329 DOI: 10.5194/tc-8-1317-2014

Rounce DR, Hock R, McNabb RW, Millan R, Sommer C, Braun MH, Malz P, Maussion F, Mouginot J, Seehaus TC, et al. 2021. Distributed Global Debris Thickness Estimates Reveal Debris Significantly Impacts Glacier Mass Balance. *Geophysical Research Letters* **48** (8): e2020GL091311 DOI: 10.1029/2020GL091311

Rounce DR, King O, McCarthy M, Shean DE, Salerno F. 2018. Quantifying Debris Thickness of Debris-Covered Glaciers in the Everest Region of Nepal Through Inversion of a Subdebris Melt Model. *Journal of Geophysical Research: Earth Surface* **123** (5): 1094–1115 DOI: 10.1029/2017JF004395

Rounce DR, Quincey DJ, McKinney DC. 2015. Debris-covered glacier energy balance model for Imja-Lhotse Shar Glacier in the Everest region of Nepal. *Cryosphere* **9** (6): 2295–2310 DOI: 10.5194/tc-9-2295-2015

Runkel RL. 2015. On the use of rhodamine WT for the characterization of stream hydrodynamics and transient storage. *Water Resources Research* **51** (8): 6125–6142 DOI: 10.1002/2015WR017201

Ryan JC, Hubbard A, Stibal M, Irvine-Fynn TDL, Cook JM, Smith LC, Cameron K, Box J. 2018. Dark zone of the Greenland Ice Sheet controlled by distributed biologically-active impurities. *Nature Communications* **9** (1) DOI: 10.1038/s41467-018-03353-2

Saberi L, Mclaughlin RT, Ng G-HC, Frenierre J La, Wickert AD, Baraer M, Zhi W, Li L, Mark BG. 2019. Multi-scale temporal variability in meltwater contributions in a tropical glacierized watershed. *Hydrol. Earth Syst. Sci* **23**: 405–425 DOI: 10.5194/hess-23-405-2019

Salisbury JW, D'Aria DM. 1994. Emissivity of terrestrial materials in the 3-5 µm atmospheric window. *Remote Sensing of Environment* **47** (3): 345–361 DOI: 10.1016/0034-4257(94)90102-3

Samani Z, Asce M, Hargreaves GH, Asce F, Tran V, Bawazir S. 2011. Estimating Solar Radiation from Temperature with Spatial and Temporal Calibration. *Journal of Irrigation and Drainage Engineering* **137** (11): 692–696 DOI: 10.1061/(ASCE)IR.1943-4774.0000342.

Samimi S, Marshall SJ. 2017. Diurnal Cycles of Meltwater Percolation, Refreezing, and Drainage in the Supraglacial Snowpack of Haig Glacier, Canadian Rocky Mountains. *Frontiers in Earth Science* **5** DOI: 10.3389/feart.2017.00006

Sato Y, Fujita K, Inoue H, Sunako S, Sakai A, Tsushima A, Podolskiy EA, Kayastha R, Kayastha RB. 2021. Ice Cliff Dynamics of Debris-Covered Trakarding Glacier in the Rolwaling Region, Nepal Himalaya. *Frontiers in Earth Science* **9**: 398 DOI: 10.3389/FEART.2021.623623/BIBTEX

Schaefli B, Gupta H V. 2007. Do Nash values have value? *Hydrological Processes* **21** (15): 2075–2080 DOI: 10.1002/hyp

Schaefli B, Hingray B, Niggli M, Musy A. 2005. A conceptual glacio-hydrological model for high mountainous catchments. *Hydrology and Earth System Sciences* **9** (1–2): 95–109 DOI: 10.5194/hess-9-95-2005

Schauwecker S, Rohrer M, Huggel C, Kulkarni A, Ramanathan AL, Salzmann N, Stoffel M, Brock BW. 2015. Remotely sensed debris thickness mapping of Bara Shigri Glacier, Indian Himalaya. *Journal of Glaciology* **61** (228): 675–688 DOI: 10.3189/2015JoG14J102

Scherler D, Wulf H, Gorelick N. 2018. Global Assessment of Supraglacial Debris-Cover Extents. *Geophysical Research Letters* **45** (21): 11,798-11,805 DOI: 10.1029/2018GL080158

Schneider T, Jansson P. 2004. Internal accumulation in firn and its significance for the mass balance of Storglaciären, Sweden. *Journal of Glaciology* **50** (168): 25–34 DOI: 10.3189/172756504781830277

Schumann K, Gewolf S, Tackenberg O. 2016. Factors affecting primary succession of glacier foreland vegetation in the European Alps. *Alpine Botany* **126** (2): 105–117 DOI: 10.1007/s00035-016-0166-6

Schweizer J, Kronholm K, Jamieson B, Birkeland KW. 2008. Review of spatial variability of snowpack properties and its importance for avalanche formation. *Cold Regions Science and Technology* **51** (2–3): 253–272 DOI: 10.1016/J.COLDREGIONS.2007.04.009

Seibert J, Vis M, Lewis E, van Meerveld HJ. 2018. Upper and lower benchmarks in hydrological modelling. *Hydrological Processes* DOI: 10.1002/hyp.11476

Sen PK. 1968. Estimates of the Regression Coefficient Based on Kendall's Tau. *Journal of the American Statistical Association* **63** (324): 1379–1389 DOI: 10.1080/01621459.1968.10480934

Seneviratne SI, Nicholls N, Easterling D, Goodess CM, Kanae S, Kossin J, Luo Y, Marengo J, McInnes K, Rahimi M, et al. 2012. Changes in climate extremes and their impacts on the natural physical environment. In: Managing the Risks of Extreme Events and Disasters to Advance Climate Change Adaptation. Cambridge University Press.

Sentlinger G, Fraser J, Baddock E. 2019. Salt Dilution Flow Measurement: Automation and Uncertainty. In *HydroSenSoft, International Symposium and Exhibition on Hydro-Environment Sensors and Software.*Madrid; 8. Available at: http://www.fathomscientific.com/wp-content/uploads/2018/12/HydroSense_AutoSalt_2019_V0.6.pdf

Shah SS, Banerjee A, Nainwal HC, Shankar R. 2019. Estimation of the total sub-debris ablation from point-scale ablation data on a debris-covered glacier. *Journal of Glaciology* **65** (253): 759–769 DOI: 10.1017/jog.2019.48

Shannon S, Smith R, Wiltshire A, Payne T, Huss M, Betts R, Caesar J, Koutroulis A, Jones D, Harrison S. 2019. Global glacier volume projections under high-end climate change scenarios. *Cryosphere* **13** (1): 325–350 DOI: 10.5194/TC-13-325-2019

Shaw TE, Brock BW, Ayala A, Rutter N, Pellicciotti F. 2017. Centreline and cross-glacier air temperature variability on an Alpine glacier: Assessing temperature distribution methods and their influence on melt model calculations. *Journal of Glaciology* **63** (242): 973–988 DOI: 10.1017/jog.2017.65

Shea JM, Moore RD. 2010. Prediction of spatially distributed regional-scale fields of air temperature and vapor pressure over mountain glaciers. *Journal of Geophysical Research* **115** (D23): D23107 DOI: 10.1029/2010JD014351

Shea JM, Immerzeel WW, Wagnon P, Vincent C, Bajracharya S. 2015. Modelling glacier change in the Everest region, Nepal Himalaya. *The Cryosphere* **9** (3): 1105–1128 DOI: 10.5194/tc-9-1105-2015

Shen YJ, Shen Y, Goetz J, Brenning A. 2016. Spatial-temporal variation of near-surface temperature lapse rates over the Tianshan Mountains, central Asia. *Journal of Geophysical Research: Atmospheres* **121** (23): 14,006-14,017 DOI: 10.1002/2016JD025711

Shook KR, Pomeroy JW. 2011. Synthesis of incoming shortwave radiation for hydrological simulation.

Hydrology Research **42** (6): 433 DOI: 10.2166/nh.2011.074

Shugar DH, Burr A, Haritashya UK, Kargel JS, Watson CS, Kennedy MC, Bevington AR, Betts RA, Harrison S, Strattman K. 2020. Rapid worldwide growth of glacial lakes since 1990. *Nature Climate Change* **10** (10): 939–945 DOI: 10.1038/s41558-020-0855-4

Sicart JE, Pomeroy JW, Essery RLH, Bewley D. 2006. Incoming longwave radiation to melting snow: observations, sensitivity and estimation in northern environments. *Hydrological Processes2* **20** (17): 3697–3708 DOI: 10.1002/hyp.6383

Skamarock WC, Klemp JB, Dudhi J, Gill DO, Barker DM, Duda MG, Huang X-Y, Wang W, Powers JG. 2008. A Description of the Advanced Research WRF Version 3 DOI: 10.5065/D6DZ069T

Skiles SMK, Flanner M, Cook JM, Dumont M, Painter TH. 2018. Radiative forcing by light-absorbing particles in snow. *Nature Climate Change* **8** (11): 964–971 DOI: 10.1038/s41558-018-0296-5

Smeets CJPP, Duynkerke PG, Vugts HF. 2000. Turbulence characteristics of the stable boundary layer over a mid-latitude glacier. Part II: Pure katabatic forcing conditions. *Boundary-Layer Meteorology* **97** (1): 73–107 DOI: 10.1023/A:1002738407295

Sobrino JA, Cuenca J. 1999. Angular variation of thermal infrared emissivity for some natural surfaces from experimental measurements. *Applied Optics* **38** (18): 3931 DOI: 10.1364/ao.38.003931

Sokolik IN, Soja AJ, DeMott PJ, Winker D. 2019. Progress and Challenges in Quantifying Wildfire Smoke Emissions, Their Properties, Transport, and Atmospheric Impacts. *Journal of Geophysical Research: Atmospheres* **124** (23): 13005–13025 DOI: 10.1029/2018JD029878

Somers LD, McKenzie JM. 2020. A review of groundwater in high mountain environments. *Wiley Interdisciplinary Reviews: Water* **7** (6) DOI: 10.1002/wat2.1475

Somers LD, Gordon RP, McKenzie JM, Lautz LK, Wigmore O, Glose AM, Glas R, Aubry-Wake C, Mark B, Baraer M, et al. 2016. Quantifying groundwater–surface water interactions in a proglacial valley, Cordillera Blanca, Peru. *Hydrological Processes* **30** (17): 2915–2929 DOI: 10.1002/hyp.10912

Somers LD, McKenzie JM, Mark BG, Lagos P, Ng GHC, Wickert AD, Yarleque C, Baraer M, Silva Y. 2019. Groundwater Buffers Decreasing Glacier Melt in an Andean Watershed—But Not Forever. *Geophysical Research Letters* **46** (22): 13016–13026 DOI: 10.1029/2019GL084730

Somers LD, McKenzie JM, Zipper SC, Mark BG, Lagos P, Baraer M. 2018. Does hillslope trenching enhance groundwater recharge and baseflow in the Peruvian Andes? *Hydrological Processes* **32** (3): 318–331 DOI: 10.1002/hyp.11423

Stahl K, Moore RD. 2006. Influence of watershed glacier coverage on summer streamflow in British Columbia, Canada. *Water Resources Research* **42** (6) DOI: 10.1029/2006WR005022

Steiner J, Litt M, Stigter EE, Shea JM, Bierkens MFP, Immerzeel WW. 2018. The Importance of Turbulent Fluxes in the Surface Energy Balance of a Debris-Covered Glacier in the Himalayas. *Frontiers in Earth Science* **6**: 144 DOI: 10.3389/feart.2018.00144

Steiner J, Pellicciotti F, Buri P, Miles ES, Immerzeel WW, Reid T. 2015. Modelling ice-cliff backwasting on a debris-covered glacier in the Nepalese Himalaya. *Journal of Glaciology* **61** (229): 889–907 DOI: 10.3189/2015JoG14J194

Stewart RL, Westoby M, Pellicciotti F, Rowan A, Swift D, Brock B, Woodward J. 2021. Using climate reanalysis data in conjunction with multi-temporal satellite thermal imagery to derive supraglacial debris thickness changes from energy-balance modelling. *Journal of Glaciology* **67** (262): 366–384 DOI: 10.1017/JOG.2020.111

Stibal M, Šabacká M, Žárský J. 2012. Biological processes on glacier and ice sheet surfaces. *Nature Geoscience* **5** (11): 771–774 DOI: 10.1038/ngeo1611

Stigter EE, Litt M, Steiner JF, Bonekamp PNJ, Shea JM, Bierkens MFP, Immerzeel WW. 2018. The Importance of Snow Sublimation on a Himalayan Glacier. *Frontiers in Earth Science* **6**: 108 DOI: 10.3389/feart.2018.00108

Stigter EE, Steiner JF, Koch I, Saloranta TM, Kirkham JD, Immerzeel WW. 2021. Energy and mass balance dynamics of the seasonal snowpack at two high-altitude sites in the Himalaya. *Cold Regions Science and Technology* **183**: 103233 DOI: 10.1016/j.coldregions.2021.103233

Stocks BJ, Mason JA, Todd JB, Bosch EM, Wotton BM, Amiro BD, Flannigan MD, Hirsch KG, Logan KA, Martell DL, et al. 2003. Large forest fires in Canada, 1959-1997. *Journal of Geophysical Research D: Atmospheres* **108** (1) DOI: 10.1029/2001jd000484

Stone RS, Anderson GP, Shettle EP, Andrews E, Loukachine K, Dutton EG, Schaaf C, Roman MO. 2008. Radiative impact of boreal smoke in the Arctic: Observed and modeled. *Journal of Geophysical Research Atmospheres* **113** (14): 14–16 DOI: 10.1029/2007JD009657

Tague C, Grant GE. 2009. Groundwater dynamics mediate low-flow response to global warming in snow-dominated alpine regions. *Water Resources Research* **45** (7): 7421 DOI: 10.1029/2008WR007179

Tague C, Grant G, Farrell M, Choate J, Jefferson A. 2008. Deep groundwater mediates streamflow response to climate warming in the Oregon Cascades. *Climatic Change* **86** (1–2): 189–210 DOI: 10.1007/s10584-007-9294-8

Tarca G, Guglielmin M. 2022. Using ground-based thermography to analyse surface temperature distribution and estimate debris thickness on Gran Zebrù glacier (Ortles-Cevedale, Italy). *Cold Regions Science and Technology* **196**: 103487 DOI: 10.1016/j.coldregions.2022.103487

Taylor KE, Stouffer RJ, Meehl GA. 2012. An overview of CMIP5 and the experiment design. *Bulletin of the American Meteorological Society* DOI: 10.1175/BAMS-D-11-00094.1

Taylor P, Lee RJJ. 1984. Simple guidelines for estimating wind speed variations due to small scale topographic features. *Climatological Bulletin* **18** (2): 3–32

Tedstone AJ, Cook JM, Williamson CJ, Hofer S, McCutcheon J, Irvine-Fynn T, Gribbin T, Tranter M. 2020. Algal growth and weathering crust state drive variability in western Greenland Ice Sheet ice albedo. *Cryosphere* **14** (2): 521–538 DOI: 10.5194/tc-14-521-2020

Tennant C, Menounos B. 2013. Glacier change of the Columbia Icefield, Canadian Rocky Mountains, 1919-2009. *Journal of Glaciology* **59** (216): 671–686 DOI: 10.3189/2013JoG12J135

Tennant C, Menounos B, Wheate R, Clague JJ. 2012. Area change of glaciers in the Canadian rocky mountains, 1919 to 2006. *Cryosphere* **6** (6): 1541–1552 DOI: 10.5194/tc-6-1541-2012

van Tiel M, Kohn I, Van Loon AF, Stahl K. 2020a. The compensating effect of glaciers: Characterizing

the relation between interannual streamflow variability and glacier cover. *Hydrological Processes* **34** (3): 553–568 DOI: 10.1002/hyp.13603

van Tiel M, Van Loon AF, Seibert J, Stahl K. 2021. Hydrological response to warm and dry weather: do glaciers compensate? *Hydrology and Earth System Sciences* **25** (6): 3245–3265 DOI: 10.5194/hess-25-3245-2021

van Tiel M, Stahl K, Freudiger D, Seibert J. 2020b. Glacio-hydrological model calibration and evaluation. *Wiley Interdisciplinary Reviews: Water* **7** (6) DOI: 10.1002/wat2.1483

Trant A, Higgs E, Starzomski BM. 2020. A century of high elevation ecosystem change in the Canadian Rocky Mountains. *Scientific Reports* **10** (1): 9698 DOI: 10.1038/s41598-020-66277-2

Troxler P, Ayala Á, Shaw TE, Nolan M, Brock BW, Pellicciotti F. 2020. Modelling spatial patterns of near-surface air temperature over a decade of melt seasons on McCall Glacier, Alaska. *Journal of Glaciology* **66** (257): 386–400 DOI: 10.1017/jog.2020.12

Verbunt M, Gurtz J, Jasper K, Lang H, Warmerdam P, Zappa M. 2003. The hydrological role of snow and glaciers in alpine river basins and their distributed modeling. *Journal of Hydrology* **282** (1–4): 36–55 DOI: 10.1016/S0022-1694(03)00251-8

Versini PA, Velasco M, Cabello A, Sempere-Torres D. 2013. Hydrological impact of forest fires and climate change in a Mediterranean basin. *Natural Hazards* **66** (2): 609–628 DOI: 10.1007/s11069-012-0503-z

Vionnet V, Marsh CB, Menounos B, Gascoin S, Wayand NE, Shea J, Mukherjee K, Pomeroy JW. 2021. Multi-scale snowdrift-permitting modelling of mountain snowpack. *Cryosphere* **15** (2): 743–769 DOI: 10.5194/TC-15-743-2021

Vionnet V, Martin E, Masson V, Guyomarc'H G, Naaim-Bouvet F, Prokop A, Durand Y, Lac C. 2014. Simulation of wind-induced snow transport and sublimation in alpine terrain using a fully coupled snowpack/atmosphere model. *Cryosphere* **8** (2): 395–415 DOI: 10.5194/tc-8-395-2014

Viviroli D, Dürr HH, Messerli B, Meybeck M, Weingartner R. 2007. Mountains of the world, water towers for humanity: Typology, mapping, and global significance. *Water Resources Research* **43** (7): 1–13 DOI: 10.1029/2006WR005653

Viviroli D, Kummu M, Meybeck M, Kallio M, Wada Y. 2020. Increasing dependence of lowland populations on mountain water resources. *Nature Sustainability* **3** (11): 917–928 DOI: 10.1038/s41893-020-0559-9

van Vuuren DPP, Edmonds J, Kainuma MLT, Riahi K, Thomson A, Hibbard K, Hurtt GC, Kram T, Krey V, Lamarque J, et al. 2011. The representative concentration pathways: An overview. *Climatic Change* **109** (1): 5–31 DOI: 10.1007/s10584-011-0148-z

Walmsley JL, Taylor PA, Keith T. 1986. A simple model of neutrally stratified boundary-layer flow over complex terrain with surface roughness modulations (MS3DJH/3R). *Boundary-Layer Meteorology* **36** (1–2): 157–186 DOI: 10.1007/BF00117466

Warren SG, Wiscombe WJ. 1980. A model for the spectral albedo of snow. II: snow containing atmospheric aerosols. *Journal of the Atmospheric Sciences* **37** (12): 2734–2745 DOI: 10.1175/1520-0469(1980)037<2734:AMFTSA>2.0.CO;2

Warscher M, Wagner S, Marke T, Laux P, Smiatek G, Strasser U, Kunstmann H. 2019. A 5 km resolution regional climate simulation for Central Europe: Performance in high mountain areas and seasonal, regional and elevation-dependent variations. *Atmosphere* DOI: 10.3390/atmos10110682

Weber M, Bernhardt M, Pomeroy JW, Fang X, Härer S, Schulz K. 2016. Description of current and future snow processes in a small basin in the Bavarian Alps. *Environmental Earth Sciences* **75** (17): 1223 DOI: 10.1007/s12665-016-6027-1

Westerling AL, Hidalgo HG, Cayan DR, Swetnam TW. 2006. Warming and earlier spring increase Western U.S. forest wildfire activity. *Science* **313** (5789): 940–943 DOI: 10.1126/science.1128834

Wheater HS, Pomeroy JW, Pietroniro A, Davison B, Elshamy M, Yassin F, Rokaya P, Fayad A, Tesemma Z, Princz D, et al. 2022. Advances in modelling large river basins in cold regions with Modélisation Environmentale Communautaire—Surface and Hydrology (MESH), the Canadian hydrological land surface scheme. *Hydrological Processes* **36** (4): e14557 DOI: 10.1002/HYP.14557

Wigmosta MS, Vail LW, Lettenmaier DP. 1994. A distributed hydrology-vegetation model for complex terrain. *Water Resources Research* **30** (6): 1665–1679 DOI: 10.1029/94WR00436

Williamson SN, Menounos B. 2021. The influence of forest fires aerosol and air temperature on glacier albedo, western North America. *Remote Sensing of Environment* **267**: 112732 DOI: 10.1016/j.rse.2021.112732

Winkler G, Wagner T, Pauritsch M, Birk S, Kellerer-Pirklbauer A, Benischke R, Leis A, Morawetz R, Schreilechner MG, Hergarten S. 2016. Identification and assessment of groundwater flow and storage components of the relict Schöneben Rock Glacier, Niedere Tauern Range, Eastern Alps (Austria). *Hydrogeology Journal* **24** (4): 937–953 DOI: 10.1007/s10040-015-1348-9

Winkler M, Juen I, Mölg T, Wagnon P, Gómez J, Kaser G. 2009. Measured and modelled sublimation on the tropical Glaciar Artesonraju, Perú. *Cryosphere* **3** (1): 21–30 DOI: 10.5194/tc-3-21-2009

WMO. 1986. Intercomparison of models of snowmelt runoff. Operational Hydrology Report No. 23. World Meteorological Organization

Wood WH, Marshall SJ, Whitehead TL, Fargey SE. 2018. Daily temperature records from a mesonet in the foothills of the Canadian Rocky Mountains, 2005-2010. *Earth System Science Data* **10** (1): 595–607 DOI: 10.5194/ESSD-10-595-2018

Wu G, Liu Y, Wang T. 2007. Methods and strategy for modeling daily global solar radiation with measured meteorological data – A case study in Nanchang station, China. *Energy Conversion and Management* **48**: 2447–2452 DOI: 10.1016/j.enconman.2007.04.011

Young GJ. 1977. Relations between mass-balance and meteorological variables. *Zeitschrift für Gletscherkunde und Glazialgeologie* **13** (1/2): 111–125

Zhou J, Pomeroy JW, Zhang W, Cheng G, Wang G, Chen C. 2014. Simulating cold regions hydrological processes using a modular model in the west of China. *Journal of Hydrology* **509**: 13–24 DOI: 10.1016/J.JHYDROL.2013.11.013

Zwaaftink CDG, Löwe H, Mott R, Bavay M, Lehning M. 2011. Drifting snow sublimation: A high-

resolution 3-D model with temperature and moisture feedbacks. *Journal of Geophysical Research Atmospheres* **116** (16): 1–14 DOI: 10.1029/2011JD015754

APPENDIX A: SUPPLEMENTARY MATERIAL FOR CHAPTER 3

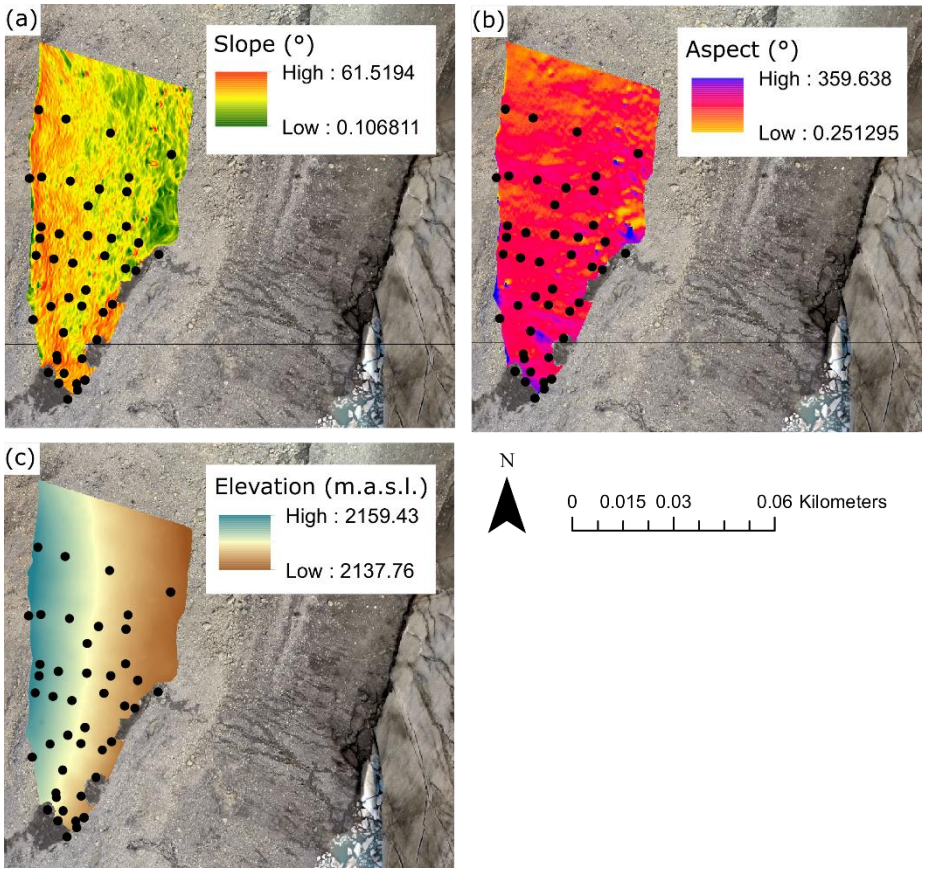

Figure A.1. Slope, aspect and elevation of the study slope derived from UAV imagery. The black circle are the location of the 44 manual excavations.

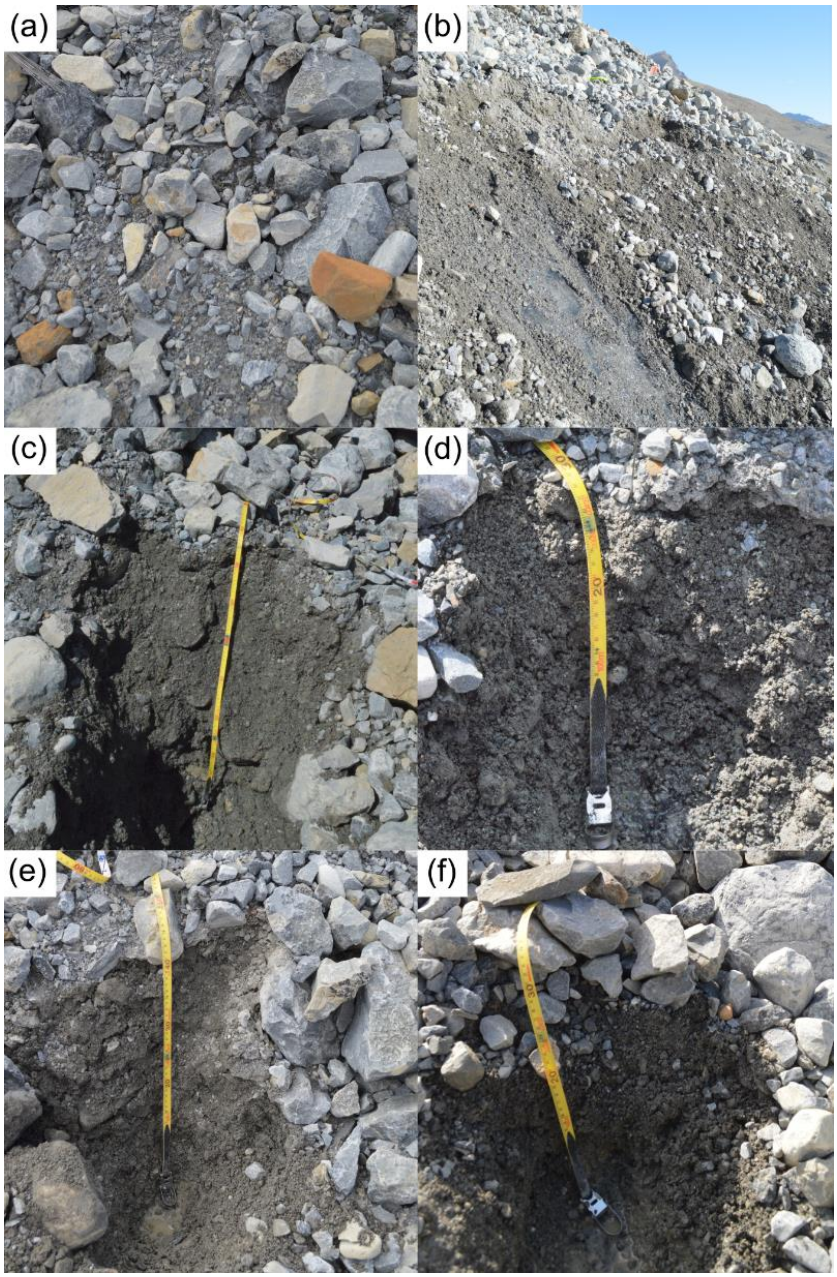

Figure A.2. Representative surface for the continuous debris (a) and the discontinuous debris (b), with example manual excavations of 85 cm, (c), 27 cm (d), 50 cm (e) and 34 cm (f).

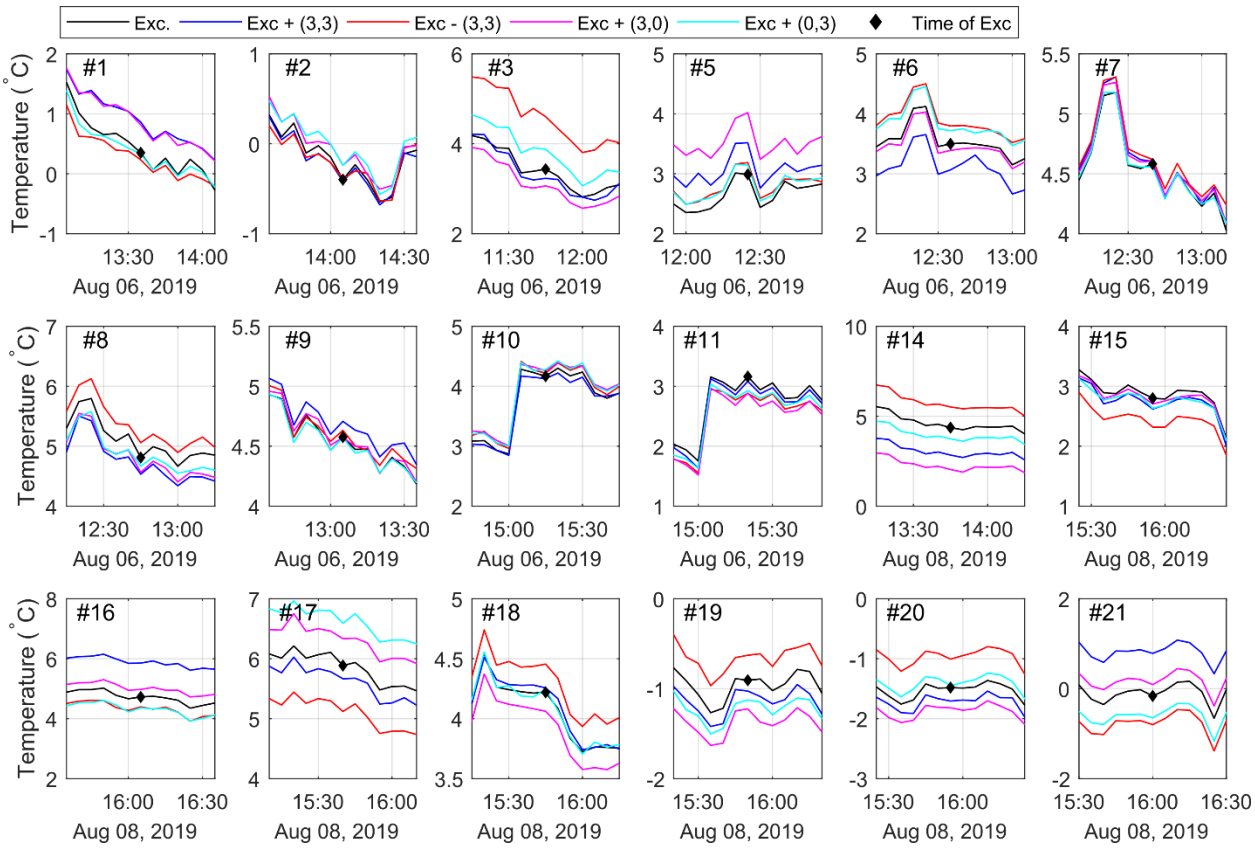

Figure A.3. Surface temperature for a 3x3 pixel area at the location of the manual excavations (black) and for four adjacent areas that were left undisturbed (coloured line). The parenthesis in the legend shows the pixel offset for each location. The black diamond shows the time of the manual excavations. If the manual excavation caused a temperature anomaly, the black line would behave differently from the other undisturbed location (colour) after the manual excavation occurred.

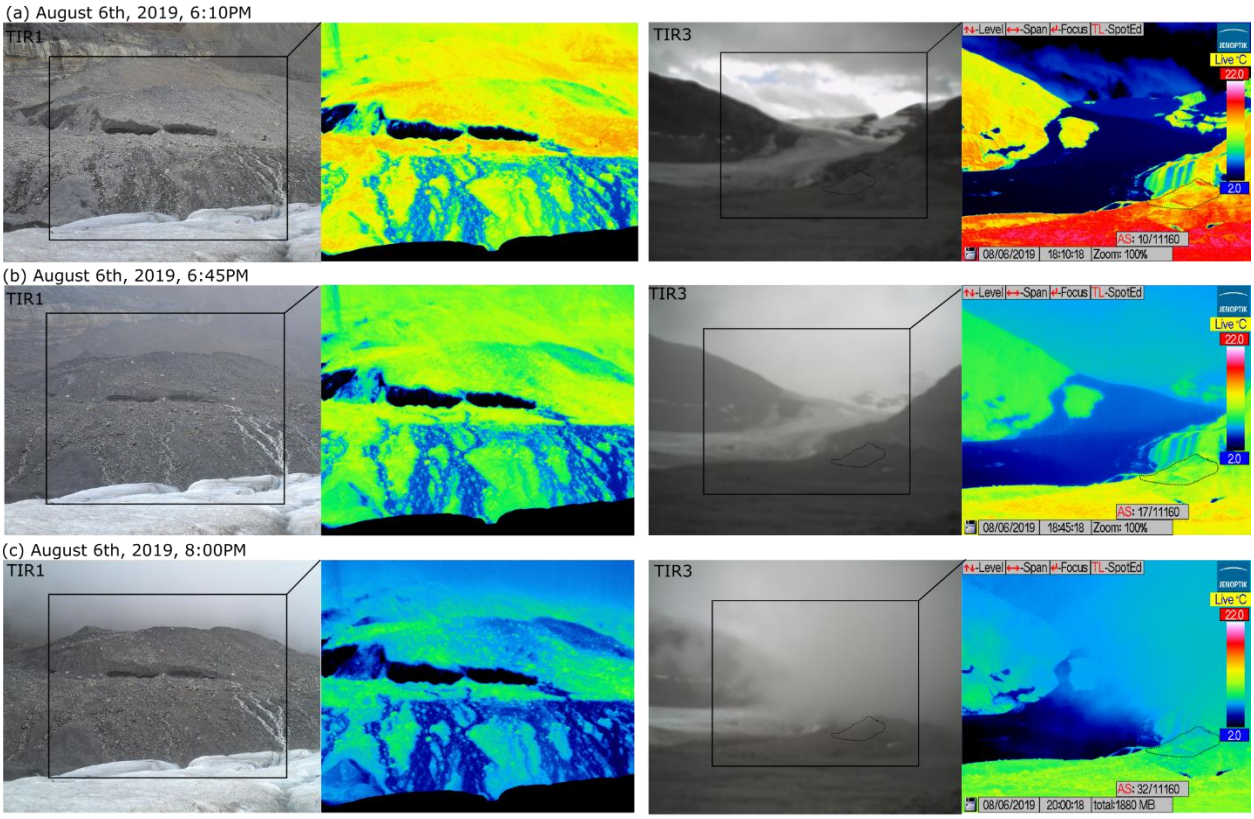

Figure A.4. Visual and raw TIR images from TIR1 and TIR3 for August 6, 2019, at (a) the beginning of the rain event (6:10 PM), (b) during the rain event (6:45 PM) and c) with low clouds (8:00 PM). Please note that the out-of-focus TIR3 images were not linked to the meteorological condition, but were due to a malfunction of the visual autofocus on the camera. The study slope in TIR3 is outlined in a dashed line.

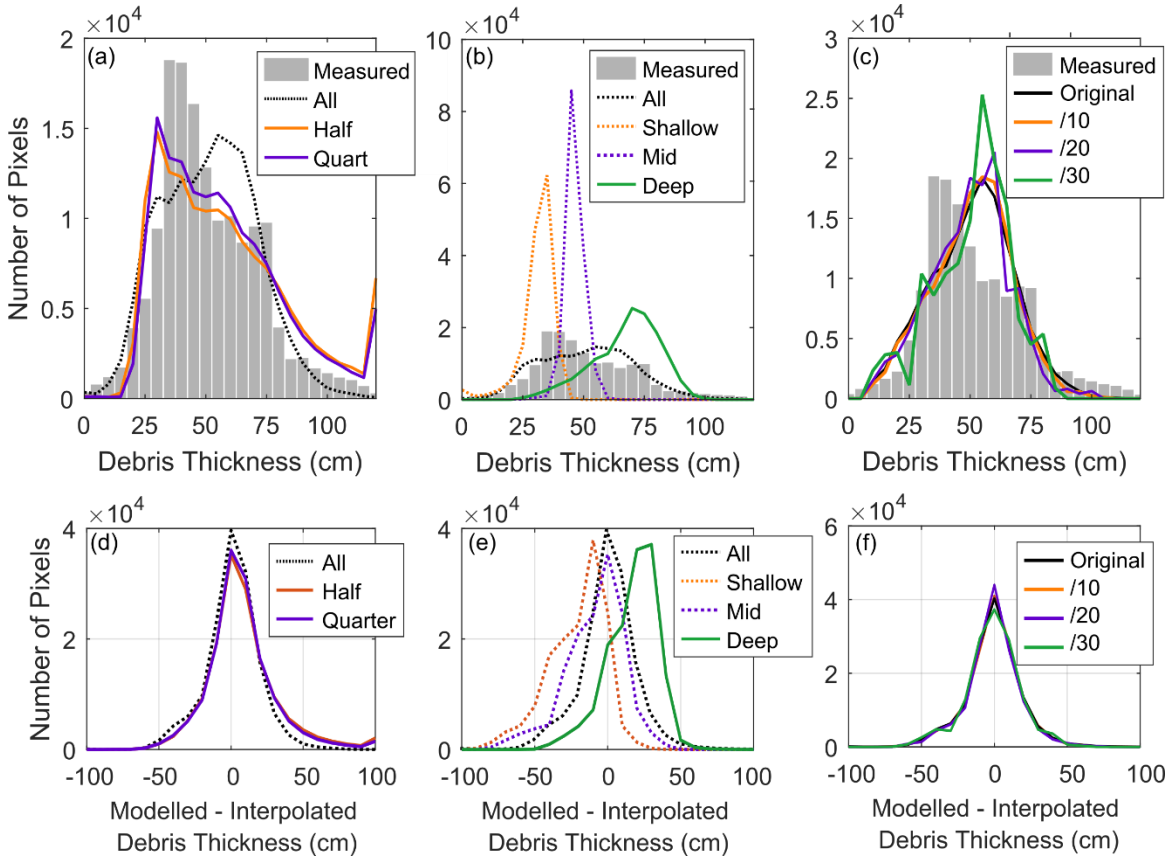

Figure A.5. Distribution of the difference between modelled and measured debris thickness depending on the number of manual excavations used to calculate the empirical models (a), the depth distribution of the excavations used (b) and the spatial resolution of the TIR images (c), and the distribution of the difference between the modelled and measured debris thickness for the corresponding scenario (d-f).

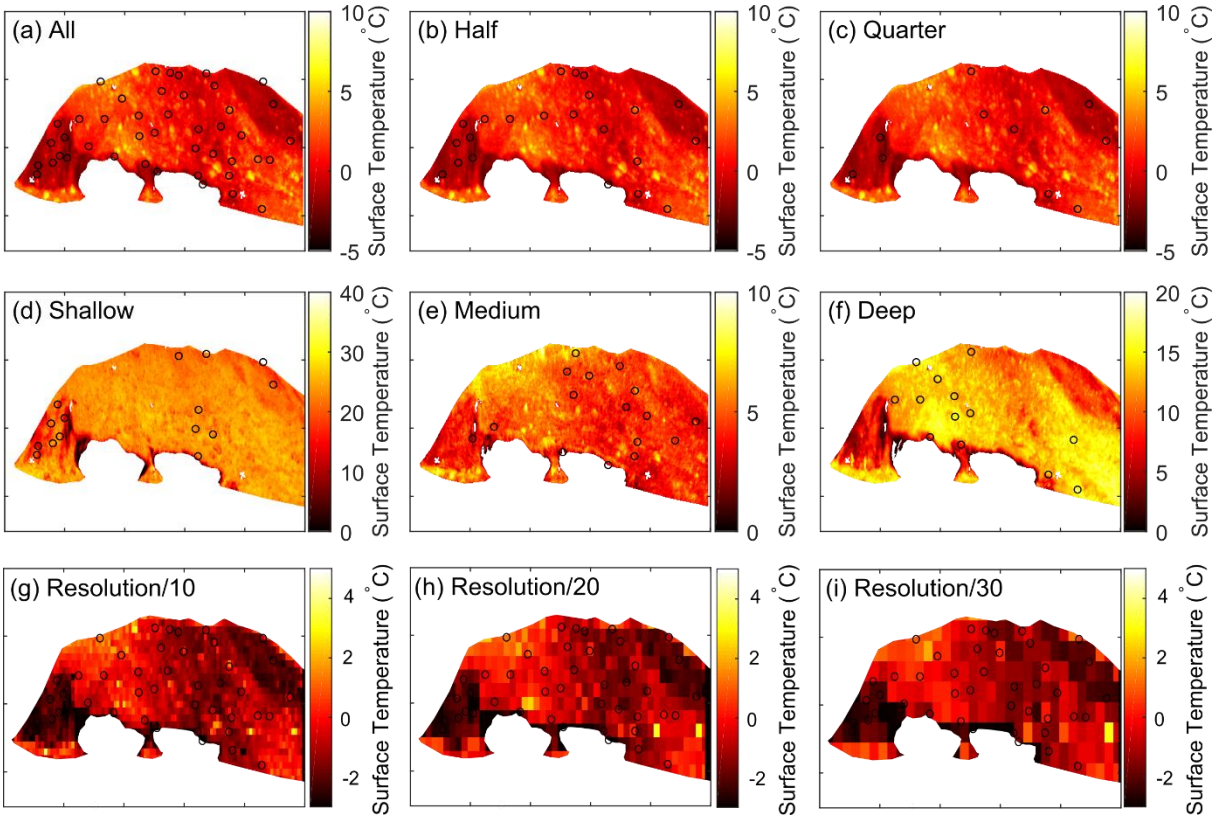

Figure A.6. The raw TIR surface temperature used to derive modelled debris thickness in the scenarios with all the manual excavations (a), half the manual excavation (b), a quarter of the manual excavations (c), and with only shallow manual excavations (d), medium depth manual excavation (e) and deep debris (f). Note the variable values of the colour bar across d-f.

APPENDIX B: SUPPLEMENTARY MATERIAL FOR CHAPTER 5

Table B.1. Meteorological measurements at the Athabasca Glacier ice and moraine automated weather stations

Station name	Location	Elevation	Variables	Interval	Gaps
Athabasca ice	52.19182, -117.25165	2177 m	U, RH, Ta, SW_{in}, LW_{in}	15 min	1 Jul - 13 Jul 2015; 25 Aug - 15 Sept 2017
			surface melt, albedo	Daily	-
Athabasca moraine	52.215362, -117.226359	1966 m	U, RH, Ta, SW_{in}, LW_{in}	15 min	-
			Precipitation	Daily	23 Jul 2019 - 3 Aug 2019; 22 Aug 2019 - 05 Sep 2019
			Time-lapse images	10AM, 1PM, 4PM	-

Table B.2. Number of time-lapse images for years 2015-2020 for each weather type, with percentages in parentheses, and number of days with consistent weather selected for the analysis of the meteorological conditions

		2015	2016	2017	2018	2019	2020	Total
Images	Clear sky	35 (15)	32 (14)	50 (19)	43 (16)	21 (9)	40 (17)	202 (15)
	Mixed	53 (23)	67 (29)	36 (23)	54 (10)	62 (27)	68 (29)	338 (24)
	Cloudy	127 (55)	132 (57)	83 (29)	68 (47)	148 (64)	114 (49)	694 (50)
	Dense Smoke	9 (4)	0	17 (16)	37 (9)	0	4 (2)	75 (5)
	Light Smoke	7 (3)	0	45 (13)	29 (19)	0	5 (2)	77 (6)
	Total	231	231	231	231	231	231	1386
Full days	Clear sky	8	9	12	8	4	12	53
	Mixed	34	40	26	21	37	37	195
	Cloudy	29	28	14	26	34	25	156
	Dense Smoke	3	0	13	8	0	1	25
	Light Smoke	2	0	10	13	0	2	27
	Total	76	77	75	76	75	77	456

Table B.3. Daily melt in mm w.e. for the four scenarios under varied weather conditions. The days where no smoke was detected show no values for the "With Smoke" and "With Fire" scenarios.

	Day	Weather type	No Fire	With Smoke	With LAIs	With Fire
2017	Aug 11	Clear	59	-	65	-
	Aug 12	Light smoke, with clear background	57	53	62	57
	Aug 13	Cloudy	36	37	38	38
	Aug 14	Smoky with background cloudy	22	21	23	22
	Aug 15	Light smoke with mixed background	43	39	47	42
	Aug 16	Light smoke with cloudy background	39	37	42	40
2018	Aug 11	Smoky with background cloudy	51	45	57	50
	Aug 12	Cloudy	35	-	37	-
	Aug 13	Clear	24	25	26	26
	Aug 14	Dense smoke with mixed background	58	56	67	64
	Aug 15	Light smoke with clear background	36	35	41	39
	Aug 16	Light smoke with clear background	56	52	65	60

Table B.4. Changes in seasonal melt compared to the "No Fire" scenario, in mm w.e. with percentage changes in parentheses

	2015	2016	2017	2018	2019
With LAIs	-116 (-3.5)	89 (2.7)	172 (4.9)	272 (7.9)	359 (10.2)
With Smoke	-17 (-0.5)	0 (-)	-97 (-2.7)	-68 (-2.0)	0 (-)
With Fire	-133 (-4.0)	89 (2.7)	67 (1.9)	193 (5.6)	359 (10.2)

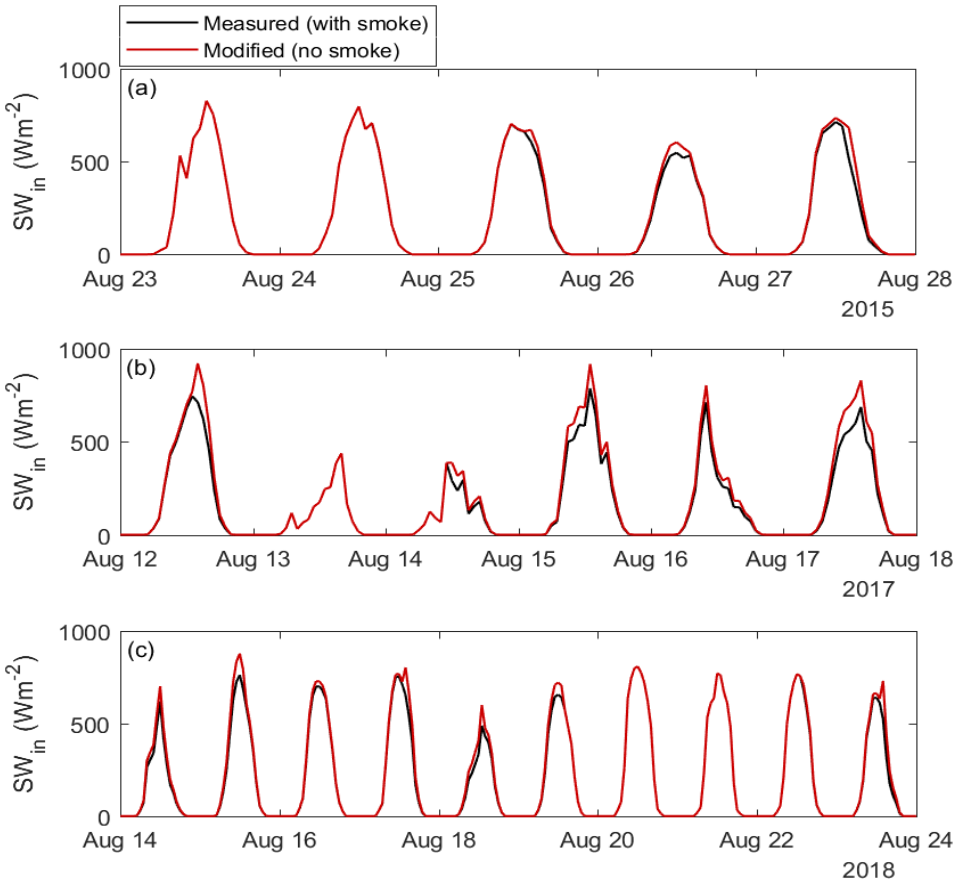

Figure B.1. Shortwave irradiance adjustment for selected smoky periods for the 2015, 2017 and 2018 melt seasons.

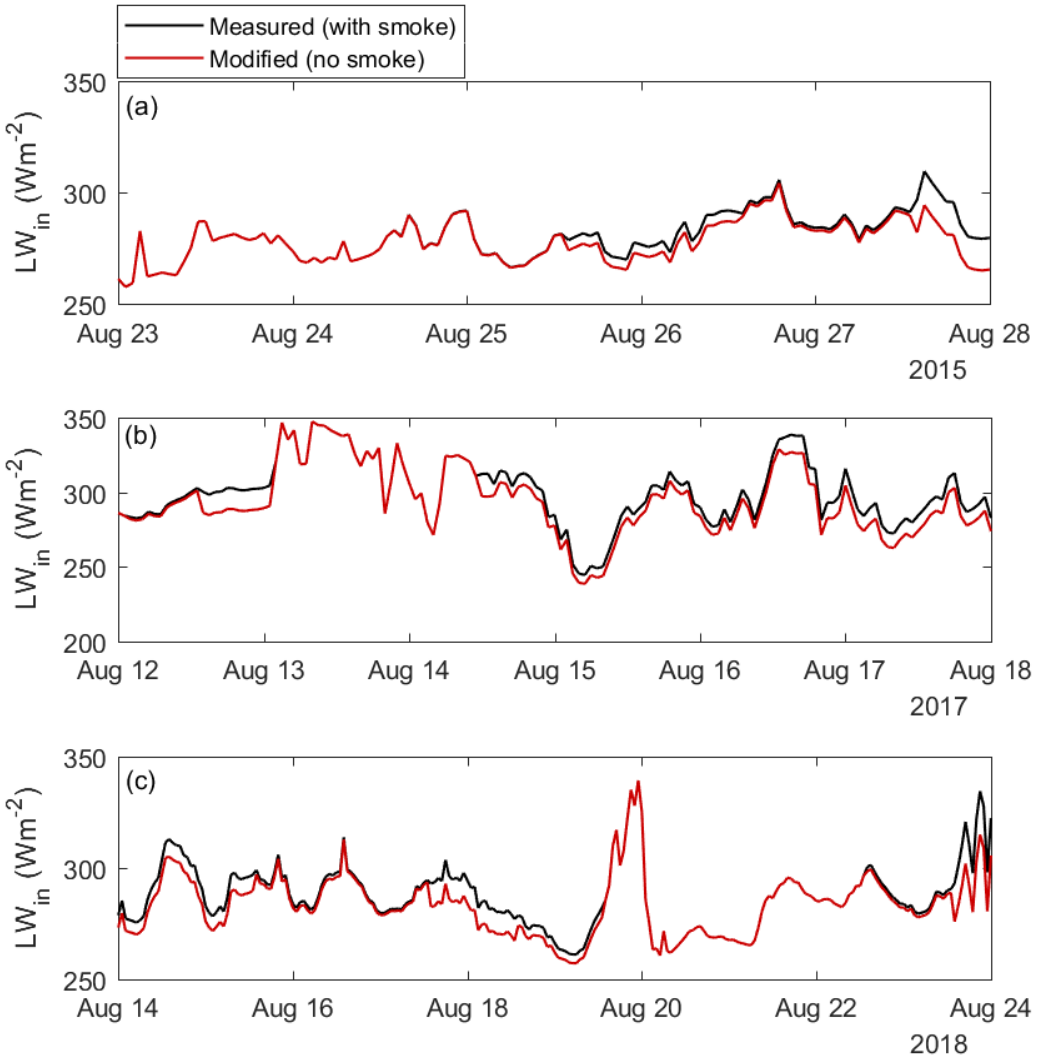

Figure B.2. Longwave irradiance adjustment for selected smoky periods for the 2015, 2017 and 2018 melt seasons.

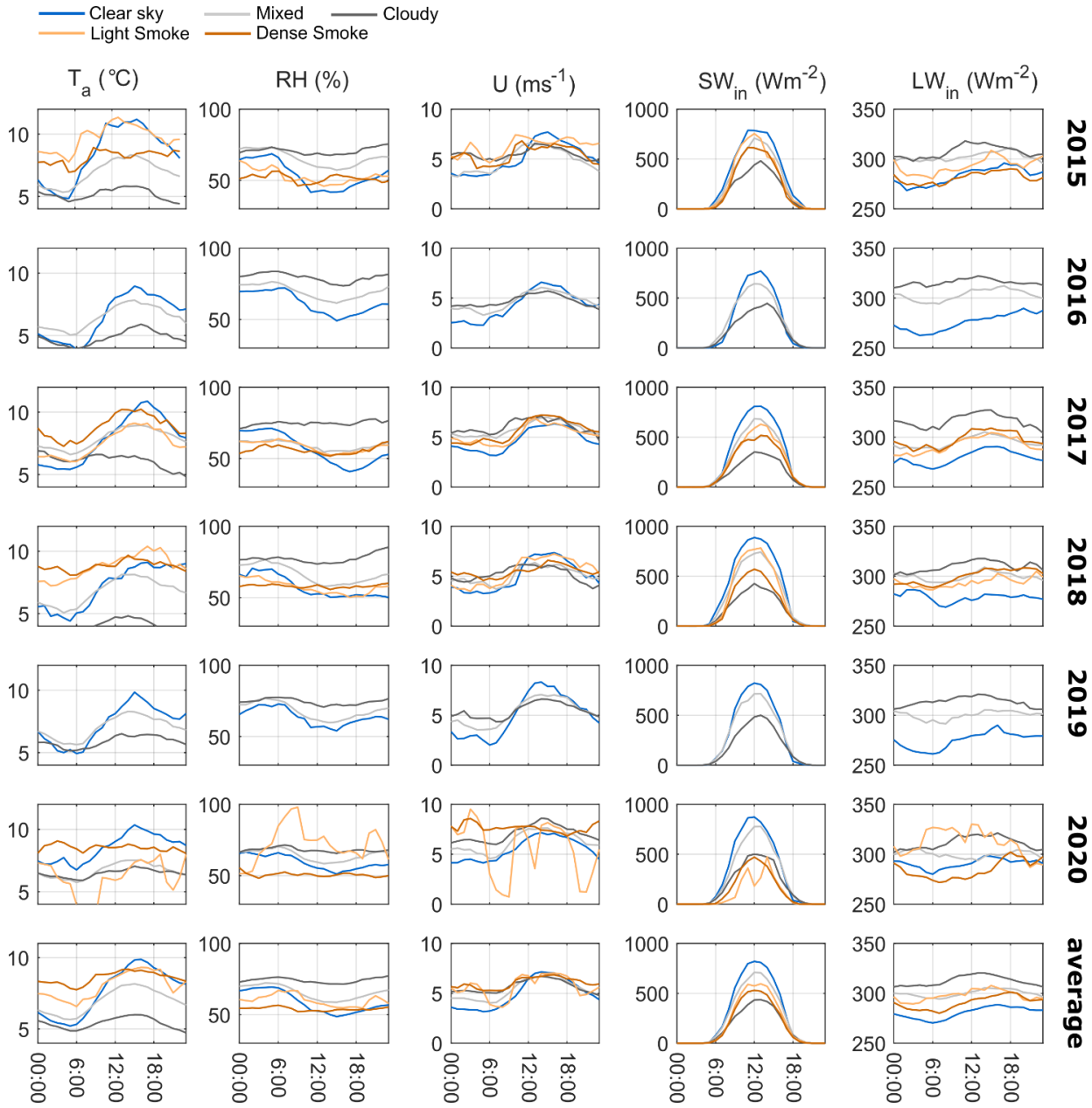

Figure B.3. Mean daily meteorological conditions for each weather type for each melt season over 2015-2020 and for the overall average conditions.

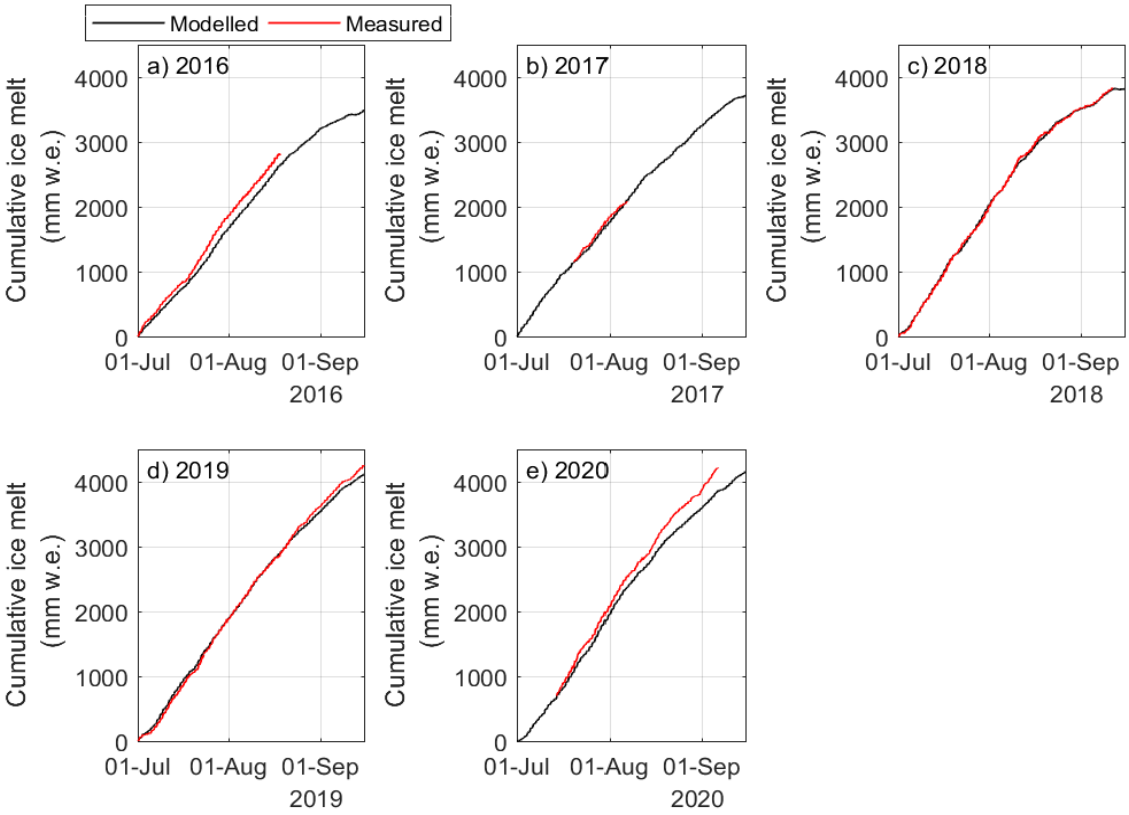

Figure B.4. Melt model evaluation, comparing measured surface melt (red) with modelled melt (black) for the 2016-2020 melt season.

APPENDIX C: SUPPLEMENTARY MATERIAL FOR CHAPTER 6

Table C.1. Geomorphic characteristics of the CRHM hydrological response units (HRUs). The HRU number are found in Figure 6.1b. The cover type refers to the landscape at the beginning of the simulation, and the land cover type in parenthesis refers to the landscape in 2015.

HRU number	Elevation (m)	Area (km^2)	Slope (°)	Aspect (°)	Cover Type
1	2949	0.3231	29.53	40	Glacier
2	2802	1.786	15.91	40	Glacier
3	2701	0.2819	5.203	344	Glacier
4	2654	0.8719	12.33	344	Glacier
5	2560	1.459	14.05	3	Glacier
6	2449	0.8744	8.181	352	Glacier
7	2252	0.3325	7.438	27	Glacier
8	2211	0.2331	4.749	350	Glacier (Moraine)
9	2176	0.2971	6.566	350	Glacier (Moraine)
10	2141	0.0863	13.96	307	Moraine
11	2956	0.2594	29.35	67	Glacier
12	2799	1.104	15.19	67	Glacier
13	2660	0.9737	15.33	60	Glacier
14	2552	0.3394	12.98	40	Glacier
15	2460	0.2731	10.9	75	Glacier
16	2405	0.2081	10.4	72	Glacier (Steep talus)
17	2251	0.0719	10.68	15	Debris-cover
18	2705	0.5981	20.14	84	Glacier
19	2545	0.3425	14.01	121	Glacier
20	2445	0.2275	10.06	111	Glacier (Moraine)
21	2200	0.1306	7.914	40	Debris-cover (Moraine)
22	2741	0.965	26.63	184	Steep talus
23	2501	0.7519	16.57	180	Moraine
24	2554	0.6163	43.62	103	Cliff
25	2273	0.4619	19.19	118	Ice-cored moraine
26	2215	0.26	14.16	145	Moraine
27	2771	1.395	27.97	250	Steep talus
28	2502	0.5512	13.54	256	Moraine
29	2285	0.4463	25.06	305	Ice-cored moraine
30	2702	0.4806	44.91	326	Cliff
31	2533	0.4644	26.58	287	Moraine
32	2375	0.9269	18.38	278	Moraine
33	2393	0.1144	8.185	33	Debris-cover
34	2413	0.1912	7.622	7	Glacier
35	2482	0.09313	24.17	70	Cliff
36	2727	0.35	30.54	80	Cliff
37	2847	0.2625	38.12	4	Cliff

Text C.1.

Glacier melt contribution to streamflow is divided between melt and wastage following Comeau *et al.* (2009), with wastage corresponding to net glacier volume loss resulting from negative mass balance and melt referring to a storage term from snowfall and snowmelt. A key difference is the inclusion of the firn melt component in the glacier ice melt calculations.

In years of positive or neutral mass balance, the glacier ice and firn melt is lower than the leftover snowfall at the end of the melt season, and no wastage occurs. During these years, the melt component equals the ice melt M_i.

$$M_i + M_f \leq P_s - M_s, \qquad Wastage = 0, \qquad Melt = M_i$$

Where M_i is the glacier ice melt, M_f is the glacier firn melt, P_s is the snowfall over the glacier area, and M_s is the snowmelt over the glacier area.

In years with negative mass balance, the ice and firn melt from the glacier area is larger than the residual snowfall at the end of the melt season:

$$M_i + M_f > P_s - M_s$$

$$Wastage = (M_i + M_f) - (P_s - M_s)$$

$$Melt = P_s - M_s$$

In years of negative mass balance, wastage is defined as the volume of ice and firn melt that exceeds the water equivalent volume of snow accumulation into the glacier.

The percentage of glacier wastage contribution to streamflow is calculated as a percentage of the annual basin yield, defined as the combination of streamflow simulated at the basin outlet and groundwater discharge from the basin.

The individual components of the wastage calculation are shown in Figure B.1. In the case of Peyto, due to both rain-on-snow events and snow redistribution from blowing snow and avalanches, the glacier area snowmelt (M_s) is slightly larger than the glacier area snowfall (P_s) for 21 out of the 32 years analyzed. In these 21 years, the snowmelt is on average 10% higher than the snowfall across the glacier, with a maximum difference of 27%.

Of the 32 years simulated, only two years do not have a wastage component, due to showing a positive mass balance with the ice melt component being smaller or equal to the snow remaining on the glacier at the end of the hydrological year ($P_s - M_s$). For the 30 years with wastage, the wastage volume was calculated as a ratio to the total basin yield (combined streamflow and groundwater) and contributed between 6% and 77% of basin yield, averaging 53%.

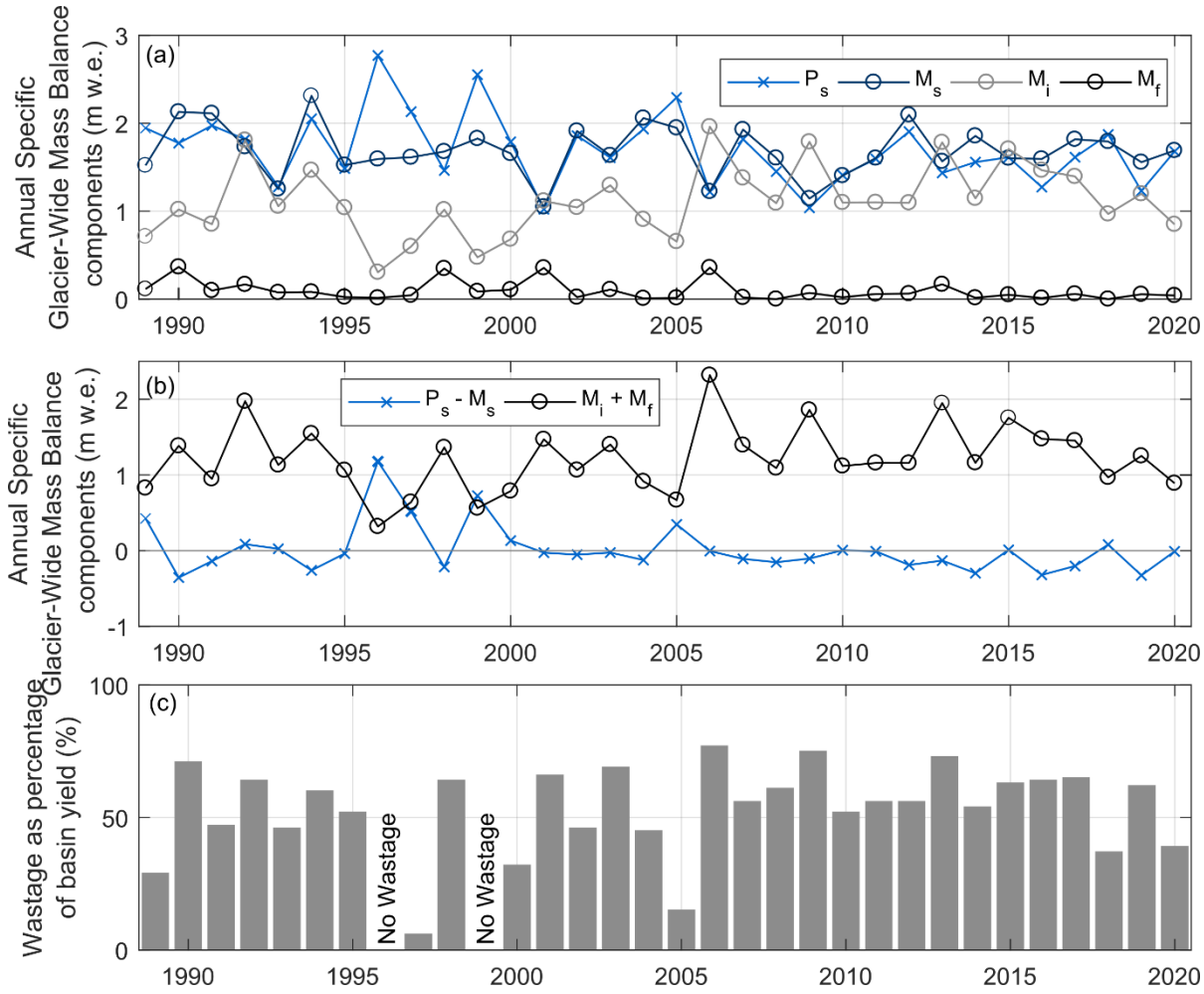

Figure C.1. Annual specific mass-balance components for the Peyto Glacier for years 1988-2020, with annual snowfall (P_s), snowmelt (M_s), ice melt (M_i) and firn melt (M_f) in (a), the combined snow components ($P_s - M_s$) and glacier ice and firn ($M_i + M_f$) and the wastage as a proportion of annual basin yield in (c).

APPENDIX D: SUPPLEMENTARY MATERIAL FOR CHAPTER 7

Table D.1. Geospatial attribute of the HRUs for the CUR and PGW geospatial attribute. The PGW attributes are indicated in parenthesis.

HRU number	Area (km^2)	Elevation (m)	Slope (°)	Aspect (°)	Cover Type
1	0.3231	2949 (2927)	30 (35)	40	Glacier
2	1.786	2802 (2744)	16 (20)	40	Glacier (Steep talus)
3	0.2819	2701 (2579)	5 (10)	344	Glacier (Steep talus)
4	0.8719	2654 (2573)	12 (15)	344	Glacier (Steep talus)
5	1.459	2560 (2484)	14 (18)	3	Glacier (Moraine)
6	0.8744	2449 (2338)	8 (14)	352	Glacier (Moraine)
7	0.3325	2252 (2141)	7 (15)	27	Glacier (Lake)
8	0.2331	2211 (2130)	5 (23)	350	Glacier (Lake)
9	0.2971	2176 (2149)	7 (25)	350	Glacier (Lake)
10	0.0863	2141	14	307	Moraine
11	0.2594	2956 (2942)	29 (35)	67	Glacier (Steep talus)
12	1.104	2799 (2751)	15 (20)	67	Glacier (Steep talus)
13	0.9737	2660 (2604)	15 (16)	60	Glacier (Steep talus)
14	0.3394	2552 (2492)	13 (15)	40	Glacier (Moraine)
15	0.2731	2460 (2393)	11 (14)	75	Glacier (Moraine)
16	0.2081	2405 (2349)	10 (22)	72	Glacier (Steep talus)
17	0.0719	2251 (2184)	11 (23)	15	Debris-cover
18	0.5981	2705 (2678)	20 (25)	84	Glacier (Steep Talus)
19	0.3425	2545 (2509)	14 (17)	121	Glacier (Moraine)
20	0.2275	2445 (2442)	10 (15)	111	Glacier (Moraine)
21	0.1306	2200 (2125)	8 (22)	40	Debris-cover
22	0.965	2741	27	184	Steep talus
23	0.7519	2501	17	180	Moraine
24	0.6163	2554	44	103	Cliff
25	0.4619	2273 (2263)	19 (21)	118	Ice-cored moraine
26	0.26	2215	14	145	Moraine
27	1.395	2771	28	250	Steep talus
28	0.5512	2502	14	256	Moraine
29	0.4463	2285	25	305	Ice-cored moraine
30	0.4806	2702	45	326	Cliff
31	0.4644	2533	27	287	Moraine
32	0.9269	2375	18	278	Moraine
33	0.1144	2393 (2287)	8 (12)	33	Debris-cover
34	0.1912	2413 (2320)	8 (16)	7	Glacier (Moraine)
35	0.09313	2482	24	70	Cliff
36	0.35	2727	31	80	Cliff
37	0.2625	2847	38	4	Cliff

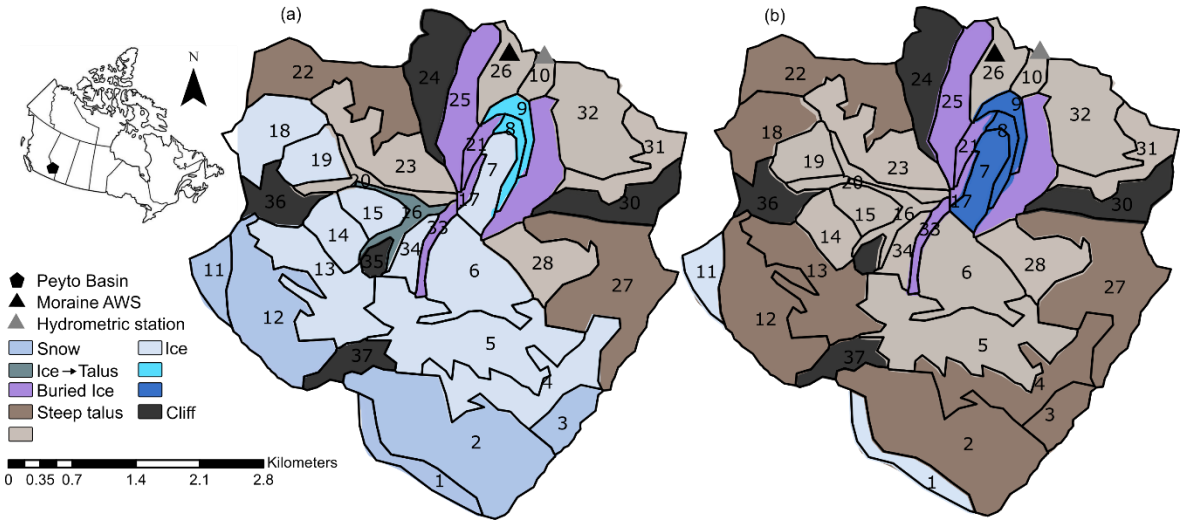

Figure D.1. HRU maps with number labels, for CUR (a) and PGW (b)

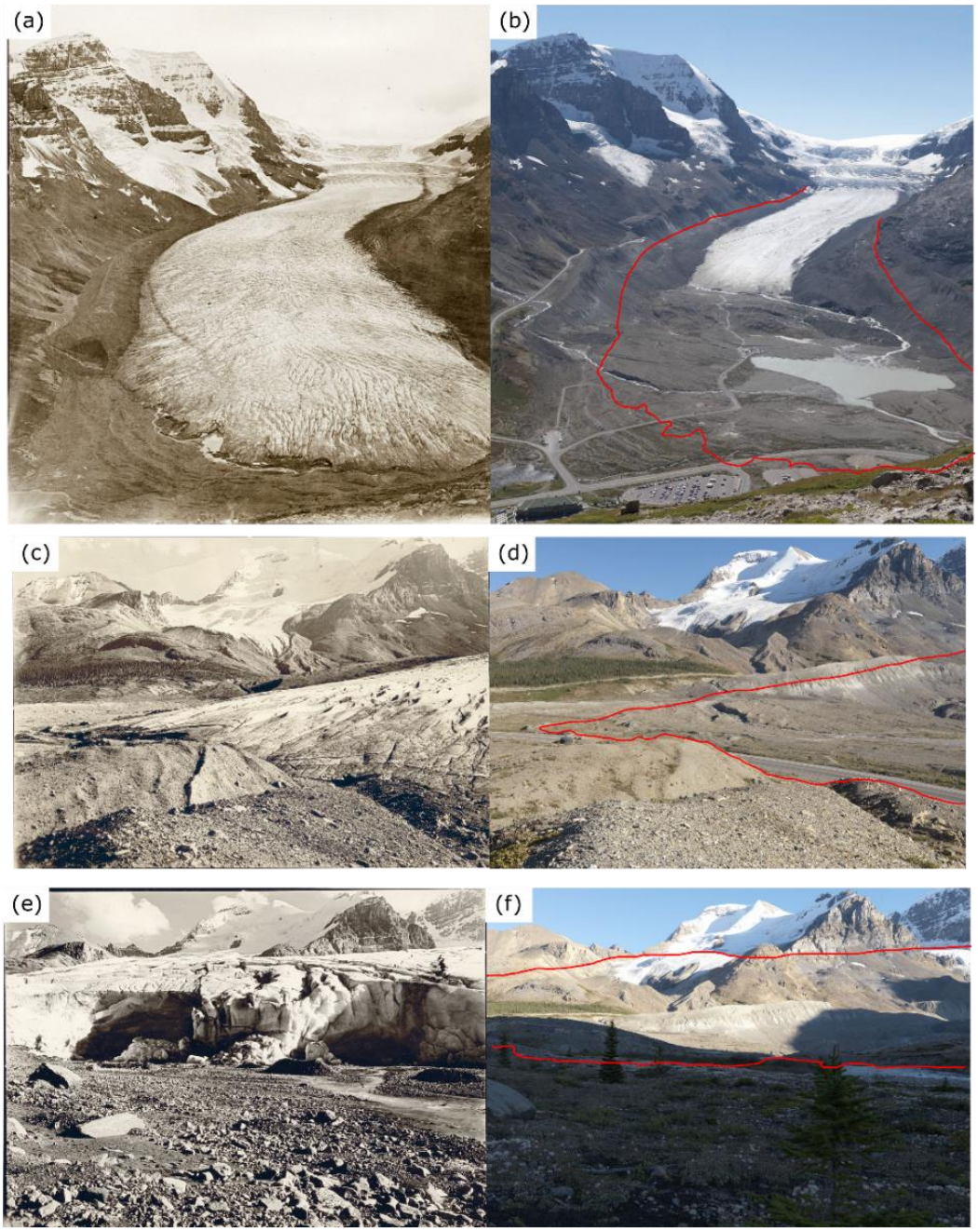

Figure D.2. Historical (1918) and current (2011) imagery from the Athabasca glacier, located100 km north of Peyto glacier. The red line in b, d, and f corresponds to the glacier extent in 1918. Imagery obtained from the Mountain Legacy Project (http://mountainlegacy.ca/)

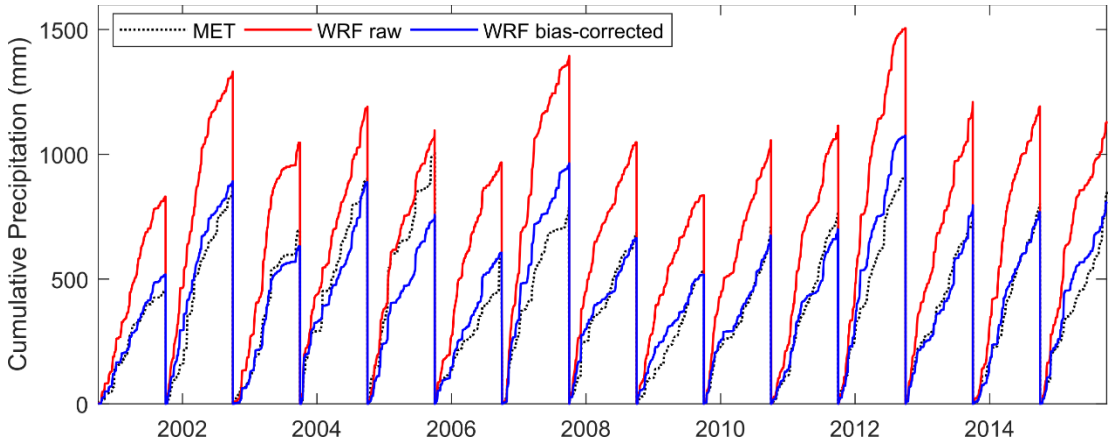

Figure D.3. Annual cumulative precipitation for Bow Summit, non-corrected WRF and bias-corrected WRF.

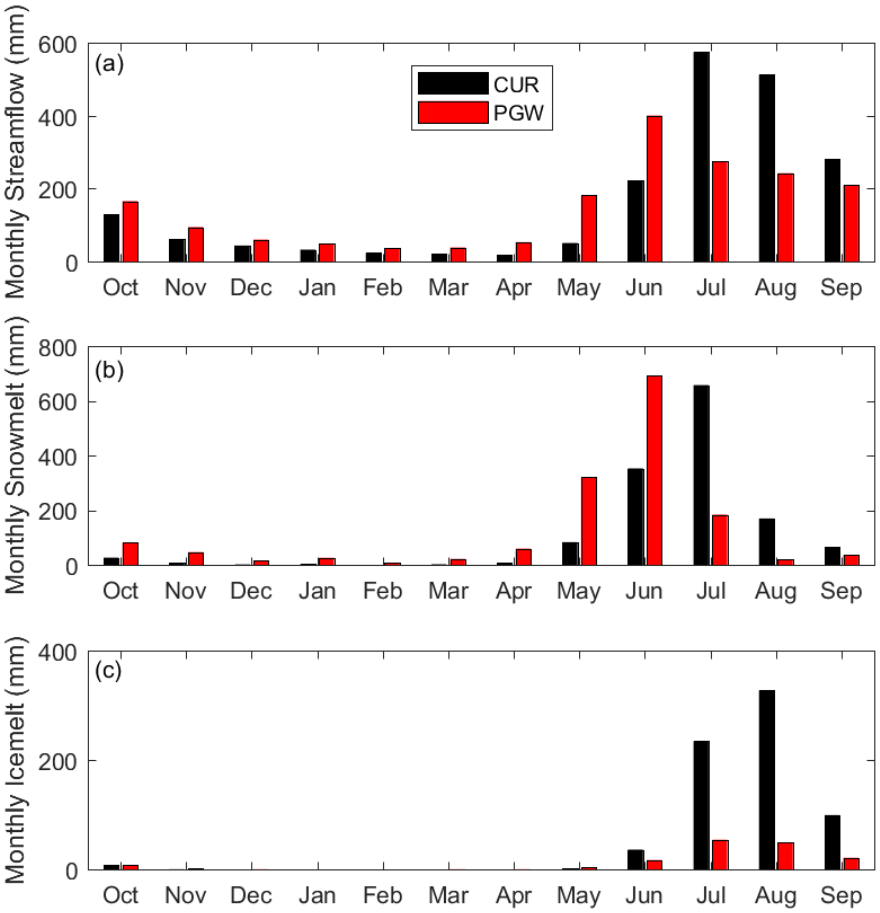

Figure D.4. Monthly basin streamflow (a) snowmelt (b) and icemelt (c) for the current (black) and PGW period (red).

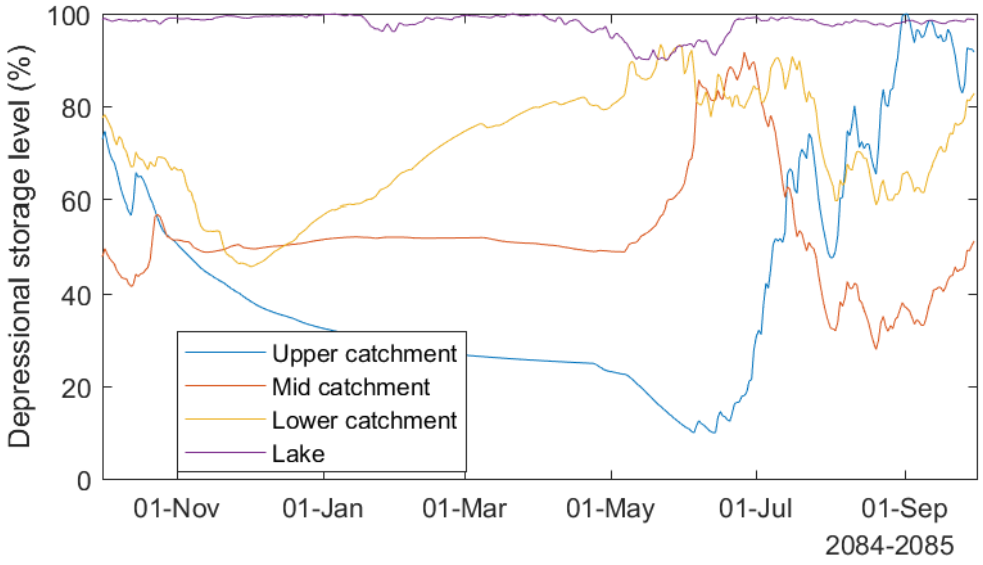

Figure D.5. Relative average depressional storage for basin elevation bands, with the lake located at the basin outlet for the PGW-Reference scenario. The proglacial lake stays near full for the entire year, decreasing its capacity to buffer streamflow in the proglacial lake scenario. The presence of ponding in the upper, mid and lower basin provide dynamic storage throughout the year.